Polymer-Integrated Organolead Halide Perovskite for Solar Cells and Self-Powered Electronic Devices

by

Rohit Saraf

A thesis

presented to the University of Waterloo

in fulfillment of the

thesis requirement for the degree of

Doctor of Philosophy

in

Chemistry (Nanotechnology)

Waterloo, Ontario, Canada, 2020

Examining Committee Membership

The following served on the Examining Committee for this thesis. The decision of the Examining Committee is by majority vote.

External Examiner	Ian Hill Professor
Supervisor	Vivek Maheshwari Associate Professor
Internal Members	Tong Leung Professor
	Pavle Radovanovic Professor
Internal-external Member	Michael Pope Assistant Professor

Author's Declaration

This thesis consists of material all of which I authored or co-authored: see Statement of Contributions included in the thesis. This is a true copy of the thesis, including any required final revisions, as accepted by my examiners.

I understand that my thesis may be made electronically available to the public.

Statement of Contributions

This thesis contains material from several published journal papers that I authored, some of which resulted from collaboration with my colleagues in the Maheshwari's group and with Professor Ting Tsui (Department of Chemical Engineering, University of Waterloo).

- Part of the content in Chapter 2 has been published in
  R. Saraf, V. Maheshwari, ACS Appl. Energy Mater. 2019, 2, 2214.
  R. Saraf conducted the experiments including device fabrication, characterization, and testing. Both authors analyzed and discussed the results and contributed to the writing of the manuscript.

- Part of the content in Chapter 3 has been published in
  R. Saraf, L. Pu, V. Maheshwari, Adv. Mater. 2018, 30, 1705778.
  R. Saraf and L. Pu contributed equally to this work. V. Maheshwari planned the idea, R. Saraf and L. Pu conducted all the experiments, and all authors analyzed and discussed the results and contributed to the writing of the manuscript.

- Part of the content in Chapter 4 has been published in
  R. Saraf, T. Tsui, V. Maheshwari, J. Mater. Chem. A 2019, 7, 14192.
  R. Saraf carried out the synthesis of the perovskite films and ZnO nanosheets, film characterization, and device measurement. T. Tsui conducted the elastic modulus testing of the perovskite films, and all authors analyzed and discussed the results and contributed to the writing of the manuscript.

- Part of the content in Chapter 5 has been published in
  R. Saraf, V. Maheshwari, ACS Appl. Mater. Interfaces 2018, 10, 21066.
  R. Saraf conducted the fabrication, characterization, and testing of the self-powered photodetector. Both authors analyzed and discussed the results and contributed to the writing of the manuscript.

Abstract

In recent years, organolead halide perovskites ($MAPbI_3$) have emerged as prospective materials for high-efficiency, inexpensive, and simple solution-processed optoelectronic devices such as solar cells, photodetectors, and LEDs. High efficiencies have been achieved in the lab for the perovskite solar cells, however, their stability under ambient operating conditions is the major concern that needs to be addressed for their commercial viability. The key factors that lead to instability are the migration of the constituting ions under electric fields (typically MA^+ and I^-) and degradation due to photo-activation and humidity. Current strategies for stabilizing perovskites typically target the interface of the perovskite layer or isolate the perovskite layer from the environment by encapsulation or use of inert conditions. But these strategies do not affect the inherent ion migration characteristics of the perovskite material itself. We show that similar to biomaterials such as bones that incorporate biopolymers (such as collagen) within an inorganic framework (hydroxyapatite crystals), by incorporating polymer chains with specific interactions in the perovskite films this challenge can be addressed.

We use the Lewis acid nature of PbI_2, a key chemical for making $MAPbI_3$ perovskite (and others) for in-situ cross-linking of polystyrene (PS) chains in the precursor solution. The resulting PS-$MAPbI_3$ devices without any encapsulating layer show a stable crystal structure in ambient conditions after more than 1000 h of continuous 1.0 sun (AM 1.5G) illumination in the air (relative humidity of 40–50%) at 45 °C, while also showing a slightly improved device performance. The stability is the result of the direct specific interaction between the polymer and the perovskite that reduces ion migration, charge recombination, trap-state density, and dark currents and at the same time leads to improve mobility and carrier lifetime. The interaction between the polymer and PbI_2 and MAI also improves the crystallization kinetics leading to larger grain size in the perovskite films. The cumulative effect of these improvements makes the reported polymer-perovskite hybrids well suited for long term device applications and presents a new avenue for making stable polymer-perovskite composites.

$MAPbI_3$ shows a distinctive combination of properties such as being semiconducting, with polarization and ion migration effects under poling by electric fields. The combination of its polarization and semiconducting nature is used to make a light harvesting, self-powered tactile sensor. Further, the integration of polymer chains leads to modulation of the mechanical

properties in $MAPbI_3$, making the films softer. As a result, these films have a lower modulus and are able to dissipate the applied mechanical stimuli. This sensor interfaces ZnO nanosheets as pressure sensitive drain on PS-$MAPbI_3$ film and once poled is operable for at least 120 h with just light illumination. The sensor is monolithic in structure, has a very wide operating range (up to 450 kPa), a high linear sensitivity over the whole range, and can operate continuously as the energy harvesting mechanism is decoupled from its pressure sensing mechanism. The films have an energy harvesting density of 1.1 W m^{-2} due to stable poling effects, which is comparable to the best reported triboelectric harvesters. The understanding of these effects in perovskite materials and their application in power source free devices is of significance to a wide array of fields where these materials are being researched and applied.

A monolith PS-$MAPbI_3$ photodetector is also presented that utilizes the material properties of $MAPbI_3$ perovskite leading for self-powered operation and achieves improved stability by compositing with PS. The self-powered operation makes this device suitable for remote sensing applications and smart systems. Improved stability of more than 20 days with performance maintained by over 80% under ambient conditions is achieved by incorporating PS without any additional fabrication steps. A plain $MAPbI_3$ device in comparison shows a performance degradation of 70−85% within 4 days of operation. The incorporation of PS also improves the current detectivity of the device by over 70 times as compared to plain perovskite. The PS-$MAPbI_3$ photodetector has a maximum photoresponsivity of 0.61 A W^{-1} and a detectivity of 1.5×10^{13} Jones. Stable self-powered operation is achieved by poling the PS-$MAPbI_3$ under a specific condition, subsequently, a sustained current (or voltage, under open-circuit conditions) is observed on illumination. These results demonstrate a simple and promising approach for developing high performance and a stable self-powered photodetector for next-generation optical communication, sensing and imaging applications.

The findings of this research to decouple the polarization and ion migration effects and using this understanding with the semiconducting properties in perovskites for developing light-powered devices will be of significant interest to the research community. This work also provides an insight into the improved perovskite stability and performance by the integration of a polymer which may lead to new avenues of polymer-perovskite composite assembly for long term device applications.

Acknowledgements

First of all, I would like to express my sincere gratitude to my supervisor, Professor Vivek Maheshwari, for giving me this wonderful opportunity to conduct my graduate studies with his research team and get valuable experience at the University of Waterloo. I am deeply grateful for him for giving me total freedom in choosing my Ph.D. research topic and showing trust in me. His unbounded commitment and overwhelming support have enabled me to successfully complete my Ph.D. thesis. I profusely thank him for his excellent guidance, encouragement and enduring throughout the four years of my graduate study. His amicable nature will always be a pleasant memory in my life.

I would also like to thank all my advisory committee members: Professor Tong Leung, Professor Pavle Radovanovic, and Professor Michael Pope for their encouragement, insightful comments, feedback, and excellent discussions during this work.

I am grateful to my fellow labmates: Long Pu, Avi Mathur, Venkatesh Gurupsarad, Fan Hua, and Shehan Salgado for stimulating discussions and their continuous support. Special thanks to Long Pu, Avi Mathur, and Venkatesh Gurupsarad for all the great moments and countless fun we have had in the last four years. I would also like to thank all my friends outside the University for making my stay in Waterloo a memorable one.

My appreciation for the help provided by Professor Ting Tsui from the Department of Chemical Engineering (University of Waterloo) with the elastic modulus measurement, Dr. Nina Heinig for providing me training on SEM machine, Dr. Joseph Palathinkal Thomas for helping me in characterizing materials in Professor Tong's lab. I would like to thank Cathy van Esch for all her administrative assistance and kindness.

Last but not the least, I owe more than thanks to my family members for their blessings, moral support, encouragement, and motivation.

Table of Contents

List of Figures

List of Tables

List of Abbreviations

Abbreviations	Full Names
2D	Two-dimensional
3D	Three-dimensional
AM	Air mass
CIGS	Copper indium gallium selenide
CNT	Carbon nanotube
CV	Cyclic voltammetry
DMF	Dimethylformamide
DMSO	Dimethyl sulfoxide
EDX	Energy-dispersive X-ray
EQE	External quantum efficiency
ETL	Electron transport layer
FESEM	Field-emission scanning electron microscopy
FF	Fill factor
FTIR	Fourier-transform infrared
FTO	Fluorine-doped tin oxide
GIXRD	Glancing incidence X-ray diffraction
GPa	Gigapascal
GPC	Gel permeation chromatography
HTL	Hole transport layer
IEC	International Electrotechnical Commission
IR	Infrared
ITO	Indium tin oxide
J_{sc}	Short-circuit current density
KPa	Kilopascal
LEDs	Light-emitting diodes
Li-TFSI	Lithium bis(trifluoromethanesulfonyl)imide
MA	Methylammonium

MAI	Methylammonium iodide
$MAPbI_3$	Methylammonium lead iodide
MEMS	Microelectromechanical systems
MG	Microgel
NMR	Nuclear Magnetic Resonance
MPP	Maximum power point
NREL	National Renewable Energy Laboratory
NW	Nanowire
P3HT	Poly(3-hexylthiophene)
PCBM	Phenyl-C_{61}-butyric acid methyl ester
PCE	Power conversion efficiency
PDMS	Polydimethylsiloxane
PEDOT:PSS	Poly(3,4-ethylenedioxythiophene) polystyrene sulfonate
PET	Polyethylene terephthalate
PL	Photoluminescence
PMMA	Polymethyl methacrylate
PS	Polystyrene
PS-$MAPbI_3$	Polystyrene-methylammonium lead iodide composite
PSC	Perovskite solar cell
PTAA	Poly[bis(4-phenyl)(2,4,6-trimethylphenyl)amine
PV	Photovoltaic
PVDF	Polyvinylidene fluoride
PVP	Polyvinylpyrrolidone
RPM	Rotations per minute
RT	Room temperature
S	Styrene
SCLC	Space charge limited current
Spiro-OMeTAD	2,2',7,7'-tetrakis(N,N-di(4-methoxyphenylamino)-9,9'-spirobifluorene
SRS	Stanford Research Systems

SWNT	Single-walled nanotubes
TFL	Trap-filled limit
TFT	Thin-film transistor
TGA	Thermogravimetric analysis
THF	Tetrahydrofuran
ToF-SIMS	Time-of-Flight Secondary Ion Mass Spectrometry
TRPL	Time-resolved photoluminescence
TW	Terawatt
UV	Ultraviolet
UV-Vis	Ultraviolet-visible
V_{oc}	Open-circuit voltage
XPS	X-ray photoelectron spectroscopy
XRD	X-ray diffraction

Chapter 1

Introduction

1.1. Organic-Inorganic Halide Perovskites

The perovskite first discovered in the Ural Mountains of Russia by Gustav Rose in 1839 was calcium titanate mineral ($CaTiO_3$) and is named after the Russian mineralogist Count Lev Alekseevich Perovski.[1] Perovskite has a specific crystal structure with the chemical formula ABX_3 (X = oxygen or halogen), in which A and B are cations and X represents an anion. The larger A cation occupies a cubo-octahedral site shared with 12 X anions, and the smaller B cation stabilized in an octahedral site shared with 6 X anions. The perovskite oxide materials are used in a wide range of applications such as ferroelectrics, high-temperature superconductors, and giant magnetoresistance devices.[2] In 1994, Mitzi and coworkers made an extensive report that layered organometal halide perovskites exhibit a semiconductor-to-metal transition with increasing dimensionality.[3] In addition to changes in electrical properties, the bandgap energy decreased with increased dimensionality from 2D to 3D, which is favorable for optoelectronic applications.[4]

Organometal lead halide perovskite ($CH_3NH_3PbX_3$ or $MAPbX_3$ (X = Br, I) was first used as a light-absorbing material in dye-sensitized solar cells by Miyasaka *et. al.* in 2009, which demonstrated 3.8% efficiency for X = I.[5] The efficiency of this configuration of perovskite-sensitized solar cells was increased to 6.5% by Park and his co-workers.[6] However, the liquid-based perovskite solar cell did not attract much attention due to an instant dissolution of ionic crystal perovskite in the polar liquid electrolyte, which leads to rapid degradation of device performance. In 2012, Park *et. al.* substituted the liquid electrolyte with a solid-hole conductor material to address the instability problem of the perovskite-based solar cells and increased their efficiency to 9.7%.[7] Since then, the $MAPbI_3$ perovskites have attracted enormous worldwide attention and prompted a dramatic increase in their power conversion efficiency to 25.2%.[8] They are also being applied in other optoelectronic devices such as sensors, photodetectors, lasers, displays, light-emitting diodes (LEDs), field-effect transistors, and resistive switching memory devices.[9–13]

1.1.1. Crystal Structure

The ideal ABX_3 perovskites are abided by the charge equation ($q^A + q^B = -3q^X$) for the neutrality.[14] For instance, the $CaTiO_3$ (metal oxide perovskite) must show up $q^A = +2$, $q^B = +4$, and $q^X = -2$ oxidation states. For $MAPbI_3$ (organic-inorganic halide perovskite), the oxidation states should be $q^A = +1$, $q^B = +2$, and $q^X = -1$. For organic-inorganic halide perovskite, the A site is occupied by monovalent organic cation, such as methylammonium ($CH_3NH_3^+$ or MA^+) or formamidinium ($HC(NH_2)_2^+$). The B site is occupied by a divalent inorganic cation, which could be Pb^{2+} or Sn^{2+}, and X is either I^-, Cl^-, or Br^- anions. The crystal structure of methylammonium lead iodide ($MAPbI_3$) is based on the cubic array of a corner-sharing network of PbI_6 octahedra, with the MA site cation located within the cuboctahedral cavities, as shown in **Figure 1.1**.[15]

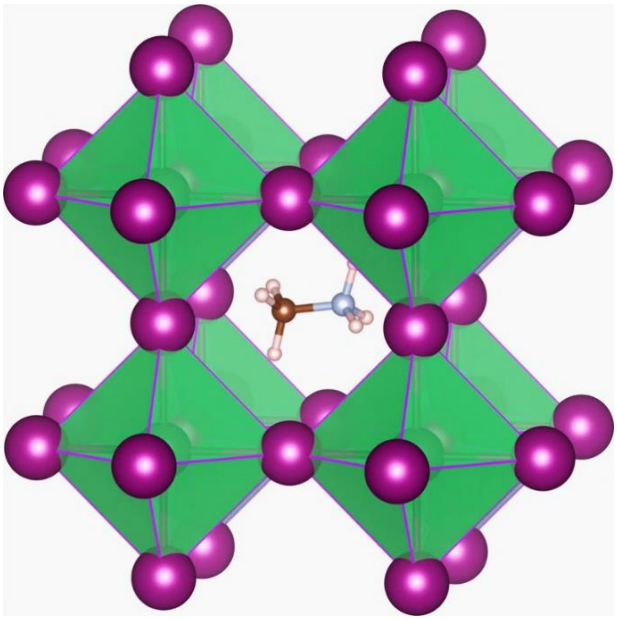

Figure 1.1. Crystal structure of 3-D methylammonium lead iodide ($MAPbI_3$) perovskite. The MA^+ is surrounded by PbI_6 octahedra. Image taken from Ref. [15].

The crystal structure of ABX_3 materials strongly depends on the size of the A and B cations, and X anion. The Goldschmidt tolerance factor introduced by V. M. Goldschmidt (1926) is a reliable empirical index to evaluate ionic size mismatches which the perovskite structure will tolerate until a different structure-type is formed.[16] The tolerance factor (t) is defined as follows:

$$t = \frac{r_A + r_X}{\sqrt{2}(r_B + r_X)} \tag{1.1}$$

where r_A is the radius of the A cation, r_B is the radius of the B cation, and r_X is the radius of the anion. In general, materials with a tolerance factor of 0.9−1.0 have an ideal perovskite with a cubic structure. While, when $t > 1.0$ or $t < 0.9$, the distortion from the ideal cubic phase will form orthorhombic, rhombohedral, tetragonal, or hexagonal structure.[17] For $MAPbI_3$ perovskite with the ionic radii of MA^+ = 270 pm, Pb^{2+} = 119 pm, and I^- = 220 pm, it tends to form a tetragonal structure at room temperature.[18] Temperature is another factor that can strongly influence the ionic radius, and consequently affect the tolerance factor and perovskite crystal structure. $MAPbI_3$ is shown to have three crystal structural phases: cubic above 327 K, tetragonal from 165 to 327 K, and orthorhombic below 165 K.[19,20] The cubic, tetragonal, and orthorhombic crystal structures have $Pm\bar{3}m$ (O_h symmetry), $I4/mcm$ (D_{4h} point group), and $Pnma$ (D_{2h} point group) space group, respectively.[14] The cavity in the inorganic cage (PbI_6) is much larger than the methylammonium cation (MA^+), which gives rise to the orientational disorder of MA^+.[21,22] When the temperature is below 165 K (i.e. orthorhombic phase), the MA^+ sublattice is fully ordered.[19] As the temperature increases, the MA^+ sublattice becomes more disordered,[19] and because MA^+ has a permanent dipole moment (~ 2.29 Debye), this disorder induces polarization and has been stipulated to cause ferroelectric effects.[23,24]

1.1.2. Optical and Electrical Properties

Organic-inorganic halide perovskites specifically $MAPbI_3$ exhibit attractive optical and electrical characteristics, which makes it a promising candidate in the optoelectronic field. $MAPbI_3$ perovskites have a very broad absorption spectrum from UV light to near IR regime.[6] The absorption coefficient of $MAPbI_3$ was estimated to be ~ 10^5–10^6 cm^{-1},[6,25] which is significantly higher than crystalline silicon and GaAs owing to its direct bandgap and higher density of state. The high absorption coefficient enables a thin perovskite layer with a thickness of around 100 nm–1 μm to efficiently absorb most of the incident light.[14] The optical bandgap energy of $MAPbI_3$ is ~ 1.58 eV, which can be tuned by partial substitution of iodide (I) with bromide (Br) or chloride (Cl).[26] According to the Shockley–Queisser limit, the optimal bandgap value under one sun illumination is ~ 1.1–1.5 eV.[27] The perovskite layer absorbs light to generate charge carriers, i.e. electrons in the conduction band and holes in the valance band. These photo-excited electrons and holes attract each other by Coulomb interaction, which gives rise to excitonic effects that modulate the optoelectronic behavior of $MAPbI_3$. The exciton binding energy in

$MAPbI_3$ is about 10 meV, which is much smaller than the thermal energy ($k_BT \sim 26$ meV; where k_B is Boltzmann constant and T is the temperature) at room temperature.[28] Thus, the exciton populations in $MAPbI_3$ are not stable at room temperature at moderate photoexcited carrier densities, and hence light absorption in $MAPbI_3$ creates free electrons and holes. These free charges are then transported toward the respective transport layers or metal electrodes by electrically induced drift and diffusion. The transport of charge carriers depends on the band structure of the material via their effective masses. The band structure E(k) can be locally approximated as[29]

$$E(\mathrm{k}) = E_0 + \frac{\hbar^2 k^2}{2m^*} \tag{1.2}$$

where E(k) is the energy of an electron at wavevector k in that band, E_0 is a constant giving the edge of the energy of that band, $\hbar(= h/2\pi)$ represent the Planck's constant, k is the effective momentum, and m^* is the effective mass. The electron and hole effective masses ($m^*_{e,h}$) are inversely proportional to the curvature of the conduction and valence bands, respectively. In $MAPbI_3$, $m^*_{e,h} \sim (0.1 - 0.15)m_0$, where m_0 is the free electron mass.[28] The charge carrier mobilities and diffusion coefficients, which indicate the carrier transport efficiency of material, are inversely proportional to the carrier effective masses. The diffusion coefficients and carrier mobilities for polycrystalline $MAPbI_3$ films have been reported to be 0.05–0.2 $cm^2\ s^{-1}$ and 1–30 $cm^2\ V^{-1}s^{-1}$, respectively.[30,31] The charge collection efficiency depends on the carrier mobility and its lifetime. The $MAPbI_3$ perovskite can conduct both electrons and holes owing to its long diffusion length. The polycrystalline $MAPbI_3$ films, under 1.0 sun illumination, have a long diffusion length of 100 nm to > 1 μm, and a long carrier lifetime of 100 ns to > 1 μs.[32,33]

1.1.3. Polarization Effect

Ferroelectric materials are characterized by a spontaneous electrical polarization (non-zero polarization even when an applied electric field is zero), that can be reversed by applying an external electric field in the opposite direction. Ferroelectricity has been extensively studied in several oxide perovskites such as $BaTiO_3$, $PbTiO_3$, $BiFeO_3$, etc, which are highly polar, and it provides a static dielectric constant in the order of 10^3. The existence of ferroelectricity in $MAPbI_3$ has been debated extensively over the past few years,[23,24,34,35] with recent reports again demonstrating the presence of ferroelectric domains in $MAPbI_3$ films at room temperature.[36,37]

The polarization in $MAPbI_3$ perovskite may arise from three major mechanisms: the rotation of dipolar MA^+ ion, the ionic polarization induced by the shift of the positive charge center of MA^+ relative to the negative charge center of the PbI_3^- cage, and the ionic polarization induced by the off-center displacement of Pb within the PbI_6 octahedra.[38,39] Theoretical calculations showed that the polarization induced by the rotation of MA^+ ions (6-8 μC cm^{-2}) is three times higher than that obtained by the Pb atom.[39] There was no obvious relation observed between the polarization direction and the average lead atoms displacement. MA^+ ion has a large dipole moment in its gas phase of 2.29 Debye, and the permanent polarization of $MAPbI_3$ is mainly contributed by the alignment of MA^+ ion.[21,38] The dipolar disordering or the rotational freedom of these MA^+ ion forms the important dipolar polarization mechanism, which has shown a significant contribution to the large dielectric constant of $MAPbI_3$ perovskite.[14] The tetragonal crystal structure of $MAPbI_3$ (stable at room temperature) has been reported to be ferroelectric due to the light-induced ordering of MA^+ ions,[40,41] and results in an internal electrical field originating from electrical polarization. The internal polarization developed during poling enables the separation of the electron-hole pairs and enhances the photovoltaic efficiency of this material.[42,43]

1.1.4. Challenges

For the optoelectronics industries, the factors determining cost per kWh by new solar technology are efficiency and long-term stability. To be considered reliable and stable, the photovoltaic (PV) modules have to pass the standard International Electrotechnical Commission (IEC) 61215 or 61646 design qualification testing protocols. To provide a warranty of PV modules (with encapsulation) for at least 25 years, the modules should retain a power output ≥ 80% of their initial output after 25 years. Despite exhibiting excellent power conversion efficiency of 25.2% in solar cells,[8] high responsivity of 10^4 A W^{-1} and detectivity of 3.7 x 10^{14} Jones in photodetectors,[44] and high photoluminescence quantum efficiency of more than 90% in quantum dots,[45], the long-term stability is the main obstacle hindering the commercialization of perovskite-based devices.[46–48] The extrinsic degradation factors (moisture, ambient air, UV illumination, and elevated temperature), and intrinsic degradation factors (ion migration effect) are the major causes that lead to the instability in the perovskites.

1.1.4.1. Extrinsic Degradation Factors

External factors such as water, heat, UV light, and oxygen strongly influence the perovskite absorber characteristics and functionality. Among different factors, moisture has been considered as one of the key challenges for the degradation of perovskites. The moisture instability originates due to the hygroscopic nature of amine salt (organic cation).[49] The methylammonium lead halide perovskites ($MAPbX_3$) endure moisture assisted degradation processes in which the methylamine group is lost via sublimation and PbI_2 is formed.[50] The decomposition of the $MAPbI_3$ crystal structure changes the perovskite film color from brown to a yellow PbI_2 film.[51] The possible degradation routes that $MAPbI_3$ films undergo in the presence of moisture are represented by the following chemical equations:[52]

$$CH_3NH_3PbI_3\ (s) \leftrightarrow PbI_2\ (s) + CH_3NH_3I\ (aq) \quad (1.3)$$

$$CH_3NH_3I\ (aq) \leftrightarrow CH_3NH_2\ (aq) + HI\ (aq) \quad (1.4)$$

$$4HI\ (aq) + O_2\ (g) \leftrightarrow 2I_2\ (s) + 2H_2O \quad (1.5)$$

$$2HI\ (aq) \leftrightarrow H_2\ (g) + 2I_2\ (s) \quad (1.6)$$

It has been reported that this reaction is reversible only if the water molecules form weak hydrogen bonds with the organic MA cation, which results in a reversible monohydrate ($CH_3NH_3PbI_3.H_2O$) perovskite phase. However, enough moisture penetration results in an irreversible dihydrate ($(CH_3NH_3)_4PbI_6.2H_2O$) phase, and leads to a permanent decomposition of the perovskite crystal.[53] As can be seen in Equation 1.5, the presence of oxygen results in more water production and hence leads to faster degradation of perovskites. Further, it has been reported that the rate of perovskite degradation will increase when high humidity is combined with UV light, heat, or an electric field.[54] Typically, the substantial degradation of perovskite devices takes place within a few hours on direct exposure at ambient conditions. One way to reduce this effect is to increase the bond strength between the MAI and PbI_2.

Besides moisture, the thermal stability of perovskites also raises a serious concern, which subjects to a high temperature causing degradation of the perovskite-based devices.[55] The decomposition temperature of $MAPbI_3$ has been reported between 200 and 300 °C. Two thermal decomposition pathways are possible based on the temperature:[55–57]

$$CH_3NH_3PbI_3\,(s) \rightarrow PbI_2\,(s) + CH_3NH_2\,(g) + HI\,(g) \quad (1.7)$$

$$CH_3NH_3PbI_3\,(s) \rightarrow PbI_2\,(s) + CH_3I\,(g) + NH_3\,(g) \quad (1.8)$$

The decomposition pathway in Equation 1.8 is thermodynamically favored as the temperature increases because its kinetic hindrance is mitigated at high temperatures.[57] When perovskite films are exposed to both light and oxygen, it will degrade the perovskite layer due to the formation of superoxide (O_2^-).[58,59] The photogenerated electrons on the perovskite reacted with molecular oxygen to form O_2^- species, which deprotonate the ammonium group in the perovskite and leads to its decomposition into methylamine (CH_3NH_2) and leaving behind PbI_2 and I_2, as shown in the following chemical equations:[54,60]

$$CH_3NH_3PbI_3\,(s) + h\nu \rightarrow CH_3NH_3PbI_3^* \quad (1.9)$$

$$CH_3NH_3PbI_3^* + O_2 \rightarrow CH_3NH_3PbI_3\,(s) + O_2^- \quad (1.10)$$

$$4CH_3NH_3PbI_3^* + O_2^- \rightarrow 4CH_3NH_2\,(g) + 4PbI_2\,(s) + 2I_2\,(g) + 2H_2O \quad (1.11)$$

1.1.4.2. Intrinsic Degradation Factors

The ion migration is detrimental to the performance of perovskite-based optoelectronics and their long-term stability.[61,62] Factors such as moisture, UV light, electric field, and heat during device operation have a catalytic effect on the ion migration in perovskites and result in a faster decay of perovskite device performance.[63] Halide-based perovskites have been known as ion conductors since the 1980s.[64] In these perovskites, the charged ions are another type of species which are mobile in addition to the charge carriers. The Schottky defects (cation and anion vacancies), Frenkel defects (interstitial sites), or structural defects (grain boundaries, interfaces, and lattice distortion by impurities) are available in the complex $MAPbX_3$ stoichiometry, which allows the migration of constituent ions along these defect sites.[65] The ion migration mobility (μ_m) can be defined as:[66]

$$\mu_m = \frac{A}{T}\exp\left(\frac{-E_A}{k_B T}\right) \quad (1.12)$$

where E_A is the activation energy for ion migration, A is material dependent constant, k_B is the Boltzmann constant (8.617×10^{-5} eV K^{-1}), and T is the absolute temperature. E_A is a measure of how easily ions can migrate, and several factors can influence the value of E_A, such as crystal

structure, ionic radius, the charge of the ions, the valence state of the ions, and the jumping distance between adjacent defects.[65] Generally, the ions migrate faster in crystals with more and bigger available interstitial sites, smaller and less charged ions, and smaller jumping distance.[65]

In $MAPbI_3$, the possible ions that can migrate are MA^+, Pb^{2+}, and I^- ions.[15,65] The theoretical and experimental studies revealed that the I^- ions migrate along the I–I edge of the PbI_6 octahedron and have the lowest E_A of 0.08–0.58 eV; the MA^+ ions migrate through the unit cell face comprising four I^- ions and have higher E_A of 0.46–0.84 eV; and the Pb^{2+} ions migrate along the diagonal of the cubic unit cell and have the highest E_A of 0.80–2.31 eV.[14,15,65] Due to the low migration-activation energies of I^- and MA^+ ions, these ions are mobile in the $MAPbI_3$ films and are responsible for the origin of *I–V* hysteresis in the perovskite solar cells.[65] Under the applied bias (electric field), these ions can move easily and can accumulate at interfaces with metal electrodes, the accumulated ions lead to the formation of an internal electric field in opposite direction inside bulk perovskite that consequently affects the device performance.[67,68] The ion migration in the presence of electric fields, if limited, can lead to local doping effects that have been shown to cause anomalous photovoltaic effects and self-powered operations.[69] But, over time, this leads to the decomposition of the $MAPbI_3$ into PbI_2 and other products such as HI, CH_3I, and NH_3. The ion migration under the electric field is related to the presence of defects in $MAPbI_3$ films.[65] Yuan *et al.* showed different ion migration channels in the solid perovskite film (**Figure 1.2**).[65] Among several possible ion migration channels, the migration through the grain boundaries is the most dominant one.[14,65] The density of vacancies at the grain boundaries is much higher than that in the bulk crystal due to the dangling bonds, lattice dislocation, and defect segregation. Owing to this, they showed that the E_A for ion migration at grain boundaries is about half of the E_A in the bulk and hence is favorable for the migration of ions.[65]

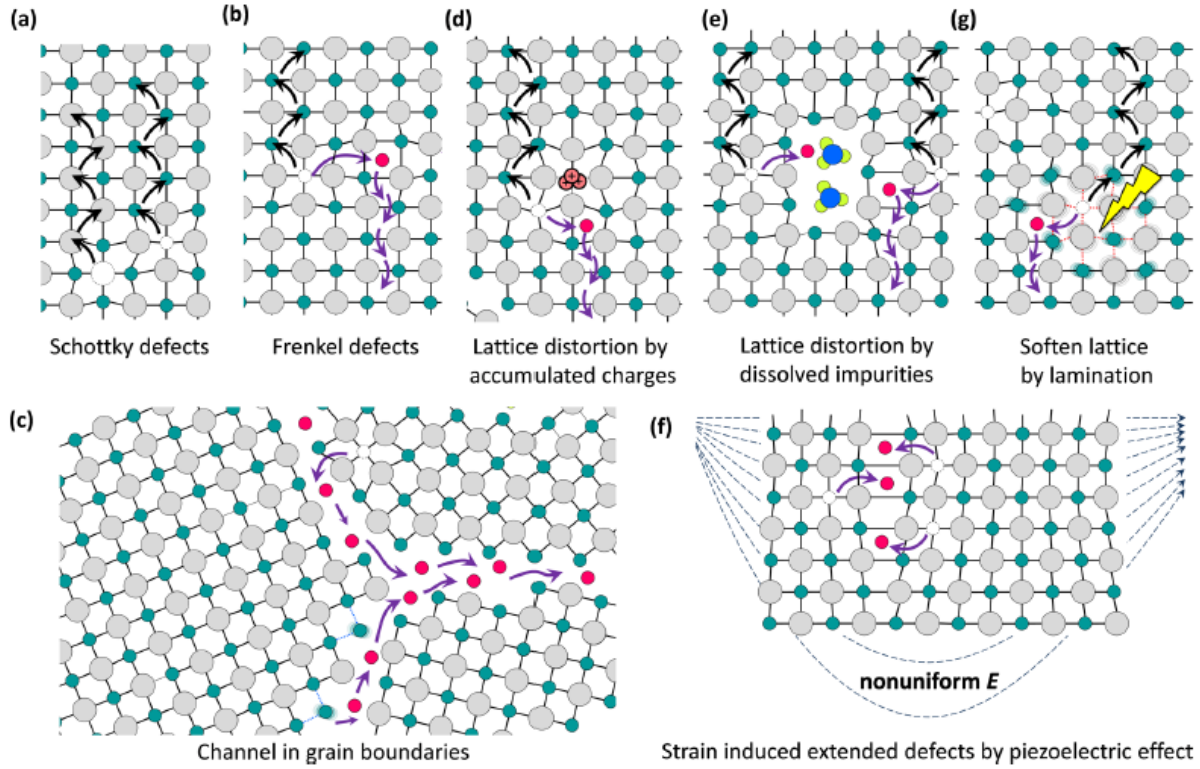

Figure 1.2. Different ion migration pathways in the perovskite film. Image taken from Ref. [65].

1.1.4.3. Strategies for Improving Stability and Suppressing Ion Migration

To overcome the stability issue and ion migration effect, a variety of strategies have been used. For instance, the constituting ions in the perovskite (MA^+ and I^-) have been substituted with other cations such as formamidinium ion (FA^+), cesium ion (Cs^+) and anions such as Cl^-, Br^-.[70] This is done for improving the weak interaction that the A cation has with B and X. However, the possible ions that can be used are limited by the constraint to maintain the crystal structure of the perovskite. Even with the use of other ions, only limited stability has been achieved. Another strategy has been to encapsulate the device or operate it in an inert atmosphere such as using N_2 or Ar.[47,71] This improves the stability and the devices can be operated for more than 1000 h, but this is hardly a viable option given the cost of running and fabricating such devices. A similar passivation approach of adding a top barrier layer made of specific chemicals such as NiO_x nanoparticles, polymers such as PMMA, graphite, and PCBM has been applied to the perovskite films.[46,72,73] These methods reduce the effects of environmental factors such as humidity, but the intrinsic instability of the perovskite (including photodegradation and electric field-induced

migration) remains untreated. The crystal grain boundaries play a critical role in both intrinsic and extrinsic instability of perovskites and also influence their properties. For instance, the mobility and charge carrier lifetimes are significantly increased by having larger grain size and passivation of defects at the grain boundaries.[14,71] At the same time, it also reduces the ion migration effects by stabilizing the structure of the perovskite films. This has led to the use of a Lewis acid-base adduct approach to make high-quality perovskite films. In this approach, the Lewis acid nature of PbI_2 (and other lead halides which are the precursor for making these perovskite films) is used in combination with a solvent that has Lewis base characteristics (such as DMF and DMSO, and additives such as Urea, etc.) to form an adduct.[74] This leads to a simple solvent-based casting method where due to the adduct formation the crystallization kinetics are favored and larger crystal grain size is observed in the perovskite films compared to synthesis in the absence of adduct formation. Still, long-term stabilization (operating for 1000's h) of these materials has not been achieved in ambient operating conditions. Progress has been made by passivating the devices and protecting it from external degradation, but such a solution is at the best partial, as long as the intrinsic instability is not being addressed.[46,47]

The motivation is to improve the intrinsic and extrinsic stability of perovskite-based devices without compromising the cost, ease of fabrication, and performance of the device. We address the stability challenge in perovskites by the use of a specific polymer (polystyrene (PS)) that interacts with the perovskite precursors. The interaction is based on the Lewis acid nature of PbI_2 that leads to cross-linking of the polymer chains, and also the interaction between the MAI and PS chains due to the cation-π electron interaction. Subsequently, this leads to a hybrid that incorporates a polymer matrix within a perovskite film. These films are stable in ambient conditions under continuous light illumination for more than 1000 h, without the use of any encapsulating layer (details in Chapter 2). We used these PS-$MAPbI_3$ films to fabricate the highly stable and efficient solar cells as well as to develop the high performance self-powered tactile sensors and photodetectors.

1.2. Solar Cells

Global energy consumption has been gradually increasing, with the Energy Information Administration predicting that the world total energy consumption in 2015 is 16 TW, and this energy demand will increase to 30 TW by 2050.[14,75] Today, more than two-thirds of the total

energy consumed is produced by conventional (or non-renewable) energy sources or fossil fuels, i.e. oil, natural gas, coal, etc. The traditional fossil energy cannot meet the needs of sustainable development in the future in accordance with renewable, clean, sufficient, and nontoxic one. So, there is a need for energy sources that are sustainable and causes less environmental pollution. Solar energy is an inexhaustible green and renewable energy source, and the energy illuminated from the sun in 1 h is sufficient to power the Earth for an entire year.[76] Photovoltaic (PV) devices convert solar energy into electricity and are promising candidates to offset carbon emissions while providing an alternative way to meet the increasing energy demands for future generations. Despite the massive potential and incredible technological progress, PVs contribute only to a small (< 2%) fraction of global energy consumption.[75,77] This can be due to the large PV market share of ~ 90% is dominated by crystalline silicon, a technology that has high manufacturing and installation costs.[78] It has managed to reach power conversion efficiencies (PCEs) of 26.1% in over half a century.[8] Further, it has inherent technological limitations such as indirect bandgap, requires high-purity materials, high-temperature processing, and can form on bulky and rigid modules (poor flexibility).[78,79] Other established inorganic solar cells such as GaAs, CdTe, and copper indium gallium selenide (CIGS) have been studied extensively over the past few decades achieving PCE of 23.4% (CIGS) and 22.1% (CdTe).[8] In less than a decade, the PCEs of perovskite solar cells have reached 25.2% and outperformed the two commercially established thin-film technologies (CIGS and CdTe).[8] The perovskite solar cells are a potentially transformative PV technology that offers several advantages as compared to other solar cells including broad absorption spectrum, direct bandgap, abundant material, low cost, and facile processability.[46,47,80] Moreover, it combines distinct merits of several predecessor PV technologies: high efficiency (crystalline silicon PV), scalable low-temperature solution processability and color tunability (organic, dye-sensitized, and quantum dot-based thin film PVs), and lightweight and flexibility (GaAs, CdTe, and CIGS thin film PVs).[81] Despite all these excellent properties of perovskite solar cells, the long-term stability (as discussed before in section 1.1.4) remains a critical hurdle for its commercialization.

The objective is to significantly enhance the stability of the perovskite solar cells while maintaining (or improving) its efficiency. We are using the specific interactions between the polystyrene and the perovskite precursors that result in the observed enhancement. The polystyrene-perovskite solar cells in ambient conditions with no encapsulating layer show stable

operation for 1000 h under continuous 1.0 sun illumination, in contrast, plain perovskite cells degrade rapidly within 20−30 h (details in Chapter 2).

1.3. Tactile Sensors

The tactile sensor is a device that can measure the pressure, vibration, shape, texture, and temperature by physical contact between the sensor and the object.[82] Human skin (with tactile sensing properties) is one of the most complex and fascinating organs, which complements our vision and sound enabling us to interact with the surrounding environment.[83,84] In human glabrous (hairless) skin, there are four main mechanoreceptors: Meissner's corpuscles, Merkel disks, Ruffini organs, and Pacinian corpuscles, organized in deep and shallow layers.[82] These receptors are highly sensitive to mechanical stimuli and will convert the mechanical stimuli into physiological signals, which are then interpreted by the brain. Through tactile perception, humans can perceive object properties such as size, hardness, temperature, contour, etc.[82,83] Tactile sensing has been a significant area of research for its applications in electronic skin (e-skin), wearable electronics, human electronics interfacing, and microelectromechanical systems (MEMS).[85−89] To mimic the properties of human skin, firstly e-skin needs to have a high tactile sensitivity over a broad operating range. For instance, low pressure (< 1 kPa) detection of acoustic sound and respiration, medium pressure (1−10 kPa) of pulse pressure and gentle touch, and large pressure (> 10 kPa) of plantar foot.[90] Secondly, e-skin should differentiate spatiotemporal tactile stimuli (static and dynamic pressure), which allows dexterous manipulation of objects and the perception of vibration and surface textures.[91] Thirdly, linear pressure-sensing capability and cyclic reliability are important requirements to use e-skins for practical applications. Tactile (or pressure) sensors are based on different sensing mechanism including piezoresistivity,[92] capacitance,[93] and piezoelectricity[94]. Among these types of pressure sensors, piezo-resistive devices, which transduce applied pressure into an electrical current, have been widely used because of the ease of signal processing. Currently, the materials used for tactile sensors are prepared by 1) coating conductive materials such as metal, graphene, single-walled nanotubes, and conductive polymers onto microstructured templates, and 2) directly forming conductive microstructures with a conductive material-elastomer mixture.[92,95−98] Although they attain a high sensitivity, achieving it in combination with a wide operating range and linear response still remains a challenge. Further, one common limitation is

that most of these sensors depend on an externally supplied power source. Although the piezoelectric and triboelectric nanogenerators are used as a self-powered sensor,[99,100] the challenge in such systems is, 1) decoupling of the sensing of the stimuli from the energy harvesting mechanism which is required for continuous operation of the devices, 2) ability to sense both static and dynamic signals in the stimuli, and 3) developing monolith structure devices to have simple configuration that reduces the cost and the complexity of manufacturing.

The motivation is to combine the high sensitivity, linearity and operating dynamic range with the self-powered operation (negating the need for an external power source) of the tactile sensor. To achieve these outstanding properties, we develop a solar/light-powered monolith tactile sensor based on perovskite material. The device continuously generates power based on the combined polarization-semiconducting property of the $MAPbI_3$ perovskite material. The tactile sensing is based on ZnO nanosheets, which acts as a dynamic electron drain on the $MAPbI_3$ film (details in Chapter 3). Further, the integration of polystyrene with $MAPbI_3$ films leads to a wide operating range (up to 450 kPa) with the linear response over the whole range and high sensitivity as well as makes these films structurally highly stable (details in Chapter 4). The use of lead-based perovskite materials in the self-powered tactile sensors will limit their use in remote sensing and space applications.

1.4. Photodetectors

Photodetectors are the optoelectronic devices that can convert incident light into an electrical signal via the photoelectric effect, which usually manifests as a photocurrent. Photodetectors are crucial for a variety of industrial and scientific applications, including optical communications, imaging, environmental monitoring, medical analysis, and safety equipment.[101–103] The significant characteristics of the desired photodetectors in practical applications include responsivity, detectivity, light switching ratio, stability, spectral selectivity, response time, and ease of fabrication.[104] Till now, a large variety of semiconductor materials have been exploited in photodetectors, including Si, InGaAs, carbon nanotubes, ZnO, quantum dots, conjugated polymers, and various two-dimensional materials (e.g., graphene, black phosphorus, $SnSe_2$).[105–109] However, their practical applications in optoelectronic devices have been limited by some unfavorable properties such as relatively wide direct bandgap (depending on the material), low absorption coefficient, high manufacturing cost, and high drive voltage.[101] In

recent years, it has been demonstrated that the organometal halide perovskites, which combine small direct bandgap, broad-spectral absorption, high absorption coefficient, high charge carrier mobility, and facile low-temperature solution processability, are ideal candidates for high-performance photodetectors.[45,47110] Despite impressively high performances, perovskite-based photodetectors face challenges such as long-term stability that prevent them from competing with established technologies.[46] Another issue limiting the application of photodetectors is that they usually require an external power supply to separate the photogenerated charge carriers, which increases the device cost and weight.[111,112] Currently, the self-powered photodetectors have been demonstrated through integrating the photodetectors with external power sources such as piezoelectric and/or triboelectric nanogenerators to realize a self-powered photodetection system.[113−115] However, they are active only in the presence of continuously varying mechanical input and hence their measurement is intermittent in nature.

The motivation is to develop a self-powered and continuously operable photodetector with improved stability. The polystyrene incorporated $MAPbI_3$ photodetector shows enhanced performance and stability, which combines with its self-powered operation due to the electric field-induced effects in $MAPbI_3$ (details in Chapter 5).

1.5. Thesis Outline

The thesis chapters are organized as follows.

Chapter 2 describes the cross-linking of polymer (PS) matrix with perovskite ($MAPbI_3$) using the Lewis acid nature of PbI_2. The effect of cross-linked PS chains on the perovskite crystal structure, solar cell performance, and its stability is investigated. To gain an understanding of improved stability and enhanced performance of PS-$MAPbI_3$ solar cells, the ion migration and dark currents, film structure, time-resolved photoluminescence (TRPL), trap-state density, charge carrier mobility, and their electrochemical impedance spectra are analyzed.

In Chapter 3, the decoupling of polarization behavior and ion migration effect in a planar $MAPbI_3$ device based on the electrical poling conditions is studied in detail. This understanding is further used to develop a light harvesting and self-powered monolith tactile sensor by combining the $MAPbI_3$ perovskite with ZnO nanostructures.

Chapter 4 discusses the modulation of the mechanical and electro-optical properties of the perovskite films by the integration of polystyrene chains for their use in the highly stable and self-powered tactile sensor. The operational stability, continuous power generation and continuous tactile sensing from the PS-$MAPbI_3$ device are described. Reproduced from Ref. [116] with permission from The Royal Society of Chemistry.

In Chapter 5, a self-powered PS-$MAPbI_3$ photodetector based on the electric field induced effects in $MAPbI_3$ (discussed in Chapter 3) with improved stability is fabricated.

The results of this thesis are summarised in Chapter 6, along with the suggestions for future work.

Chapter 2

PbI_2 Initiated Cross-Linking Strategy for Efficient and Highly Stable Perovskite Solar Cells

2.1. Introduction

The poor stability of organic-inorganic hybrid perovskites, such as $MAPbI_3$, which leads to loss of performance in optoelectronic devices has become one of the biggest obstacles for their commercial viability.[59,61,62,117,118] The Lewis acid-base adduct approach by the choice of proper solvents and their interaction with the precursor PbI_2 (a known Lewis acid) has been an effective methodology for making high-quality perovskite films such as those of $MAPbI_3$ with large grain size, better crystallinity, and long carrier lifetimes.[74,119–121] This has led to a simple fabrication and synthesis process. However, the challenge of stability under normal operating conditions still needs to be addressed using a simple approach. Though strategies such as incorporating a barrier layer or interfacial layer made of specialty chemicals,[122,123] complex formation,[124] encapsulation of the device,[125,126] altering the constituting ions in the perovskite,[70,127,128] additives,[129–132] and polymer doping[133,134] have been used to this effect, limitations arise as they require the use of inert operating conditions or indirect exposure of the perovskite layer to illumination and ambient environment or apply specialty chemicals and extra processing steps. A primary reason for this is that the strategies do not use any specific interactions between the added species and the constituting ions of the perovskite to limit the degradation. We address this challenge by applying the Lewis acid characteristics of PbI_2 for interaction with polymer chains (polystyrene (PS)) in the precursor solution (of PbI_2, MAI, and PS dissolved in DMF and DMSO), leading to the formation of a cross-linked polymer network within which the perovskite films are formed. This composite of perovskite-polymer (PS-$MAPbI_3$) network leads to highly stable solar cells which operated in ambient conditions (normal air atmosphere, 40−50% relative humidity, and continuous 1.0 sun illumination) at 45 °C without any other encapsulating interface for >1000 h and maintain 85% of their performance (>90% after 400 h). In contrast, the pure (or plain) $MAPbI_3$ solar cells efficiency drops to 20% of their initial value after 48 h. The PS-$MAPbI_3$ devices also show stable continuous operation (under ambient air, full-sun (AM 1.5 G) illumination, and relative humidity conditions) at maximum power point (MPP) retaining

>93% of their initial efficiency after 100 h, whereas the efficiency of pure $MAPbI_3$ dropped to zero in just 30 h at MPP. They also have better efficiency and reduced hysteresis compared to pure perovskite solar cells. We show that these gains in the performance are due to reduced ion migration and charge recombination, better mobility and carrier lifetime, larger grain size, and lower dark current in these perovskite-polymer films. The interaction of the PS with the constituting anions and the cations in the perovskite crystal is observed in characterization results and is proposed as the basis of the enhanced stability due to its in situ cross-linking with PbI_2.

This simple and scalable one-step fabrication process with the use of a low-cost polymer additive is crucial for the cost-effective commercialization of thin-film solar cells based on hybrid organolead halide perovskites. Specifically using this approach, we also improved the solar cell efficiency from 15.5% (pure $MAPbI_3$) to 16.8% (1 wt % PS-$MAPbI_3$) for the best devices. We also find that the extent of polystyrene cross-linking (controlled by its fraction in the casting solution) directly affects the performance of the perovskite films and their stability. With a higher degree of cross-linking though the stability of the film increases, its performance does not follow a monotonic trend with an observed maximum at 1 wt % PS concentration. To further illustrate that the effect of cross-linking is crucial to the observed stability enhancement, we also find that using just styrene (S) monomer limited enhancement in the stability of the perovskite films is observed.

2.2. Experimental Section

2.2.1. Synthesis of CH_3NH_3I (MAI)

Methylammonium iodide (MAI) was synthesized according to the method reported elsewhere.[119] Methylamine (27.8 ml, 33 wt.% in absolute ethanol, Sigma Aldrich) was reacted with hydroiodic acid (30 ml, 57 wt.% in water, Sigma Aldrich) at 0 °C and stirred for 2 h. After stirring for 2 h, the dark yellow precipitate was obtained by evaporating the solvent at 60 °C for 1 h using a rotary evaporator. The resulting precipitate was washed with diethyl ether (Sigma Aldrich) several times until the color of the precipitate changed to white, and then recrystallized with ethanol. The white precipitate was dried under vacuum for 24 h to get a final MAI product.

2.2.2. Preparation of $MAPbI_3$, PS-$MAPbI_3$ and S-$MAPbI_3$ Precursor Solutions

$MAPbI_3$ solution was prepared by dissolving lead iodide (PbI_2, Sigma Aldrich), MAI, and dimethyl sulfoxide (DMSO, Sigma Aldrich) in 1:1:1 molar ratio into N,N-dimethylformamide

(DMF, Sigma Aldrich) at 50 wt %.[119] To prepare the PS-$MAPbI_3$ precursor solution, different concentrations of PS were dissolved in DMSO and DMF and stirred for 30 min. The polystyrene (with M_w 60,000) was purchased from Scientific Polymer Products. MAI and PbI_2 at a molar ratio of 1:1 were then added to the above PS solution, which was stirred at room temperature for 1 h. Similarly, styrene (S) was used instead of polystyrene to synthesize the S-$MAPbI_3$ precursor solution.

2.2.3. Device Fabrication

Indium tin oxide (ITO) coated glass substrates with a size of 25 × 25 mm^2 were cleaned sequentially in acetone, isopropanol, and deionized water by ultrasonication for 20 min, and then were dried by an air gun. A ZnO nanoparticles dispersion solution with <100 nm particle size (Sigma Aldrich) was spin-coated on the cleaned ITO substrate at 3000 rpm for 30 s and annealed at 200 °C for 15 min to form a compact electron extraction layer. Then, the $MAPbI_3$ or PS-$MAPbI_3$ or S-$MAPbI_3$ perovskite films were deposited by a one-step spin-coating process, with antisolvent dripping. The precursor solution was spin-coated at 4000 rpm for 30 s onto the ZnO/ITO substrate. 200 μL of diethyl ether was dropped onto the rotating substrate in 10 s before the surface changed to be turbid due to the rapid vaporization of DMF. The obtained films were then heated at 65 °C for 2 min and 100 °C for 3 min. A 2,2',7,7'-tetrakis(N,N-di(4-methoxyphenylamino)-9,9'-spirobifluorene (spiro-OMeTAD) solution, consisting of 72 mg spiro-MeOTAD, 17.5 μL of lithium bis(trifluoromethanesulfonyl)imide (Li-TFSI) solution (520 mg Li-TSFI in 1 mL acetonitrile) and 28.8 μL of 4-tert-butyl pyridine in 1mL of chlorobenzene, was spun at 3000 rpm for 30 s onto the perovskite film as a hole conductor. The devices were completed by evaporating 80 nm gold in a vacuum chamber using a shadow mask to pattern the electrodes. The active device area was 9 mm^2.

2.2.4. Perovskite Films and Solar Cell Characterization

Gel permeation chromatography (GPC) was used to measure the molecular weight of cross-linked polystyrene. Samples dissolved in THF were injected into a Viscotek VE 2001 GPC instrument equipped with PolyAnalytik SupeRes mixed bed columns, TDA 305 triple detector array and a 2600 UV detector, using THF as the eluent. The columns were maintained at a temperature of 35 °C and the flow rate was 1 mL min^{-1}. For characterization of the molecular weight of the PS in the casted PS-$MAPbI_3$ films, multiple films were made and then dissolved in DMF. The PS was precipitated by adding methanol and then it was re-suspended in THF. ^1H

NMR spectra were obtained in DMF-d_7 and DMSO-d_6 solvents using Bruker 500 MHz spectrometer. Thermogravimetric analysis (TGA) was performed using TGA Q500 (TA Instruments), heating at a steady constant rate of 10 °C min^{-1} from 25 °C (room temperature) to 600 °C under a constant 40 mL min^{-1} N_2 gas flow. XRD diffraction patterns were obtained from the perovskite films deposited on the glass substrate using a glancing incidence X-ray diffraction (GIXRD) using a PANalytical X'Pert Pro MRD diffractometer with Cu Kα radiation (λ = 1.54 Å) at an incidence angle of 0.4°. The surface morphology was acquired by Field-emission scanning electron microscopy (FESEM, Zeiss Ultraplus). Raman measurements were performed using a Horiba HR800 spectrometer in the backscattering configuration. The excitation wavelength of the laser was 532 nm and the power was 0.6 mW to avoid any sample degradation effects. The measurements were conducted at room temperature and in air. UV-Visible absorption spectra were recorded using Perkin Elmer Lambda 750 spectrophotometer and the optical energy bandgap (E_g) was estimated from these absorption spectra using Tauc relation, which is given by $\alpha h\nu = A(h\nu - E_g)^n$ where α is the absorption coefficient, $h\nu$ is the photon energy, A is a proportional constant, E_g is the energy bandgap, and n depends on the characteristics of the transition in a semiconductor. (n = 1/2, 2, 3/2, or 3 for allowed direct, allowed indirect, forbidden direct, and forbidden indirect electronic transitions, respectively). $MAPbI_3$ exhibits an optical absorption spectrum governed by direct electronic transitions (n = 1/2). The time-of-flight secondary ion mass spectrometry (ToF-SIMS) measurements were performed using model ToF-SIMS 5, ION-ToF GmbH, with the Cs^+ ion source (500 eV) for the sputtering and a Bi^{3+} ion source (30 keV) for the analysis. The ToF-SIMS measurement was carried out in the negative polarity mode with a cycle time of 200 µs, a sputtering area of 350 μm^2 and an analysis area of 150 μm^2. The evolved hydrogen gas was analyzed by the Stanford Research Systems (SRS) Universal Gas Analyzer. Photoluminescence (PL) spectra were recorded with a Horiba Jobin Yvon system with a red-light source with an excitation at 633 nm. The time-resolved photoluminescence (TRPL) experiments were performed using an Edinburgh fluorescence spectrometer with a time-correlated single-photon counting capability. The PL decay spectra were fitted by a biexponential decay function: $Y = A_1\exp(-t/\tau_1) + A_2\exp(-t/\tau_2) + y_0$ where A_1 and A_2 are the relative amplitudes, and τ_1 and τ_2 are the lifetimes for the fast and slow recombination, respectively.[121] The current-voltage characteristic of the ITO/PS-$MAPbI_3$ (or $MAPbI_3$)/Au films was measured in dark and analyzed using the space charge limited current (SCLC)

model.[117,165,166] The trap-state density (n_{trap}) was determined by the trap-filled limit voltage (V_{TFL}) as follows:[134]

$$n_{trap} = \frac{V_{TFL}\varepsilon\varepsilon_0}{eL^2} \quad (2.1)$$

where L is the thickness of the film, ε is the relative dielectric constant of $MAPbI_3$ ($\varepsilon = 32$), ε_0 is the vacuum permittivity, and e is the electron charge. The SCLC charge mobility (μ) of the perovskite films was calculated using:[117,165]

$$J = \frac{9\mu\varepsilon\varepsilon_0 V^2}{8L^3} \quad (2.2)$$

where J is the current density, V is the applied voltage, ε is the relative dielectric constant of $MAPbI_3$ ($\varepsilon = 32$), ε_0 is the vacuum permittivity, and L is the thickness of the film. The current density–voltage (J–V) curves of the devices were measured using a Keysight 3458A Digital multimeter under the AM 1.5 G (one sun illumination, 100 mW cm^{-2}), generated using a Xenon-lamp based solar simulator (Newport Oriel Instrument 67005, 150 W Solar Simulator). The light intensity was calibrated by a NREL calibrated KG5 silicon reference cell to minimize spectral mismatch. All J–V measurements were recorded with a scan rate of 100 mV s^{-1}. The hysteresis index of the devices was calculated by:[134] Hysteresis index = ($PCE_{reverse}$-$PCE_{forward}$)/ $PCE_{reverse}$. The impedance spectra were recorded at 20 mV AC oscillating amplitudes from 1 Hz to 1 MHz.

The long-term stability test of the devices (with and without HTL) was performed in an ambient environment without encapsulation by exposing the devices under continuous one-sun illumination in ambient air with 40–50% relative humidity, while the temperature of the cells was around 45 °C. The operational stability of the devices with HTL was carried out in an ambient atmosphere by applying an external bias identical to the voltage at maximum power point (V_{MPP}) in the J–V curves and then tracking the current output. During measurements, the devices were maintained at a constant voltage (V_{MPP}) and subjected to continuous 1 sun, AM 1.5G illumination in ambient air with 40–50% relative humidity at 45 °C. The humidity was measured by a portable RH sensor and was controlled by adjusting the flow rate of the carrier gas (dry N_2) and moist gas (N_2 bubbled through water). The temperature was controlled by placing the device on the hot plate at 60 °C, which maintains the temperature of the device at 45 °C. Throughout the experiment, the temperature of the solar cells was monitored with an IR thermal gun.

2.3. Results and Discussion

Lewis acids such as $AlCl_3$ (and other aluminum halides) are known to interact with PS, and one of the reaction pathways leads to the formation of carbonium ions that subsequently cause cross-linking of the PS chains.[135] The cross-linking of the PS on mixing with PbI_2 (also a Lewis acid) is confirmed by the gel permeation chromatography (GPC) results, as shown in **Figure 2.1**a. The standard (for calibration) and the used plain PS (control samples) have a molecular weight (M_w) of 90000 and 60000, respectively. A 1 wt % PS solution in PbI_2 (62 wt %) characterized after 12 h shows a M_w of 359000 (an increase of ~6 times as compared to plain PS), which reveals the cross-linking of the polymer. The M_w increases with reaction time and also with the wt % of PS in the solution (inset of Figure 2.1a). The PS from casted PS-$MAPbI_3$ films shows a M_w of 187000, which confirms the cross-linking of PS within $MAPbI_3$ film. Nuclear magnetic resonance spectra (^{1}H NMR) show a shift in the PS peaks due to interaction with PbI_2 and formation of intermediate cation complex that subsequently loses hydrogen and leads to the formation of carbonium ions (Figure 2.1b and Figure A2.1, Appendix). The carbonium ions are then proposed to react with other polystyrene chains at the site of the tertiary carbon atom, leading to the cross-linking of the polymer chains (a more detailed mechanism is given in the Appendix).[136,137] In addition, we have observed the evolution of hydrogen gas (Figure A2.2, Appendix) from the PS and perovskite reaction mixture which substantiates the proposed cross-linking mechanism of PS due to the Lewis acid nature of PbI_2. This direct interaction should lead to slower crystallization kinetics in the perovskite films and improve the quality of the crystals. Direct interactions between inorganic crystals and organic moieties are well reported in natural systems where they are used to develop composite materials such as bones and shells that have distinct properties compared to their pure inorganic counterparts.[138,139] Following this, the effect of the cross-linking on the performance of PS-$MAPbI_3$ solar cells, its stability, and structure is analyzed and compared to pure $MAPbI_3$. The device configuration of the perovskite solar cells (PSCs) is shown in Figure 2.1c, with a representative cross-sectional field emission scanning electron microscopy (FESEM) image illustrated in Figure 2.1d. A ZnO film was deposited on indium tin oxide (ITO) glass substrate as the electron transport layer (ETL), the PS-$MAPbI_3$ (or pure $MAPbI_3$) film was grown as the active light-absorbing layer by a facile one-step solution casting method, Spiro-OMeTAD as the hole transport layer (HTL), and gold (Au) as the top electrode (details in the Experimental section). The energy level diagram of the device is

presented in Figure A2.3, Appendix. Further, the interaction between the MAI and the PS chains due to the cation-π electron interaction is confirmed by a series of experiments. We observe that on mixing PS solution with MAI solution (both in DMF) a slow precipitation of the PS chains is observed, as seen by the cloudiness of the solution in the optical image (see inset of Figure 2.1e). The UV-Vis absorption spectra (Figure 2.1f) of the mixture correspondingly show an increase in the background scattering that leads to a broad increase over the complete wavelength range. The precipitated PS chains are collected and analyzed by Thermogravimetric analysis (TGA) (Figure 2.1e). For plain PS chains a broad decomposition is observed (Figure 2.1e), with 10 % decomposition occurring by 335 °C, and 90 % by 427 °C. In contrast, the PS chains precipitated from the MAI solution show a 10 % decomposition by 362 °C and 90 % by 424 °C (Figure 2.1e). The corresponding first derivative curves are presented in Figure A2.4, Appendix. The shifting of the initial decomposition of PS to higher temperatures shows their thermal stabilization due to the extra energy of the interaction with MAI.[140,141] Further, the Raman spectrum of PS-MAI precipitate (Figure A2.5, Appendix) also confirms this interaction as most of the peaks in PS-MAI are shifted to a higher wavenumber as compared to PS.

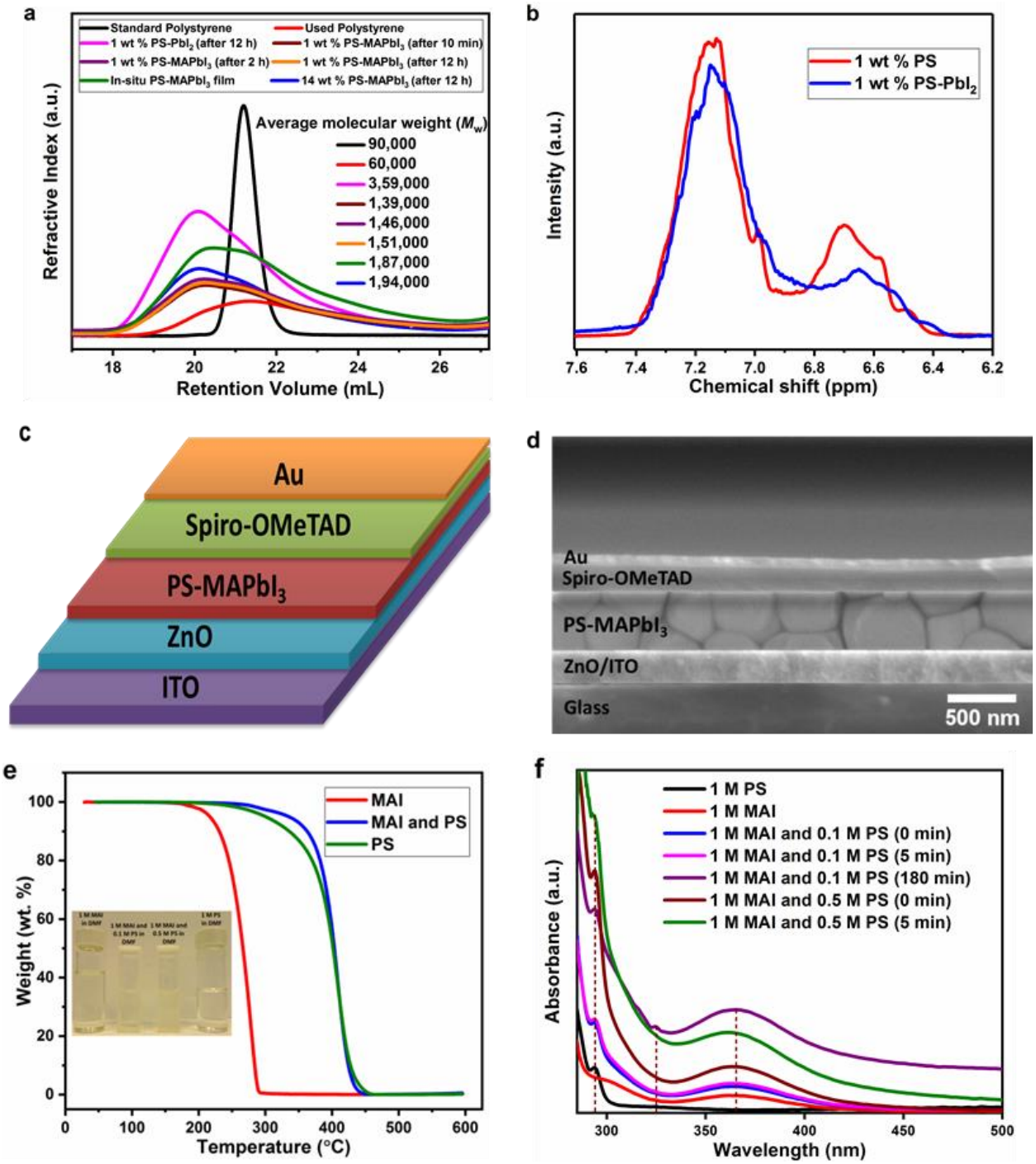

Figure 2.1. Cross-linking of the polystyrene within $MAPbI_3$ and the device configuration. (a) Gel permeation chromatography refractive index traces for different samples in THF. (b) ^1H NMR spectra of the 1 wt % PS solution and 1 wt % PS-PbI_2 solution collected in DMF-d_7 and DMSO-d_6 (magnification of the scale between 6.2 and 7.6 ppm). (c) Schematic diagram of the device architecture. (d) Cross-sectional SEM image of a complete solar cell. (e) TGA curves confirming the interaction between MA^+ cation and PS, with the inset showing the optical images of the solutions. (f) UV-Vis absorption spectra of plain PS, MAI, and MAI with PS in DMF solution.

The performance of perovskite solar cells with varying amount of PS content (0, 0.5, 1, 2, 4, and 14 wt %) and without HTL is measured under illumination (Figure A2.6, Appendix) and in the dark (Figure A2.7, Appendix), with the detailed device parameters listed in Table A2.1. It is observed that the 1 wt % PS-$MAPbI_3$ device without HTL exhibits the best performance, with a PCE of 3.04%, short-circuit current density (J_{sc}), open-circuit voltage (V_{oc}), and fill factor (FF) of 5.21 mA cm^{-2}, 0.784 V, and 0.745, respectively. In comparison, the pure $MAPbI_3$ device without HTL showed a PCE of 2.49% with a J_{sc} of 4.61 mA cm^{-2}, V_{oc} of 0.775 V, and FF of 0.696. Increasing the PS content further decreases the device performance, as seen for 4 wt % PS-$MAPbI_3$ that has a PCE of 2.00%, and for 14 wt % PS-$MAPbI_3$ the PCE reduces to just 0.68%. The *J*−*V* curves measured in the dark (Figure A2.7, Appendix) show that the current density decreases with increasing PS content, revealing that the electrically insulating nature of PS reduces the dark current in these devices. The performance of the solar cells with a HTL also follows a similar trend. **Figure 2.2**a shows the *J*−*V* characteristics of the pure $MAPbI_3$, PS-$MAPbI_3$ (1 and 14 wt %), and 14 wt % S-$MAPbI_3$ devices with HTL, and the corresponding device parameters are summarized in Table A2.2. The 1 wt % PS-$MAPbI_3$ device shows the highest PCE of 12.27%, with a V_{oc} of 1.044 V, J_{sc} of 15.80 mA cm^{-2}, and FF of 0.744. In contrast, the pure $MAPbI_3$ device showed a PCE of 11.02% with a V_{oc} of 1.033 V, J_{sc} of 14.88 mA cm^{-2}, and FF of 0.717, which is comparable with the previous reports.[142,143] Note the performances reported here are for 10 typical devices; the best 2 devices have a PCE of ∼15.5% for pure $MAPbI_3$ and 16.8% for 1 wt % PS-$MAPbI_3$. In addition, we compared the PCE of different devices with and without HTL, and these are displayed as a bar graph in Figure A2.8 (Appendix). The forward and reverse *J*−*V* scans of the 1 wt % PS films show a hysteresis index of 0.017 compared to 0.032 for pure $MAPbI_3$ (Figure 2.2b). The detailed parameters for the hysteresis analysis are listed in Table A2.3. This shows that the hysteresis challenge is considerably alleviated in the presence of cross-linked PS. We attribute this to reduced ion migration in the PS-$MAPbI_3$ active layer, as is illustrated by later results.

The influence of PS cross-linking on the perovskite crystal structure is investigated by X-ray diffraction (XRD), UV−Vis absorption spectra, and Raman spectroscopy. XRD patterns (Figure 2.2c) showed no change in the crystalline phase of perovskite with or without PS and S but displayed the difference in the diffraction intensities and sharpness (see the inset of Figure 2.2c). The diffraction intensity of 1 and 14 wt % PS-$MAPbI_3$ films is higher than that of the pure

$MAPbI_3$ and 14 wt % S-$MAPbI_3$ films, suggesting a higher crystallinity in the presence of PS. In addition, we observed that the crystallinity improves on increasing PS content from 1 to 14 wt % and is suppressed with the styrene monomer.[124] These results indicate that the PS incorporation into $MAPbI_3$ has a significant effect on crystallization behavior. The energy bandgap (Figure A2.9, Appendix) calculated using absorption spectra shows no obvious change with and without PS and S. From the Raman spectra as shown in Figure 2.2d, the sharp characteristic bands at 85 and 143 cm^{-1} can be attributed to the Pb−I and MA^+ libration modes, respectively, which are in good agreement with the previous studies.[144,145] The broad band with maxima around 240 cm^{-1} assigned to the torsional mode of MA^+ in the $MAPbI_3$.[145] We observe a shift (Figure 2.2e and Figure A2.10, Appendix) in the Pb−I, MA^+ libration, and MA^+ torsional modes from 85 to 89 cm^{-1}, 143 to 149 cm^{-1}, and 240 to 247 cm^{-1}, respectively, with the increase in the polystyrene concentration. This Raman shift toward higher wavenumber reflects the interaction of the PS with $MAPbI_3$. In addition, the signal at 998 cm^{-1} ascribed to C−C aromatic (stretching mode) and the band at 1030 cm^{-1} which corresponds to C−H aromatic (bending mode) are present both in PS-$MAPbI_3$ (and S-$MAPbI_3$) films, signifying the incorporation of PS (or S) into $MAPbI_3$.[146,147] In addition, we have measured the photocurrent (Figure A2.11, Appendix) for a vertical device configuration (see the Appendix) to confirm that the cross-linked PS is included in the bulk $MAPbI_3$. The time-of-flight secondary ion mass spectrometry (ToF-SIMS) depth profiling was conducted to characterize the perovskite films. In the depth profile of pure $MAPbI_3$ (Figure 2.2f) and 1 wt % PS-$MAPbI_3$ (Figure 2.2h) films, the PbI^- and NH^- are detected (indicative of $MAPbI_3$) with relatively constant intensities throughout the sputtering of perovskite film (up to 500 s). The decrease in the signals from PbI^- and NH^- ions, and the appearance of In^- and SnO^- peaks at the perovskite/ITO interface has been observed in both pure $MAPbI_3$ and 1 wt % PS-$MAPbI_3$ films. The detection of C_3^-, C_4^-, C_4H^-, C_5^-, C_6^-, and C_8^- signals that represent polystyrene (shown in Figure 2.2g) are only observed in 1 wt % PS-$MAPbI_3$ films but not in pure $MAPbI_3$. The high-intensity signals (around 1000–2500 counts) from PS in 1 wt % PS-$MAPbI_3$ film gradually drop to 200–600 intensity counts within an initial 15 s of sputtering time, which reveals the presence of a very thin layer of PS on the top surface of PS-$MAPbI_3$ film that protects the perovskite film with the extrinsic degradation factors. The 200–600 intensity signals from PS in 1 wt % PS-$MAPbI_3$ films present during the whole sputtering process, which implies the uniform distribution of PS in the entire PS-$MAPbI_3$ film. The photocurrent for 1 wt % PS-

$MAPbI_3$ is higher as compared to the pure $MAPbI_3$, which reveals the successful incorporation of PS matrix into the perovskite film and not just as an insulating layer on the surface. Based on these results, we believe that PS chains are incorporated at the grain boundaries of the perovskite crystals.

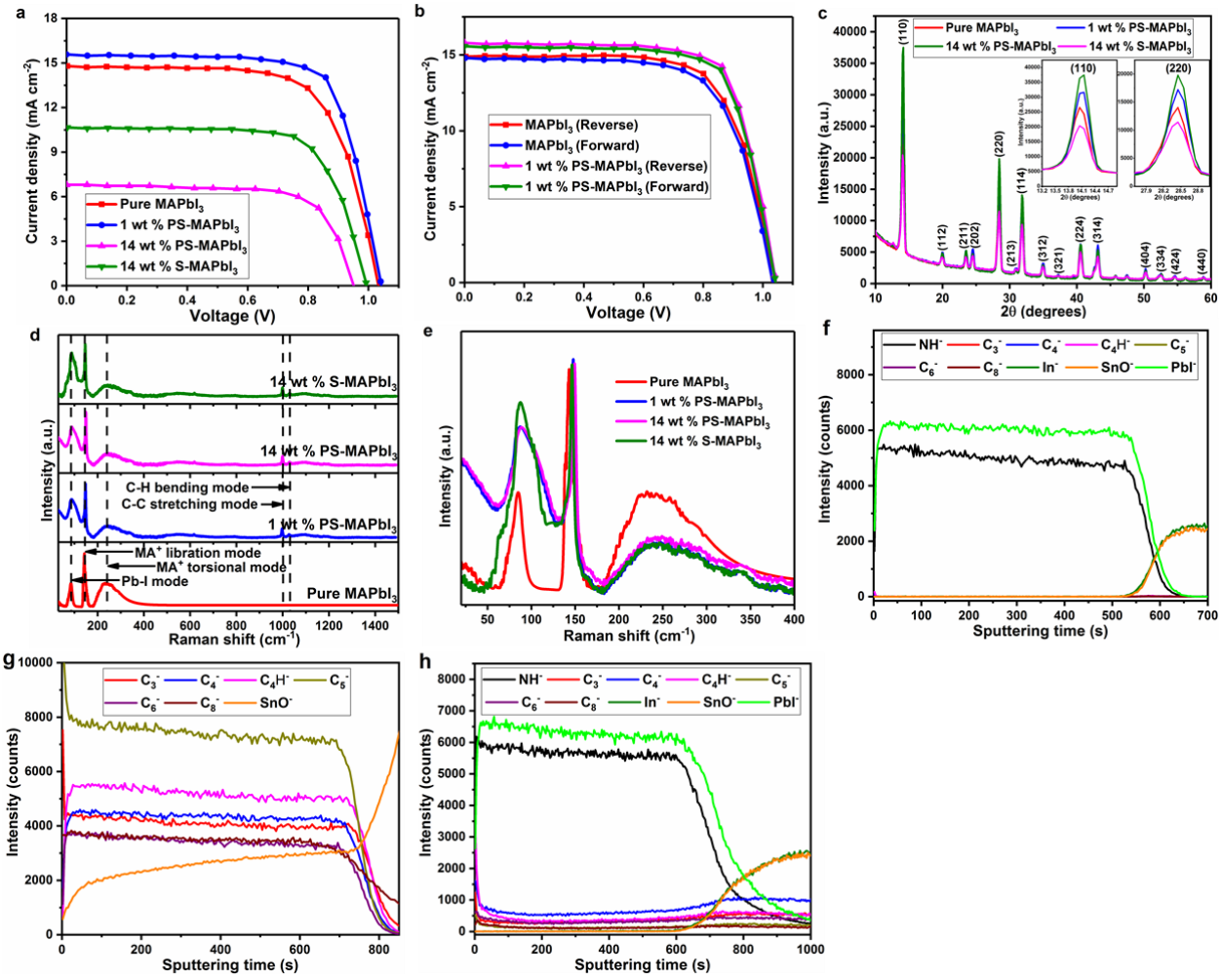

Figure 2.2. Effect of cross-linked PS chains on the perovskite photovoltaics performance and crystal structure. (a) *J–V* curves of the pure $MAPbI_3$, 1 and 14 wt % PS-$MAPbI_3$, and S-$MAPbI_3$ devices with HTL under one sun illumination. (b) *J–V* characteristics of the pure $MAPbI_3$ and 1 wt % PS-$MAPbI_3$ solar cells under the reverse and forward scan directions. (c) XRD patterns with inset showing the increase in diffraction intensity with PS content, (d) Raman spectra, and (e) Enlarged view of Raman spectra from 20 to 400 cm^{-1} for pure $MAPbI_3$, 1 and 14 wt % PS-$MAPbI_3$, and 14 wt % S-$MAPbI_3$ films. ToF-SIMs depth profile of (f) pure $MAPbI_3$, (g) plain PS, and (h) 1 wt % PS-$MAPbI_3$ films on ITO substrate.

Despite exhibiting high photovoltaic efficiency, one major concern of perovskite solar cells and devices is their long-term stability.[148] Therefore, the stability of the devices and films without any encapsulation layer was monitored in ambient air at 45 °C, under continuous 1.0 sun

illumination (including UV light) and moisture (relative humidity of 40−50%). As observed in the XRD pattern of pure $MAPbI_3$ (**Figure 2.3**a), the PbI_2 peak at 12.65° starts appearing along with the typical $MAPbI_3$ peaks after 12 h of continuous exposure, and the film completely turns into PbI_2 after just 36 h, whereas the diffraction patterns of 1 wt % PS-$MAPbI_3$ film (Figure 2.3b) reveal that the $MAPbI_3$ crystal structure remains stable (no degradation) even after 720 h (30 days). We further compared the Raman spectra of pure $MAPbI_3$ and 1 wt % PS-$MAPbI_3$ films (Figure 2.3c) to gain more insight into the degradation. After 36 h of exposure for the pure $MAPbI_3$ film, the MA^+ torsional mode disappeared and we observe two new bands at 73 and 95 cm^{-1} which are due to the degradation of $MAPbI_3$ into PbI_2,[149] while for the 1 wt % PS-$MAPbI_3$ film MA^+ libration and torsional modes remain intact after 30 days. This signifies the effect of the cross-linking of PS on increasing the stability of the PS-$MAPbI_3$ films. Following this, we investigated the stability of pure $MAPbI_3$ (reference), and 1 wt % PS-$MAPbI_3$ (optimized) solar cells with and without HTL by exposing them simultaneously to three factors of moisture, oxygen, and 1.0 sun illumination. The stability data were recorded for the devices with the best efficiency (16.8% for 1 wt % PS-$MAPbI_3$). In all cases cross-linking of PS into the devices presents further substantial improvement in the stability of PSCs. Figure 2.3d illustrates the PCEs for the devices with HTL recorded as a function of time under a constant bias voltage at the MPP (0.80 V for the $MAPbI_3$ and 0.86 V for the 1 wt % PS-$MAPbI_3$ device) and under continuous ambient air (relative humidity of 40−50%) and 1 sun illumination at 45 °C. The 1 wt % PS-$MAPbI_3$ devices maintain >93% of their initial PCE after 100 h, whereas under the same conditions the PCE of pure $MAPbI_3$ dropped to zero within 30 h. We also examined the long-term stability of the PSCs without HTL (Figure 2.3e) and with HTL (Figure 2.3f) by exposing the devices to ambient air, moisture (40−50% relative humidity), and full sun illumination (including UV light) at 45 °C. Figure 2.3e shows that the PCE for 1 and 14 wt % PS-$MAPbI_3$ PSCs without HTL retained 68% and 80% of their initial values after 42 days, respectively. In contrast, the PCEs for pure $MAPbI_3$ and 14 wt % S-$MAPbI_3$ devices dropped to 20% of their initial values after 24 and 72 h, respectively. The other normalized solar cell figures of merit (V_{oc}, J_{sc}, and FF) without and with HTL are presented in Figures A2.12 and A2.13, respectively. Figure A2.13a shows that the 1 wt % PS-$MAPbI_3$ devices retained >97% of their initial V_{oc} after 1008 h (42 days), whereas under the same conditions the V_{oc} decreased to zero (after 144 h) in pure $MAPbI_3$ solar cells. A similar trend can be found for J_{sc} (Figure A2.13b, Appendix) and FF

(Figure A2.13c, Appendix). Figure 2.3f illustrates that the 1 wt % PS-$MAPbI_3$ PSCs with HTL maintained 85% of their peak PCE after exposing continuously in full sun illumination and ambient air at 45 °C with a relative humidity of 40−50% for 42 days, while the pure $MAPbI_3$ PSCs retained only 20% of their initial PCE after 48 h. This result confirms that the perovskite film with PS is more stable at harsh environmental conditions. We anticipate that the improved device stability is due to the direct interaction between the $MAPbI_3$ grain boundaries and the cross-linked PS, which will block the ion migration and also prevent the penetration of oxygen and water (moisture) into the perovskite layer and hence impede the decomposition of $MAPbI_3$ under the light. The long-term stability comparison of PS-$MAPbI_3$ solar cells with several other device configurations under different conditions is shown in **Table 2.1**.[122,125,126,128,150−160] It should be noted that our device without any encapsulation shows superior stability.

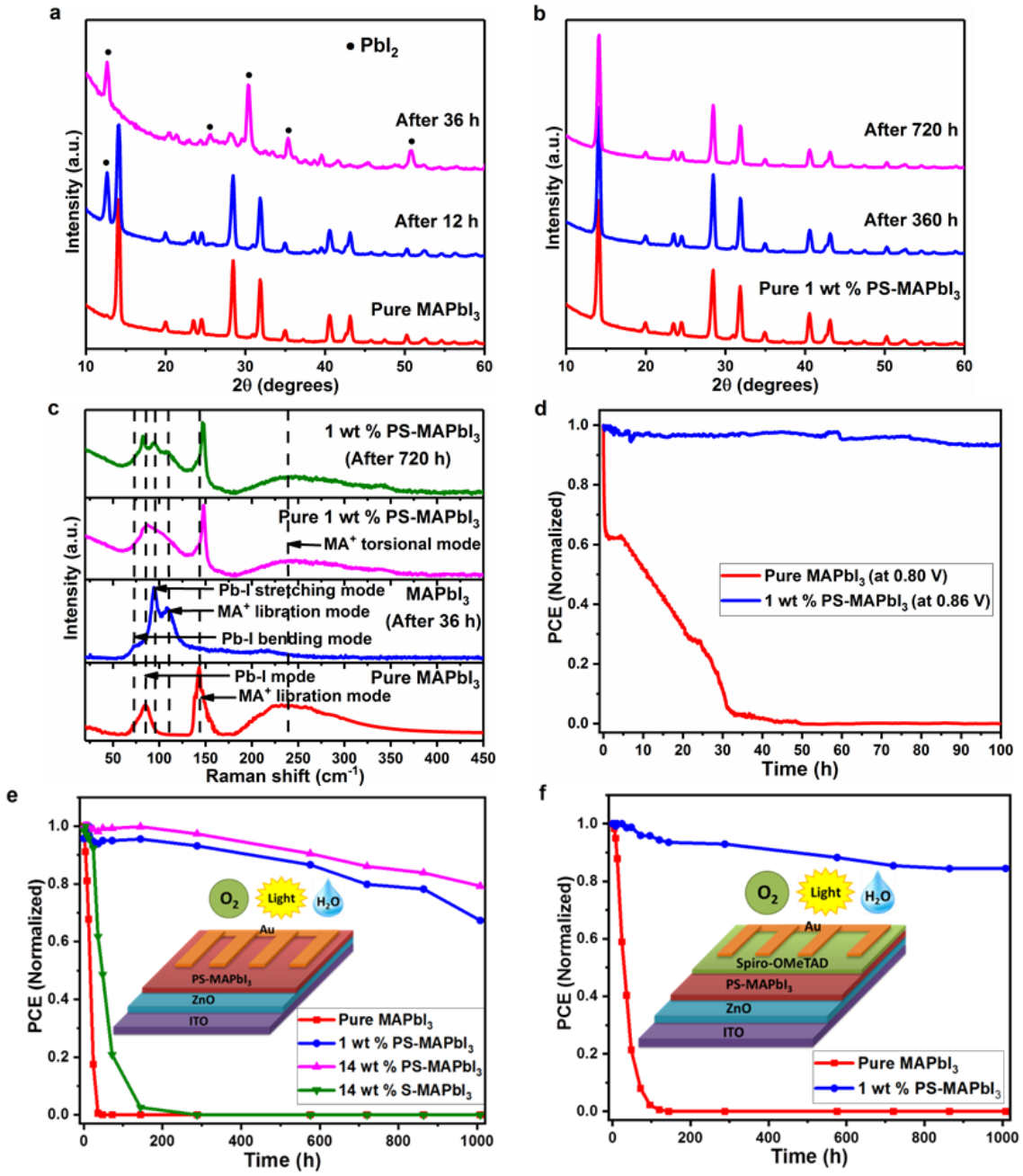

Figure 2.3. Stability characterization of perovskite solar cells. XRD patterns of (a) $MAPbI_3$ and (b) 1 wt % PS-$MAPbI_3$ films after exposing them under continuous one-sun illumination in an ambient environment with 40–50% relative humidity for different times. (c) Raman spectra of $MAPbI_3$ and 1 wt % PS-$MAPbI_3$ films after incessant light and moisture exposure. (d) Operational stability of the cells examined at maximum power point with a constant bias of 0.80 V for $MAPbI_3$ and 0.86 V for 1 wt % PS-$MAPbI_3$ devices with HTL under continuous full-sun illumination in air and moisture at 45 °C. (e) Normalized PCEs for the pure $MAPbI_3$, 1 and 14 wt % PS-$MAPbI_3$, and 14 wt % S-$MAPbI_3$ solar cells without HTL after aging continuously in full sun illumination, ambient air at 45 °C, and 40–50% relative humidity for 1008 h (42 days). (f) Normalized PCEs for the pure $MAPbI_3$, and 1 wt % PS-$MAPbI_3$ solar cells with HTL under the same testing conditions as in (e).

Table 2.1. Comparison of the stability of organic-inorganic hybrid perovskite solar cells with various device configurations under different conditions.

Device structure	Time (h)	Light (Intensity) or Dark	Atmosphere (Relative humidity)	Encap-sulation	Remaining performance (%)	Ref.
ITO/ZnO/PS-$MAPbI_3$/Spiro-OMeTAD/Au	1008	Light (100 mW cm^{-2})	Air (40-50%)	No	85	This work
FTO/TiO_2/$MAPbI_3$/Al_2O_3/Spiro-OMeTAD/Au	18	Light (100 mW cm^{-2})	Air (60%)	Yes	52	[122]
ITO/SnO_2/PVP-$MAPbI_3$/Spiro-OMeTAD/Au	2500	Dark	N_2	Yes	85	[125]
ITO/TiO_2/$MAPbI_{3-x}Cl_x$/P3HT/Polystyrene (MG)/Au	984	Dark	Air (40%)	Yes	50	[126]
FTO/TiO_2/$FA_{0.75}MA_{0.25}Pb(I_{11/12}, Br_{1/12})_3$/PS-5/Spiro-OMeTAD/ Au	60	Dark	Air (80%)	No	73	[128]
FTO/TiO_2/$MAPbI_3$/HS-PhF_5/Spiro-OMeTAD/Au	4	Light (100 mW cm^{-2})	Air (45%)	Yes	36	[150]
FTO/TiO_2/$MAPbI_3$/CuI/ Graphite/Cu tape	600	Dark	Air	Yes	60	[151]
ITO/PEDOT:PSS/VO_x/$MAPbI_{3-x}Br_x$/$PC_{60}BM$/AM-TiO_x (CIL)/Ag	12	Light (100 mW cm^{-2})	N_2	Yes	80	[152]
FTO/TiO_2/$MAPbI_3$/PEH-2/Au	850	Light (100 mW cm^{-2})	Argon	No	65	[153]
FTO/TiO_2/$MAPbI_3$+F-N2200 or PF-1/Spiro-OMeTAD/Au	50	Light (100 mW cm^{-2})	Air (30%)	No	80	[154]
FTO/C_{60}/$MAPbI_{3-x}Cl_x$/Al_2O_3/Spiro-OMeTAD/Au	500	Light (81.1 mW cm^{-2})	Air	Yes	50	[155]
FTO/TiO_2/CsBr/$MAPbI_{3-x}Cl_x$/Spiro-OMeTAD/Au	0.83	Light (365 nm, 523 mW cm^{-2})	Air	No	50	[156]
FTO/Al doped TiO_2/Al_2O_3/$MAPbI_{3-x}Cl_x$/ Spiro-OMeTAD/Ag	35	Dark	Inert atmosphere	Yes	34	[157]
FTO/TiO_2/$MAPbI_3$(with Ethyl cellulose)/Spiro-OMeTAD/Au	168	Indoor light (0.2% sun intensity)	Air (60%)	No	0	[158]
ITO/CPE-K/$MAPbI_{3-x}Cl_x$/PCBM/Al	0.58	Dark	Air (40%)	Yes	45	[159]
ITO/PEDOT:PSS-GeO_2/$MAPbI_{3-x}Cl_x$/PCBM/Ag	78	Light (100 mW cm^{-2})	Air	No	28	[160]

To gain an understanding of the greater stability combined with higher performance in the PS-based perovskite films compared to plain films, ion migration and dark currents, film structure, time-resolved photoluminescence (TRPL), trap-state density and carrier mobility, and their electrochemical impedance spectra are analyzed. The current response under dark and light illumination from a planar lateral device of configuration Au/PS-$MAPbI_3$ (or $MAPbI_3$)/Au at a

constant bias of 5 V is measured. As shown in **Figure 2.4**a under dark, the initial current at t = 0 s for PS-$MAPbI_3$ (1.18 nA) is more than an order of magnitude less compared to $MAPbI_3$ (15.3 nA) which is attributed to the presence of polystyrene (insulating material) in the perovskite film. After 850 s, the current for PS-$MAPbI_3$ maintained 52% of its initial value, whereas the current for $MAPbI_3$ dropped to 91% of its initial value which reveals that the ion migration effects are significantly reduced in PS-$MAPbI_3$ device.[161] Under illumination (Figure 2.4b), it is clearly observed that the PS-$MAPbI_3$ device shows a higher photocurrent generation (760 nA) with no observable decay, whereas the $MAPbI_3$ device shows a lower photocurrent (500 nA) and it decays by 16% within 28 s due to the back diffusion of ions and recombination of charge carriers.[161–163] These results confirm that the cross-linking of polystyrene into the perovskite material suppresses the ion migration effects and at the same time also enhances the efficiency of photocarrier generation. To analyze the charge carrier recombination and emission properties, time-resolved photoluminescence (TRPL) and steady-state PL were conducted. As displayed in the inset of Figure 2.4c, the emission wavelength for both the films was obtained at 775 nm. However, the PL emission for 1 wt % PS-$MAPbI_3$ film is higher as compared to the pure $MAPbI_3$ film which can be attributed to the reduced surface-trap states and defects in the PS-incorporated perovskite film.[121,132] Figure 2.4c presents the PL decay for perovskite films with and without PS. The PL decay curves were fitted to a biexponential rate law (details in the Appendix). The 1 wt % PS-$MAPbI_3$ film exhibits fast and slow phase lifetimes of τ_1 = 22.9 ns and τ_2 = 264.6 ns, while the pure $MAPbI_3$ film shows lifetimes of τ_1 = 17.9 ns and τ_2 = 142.5 ns. This increase in the lifetimes for PS-$MAPbI_3$ film indicates a lower defect concentration and hence improves the device performance and stability.[121,164] In addition, we calculated the trap density and carrier mobility from the dark I–V characteristics using the standard space charge limited current (SCLC) method (details in the Appendix).[165,166] As shown in Figure 2.4d, the I–V traces have the Mott-Gurney's power law dependence ($I \propto V^n$), n = 1 is the ohmic region, n > 3 is the trap-filled limit (TFL) regime, and n = 2 is the trap-free SCLC regime.[165] The V_{TFL}, trap density (n_{trap}), and carrier mobility for pure $MAPbI_3$ film were measured to be 0.12 V, 2.36 × 10^{15} cm^{-3}, and 0.21 $cm^2\ V^{-1}\ s^{-1}$, respectively. In contrast, the 1 wt % PS-$MAPbI_3$ film resulted in the reduction of V_{TFL} (0.07 V) and trap density (1.37 × 10^{15} cm^{-3}); and improvement in the carrier mobility to 0.41 $cm^2\ V^{-1}\ s^{-1}$. The lower V_{TFL} in the 1 wt % PS-$MAPbI_3$ film signifies that at lower voltage all the available trap states were filled by the injected carriers, and consequently

lower the density of trap states. This leads to superior device performance and improved stability for the PS-$MAPbI_3$ film. The structure of these films is analyzed by FESEM (Figure 2.4e,f and Figure A2.14, Appendix). It is observed that the pure $MAPbI_3$ and 1 wt % PS-$MAPbI_3$ form compact and uniform multicrystalline films. The average grain size of pure $MAPbI_3$ is 240 nm, while 1 wt % PS-$MAPbI_3$ has larger crystal grains with an average size of 450 nm. The corresponding cross-sectional images (inset of Figure 2.4e,f) clearly indicate that the grain size of the perovskite film increases with the incorporation of PS (1 wt %) into $MAPbI_3$. On increasing the PS concentration to 14 wt %, the grains aggregated and form large-sized dendritic bundle-like crystals with poor film coverage (Figure A2.14a, Appendix). The 14 wt % S-$MAPbI_3$ film produces smaller grains with an average size of 65 nm with several pinholes (Figure A2.14b, Appendix). Figures 2.4g and 2.4h illustrate the typical impedance spectra for the $MAPbI_3$ and 1 wt % PS-$MAPbI_3$ devices measured by applying 20 mV AC voltage in dark and light illumination, respectively. The equivalent circuit can be simplified to the circuit model shown in the inset of Figure 2.4g composed of the series or electrode resistance of the device (R_1), charge transfer resistance (R_2), ion diffusion resistance (R_3), and charge carrier recombination resistance (R_4).[167−169] The fitted parameter values for $MAPbI_3$ and PS-$MAPbI_3$ devices and their relative errors are listed in Table A2.4. The resistance ratios of 1 wt % PS-$MAPbI_3$ to pure $MAPbI_3$ device calculated using the equivalent circuit model under dark and light illumination are listed in the table (see the inset of Figure 2.4h). The R_1 ratio of the pure $MAPbI_3$ and 1 wt % PS-$MAPbI_3$ devices is almost similar due to an identical electrode of the device. The R_2 value in the dark for 1 wt % PS-$MAPbI_3$ is 42 times higher as compared to pure $MAPbI_3$, whereas in light the R_2 value for 1 wt % PS-$MAPbI_3$ is 0.73 times lower than pure $MAPbI_3$. This is ascribed to the lower dark current and higher photocurrent for 1 wt % PS-$MAPbI_3$ device. The R_3 value for 1 wt % PS-$MAPbI_3$ is twice as compared to pure $MAPbI_3$ under both conditions and can be attributed to lower ion migration effect in 1 wt % PS-$MAPbI_3$ device. For 1 wt % PS-$MAPbI_3$, the R_4 value is thrice (in dark) and twice (in light) than pure $MAPbI_3$, which is due to fewer defect-assisted traps, indicating more efficient charge transfer and effective suppression of the charge recombination in 1 wt % PS-$MAPbI_3$ device. The combined results show that 1 wt % PS-$MAPbI_3$ devices have the best performance and stability resulting from the combination of higher photocarrier generation due to a higher mobility and lifetime due to larger crystal grain size and passivation of defects by direct interaction between

PS chains and perovskite crystals, coupled with significantly reduced dark current, charge recombination, and ion migration effects due to the insulating nature of the cross-linked PS matrix that is incorporated into the perovskite film.

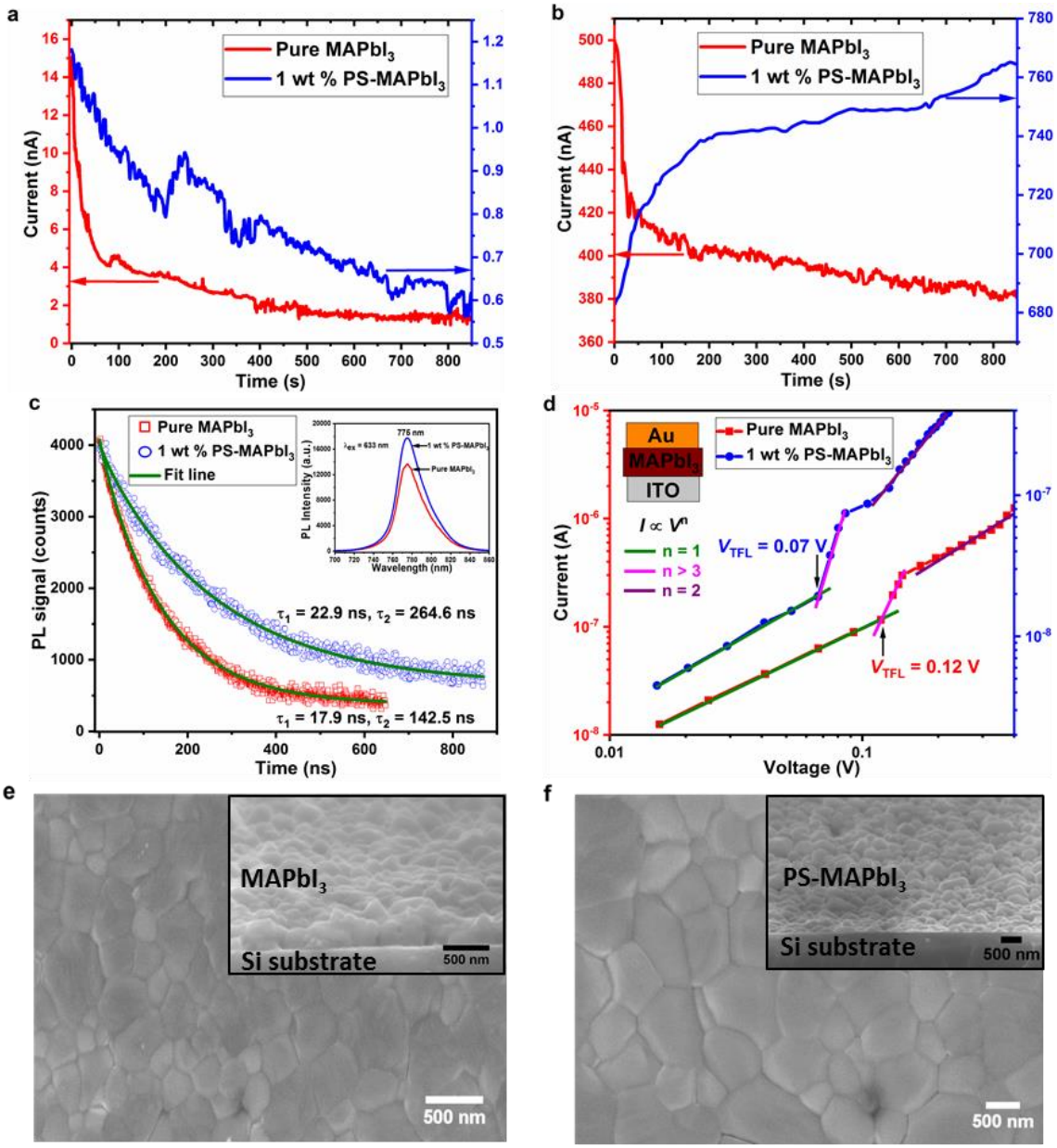

Figure 2.4A. Role of cross-linked PS in improving stability and enhancing the performance of perovskite solar cells. Current-response under (a) dark and (b) light illumination from a symmetric lateral Au/PS-$MAPbI_3$ (or $MAPbI_3$)/Au device structure at 5 V. (c) Time-resolved photoluminescence (TRPL) decay spectra of $MAPbI_3$ and 1 wt % PS-$MAPbI_3$ films, with the inset showing the steady-state PL spectra. (d) Dark *I–V* measurements of $MAPbI_3$ and 1 wt % PS-$MAPbI_3$ films exhibiting different regions, with the inset illustrating the device structure. FESEM images of (e) Pure $MAPbI_3$, (f) 1 wt % PS-$MAPbI_3$ and the inset shows the corresponding cross-sectional image of perovskite on Si substrate.

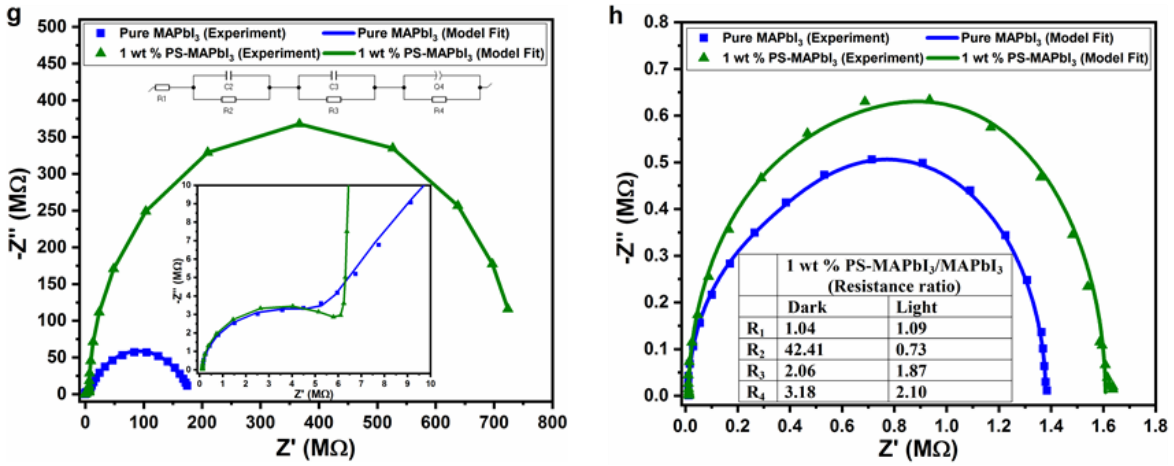

Figure 2.4B. Nyquist plots of impedance (Z) spectra for Au/PS-$MAPbI_3$ (or $MAPbI_3$)/Au device measured under (g) dark and (h) light illumination (1.0 sun irradiation) conditions. The inset of (g) displays the equivalent circuit for analysis and the high-frequency component showing the charge transport regime. The inset of (h) is the extracted resistance ratio of 1 wt % PS-$MAPbI_3$ to pure $MAPbI_3$ device in both dark and light illumination conditions.

To ascertain the effect of PS not just on the grain boundaries but also on the crystallization process, passivation of defects in the perovskite crystals and its ability to restrict the inherent ion migration effects, single perovskite crystals were grown with and without PS. We observed that the PS cross-linking and its strong interaction with PbI_2 and MAI result in the control of the crystallization process. The PS concentration modulates the nucleation time, crystal size and the number of perovskite single crystals. At low PS concentration from 0.1 wt % to 1 wt %, the rate of nucleation reduces, the time for nucleation increases and the growth of $MAPbI_3$ crystal slows down due to its interaction with PbI_2 and MAI that leads to a large high-quality perovskite single crystal. When the PS concentration increased from 1 wt % to 2 and 5 wt %, the nucleation time, number of crystals, and crystal size remains the same. At high PS concentration (7 and 10 wt %), the crosslinking leads to the formation of a gel with the polymer chains, and hence the crystallization is affected by the effects of confinement and excluded volume effects. As a result, we observe that the rate of nucleation increases, the time for nucleation reduces, and the crystal size decreases at high PS content. In addition, the hydrophobic PS that is present on the surface of the single crystals and polycrystalline films retards the penetration of environmental oxygen and water into the crystal (or film), and thus prevents $MAPbI_3$ decomposition under the light. The high crystallinity and quality of 1 wt % PS-$MAPbI_3$ crystals as compared to the plain crystals show passivation of defects, and greatly reduced the ion migration effects, the density of trap states, dark current, and charge

recombination as well as improved the carrier mobility and lifetime. We observed that the dark current for 1 wt % PS-$MAPbI_3$ single crystal is an order of magnitude less than plain $MAPbI_3$ due to the presence of PS (insulating material) on the single crystal. The 1 wt % PS-$MAPbI_3$ devices show less decay in dark current (retained 84% of their initial dark current values) as compared to the plain $MAPbI_3$ (maintained only 21% of its initial value), which reveals that the ion migration effects are significantly reduced in the presence of 1 wt % PS. The trap density in PS-$MAPbI_3$ single crystal is decreased by 4 times with the use of 1 wt % PS and carrier mobility is improved by 2.6 times compared to the plain $MAPbI_3$ crystal due to fewer defects. The charge carrier recombination resistance for 1 wt % PS-$MAPbI_3$ is 4.5 times higher than the plain $MAPbI_3$ single crystal device, indicating the suppression of the charge recombination in PS-$MAPbI_3$ devices. These results indicate that the higher stability and improvement in the electro-optical properties of the PS-$MAPbI_3$ films are due to multiple effects associated with the interaction between the PS and $MAPbI_3$.

2.4. Conclusions

The integration of a cross-linked polystyrene network with $MAPbI_3$ films using the Lewis acid characteristic of PbI_2 is presented as an effective method to make highly stable perovskite films. This stability is presented in the performance of solar cells which maintain 85% of their peak PCE even after 42 days of continuous 1.0 sun illumination and under direct ambient conditions at 45 °C. At the same time, the optimized PS ratio (1 wt %) also improves the performance of these devices. The use of the organic moiety (PS) in combination with inorganic crystalline material ($MAPbI_3$) leads to suppression of the ion migration, dark currents, and trap density which we attribute to the insulating nature of the PS network and suppression of the charge recombination. At the same time, the larger grain size of the 1 wt % PS films can be attributed to the better crystallization kinetics due to the direct interaction between PS and PbI_2 and MAI, which also contributes to the observed better performance. The interaction between PS and MAI is a possible stabilizing factor for PS-$MAPbI_3$ films. This simple and low-cost (without encapsulating materials) method of fabricating highly stable and efficient perovskite films presents an effective way to address the challenge of stability of perovskite-based devices and is needed for their viable commercialization.

Chapter 3

Light Harvesting, Self-Powered Monolith Tactile Sensor Based on Electric Field Induced Effects in $MAPbI_3$ Perovskite

3.1. Introduction

The development of material and device configurations that combine sensing and continuous energy harvesting for self-powering in a single structure significantly simplify their use by eliminating the need to develop and wire external power sources for their operation. It also improves the seamless interfacing of such devices and sensors with the environment to act as a medium for information collection to drive robotics and human-AI interactions. The challenge in such systems is to decouple the sensing of the stimuli from the energy harvesting mechanism to ensure their continuous operation irrespective of the applied stimuli and also the ability to sense both static and dynamic signals in the stimuli.[100,170–174] This has to be done while keeping the device architecture simple for ease of manufacturing and cost-effectiveness. In this aspect, Organolead trihalide perovskites materials specifically methylammonium (MA) lead iodide ($MAPbI_3$) (and its other analogs such as $MAPbBr_3$ and inorganic analogs such as $CsPbI_3$) have multiple characteristics that have led to their widespread application in the development of high efficiency, cost-effective solar cells, and optoelectronic devices.[175–178] Recently, specifically, $MAPbI_3$ has been reported as semiconducting material that has a polarization effect.[23,24,35] Using this polarization-semiconducting combination of properties in $MAPbI_3$ we demonstrate a solar-powered tactile sensor by interfacing it with a nano-structured ZnO layer that acts as a pressure-sensitive electron extraction layer.[72] The device has a monolith structure[179,180] while separating the energy harvesting from the sensing mechanism and hence is able to sense both static and dynamic pressure stimuli.[173,174] Once poled, the device is operable for at least 72 h with just light illumination over the whole visible spectrum. The device has a pressure sensitivity of 0.57 kPa^{-1} (which is better than most reported transistor-based sensors), with a current density of 0.2 mA cm^{-2}. The device also has a linear response till 76 kPa with a minimum pressure sensing ability of 0.5 kPa. The linear response of the device combined with the ease of manufacturing and being powered with just ambient light presents a significant step that greatly

simplifies the application of the device as part of continuous monitoring systems for information collection.

Besides being a semiconducting material with a polarization effect, $MAPbI_3$ also has ion migration effects that have been proposed to lead to the formation of reversible p-n (or p-i-n) kind of structures, resulting in switchable photovoltaic effect and the anomalous photovoltaic effects (ion migration effects).[69,162,181] Both the ion migration and polarization effects in $MAPbI_3$ have been reported in literature separately as distinct features of these materials.[23,35,69,162] The origin of each phenomenon is distinct, but both depend on the electric field induced changes to the material, and understanding their combined dynamics is critical to the application of these $MAPbI_3$ materials (and its analogs) in optoelectronics and to further build on it to make new and improved devices. It has been proposed that ion migration (MA^+ and I^- predominately) in $MAPbI_3$ leads to the formation of MA^+ rich regions (n-type) and I^- rich regions (p-type), generating internal p-n junctions that aid the separation of photo-generated electron-hole pairs and hence lead to an observed anomalous photovoltaic effect.[162,181,182] Similarly, the tetragonal phase (stable at room temperature and till 327 K) of $MAPbI_3$ has been reported to be ferroelectric due to the light-induced ordering of polar organic cations,[40,41] MA^+ in $MAPbI_3$, and results in an internal electrical field originating from electrical polarization. The internal polarization developed during poling also aids the separation of the electron-hole pairs and enhances the photovoltaic efficiency of this material.[41–43] Here we show using planar $MAPbI_3$ device (lateral structured, Au/perovskite/Au) that both these effects are present simultaneously in $MAPbI_3$ and either can dominate based on the poling conditions. This is also of substantial interest for fabricating hybrid energy harvesting devices.[183–185] Specifically, our results show that poling done under N_2 atmosphere and in dark leads to domination of the proposed ion migration effects, while poling done under illumination and in the ambient atmosphere (presence of O_2) lead to polarization effect domination. The distinction between the two effects is based on the reversal of the sign in the open-circuit voltage (V_{oc}) and the observed short-circuit current density (J_{sc}). To further ascertain the dominance of each effect, corroboration is done by studying the effect of polarized light and phase transition from tetragonal to cubic on the poled samples. We further observe that the polarization effect leads to a more sustained response. The J_{sc} in these devices is limited due to the high internal dc resistance of the perovskite layer. Using this limitation and the developed understanding of the

polarization-semiconducting property of $MAPbI_3$, our reported tactile sensor is made by interfacing a top electrode of ZnO nanosheets with the perovskite layer. These ZnO sheets act as an electron extraction layer[72,186,187] and enhance the J_{sc} in a dynamic fashion, due to the load sensitivity of the interaction area between the sheets and the perovskite layer. Unlike other transistor-based tactile sensors,[93,94,188–190] the combination of polarization effects and semiconducting properties of $MAPbI_3$ allows this device to be operated with just solar/light energy.

3.2. Experimental Section

3.2.1. $MAPbI_3$ Film Preparation on Gold Chip

For lateral $MAPbI_3$ device, gold (Au) chips with an electrode spacing of 2 µm were fabricated on the top of 200 nm thick SiO_2 layer by photolithography with a Cr adhesion layer. Gold chips were washed with Millipore water and then sonicated in a 1:1 mixture of acetone and isopropanol for 10 minutes, followed by another 10 minutes sonication in Millipore water. Piranha solution was used to clean organic matter off the gold substrate. Gold chip was washed thoroughly with Millipore water after being immersed in the piranha solution for 3 minutes. The $MAPbI_3$ film was prepared on Au chip using the solvent engineering method in the one-step spin coating. In particular, 230.5 mg of lead iodide (PbI_2), 79.5 mg of CH_3NH_3I, and 39 mg of Dimethyl sulfoxide (DMSO) were mixed in 300 mg of Dimethylformamide (DMF) solution at room temperature with stirring for 1 h to prepare a $CH_3NH_3I{\bullet}PbI_2{\bullet}$DMSO adduct solution.[119] 90 µl of this adduct solution was dropped onto the Au chip and was then spun at 8000 rpm for 30 s. After seven seconds of rotation, 0.7 ml of diethyl ether was slowly dripped onto the center of the Au chip in 10 seconds. The obtained film on the Au chip was heated at 65 °C for 2 min and 100 °C for 3 min.

3.2.2. Electrochemical Deposition of ZnO nanosheets

For the growth of ZnO nanosheets, SiO_2 passivated Indium tin oxide (ITO) or Kapton coated Au on one surface with sheet resistance, R_s = 8−12 Ω/sq was used. ITO was purchased from Delta Technologies was used as a substrate. The electrochemical deposition was carried out using an Ivium CompactStat Electrochemical Analyser with a standard three-electrode setup. An Ag/AgCl electrode was used as the reference electrode, with a platinum wire as the counter electrode and a clean ITO substrate as the working electrode. A mixture of 28 mM $ZnCl_2$ and 0.1

M KCl aqueous solutions was used as the electrolyte. A beaker filled with the electrolyte solution was immersed in a silicone oil bath, which was heated on a hot plate to maintain a steady temperature of 70 °C during the deposition. A constant electric potential of -1.035 V was applied for 1 h. After the deposition, the substrate was washed with Millipore water and then annealed at 335 °C for 1 h.

3.2.3. Materials and Device Characterization

Zeiss Ultraplus Field-emission Scanning Electron Microscopy (FESEM) equipped with energy dispersive X-ray spectroscopy (EDX) was used to examine the morphologies of $MAPbI_3$ and ZnO nanosheets. The crystal structure of $MAPbI_3$ was characterized by glancing incidence X-ray diffraction (GIXRD) using a PANalytical X'Pert Pro MRD diffractometer with Cu Kα radiation (λ = 1.54 Å) at an incidence angle of 0.4°. Measurements on the symmetric lateral structure cell configuration were conducted using a probing station. A two probe method was used by connecting one probe to the Au pad on the Au chip and another probe connected to the ground. A Keysight 6614C 50 Watt system power supply with a maximum voltage output of 100 V was used for the poling process. The $MAPbI_3$ device was poled at different voltages for 5 min. After poling, the open circuit voltage (V_{oc}) and the short circuit current density (J_{sc}) were measured using a Keysight 3458A Digital multimeter. The film was connected in series with the multimeter and power supply to form a circuit. Electrical poling was done under the N_2 atmosphere and in dark condition for the p-n effect, while for the polarization effect poling was done under illumination and in the ambient atmosphere (presence of O_2). V_{oc} and J_{sc} measurements were performed under simulated air mass 1.5 global irradiation (100 mW cm^{-2}); generated using a Xenon-lamp based solar simulator (Newport Oriel Instrument 67005, 150 W Solar Simulator). Cyclic voltammetry (CV) measurements were done using an Ivium CompactStat Electrochemical Analyser by connecting one Au pad to the working electrode and other Au pad to counter/reference electrode. A NREL calibrated KG5 silicon reference cell was used to calibrate light intensity in order to minimize spectral mismatch. For nitrogen effect, the films were kept in a steady N_2 flow during the poling and measurements to prevent the absorption of oxygen and moisture. The light polarization measurements were carried out at room temperature using a 633 nm laser source, polarizer, and wave plate from Newport. The poled $MAPbI_3$ film was illuminated with linearly polarized light to measure the variation of J_{sc} as a function of the light-polarization. UV-Visible absorption spectra were recorded using Perkin

Elmer Lambda 750 spectrophotometer. For the solar-powered tactile sensor, ZnO nanosheets on ITO/Kapton substrate was used as the top sample and Au/$MAPbI_3$/Au lateral structure was used as the bottom sample. First, the $MAPbI_3$ film was poled under 1.0 sun illumination in an ambient atmosphere and then the ZnO nanosheets were interfaced with the perovskite layer. Three probes system was used; the first probe connected to the Au pad, the second probe connected to the Au ground electrode on Au chip, and the third probe was connected to the ITO/Kapton substrate. An MFA Motorized Miniature Linear Stage was used to apply the load to the samples. A Honeywell Model 31 Miniature Load Cell was connected to the stage for measuring the load. Combined with a micro-pro series digital panel meter, we were able to read out the measurements and record the data.

3.3. Results and Discussion

The schematic in **Figure 3.1**a shows the proposed ion-migration effects in the $MAPbI_3$ film. The resulting internal field (due to the p-n junctions) will lead to separation of the charge carriers (electron-hole pairs) generated on light illumination and the resulting V_{oc} (and J_{sc}) will be of the same polarity as that of the poling field. Figure 3.1b shows the observed V_{oc} and J_{sc} in the $MAPbI_3$ film when poled under N_2 in dark conditions are consistent with the proposed ion migration effects in the perovskite layer. Poling of the $MAPbI_3$ film in air and under light illumination (1.0 sun) leads to polarization of the $MAPbI_3$ film (also shown in the schematic of Figure 3.1a). In this case, however, due to the presence of metal electrode, a charge compensating layer (due to the free electrons in the metal) is formed and the resulting V_{oc} and J_{sc} are of opposite polarity compared to the poling field direction.[42,191] Figure 3.1c shows the observed V_{oc} and J_{sc} as indeed being of reverse polarity as compared to the ion migration effects. In the case of ion migration, the internal electric field results from the formation of a depletion region in the material. It has been proposed that O_2 is adsorbed at the grain boundaries and the defects in the $MAPbI_3$, and suppresses the formation of p-n junctions.[162] More detailed studies are required to ascertain the exact nature of this interaction. Also, the model of the polarization behavior based on the charge compensating layer in the metal electrodes and the observed V_{oc} and J_{sc} is consistent with reported experiments using ferroelectric polymers in solar cells.[42,191] Further, the domination of the polarization behavior under poling with illumination is consistent with the observation that orientation of the MA^+ ions which plays a critical role in

ferroelectricity is significantly enhanced under illumination (due to photoexcitation).[40] The reversal of the V_{oc} and J_{sc} depending on the poling conditions is critical to the functioning of $MAPbI_3$ (and other similar materials)-based optoelectronic devices.

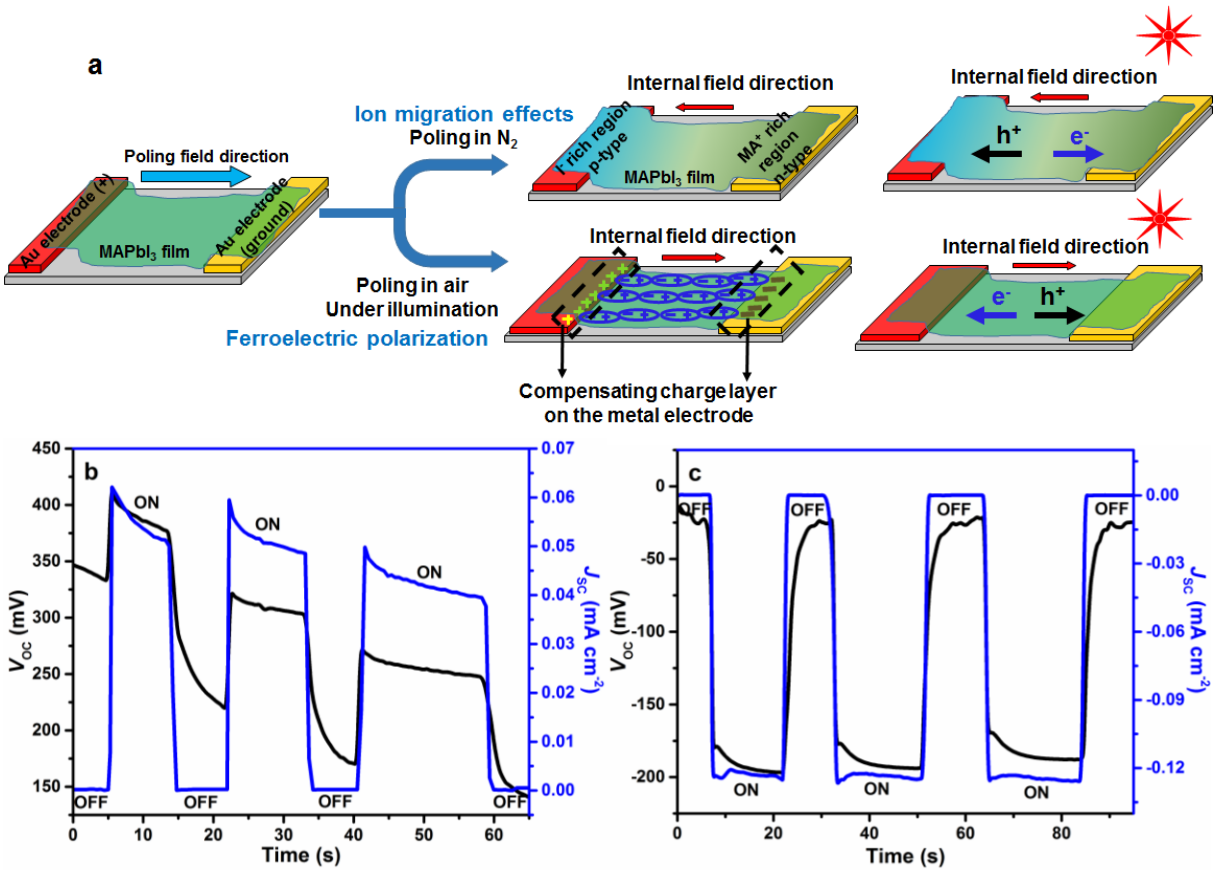

Figure 3.1. Ion migration and polarization effects in Au/$MAPbI_3$/Au device. (a) Schematic showing the proposed ion migration effects (leading to p-n junctions) and polarization in Au/$MAPbI_3$/Au device with reversal of the internal electric field between the two cases. (b) The observed V_{oc} and J_{sc} in the $MAPbI_3$ films poled at 1.5 V µm electric field for 5 min under N_2 in dark conditions show the ion migration effects which is consistent with the model in a. (c) When poled at 1.5 V μm^{-1} electric field for 5 min in the air under light illumination (1.0 sun) results in polarization and the observed V_{oc} and J_{sc} in the $MAPbI_3$ film are reversed. OFF refers to V_{oc} and J_{sc} measured under dark and ON refers to V_{oc} and J_{sc} measured under 1.0 sun illumination.

The ion migration effect in $MAPbI_3$ films is characterized by poling under an N_2 atmosphere in dark. **Figure 3.2** shows the effect of the poling field on the V_{oc} and J_{sc} generated in these films due to the ion migration effects. From Figure 3.2a,b, both V_{oc} and J_{sc} show a sustained effect on illumination with 1.0 solar light. The effect, however, is gradually decreasing over the cycles, which is consistent with the re-homogenization of the ions that were diffused

due to the poling fields.[162] It should be noted that the poling field strength and time are kept limited to prevent complete segregation of the ions which will lead to the formation of PbI_2[192] and the observed ion migration and polarization behavior disappears (Figures A3.1a−c and A3.2a,b, Appendix). There is no electrode reaction observed during the poling process as confirmed by elemental analysis (Figure A3.3, Appendix). Multiple current-voltage (*I*−*V*) scans done within the voltage range based on the electric field limit and at room temperature show a consistent response from the perovskite layer which indicates that no degradation of the material is occurring (Figure A3.4, detailed discussion in Appendix). Through field emission scanning electron microscopy (FESEM) image, we do not observe any change in the material during the controlled poling process under N_2 (Figure A3.1d, Appendix). The V_{oc} increases monotonically with the poling field strength (Figure 3.2c) due to greater ion migration, which increases the strength of the observed effects. J_{sc} (shown in Figure 3.2c) however reaches a maximum and then reduces with poling indicative of higher film resistance. The non-ferroelectric nature of this response is further ascertained by illuminating the poled $MAPbI_3$ film with linearly polarized light (using a 17 mW laser of 633 nm). As seen in Figure 3.2d, J_{sc} does not show any appreciable dependence on the relative direction of polarization of the electric field of the incident light and the film sample plane. It is also known that $MAPbI_3$ undergoes a phase transition from tetragonal (which is ferroelectric) to cubic (which is not ferroelectric) above 327 K (also confirmed by UV-Vis absorption spectroscopy, see Figure A3.5 in the Appendix).[18,193] On heating these films to 330 K and poling them we observe that both V_{oc} and J_{sc} rather than disappearing increase in magnitude (Figure 3.2e,f). This is consistent with increased ion migration (due to greater mobility) at higher temperatures.[64,181,192] The contribution from ion back diffusion currents is negligible in these samples under the applied conditions. This has been characterized by cyclic voltammetry (CV) using a potentiostat (see Appendix). We observe that the ion diffusion current which would lead to a capacitive behavior are negligible compared to normal electronic currents.[194] Further, no J_{sc} is observed in dark (after poling; Figure A3.6, Appendix) indicating that there is no significant ion back diffusion occurring. However, with light illumination J_{sc} is observed, attesting to the presence of an internal electric field that leads to separation of the photogenerated electron-hole pairs. Unpoled perovskite samples do not show any J_{sc} in the presence or absence of light illumination (Figure 3.2f). We believe that the absence of any ion back-diffusion currents can be attributed to a very slow back diffusion process which leads to an

insignificant magnitude of these currents, as indicated by the presence of the J_{sc} (under illumination) even more than 6 h after the poling process in N_2. The stability of the perovskite layer against redox reaction and decomposition to products such as PbI_2 (an insulator) within the voltage and temperatures used in these experiments is also characterized (details in Appendix). We do not observe any oxidation or reduction evidence from CVs at room temperature within the applied voltage magnitudes, rather a consistent current response is observed confirming that the perovskite layer is stable (Figure A3.4a and A3.7, Appendix). At higher temperatures (325 K and 350 K), we start to observe the evidence of redox reaction occurring from CV scans (Figure A3.7, Appendix). Following this, there is a steep drop in the current response from the sample (more than 80 times, Figure A3.8, Appendix). We believe this is due to redox decomposition of the perovskite to PbI_2 which being an insulator leads to the observed current drop. The FESEM images further confirm this as a change in morphology and composition is observed only in the elevated temperature samples (Figure A3.9a−c, Table A3.1, Appendix). Following this change, consistent with the decomposition of the perovskite layer the poling of the device does not lead to any observable V_{oc} or J_{sc}.

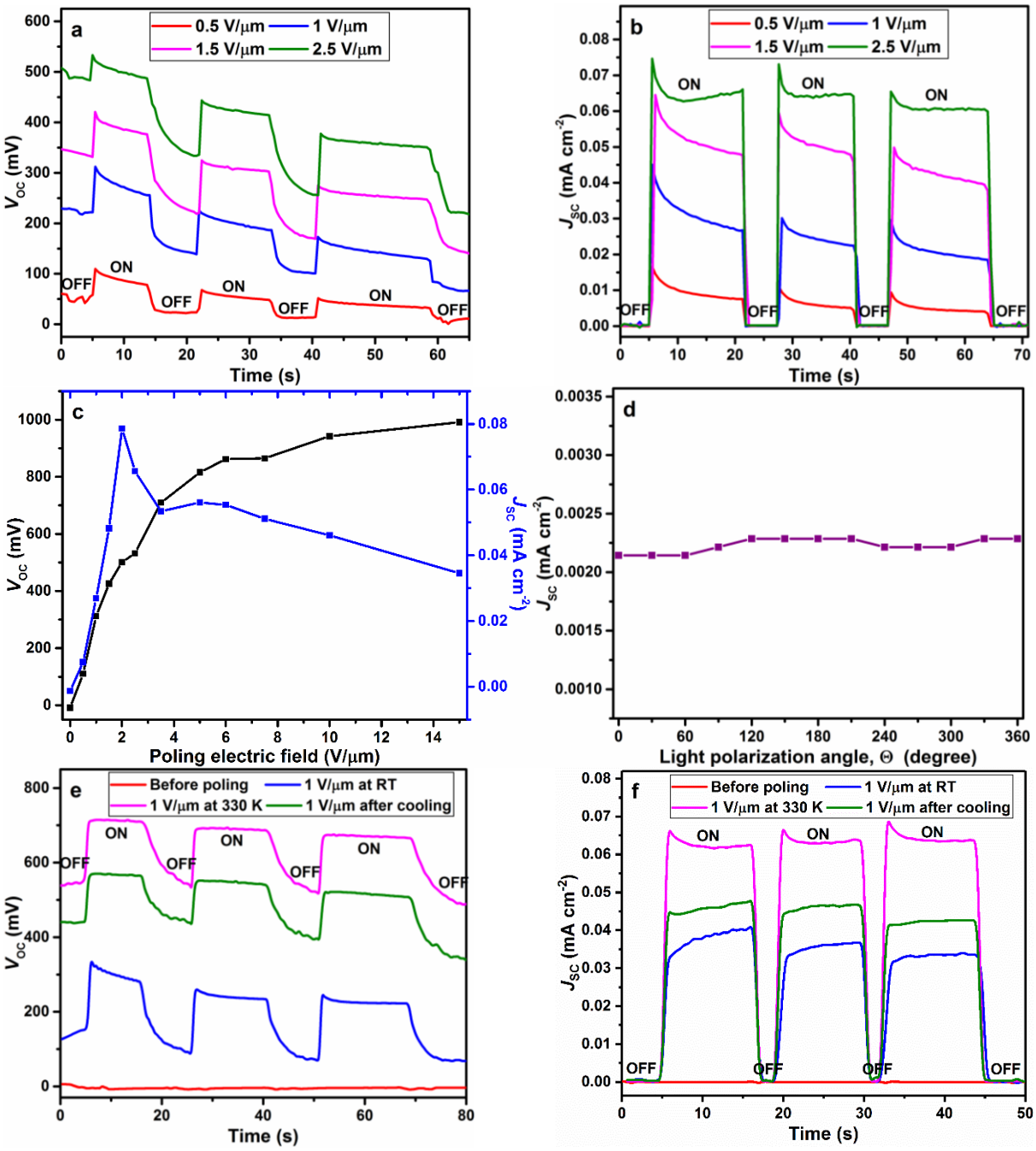

Figure 3.2. Ion migration effect in lateral $MAPbI_3$ device after poling under N_2 in dark condition. (a) V_{oc} and (b) J_{sc} cycles after 0.5, 1, 1.5, and 2.5 V μm^{-1} poling for 5 min. (c) V_{oc} and J_{sc} dependence on strength of the poling electric fields, under 1.0 sun illumination. (d) J_{sc} measured as a function of polarization angle (θ) of the linearly polarized light with respect to the film plane after poling the device at 1.5 V μm^{-1} for 5 min. (e) V_{oc} and (f) J_{sc} of $MAPbI_3$ device before poling at room temperature (RT) and after 1 V μm^{-1} poling for 5 min at RT, 330 K and after cooling to RT. OFF refers to V_{oc} and J_{sc} measured under dark and ON refers to V_{oc} and J_{sc} measured under 1.0 sun illumination.

The proposed polarization effect in the $MAPbI_3$ films and its effect on generating V_{oc} and J_{sc} were investigated by poling under 1.0 sun illumination and in ambient air conditions. These conditions reflect that light stimulated ordering of MA^+ ions enhance the polarization behavior of $MAPbI_3$, while the presence of O_2 will subdue the proposed p-n junction behavior.[40,162] Further, optical photography shows the transformation of $MAPbI_3$ films during the controlled poling process (Photo A3.1 and A3.2, Appendix).[192] On reversing the field direction, the observed transformation also reverses its spatial orientation (Photo A3.3, Appendix). Such an effect is not observed optically when poling is conducted under the N_2 atmosphere (Photo A3.4, Appendix). Again here also we limit the poling field strength to prevent material decomposition. The V_{oc} and J_{sc} due to the polarization effect are shown in **Figure 3.3**a,b. We observe that both are reversed in direction compared to the proposed ion migration effects, consistent with the model of Figure 3.1a, further the response is stable with no observable decay in their magnitude. This is crucial as it infers that unlike the diffusion of ions, the polarization due to the orientation of MA^+ ions is sustained over a longer time. We study the ferroelectric nature of this process by observing (Figure 3.3c) that unlike the ion migration effects, J_{sc} has a sinusoidal like dependence on the angle (θ) between the electric field of the incident polarized light and the sample plane (the in-plane ferroelectric polarization) due to second-order optical effects.[195,196] This dependence has a periodicity of 180^o with maximum response observed at $\theta = 0$, when the electric field of the incident light is along the in-plane ferroelectric polarization. By heating the films to 330 K which leads to a phase transition from tetragonal to cubic structure we observe that both V_{oc} and J_{sc} effects disappear (Figure 3.3d,e), shows that the polarization effects probably are ferroelectric in nature.[19,23] The effects are restored on cooling the film back to room temperatures ($\sim$296 K).

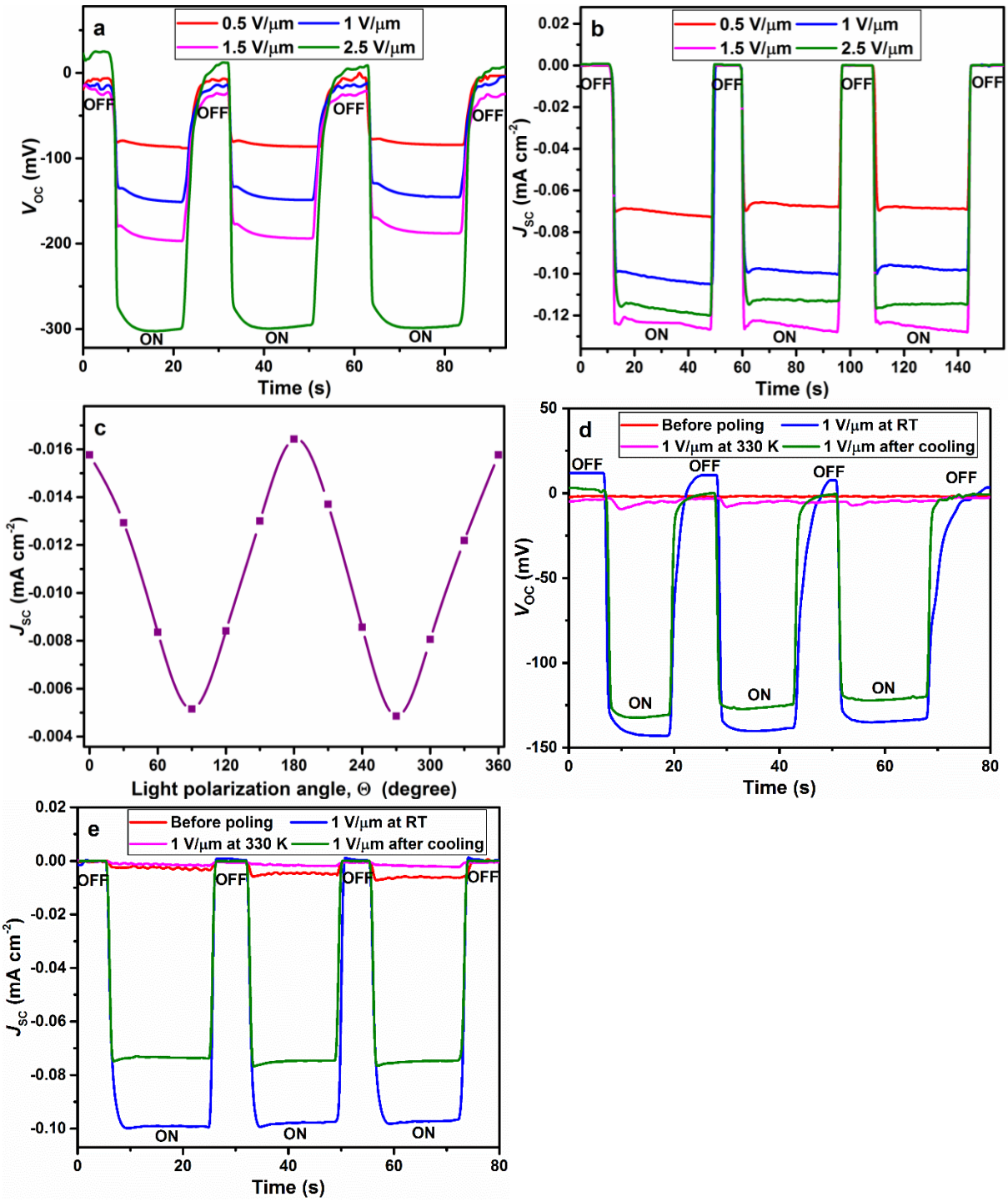

Figure 3.3. Polarization effect in lateral $MAPbI_3$ device after poling in the air under light illumination. (a) V_{oc} and (b) J_{sc} cycles after 0.5, 1, 1.5, and 2.5 V μm^{-1} poling for 5 min. (c) J_{sc} measured as a function of polarization angle (θ) of the linearly polarized light with respect to the film plane after poling the device at 1.5 V μm^{-1} for 5 min. (d) V_{oc} and (e) J_{sc} of $MAPbI_3$ device before poling at room temperature (RT) and after 1 V μm^{-1} poling for 5 min at RT, 330 K and after cooling to RT. OFF refers to V_{oc} and J_{sc} measured under dark and ON refers to V_{oc} and J_{sc} measured under 1.0 sun illumination.

Knowing the conditions for domination by the polarization effect, we now demonstrate a light/solar-powered tactile sensor. The $MAPbI_3$ films are poled at 0.5−1.5 V μm^{-1} in the air for 5 min in these studies. The basic schematic of the sensor is presented in **Figure 3.4**a. Specifically, we interface the $MAPbI_3$ film with micro-structured ZnO sheets acting as a dynamic drain electrode for electron extraction. The inset of Figure 3.4a shows the FESEM image of the cross-section of the device where ZnO sheets are in direct contact with the perovskite layer (XRD of the $MAPbI_3$ and ZnO sheets are included in Appendix, Figure A3.10). Such an electron extraction layer is required for $MAPbI_3$ films to improve their photocurrent efficiency since holes are extracted efficiently from them compared to electrons.[197] The V_{oc} generated due to polarization is on the order of 100's of mV, but J_{sc} is limited to very small values of ~ 0.1 mA cm^{-2} due to large dc resistance of these materials[35,193] and also the large path lengths that the charge carriers must diffuse to reach the electrodes (on the scale of 2 µm - 20 µm). By interfacing ZnO sheets across the surface of the $MAPbI_3$ film the generated charge carries (due to illumination) will separate under the polarization field and the photoelectrons should be easily collected by these sheets leading to increased J_{sc}. The band structure of the ZnO is suited for acting as an electron collector from the perovskite layer (Figure A3.11, Appendix). The ZnO sheets are vertically oriented and hence have a limited area of interaction with the perovskite layer (inset of Figure 3.4a). On the application of pressure, the contact area of ZnO sheets with the planar $MAPbI_3$ film increases either due to bending or penetration of the ZnO sheets.[198,199] This will effectively increase their interfacing area with the $MAPbI_3$ film leading to a higher charge collection, and hence a pressure sensitive modulation in J_{sc} will be observed. Figure 3.4b shows that the device does indeed works as a pressure sensor and the observed J_{sc} is in step with the modulation of the applied pressure. A clear correspondence is seen in the plot of Figure 3.4c, which plots the derivative of the pressure and J_{sc} responses with respect to time. A more controlled response is shown in Figure 3.4d to pressure cycles of different magnitude and in Figure 3.4e to pressure cycles at different speeds. Both these responses show that the J_{sc} is critically dependent on the modulation of contact area between the ZnO sheets and the perovskite film due to applied pressure, and the sheets are effective in their role as a dynamic drain. In the linear response range, the maximum load sensing ability of the device is 76 kPa with minimum detection of 0.5 kPa, as seen in the inset of Figure 3.4f. The linearity in response is a critical advantage for sensors to relate their measured signal to the applied stimuli. The device also

shows a consistent response over 100 load cycles signifying a reliable response (Figure 3.4g). We also observe (Figure 3.4f) that the sensitivity of the device increases with the strength of the electric field used to pole the $MAPbI_3$ films. This is in line with a more effective charge separation at higher polarization of the $MAPbI_3$ films which will improve their collection efficiency by the ZnO films making the device more sensitive to pressure modulations. The sensitivity of 0.57 kPa^{-1} observed at poling fields of 1.5 V μm^{-1} is higher than other tactile sensors that have been reported with a linear response as shown in **Table 3.1**.[93,95,97,188,189,200–206] This device also, however, does not require an active power source for operation and once poled can easily function for more than 72 h (see Figure 3.4h) by using light/solar illumination. This limit is based on a 30% decrease in the base J_{sc} (at base pressure) which relates to loss of poling (Figure A3.12, Appendix). The failure of the device occurs at pressures exceeding 500 kPa at which the ZnO sheets fracture (Figure A3.13, Appendix). The perovskite/ZnO device is stable for more than 5 days and shows no degradation of the $MAPbI_3$ layer, while bare exposed $MAPbI_3$ degrades within a day (Figure A3.14, Appendix). The presence of the top ZnO layer which is also hydrophobic minimizes direct contact of the $MAPbI_3$ layer to ambient oxygen and moisture enhancing its stability (Figure A3.15, Appendix).

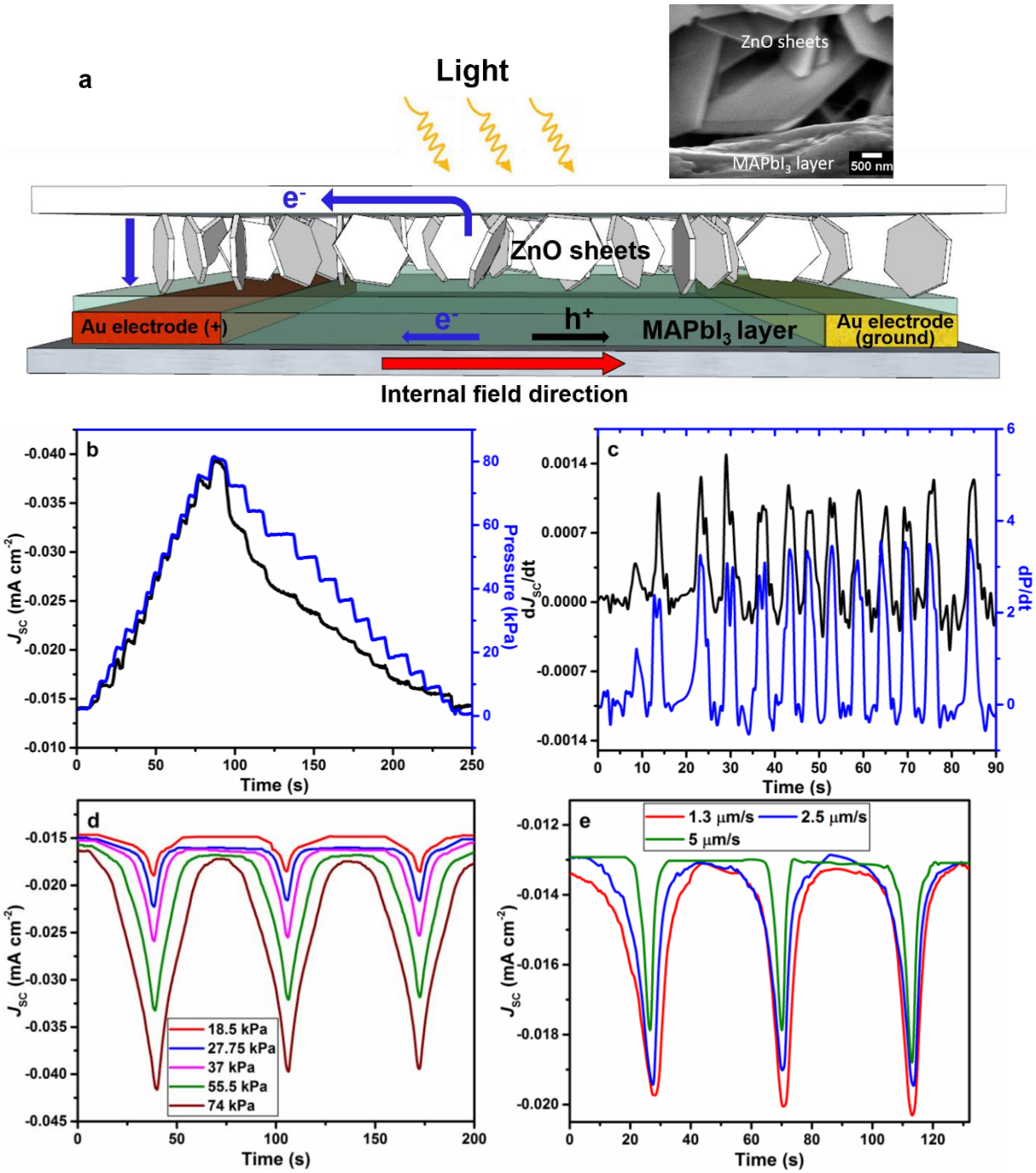

Figure 3.4A. Characterization of solar-powered tactile sensor. (a) Schematic of the solar-powered tactile sensor where ZnO sheets are interfaced with the $MAPbI_3$ channel/film. Inset shows the direct contact of ZnO sheets on the perovskite layer. (b) J_{sc} is in step with the modulation of the applied pressure after 0.5 V μm^{-1} poling for 5 min in the air under 1.0 sun illumination. (c) The derivative of the response tracks that of the applied pressure stimuli with accuracy. (d) J_{sc} cycles as a function of different pressures show the reproducibility of the device. (e) J_{sc} cycles as a function of different speeds with a maximum 37 kPa pressure show that the sensor responds with little delay to the stimuli.

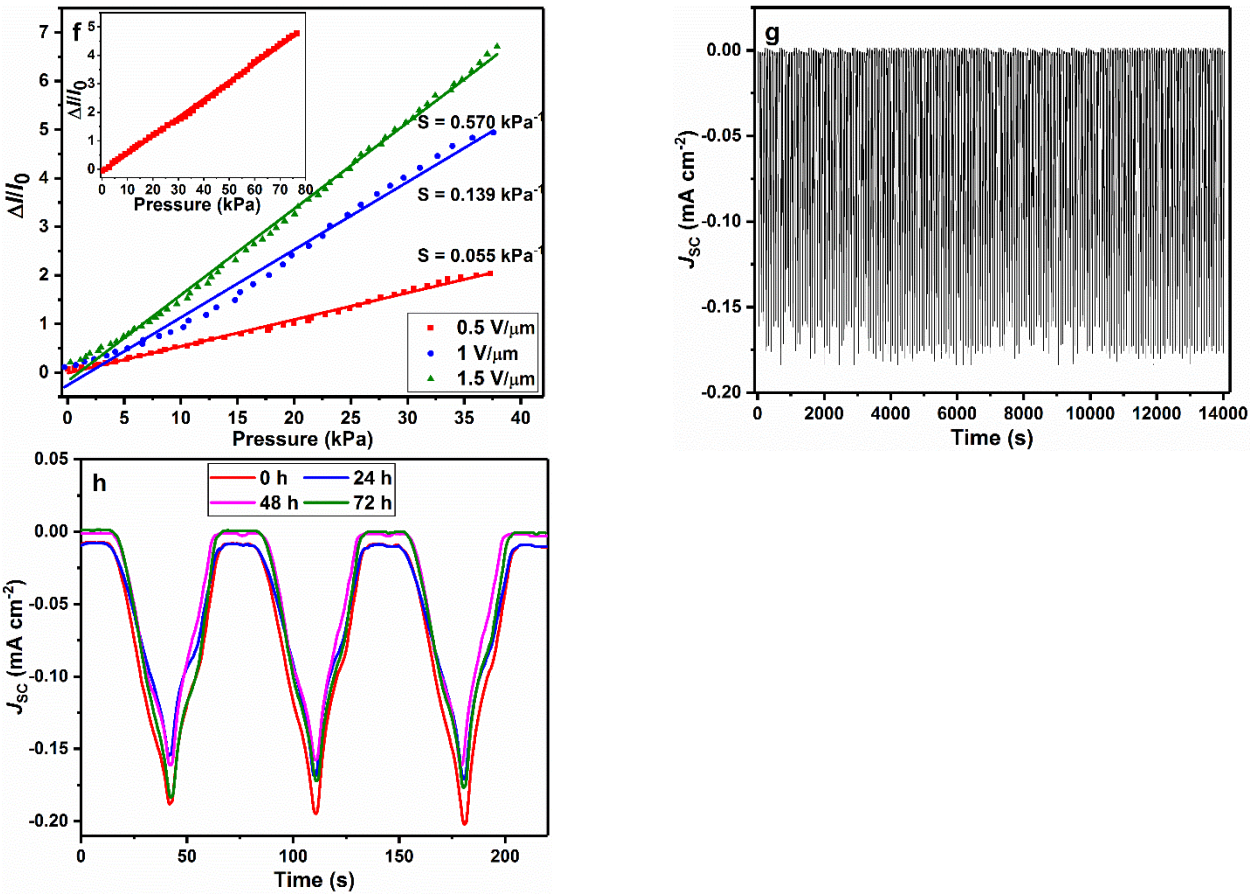

Figure 3.4B. (f) The sensitivity of the device increases with the strength of the poling electric fields, as calculated from their pressure response. Inset shows the device has a linear response with a maximum load detection of 76 kPa and the minimum detection limit is 0.5 kPa. (g) A consistent response is observed over 100 load cycles of 37 kPa. (h) J_{sc} response to load cycles of 37 kPa is maintained over 72 h in the device after initial poling at 1.5 V μm^{-1} for 5 min.

Table 3.1. Summary of materials used, operating voltage, power density, sensitivity, limit of detection, and linearity of different tactile sensors.

Sensor Type	Materials	Operating voltage /Power density	Pressure Sensitivity	Limit of Detection (kPa)	Linearity	Ref.
Transistor	ZnO nanosheets/ $MAPbI_3$	Solar driven	0.57 kPa^{-1}	0.5	Linear (0−76 kPa)	This work
Transistor	Graphene/ion gel	< 2 V/ 0.015 mW cm^{-2}	0.12 kPa^{-1}	5	Linear (0−40 kPa)	[200]
Transistor	Cu/PVDF-TrFE matrix	15 V/10.45 mW cm^{-2}	0.67 × 10^{-3} kPa^{-1}	200	Linear	[201]
Transistor	ITO/Au/ micropatterned PDMS/PiI2T-Si	100 V	0.38-8.4 kPa^{-1}	-	Non-linear (0−55 kPa)	[202]
Transistor	Ge/Si NW-array	3 V/0.022 mW cm^{-2}	11.5 µS kPa^{-1}	∼2	Linear (0−15 kPa)	[188]
Transistor	Carbon nanotube TFT active-matrix backplane	5 V/125 mW cm^{-2}	42.7 Cdm^{-2} kPa^{-1}	5	Linear (0−98 kPa)	[189]
Capacitance	CNTs/Ecoflex/ PDMS	-	0.23 × 10^{-3} kPa^{-1}	50	Linear (0−900 kPa)	[93]
Capacitance	CNT microyarn/ Ecoflex/PDMS	-	0.5 × 10^{-3} kPa^{-1}	0.0004	Linear (10−25 kPa)	[203]
Capacitance	Microstructured PDMS	80 V/0.75 mW cm^{-2}	0.15-0.55 kPa^{-1}	-	Non-linear (0−7 kPa)	[204]
Capacitance	Single-layer graphene	-	0.01 kPa^{-1}	0.11	Linear (0−20 kPa)	[205]
Piezoresistance	Graphene–Polyurethane Sponge	< 1 V/4 mW cm^{-2}	0.03-0.26 kPa^{-1}	0.009	Non-linear (0−10 kPa)	[95]
Piezoresistance	Laser-scribed graphene	-	0.005-0.96 kPa^{-1}	5	Non-linear (0−113 kPa)	[206]
Piezoresistance	SWNT/PDMS	2 V/0.007 mW cm^{-2}	1.8 kPa^{-1}	0.0006	Non-linear (0−1.2 kPa)	[97]

To ascertain that the device can function under illumination from light of different wavelengths, we modulated the light of the solar illuminator by placing long pass filters of 400 nm, 495 nm and 570 nm in its path. As seen in **Figure 3.5**a, the 400 nm filter which eliminates

UV light leads to a less than 10% reduction in the J_{sc} response. This also illustrates that the photoexcitation of the ZnO sheets (which have a bandgap of 3.4 eV) does not play any significant role in the functioning of the device. Placing the 495 nm filter reduced the J_{sc} response by 30% and 570 nm filter reduces it by more than 50% which is consistent with the broad absorbance spectrum of $MAPbI_3$ from 300 nm to 780 nm.[64] The FESEM image of the $MAPbI_3$ film taken after multiple days of pressure measurements and removal of the ZnO electrode show the presence of the residual sheets on the $MAPbI_3$ film (Figure 3.5b). The energy dispersive X-ray spectrum of Figure 3.5c confirms the elemental composition of the sheet fragment to be ZnO. This observation further confirms the device structure and the model presented in Figure 3.4a.

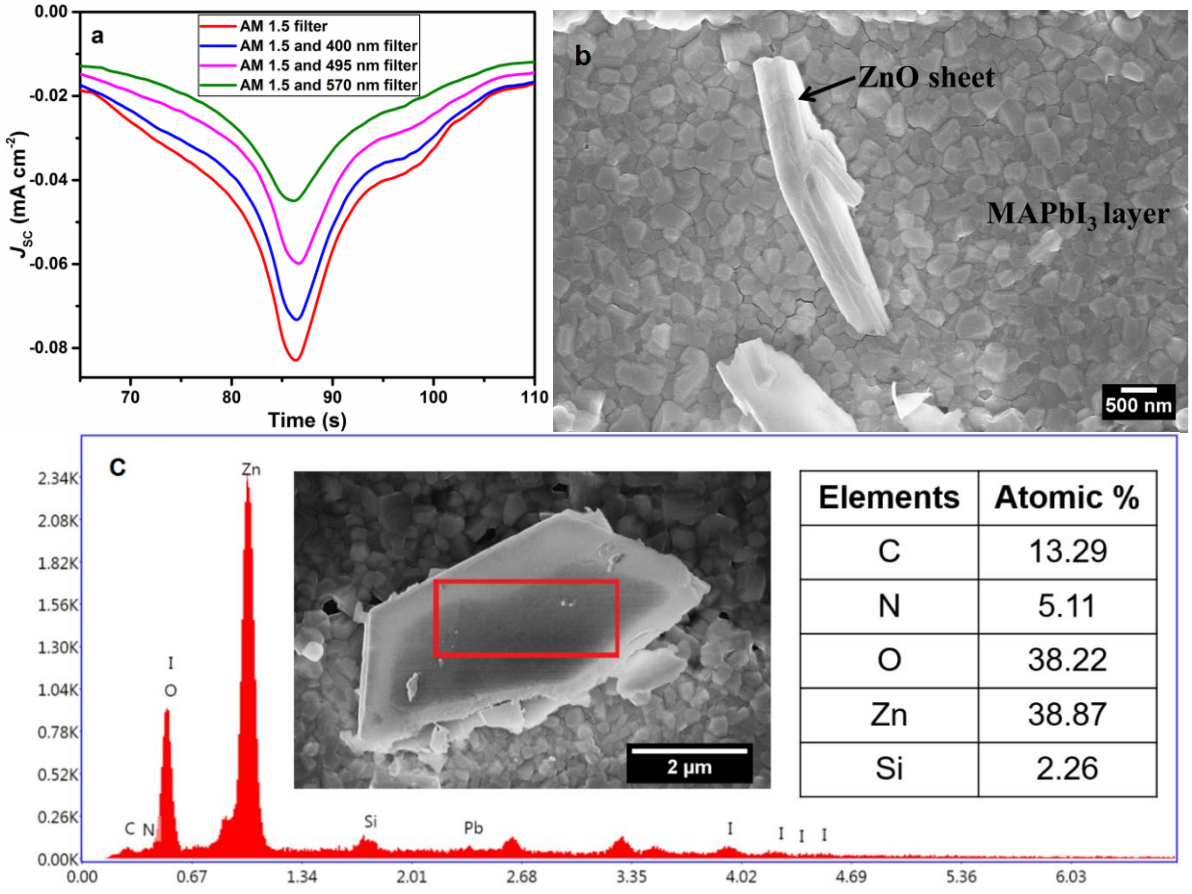

Figure 3.5. Effect of filters and confirmation of ZnO sheets on $MAPbI_3$ film. a) The device response in J_{sc} to load cycle of 37 kPa gradually decreases but is sustained on progressively placing long pass filters of increasing wavelengths in the light path. The device was poled at 1 V µm^{-1} field for 5 min. b) FESEM image of $MAPbI_3$ film shows the presence of the ZnO sheet that was used to press on it as a dynamic drain. c) EDX spectrum and elemental composition confirm the sheet fragment to be ZnO.

3.4. Conclusions

Both polarization and ion migration behavior is observed in $MAPbI_3$ films based on the conditions used for poling the films. The effects are the result of the material's response to applied poling fields, with each dominating under particular conditions. Further, the ion back-diffusion effects and redox-based degradation is minimal in these devices under the operating conditions. These effects are however critical and can become dominating at other conditions that might be used in perovskite-based devices and need to be carefully considered. The two proposed effects are also distinguished based on the observed reversal of the polarity of the V_{oc} and J_{sc}. We also believe that more experiments need to be performed to ascertain the proposed mechanism for the observed effects and especially the role of O_2 adsorption and defects in $MAPbI_3$. The polarization effect combined with the semiconducting nature of these $MAPbI_3$ films leads to a sustained V_{oc} on the order of a few hundreds of mV and a small J_{sc}. Using this polarization-semiconducting nature of the $MAPbI_3$ films, we have then demonstrated a solar (light) powered tactile sensor that functions for more than 72 h after poling for just 5 min at 1.5 V μm^{-1}. The device functions by using a dynamic drain made from ZnO nanosheets whose interfacing area with the $MAPbI_3$ channel modulates in response to the applied pressure. The only electrical energy required to operate the device is during the poling process which is $\sim$55 μW h cm^{-2}. Such low energy cost and solar-driven devices are highly relevant for remote sensing, and continuous monitoring applications. The use of polarization-semiconducting nature of the $MAPbI_3$ films opens the avenue to explore these effects in other similar materials and use them for the development of new low-cost solar-light driven devices and sensors.

Chapter 4

Modulation of Mechanical Properties and Stable Light Energy Harvesting by Poling in Polymer Integrated Perovskite Films*

4.1. Introduction

Integration of polymers with inorganic crystals and materials leads to versatile behavior in many natural systems such as bones and mollusk shells.[207–209] The flexibility of polymer chains with the ability to dissipate energy, the regular presence of functional groups and their versatile nature in having hydrophobic or hydrophilic groups, and the ability to have limited or high electronic and ionic conductivity are the properties that make their integration into such systems complementary to the characteristics of the inorganic components.[210–212] This concept has therefore been actively researched to develop materials with high mechanical strength and toughness, high electrochemical performance, and sensitivity for the detection of stimuli.[213–217] Here we show polystyrene (PS) coupled organolead halide perovskite ($MAPbI_3$) films whose mechanical properties can be tuned by varying their polymer content. Specifically, the modulus of the films can be varied from ~23 GPa to ~15 GPa based on the PS content. Further, due to the restriction of ion-migration in PS-$MAPbI_3$, these films are stable for more than 1000 h under ambient conditions and can be poled at high voltages leading to a continuous and stable power generation density of 1.1 W m^{-2} on illumination. The combination of softness and stability in the PS-$MAPbI_3$ films allows them to be applied as a pressure sensor that has a linear response with high sensitivity (up to 20 kPa^{-1}) over a very wide and tunable operating range (up to 450 kPa) and a minimum detection limit of 4 Pa in a single structure. Further, they can be self-powered by just light illumination. This combination of characteristics is crucial for monitoring diverse stimuli ranging from low pressure (<1 kPa) to high pressure range (>100 kPa). Moreover, as the pressure sensor operates in a linear regime, the user can obtain accurate information from its output without the need for any additional signal processor thus meeting the increasing demand for device miniaturization and low power consumption. Although several nano-micro structuring approaches have been adopted in order to attain high sensitivity, achieving it in combination with a wide operating range and linear response still remains a challenge, limiting their practical use. This challenge is addressed in a simple monolithic pressure sensor fabricated by integrating an organic polymer (PS) with an organolead halide perovskite ($MAPbI_3$).

* Reproduced with permission from The Royal Society of Chemistry.

The hydrophobic (organic) PS interacts with PbI_2 (due to its Lewis acid characteristics) and MA^+ cations (due to the π electrons of PS), resulting in these stable PS-$MAPbI_3$ films. Poling generates an internal polarization in the films and on illumination the generated charge carriers are separated and collected by electrodes.[10] These films can hence harvest energy from ambient light. A maximum power density of 1.1 W m^{-2} is obtained on illumination with 0.1 sun for devices poled for 5 min. They continuously generate power for more than 24 h and can then be repoled to regain their energy harvesting efficiency. Although triboelectric and piezoelectric nanogenerators have been actively researched for the harvesting of mechanical energy for powering devices, they cannot continuously produce energy from static pressure due to the conceptual limitation.[99,173,218] The semiconducting nature of the perovskite combined with its polarization effects and integration with PS presents a method to complement the capabilities of triboelectric and piezoelectric generators for use in a variety of energy harvesting devices for broader application.[219–221] This capability can also be integrated with the sensing of stimuli as the active layer in the device is a semiconducting perovskite.

4.2. Experimental Section

4.2.1. $MAPbI_3$ and PS-$MAPbI_3$ Precursor Solutions Preparation

The $MAPbI_3$ precursor solution (1.35 M) was prepared by dissolving PbI_2, MAI, and DMSO (molar ratio = 1:1:1) in anhydrous DMF. The 1wt %, 3 wt %, and 7 wt % PS-$MAPbI_3$ precursor solutions were prepared by first dissolving the required amount of PS in DMSO (53.3 µL) and DMF (317.5 µL). Then, MAI and PbI_2 (1/1 by molar) were added to the above PS solution with constant stirring for 1 h (time for crosslinking) at room temperature.

4.2.2. Perovskite Thin Film Fabrication

The silicon chips with a dimension of 1.3 cm × 1.3 cm patterned with gold electrodes were fabricated on the top of 200 nm thick SiO_2 layer by photolithography with a Cr adhesion layer. At the center of the chip, the alternating fingers form the Au positive electrode and the Au ground (negative) electrode with an electrode spacing of 2 µm. The patterned Au chips were cleaned sequentially in an ultra-sonication bath in acetone, isopropyl alcohol, and water for 20 min. The chips were then treated by piranha solution to remove trace amounts of organic residues and to make the surface hydrophilic for ensuring proper wetting by the perovskite film. Then, the chips were washed thoroughly with the Millipore water and dried by an air gun. The $MAPbI_3$ or PS-$MAPbI_3$ precursor solution was spun on a cleaned Au chip at 4000 rpm for 30 s.

After 8 s of rotation, the diethyl ether was dropped onto the center of the Au chip. Thereafter, the chip was annealed at 65 ℃ for 2 min and 100 ℃ for 3 min.

4.2.3. Film Characterization

A ZEISS Ultraplus Field-emission scanning electron microscopy (FESEM) was used to study the morphology of the perovskite films and ZnO nanosheets. A glancing incidence X-ray diffraction (GIXRD) patterns were measured on PANalytical X'Pert Pro MRD diffractometer utilizing a Cu Kα radiation at an incidence angle of 0.4°. A Horiba HR800 spectrometer in the backscattering configuration was used to measure the Raman spectra. The excitation wavelength of the laser was 532 nm and the power was 0.6 mW to avoid any sample degradation effects. The elastic modulus and hardness were measured using an in situ nanoindenter (Nanomechanics Inc. Knoxville, TN) equipped with a dynamic control module and a sharp Berkovich diamond tip. Harmonic displacement and frequency were targeted at 1 nm and 75 Hz respectively. Thin film specimen Poisson's ratio was assumed to be 0.25. Experiments were performed when the instrument thermal drift rate was less than 0.05 nm/s. Data were analyzed according to the Oliver and Pharr model.[224] Area function was validated with a fused silica specimen at indentation depths in the range of 50 and 300 nm.

4.2.4. Device Measurement

Simulated AM 1.5G irradiation (10 mW cm^{-2}) with a xenon-lamp based solar simulator (Newport Oriel Instrument 67005, 150W Solar Simulator) was used as the illumination source. The light intensity was calibrated before photocurrent measurement by a silicon (Si) diode (Hamamatsu S1133) equipped with a Schott visible-color glass-filtered (KG5 color-filtered) to minimize spectral mismatch. A black box was used to avoid stray light. The probing station was used to conduct the measurements on the symmetric lateral Au/PS-$MAPbI_3$ (or $MAPbI_3$)/Au structure cell configuration. The plain $MAPbI_3$ or PS-$MAPbI_3$ films were poled at different voltages for 5 min, by connecting one probe to the Au pad on the Au chip and another probe connected to the Au ground. The poling was done under 0.1 sun illumination and in the ambient atmosphere (presence of O_2) to generate an internal polarization in the films. A Keysight 6614C 50 Watt system power supply with a maximum voltage output of 100 V was used for the poling process. After poling the device, the short circuit current density (J_{sc}) and the open circuit voltage (V_{oc}) were recorded using a Keysight 3458A Digital multimeter. The film was connected

in series with the multimeter and power supply to form a circuit. For measuring the power (or energy) density of the plain $MAPbI_3$ and PS-$MAPbI_3$ films, first, the film was electrically poled at a particular voltage for 5 min and then the J_{sc} was recorded as a function of external load resistance. For the self-powered tactile sensor, ZnO nanosheets on the ITO substrate were used as the top sample and Au/PS-$MAPbI_3$ (or $MAPbI_3$)/Au lateral structure was used as the bottom sample. First, the PS-$MAPbI_3$ (or $MAPbI_3$) film was poled under 0.1 sun illumination in an ambient atmosphere and then the ZnO nanosheets were interfaced with the perovskite layer. Three probes system was used; the first probe was connected to the Au pad, the second probe was connected to the Au ground electrode on Au chip, and the third probe was connected to the ITO substrate. An MFA Motorized Miniature Linear Stage was used to apply the pressure load to the samples. A Honeywell Model 31 Miniature Load Cell was connected to the stage for measuring the load. Combined with a micro-pro series digital panel meter, we were able to read out the measurements and record the data. The operational stability and continuous power generation from the 1 wt % PS-$MAPbI_3$ device (with or without the ZnO interface) was carried out in an ambient environment by initially poling the device for 5 min (under 0.1 sun illumination and in ambient air), and then tracking the J_{sc} response by applying an external load resistance identical to the resistance at maximum power point (R_{MPP}) in the current-resistance curves. During measurements, the devices were maintained at a constant resistance (R_{MPP}) and subjected to continuous 0.1 sun, AM 1.5G illumination in ambient air with 40–50% relative humidity. All measurements were conducted in ambient air without device encapsulation.

4.3. Results and Discussion

The plain $MAPbI_3$ and PS-$MAPbI_3$ films are made by the standard solution casting and solvent annealing methods.[222] For the PS-$MAPbI_3$ films, the wt % of PS is controlled in the precursor solution and the time for crosslinking is kept constant for all the films. The FESEM images of the plain $MAPbI_3$ and 1, 3, and 7 wt % PS-$MAPbI_3$ films are shown in **Figure 4.1**a–d, and uniform crystalline films are observed in all cases. The corresponding X-ray diffraction and Raman spectra are presented in the Appendix (Figure A4.1 and A4.2). Specifically, we observe a Raman shift in the Pb−I mode from 84 cm^{-1} in plain $MAPbI_3$ films to 92 cm^{-1} in 7 wt % PS-$MAPbI_3$ films, which is attributed to the interaction between PS and PbI_2 (Figure 4.1e).[222] We also observe that the MA^+ libration mode shifts from 143 cm^{-1} in plain $MAPbI_3$ films to progressively higher energy as the PS content is

increased, reaching 150 cm^{-1} for 7 wt % PS-$MAPbI_3$ films (Figure 4.1f). Similarly, the MA^+ torsional mode also shifts from ~247 cm^{-1} in plain $MAPbI_3$ films to ~258 cm^{-1} in 7 wt % PS-$MAPbI_3$ films (Figure 4.1g). The MA^+ libration and torsional shifts signify the interaction between the π-electrons of PS and the MA^+ cations, which directly impacts its local motion in the perovskite lattice.[222] We have reported the cross-linking of the PS chains due to the Lewis acid nature of PbI_2 by gel permeation chromatography in Chapter 2.[222]

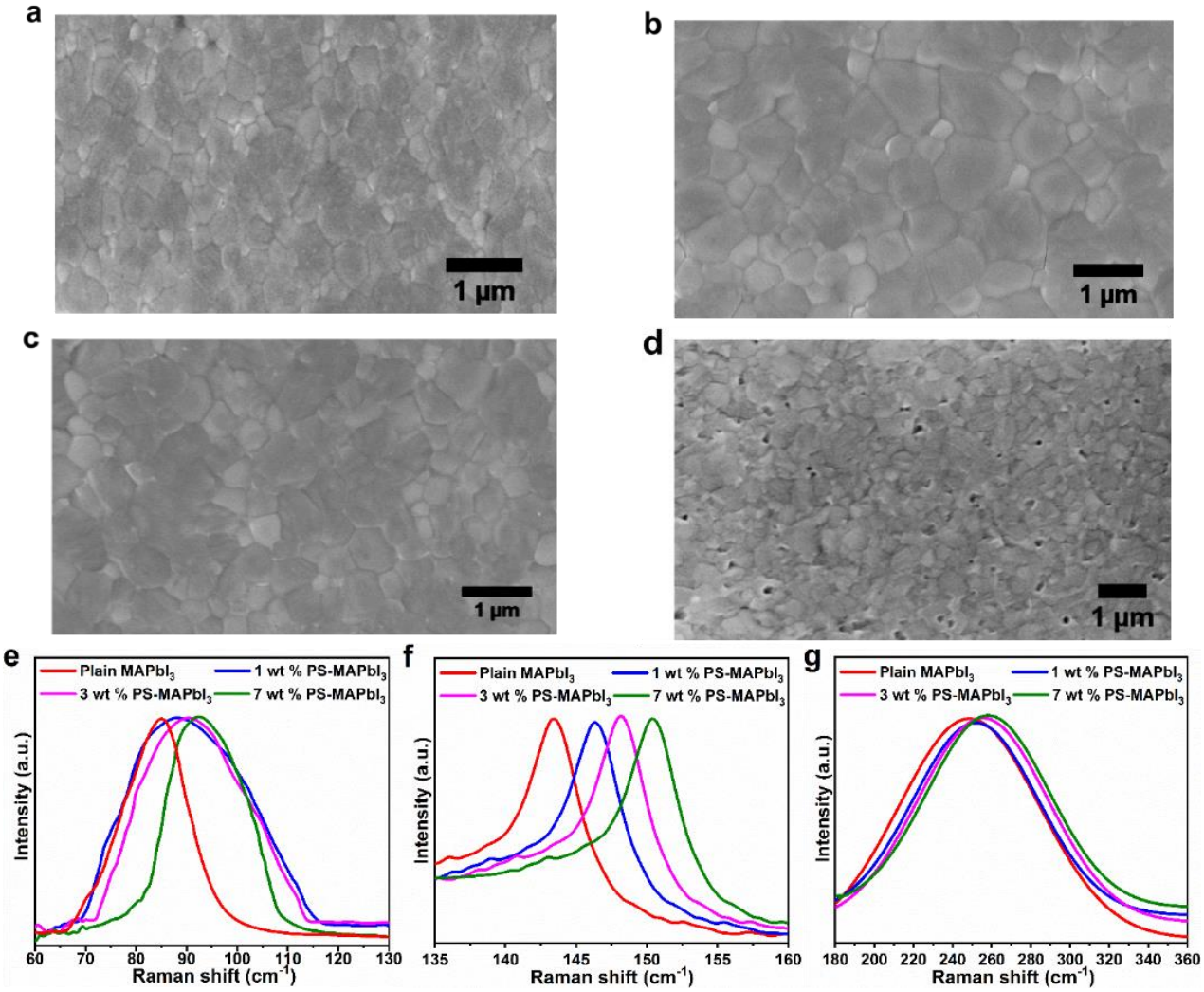

Figure 4.1. Characterization of plain and polystyrene-incorporated perovskite films. (a–d) FESEM images of (a) Plain $MAPbI_3$, (b) 1 wt % PS-$MAPbI_3$, (c) 3 wt % PS-$MAPbI_3$, and (d) 7 wt % PS-$MAPbI_3$ films. (e–g) Raman spectra of plain $MAPbI_3$, 1 wt %, 3 wt %, and 7 wt % PS-$MAPbI_3$ films at (e) 60–130 cm^{-1}, (f) 135–160 cm^{-1}, and (g) 180–360 cm^{-1} wavenumbers show the shift towards higher wavenumber with PS content.

The short-circuit current density (J_{sc}) and open-circuit voltage (V_{oc}) characteristics of plain $MAPbI_3$ and PS-$MAPbI_3$ films with varying amounts of PS in the precursor solution after poling at

electric fields of 2.5 V μm^{-1} (applied for 5 min) are shown in **Figure 4.2**a and b, respectively. We observe that all films show J_{sc} and V_{oc} generation, however, the 1 wt % PS films have the highest response. These films are therefore studied in greater detail. Further, ion migration in the films is recorded from their current response to a constant bias in the dark; the observed decay in current is a direct measure of the extent of ion migration. As seen in Figure 4.2c the presence of PS significantly reduces the ion migration current, which allows these PS films to be poled at higher field strengths compared to the plain $MAPbI_3$ films. The 1 wt % PS-$MAPbI_3$ films show a monotonous increase in power density with poling fields (Figure 4.2d), consistent with the expectation that higher fields will increase internal polarization. The maximum power density of the 1 wt % PS-$MAPbI_3$ films is recorded as 215 mW m^{-2} using an external load resistor as shown in Figure 4.2e, after poling at 5 V μm^{-1}. Perovskite films are good hole conductors but their electron conductivity is limited,[197] and hence to further improve the performance of energy harvesting a top layer of ZnO nanosheets (morphology is shown in Figure A4.3, Appendix) is interfaced with the PS-$MAPbI_3$ films (schematic in Figure 4.2f, with a static load of 100 kPa) for more efficient extraction of electrons. As a result, the power density increases to 1.1 W m^{-2} (Figure 4.2e). The band diagram of the device (Figure A4.4, Appendix) shows efficient electron extraction with the use of the ZnO layer. Continuous and stable power generation is observed in these films (with the ZnO layer) for more than 24 h (Figure 4.2g), and subsequently, on repoling, the efficiency is recovered. The loss is hence attributed to the depolarization of the films and not to any structural degradation. 1 wt % PS-$MAPbI_3$ films without the ZnO interface also show similar behavior (see Figure A4.5, Appendix). Since continuous power generation is observed with light illumination and under constant interfacing (static load) with the ZnO layer, the observed effect is attributed to the polarization effects in the perovskite layer.

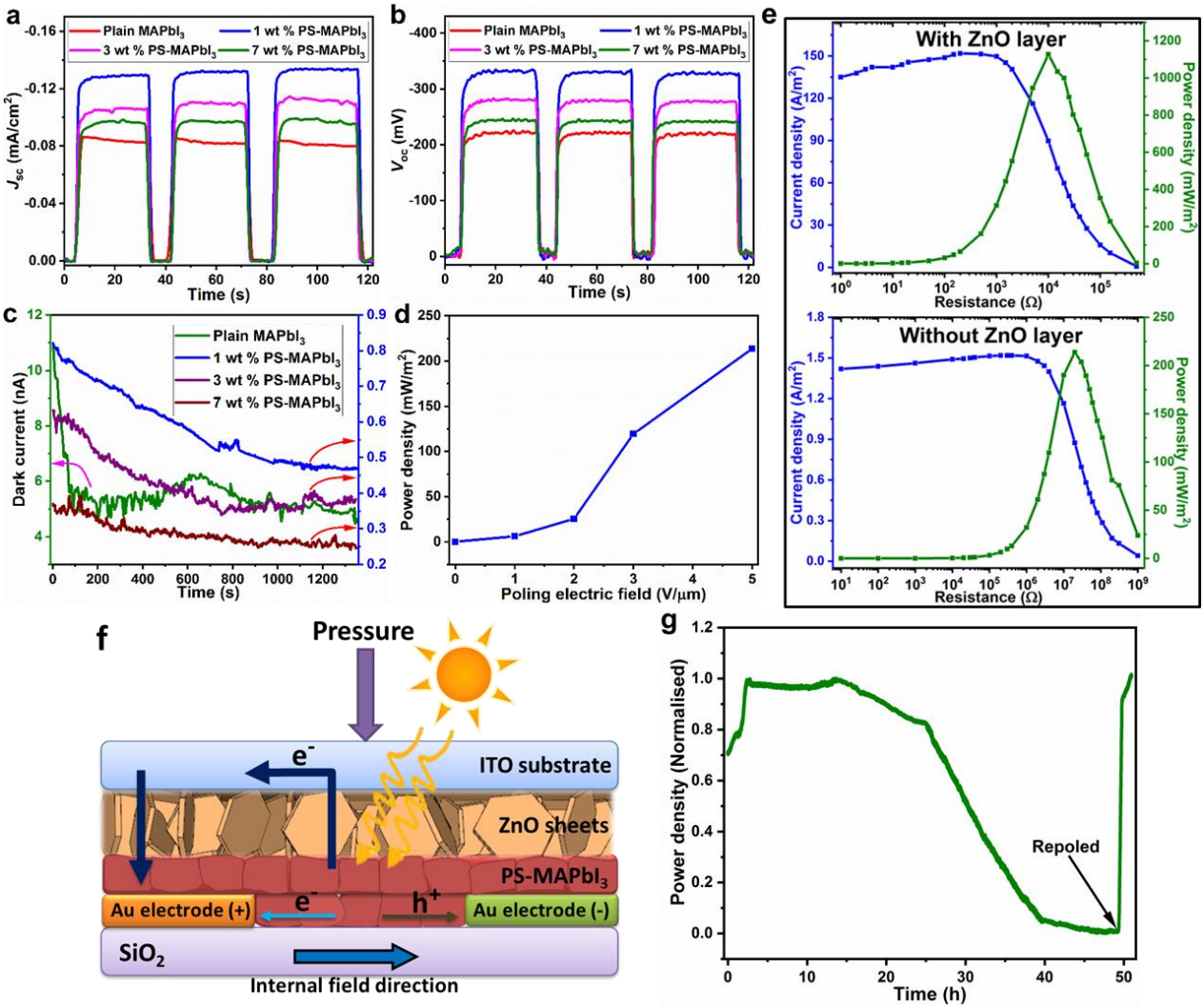

Figure 4.2. Device performance, structure, and energy-harvesting capability. (a) J_{sc} and (b) V_{oc} cycles of plain $MAPbI_3$, 1 wt %, 3 wt %, and 7 wt % PS-$MAPbI_3$ devices after 2.5 V μm^{-1} poling for 5 min in the air under 0.1 sun illumination. (c) Dark current (and ion migration current) response from the perovskite devices at a constant bias of 3 V. (d) Power density dependence on strength of the poling electric fields for 1 wt % PS-$MAPbI_3$ device without ZnO layer. (e) Output current and power density as a function of different external resistances for 1 wt % PS-$MAPbI_3$ device (after 5 V μm^{-1} poling) with and without the ZnO layer. (f) Schematic diagram of the self-powered PS-$MAPbI_3$ pressure sensor where ZnO nanosheets are interfaced with the PS-$MAPbI_3$ film. (g) Operational stability and continuous power generation from the 1 wt % PS-$MAPbI_3$ device (after 5 V μm^{-1} poling) interfaced with ZnO nanosheets, examined at maximum power point with a constant resistance of 10 kΩ and a static load of 100 kPa under continuous 0.1 sun illumination in air.

Plain $MAPbI_3$ films have a reported elastic modulus of ~22 GPa.[223] The integration of softer PS (with a reported modulus of ~3–4 GPa) should affect the mechanical properties of the PS-$MAPbI_3$ films. Measured by nano-indentation, we see (**Figure 4.3**a) that as the wt % of PS is

increased in the precursor solution the films become softer. The elastic modulus for plain $MAPbI_3$ films measured at an indentation depth of ~75 nm is recorded as ~23 GPa, and this reduces to 19.2 GPa and 15.4 GPa as the PS content in the precursor solution is increased to 1 and 7 wt %, respectively. The corresponding hardness values as a function of indentation depths are shown in Figure A4.6 (Appendix). The ability to modulate the mechanical properties of these films has direct implications for their use in electromechanical and optomechanical devices. We apply this ability towards making tunable range pressure sensors that are also combined with the light harvesting properties of these films resulting in light-powered tunable pressure sensors. The concept is based on modulating the interface between the ZnO nanosheets and the PS-$MAPbI_3$ films by an applied pressure (Figure 4.2f). The response of a 1 wt % PS-$MAPbI_3$ film under 0.1 sun illumination to applied pressure after poling at 5 V μm^{-1} is shown in Figure 4.3b, where a direct correlation between J_{sc} and the applied pressure is observed. The derivative of current density and pressure shown in Figure 4.3c further illustrates that the current accurately tracks the changes in applied pressure both in magnitude and rate. The interface of the sheets with the perovskite film can be taken as being similar to a flat surface indenter interacting with a plain film. The increase in the interaction area with the load then follows a linear relationship, similar to the observed behavior.[10,224] Further, the observed increase in current can be attributed to the increase in contact area (and not piezoelectric or triboelectric effect) as with time under a constant load the current response is maintained (Figure A4.7, Appendix). The sudden variations in the pressure rates (dP/dt) during the loading steps are the result of the feedback loop of the motor, as confirmed by the similar loading curves of pressure on using just glass slides (Figure A4.8, Appendix). The response from the sensor is correlated with the magnitude of the applied pressure as seen in cycling at different pressure loads in Figure 4.3d. Further, the sensor is highly stable as there is no loss in response to more than 200 rapid loading cycles (Figure 4.3e). The FESEM images of the ZnO sheets after testing (Figure A4.9, Appendix) show that their morphology is not altered, further attesting to the stability of the device. Control experiments show that the effect is due to the ZnO sheets, and these were done by observing current modulation in just the perovskite layer and ZnO layer (Figure A4.10, Appendix) in the same set-up. No modulations were observed in current through the perovskite layer with a load while the current through the ZnO sheets followed identical modulation behavior to the device.

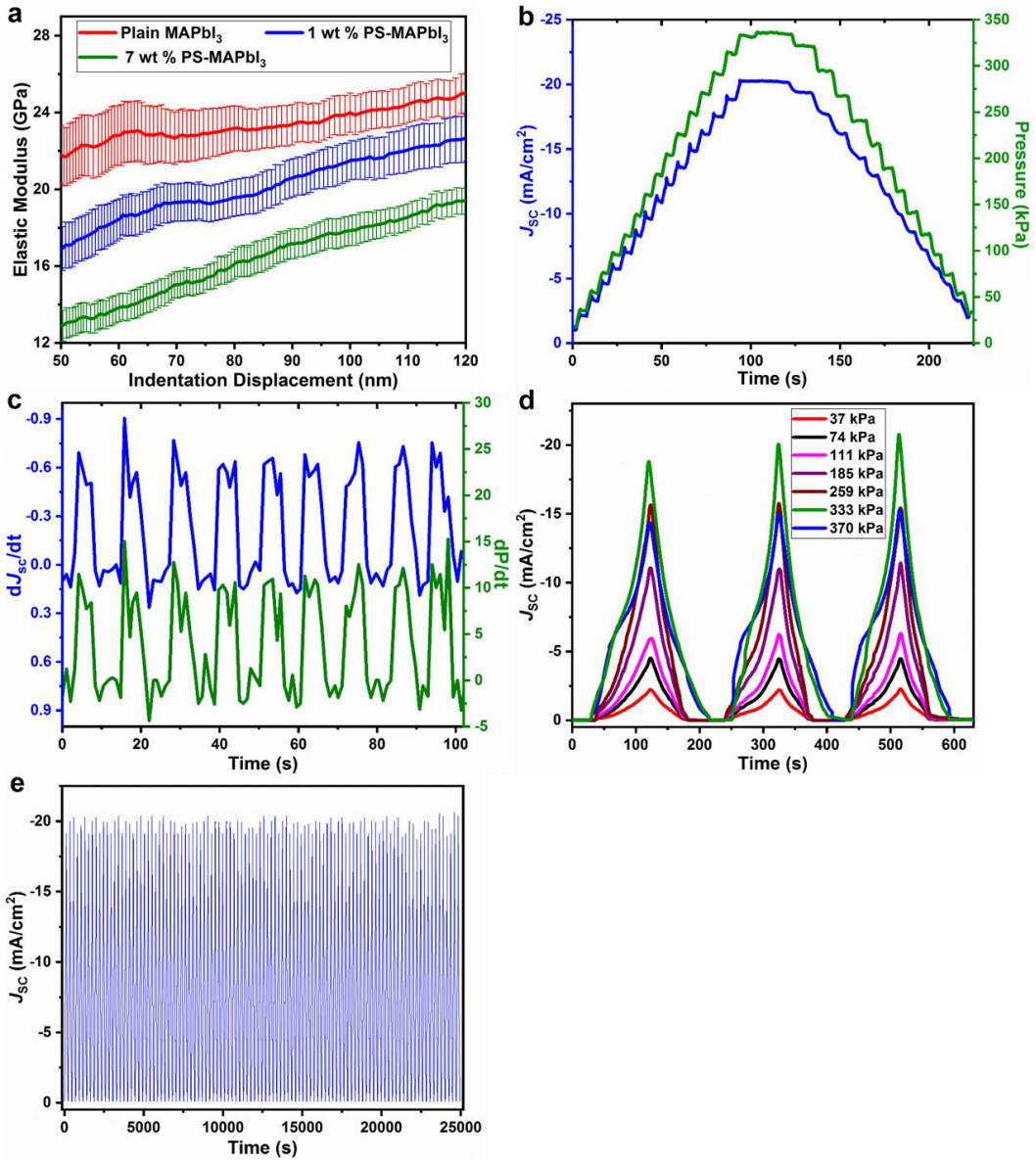

Figure 4.3. Mechanical properties and pressure-sensing capabilities of monolithic 1 wt % PS-$MAPbI_3$ pressure sensor. (a) Elastic modulus for plain $MAPbI_3$ and PS-$MAPbI_3$ films with varying amounts of PS show the stiffness of the films. The standard error is based on sampling over 8–10 different indentation spots. (b) J_{sc} response is in step with the dynamic and static pressure modulation. (c) Derivative of the J_{sc} response tracks that of the applied pressure with accuracy. (d) J_{sc} cycles with various applied pressure stimuli show a consistent response. (e) Cyclic stability and durability test of the pressure sensor under repetitive high-pressure loading of 333 kPa. The response from the pressure sensor was monitored after 5 V μm^{-1} poling for 5 min under 0.1 sun illumination in air.

Varying the PS content in the PS-$MAPbI_3$ films will directly affect their functioning as a pressure sensor due to the change in their mechanical modulus. This is confirmed by observing the response of PS-$MAPbI_3$ films with varying amounts of PS in the precursor solution (**Figure 4.4**a).

Two effects are observed: first, as the PS content increases the dynamic range for pressure sensing increases, and second, however, the sensitivity does not follow a monotonic trend. Plain $MAPbI_3$ films are limited to ~100 kPa pressure range before saturation in J_{sc} is observed. Introducing PS increases the dynamic range of the device progressively to more than 400 kPa with 7 wt % PS-$MAPbI_3$ films. The maximum sensitivity in response is, however, observed for the 1 wt % PS-$MAPbI_3$ films, as seen in Figure 4.4b. At a maximum poling field of 5 V μm^{-1}, the 1 wt % PS-$MAPbI_3$ devices attain a high sensitivity of 19.77 kPa^{-1} (with a linear response up to 333 kPa), which is 30 times more than the maximum sensitivity possible with the plain $MAPbI_3$ films (0.64 kPa^{-1}) (Figure 4.4c). We observe that the sensitivity of the 1 wt % PS-$MAPbI_3$ device increases with the strength of the poling electric field (Figure 4.4d). This is consistent with the increased internal polarization which will lead to more effective charge separation, thus improving both the charge collection efficiency by the ZnO films and the sensitivity to pressure modulations. However, the sensitivity of the plain $MAPbI_3$ device increases up to 3 V μm^{-1} poling field; subsequently, at higher poling fields (>3 V μm^{-1}) the performance decreases due to the segregation of the ions which results in the formation of PbI_2 and hence the observed polarization effect decreases. Further, the 1 wt % PS-$MAPbI_3$ device can sense pressure as low as 4 Pa (50 µL water droplet) as shown in Figure A4.11 (Appendix). A softer perovskite film due to the incorporated polymer is better able to dissipate the mechanical energy and hence extend the linear operating pressure range of these devices, which is similar to the observation with indentation of softer films.[225] The sensitivity is however dependent on both the poling effects (resulting in the generation of J_{sc}) and the mechanical properties. Hence, better sensitivity is observed with the 1 wt % PS-$MAPbI_3$ devices. In general, the incorporation of the polymer increases the sensitivity and linearity range of the PS-$MAPbI_3$ films compared to plain $MAPbI_3$ films. This allows us to tune the operating range, sensitivity, and linear range of these pressure sensors based on the polymer content. Further, the 1 wt % PS-$MAPbI_3$ device once poled at 5 V μm^{-1} for 5 min can be easily operable for more than 120 h without a power source and after that, the device can be repoled to recover the performance (Figure 4.4e), whereas the plain $MAPbI_3$ and 3 wt % and 7 wt % PS-$MAPbI_3$ devices are operable only for 48 h, 72 h, and 48 h, respectively (see Figure A4.12, Appendix). It can be clearly observed that compared with the previous literature, the monolithic 1 wt % PS-$MAPbI_3$ pressure sensor exhibits one of the best combinations of high sensitivity with a linear response over a broad dynamic pressure range, as well as the device can be self-powered (Figure 4.4f and Table A4.1).[90,92,93,95,96,99,173,200,202,204–206,226–

[236] Further, this is achieved in a simple device structure with the ability to sense both constant static stimuli and also dynamic stimuli, which is a challenge in many architectures.

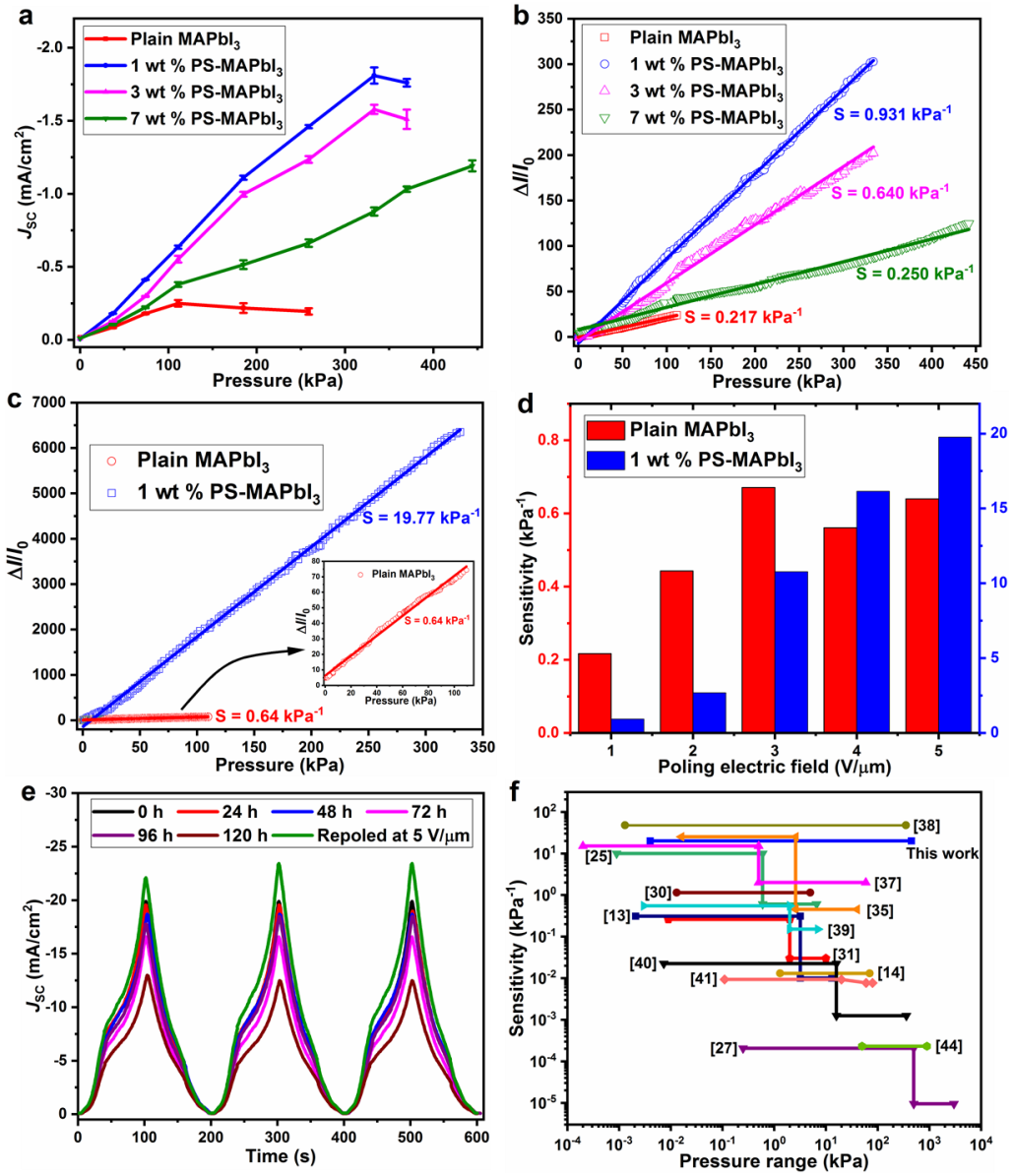

Figure 4.4. Pressure sensitivity, linearity, and self-powered operation of the devices. (a) Variation of J_{sc} as a function of applied pressure for plain $MAPbI_3$, 1 wt %, 3 wt %, and 7 wt % PS-$MAPbI_3$ devices after 1 V μm^{-1} poling for 5 min in the air under 0.1 sun illumination. (b) Relative current of the devices (after 1 V μm^{-1} poling) in response to the applied pressure shows the linear response over the broad dynamic range. (c) The sensitivity and pressure range of 1 wt % PS-$MAPbI_3$ device (after 5 V μm^{-1} poling) is more than the plain $MAPbI_3$ device. (d) The sensitivity of the 1 wt % PS-$MAPbI_3$ device increases with the poling field strength. (e) J_{sc} response is maintained over 120 h to load cycles of 333 kPa for the 1 wt % PS-$MAPbI_3$ device after initial poling at 5 V μm^{-1} for 5 min. (f) Comparison of the sensitivity, linear sensing response, and dynamic pressure range of this work with the previously reported pressure sensors.

4.4. Conclusions

Polystyrene chains having specific π–cation interactions with the perovskite matrix are incorporated into perovskite films and this modulates their mechanical and electrical properties. As a result, we show that the PS-$MAPbI_3$ films have highly reduced ionic currents with greater stability that allows them to be poled at higher electric fields. The poling effects result in a stable and continuous power generation of more than 1.1 W m^{-2} under light illumination, comparable to the best reported energy harvesting densities with triboelectric generators, which are intermittent in nature. The incorporation of PS also makes the films softer which combined with the stable energy generation leads to light powered tactile sensors that have a wide dynamic range and linear response and high sensitivity in a single structure. The ability to develop such organic-inorganic films with tunable properties using semiconducting perovskites have wide-ranging implications for their application in energy harvesting and detection, *e.g.*, light-powered sensors, quantum electronics, and electro-optical devices, due to their greater stability and higher polarization effects.

Chapter 5

Self-Powered Photodetector Based on Electric Field Induced Effects in $MAPbI_3$ Perovskite with Improved Stability

5.1. Introduction

Self-powered devices and detectors are crucial for the development of interconnected systems ranging from smart buildings and cities to personal monitors. They reduce the energy cost of operating such systems and ease the need to develop and integrate a separate power source.[237−239] For example, photodetectors with a self-powered operation are desirable for monitoring ambient sunlight and adjusting the illumination levels inside buildings accordingly. They are also required for applications in imaging and communications. Intense research is currently focused on developing such self-powered photodetectors. Piezoelectric and triboelectric generators, for example, harvest mechanical energy to power such devices and hence have been actively researched to develop such systems.[240−242] However, they are active only in the presence of continuously varying mechanical input such as due to human activity of walking and finger tapping, and hence their measurement is also intermittent in nature. Here we show a self-powered, continuously operable photodetector made with Organolead halide perovskites $MAPbX_3$ ($MA = CH_3NH_3$, X = I). Self-powered operation is achieved because of the combination of the effects of electric field poling in $MAPbI_3$ and its semiconducting nature.[10,24,243] Further, both the self-powering operation and photodetection are combined in a single perovskite layer, resulting in a monolith form for the detector and a simple one-step fabrication process. The detector has a photoresponsivity of more than 0.61 A W^{-1}, and a detectivity of 1.5×10^{13} Jones while attaining an I_{ph}/I_{dark} (on-off ratio) of more than 3×10^4 without the use of any external power source. Loss of stability and performance due to photodegradation and ion migration under electric fields are a major concern for perovskite devices.[10,244−247] We also report a significantly improved device stability and performance by compositing the precursor perovskite solution with polystyrene (PS), prior to the solution casting of the perovskite layer (as mentioned in Chapter 2). We observe that when stored under the ambient condition, the PS-$MAPbI_3$ devices show stable structure for more than 20 days. In

contrast, plain $MAPbI_3$ devices degrade in just 4 days. Further, the PS-$MAPbI_3$ device has 70 times better detectivity in comparison to the plain $MAPbI_3$ device.

$MAPbI_3$ perovskite (and other similar analogs) are characterized by properties such as high charge carrier mobility, broad absorption spectrum and easy fabrication process that has led to their widespread application in solar cells, photodetectors, and other optoelectronic devices.[248−252] At the same time, $MAPbI_3$ is a semiconductor with reported polarization effect (or ferroelectric nature) and also electric field induced ion migration effects.[23,34,65] We have reported in Chapter 3 that a stable open circuit voltage (V_{oc}) and short circuit current (I_{sc}) can be generated in planar lateral devices of configuration Au/$MAPbI_3$/Au after poling them under air and light illumination.[10] The electrode gap in these devices is between 2 and 4 μm and the poling fields are kept limited (to a maximum of 5.0 MV m^{-1}) to avoid degradation reactions. In contrast, poling done under N_2 and in dark conditions results in an unstable V_{oc} and I_{sc} response. Both these responses result from poling field effects but there is a sign reversal in the generated V_{oc} and I_{sc} between the two conditions signifying their distinct origin.[10] Here, we specifically use stable poling conditions to develop a self-powered photodetector. We also see that the response from the PS-$MAPbI_3$ device is more stable and it generates a greater V_{oc} and I_{sc} than plain $MAPbI_3$ device, signifying PS's impact on the stability of the perovskite layer while also enhancing the performance.

5.2. Experimental Section

5.2.1. Fabrication Process of Self-Powered Photodetectors

For planar lateral device, gold (Au) chips with an electrode spacing of 2 μm were fabricated on the top of 200 nm thick SiO_2 layer by photolithography with a Cr adhesion layer. Au chips were washed with Millipore water and then sonicated in a 1:1 mixture of acetone and isopropanol for 10 minutes, followed by another 10 minutes sonication in isopropanol and then Millipore water. Piranha solution was used to clean organic matter off the Au substrate. After being immersed in the piranha solution for 3 minutes, the Au chip was washed thoroughly with Millipore water and dried with an air gun. The $MAPbI_3$ and PS-$MAPbI_3$ films were prepared on Au chip via a one-step solvent engineering method. The prepared perovskite solutions were spin-coated on the Au chip at 4000 rpm for 30 s. After 7-8 seconds of rotation, 200 μL of diethyl ether was added dropwise to form an intermediate phase that prevented the MAI and PbI_2 reagents from reacting

too quickly, thus enabling a uniform film. The obtained films were annealed at 65 °C for 2 min and 100 °C for 3 min.

5.2.2. Photodetector Characterization

Field emission scanning electron microscopy (FESEM, Zeiss Ultraplus) system was used to acquire images of the crystallized $MAPbI_3$ and PS-$MAPbI_3$ films. XRD diffraction patterns were obtained from the perovskite films by glancing incidence X-ray diffraction (GIXRD) using a PANalytical X'Pert Pro MRD diffractometer with Cu Kα radiation (λ = 1.54 Å) at an incidence angle of 0.4°. X-ray photoelectron spectroscopy (XPS) spectra were recorded on a Thermo-VG Scientific ESCALab 250 Microprobe, which is equipped with an Al Kα monochromatic X-ray source (1486.6 eV). Measurements on the symmetric lateral structure cell configuration were conducted using a probing station. A two probe method was used by connecting one probe to the Au pad on the Au chip and another probe connected to the ground. A Keysight 6614C 50 Watt system power supply with a maximum voltage output of 100 V was used for the poling process. Both films were poled at different voltages for 10 min. After poling, the open circuit voltage (V_{oc}) and the short circuit current (I_{sc}) were measured using a Keysight 3458A Digital multimeter. The film was connected in series with the multimeter and power supply to form a circuit. Electrical poling was done under the N_2 atmosphere and in dark condition for the ion-migration effect, while for polarization effect (stipulated ferroelectric) poling was done under illumination and in the ambient atmosphere (presence of O_2). Photocurrent, V_{oc}, and I_{sc} measurements were performed under simulated air mass 1.5 global irradiation (100 mW cm^{-2}), generated using a Xenon-lamp based solar simulator (Newport Oriel Instrument 67005, 150 W Solar Simulator). A NREL calibrated KG5 silicon reference cell was used to calibrate light intensity in order to minimize spectral mismatch. For nitrogen effect, the films were kept in a steady N_2 flow during the poling and measurements to prevent the absorption of oxygen and moisture. For the stability test, the films were stored in an ambient condition (moisture and oxygen) over 20 days.

To evaluate the performance of self-powered photodetectors, some key parameters such as the on-off ratio, voltage responsivity, and external quantum efficiency (EQE) were calculated by the following equations. The on-off ratio is the ratio between photocurrent (I_{ph}) and dark current (I_{dark}) and can be written as I_{ph}/I_{dark}. The Voltage responsivity can be defined as (V_{dark}-V_{ph})/P, where V_{dark} is the dark current when the light is off, V_{ph} is the photocurrent when the light

is on, and P is the irradiance power density. EQE is described as the electrons generated divided by the incident photons and can be expressed as $Rhc/e\lambda$, where R is the current responsivity, h represents the Planck's constant, c is the velocity of light, e is the electronic charge, and λ is the wavelength of the incident light.

5.3. Results and Discussion

A typical device configuration is shown in **Figure 5.1**a. The photocurrent response from both the type of devices at a constant bias of 5 V before poling and under varying light illumination intensities (using a solar simulator) is shown in Figure 5.1b (without PS) and 5.1c (with PS). We clearly observe that the PS-$MAPbI_3$ (1 wt % of the PS in the precursor solution of $MAPbI_3$) device shows a higher photocurrent generation as compared to the plain $MAPbI_3$ and with no observable decay. Further, increasing the PS concentration to 2 wt % severely reduced the photocurrent (Figure A5.1, Appendix) for the device. Hence, only the 1 wt % device was characterized in detail for performance as a photodetector. The FESEM images for both plain $MAPbI_3$ (Figure 5.1d) and PS-$MAPbI_3$ (Figure 5.1e) shows a multicrystalline film with different grain sizes. The PS-$MAPbI_3$ produces larger crystal grains with an average size of 390 nm, whereas the average grain size of plain $MAPbI_3$ is 210 nm. The presence of PS hence improves the crystalline nature of the $MAPbI_3$. X-ray diffraction (XRD) results (Figure A5.2a, Appendix) confirmed that the crystal structure of the PS-$MAPbI_3$ is identical to plain $MAPbI_3$. X-ray photoelectron spectroscopy (XPS) results (Figure A5.2b, Appendix) also show identical elemental signatures from I, Pb, N, and C in both PS-$MAPbI_3$ and plain $MAPbI_3$ films. The atomic ratios of N:Pb:I for the plain $MAPbI_3$ and PS-$MAPbI_3$ are 1.25:1.00:3.09 and 1.21:1.00:3.12, respectively, which are in good agreement with the $MAPbI_3$ stoichiometry.

The I_{sc} response to different light illumination intensities for plain $MAPbI_3$ and PS-$MAPbI_3$ devices after poling at varying voltages under stable conditions (in air and under illumination) is shown in Figure 5.1f,g. From these results the current responsivity, R (which indicates the efficiency of the detector in responding to an optical signal), can be defined as follows:[251]

$$R = \frac{I_L - I_D}{P \times A} \tag{5.1}$$

where I_L is the photocurrent, I_D is the dark current, P is the irradiance power density, and A is the effective illuminated area.

The corresponding current responsivities are shown in Figure 5.1h,i. We observe that the PS-$MAPbI_3$ device attains a maximum responsivity of 0.61 A W^{-1} at illumination intensity of 0.01 mW cm^{-2}. In contrast, the plain $MAPbI_3$ device reaches only 0.19 A W^{-1}. Further, we also observe that the performance of the PS-$MAPbI_3$ device increases monotonically with poling voltage while that of the plain device reaches a maximum at 7 V. This results as during poling the plain device starts to degrade above potentials of 7 V, while the PS-$MAPbI_3$ device remains stable even at 10 V poling bias. The stability of PS-$MAPbI_3$ after poling at 10 V was confirmed by XRD and FESEM and no change was observed in its crystal structure (Figure A5.3, Appendix) and morphology (Figure A5.4g,h, Appendix). In contrast, poling at 10 V induced a new phase, PbI_2, (Figure A5.3, Appendix) in the $MAPbI_3$ device and shows the complete segregation of the material in the FESEM images (Figure A5.4c,d, Appendix). Similarly, the photocurrent measured during poling at 10 V for plain $MAPbI_3$ device (Figure A5.5a, Appendix) also suddenly increased to 7.2 mA, which is 4 orders of magnitude higher than the current observed during poling at 5 V. Such high current are indication of material decomposition and migration resulting in the observed distorted morphology (Figure A5.4c,d, Appendix) and the phase change. While for the PS-$MAPbI_3$ device, the photocurrent is maintained in the range of 610−780 nA and 940−1060 nA during 5 and 10 V poling respectively (Figure A5.5b, Appendix) and hence the morphology remains intact (Figure A5.4e−h, Appendix). This signifies the effect of PS in increasing the stability of the PS-$MAPbI_3$ devices. The response in V_{oc} also shows that PS-$MAPbI_3$ devices have a better performance than plain $MAPbI_3$ devices (Figure A5.6a,b, Appendix). Further, we also observe that the devices respond in a continuous and stable manner to incessant light illumination. This ability of the device is crucial for continuous monitoring of light and optical signals without any intermittency and without any external power source.

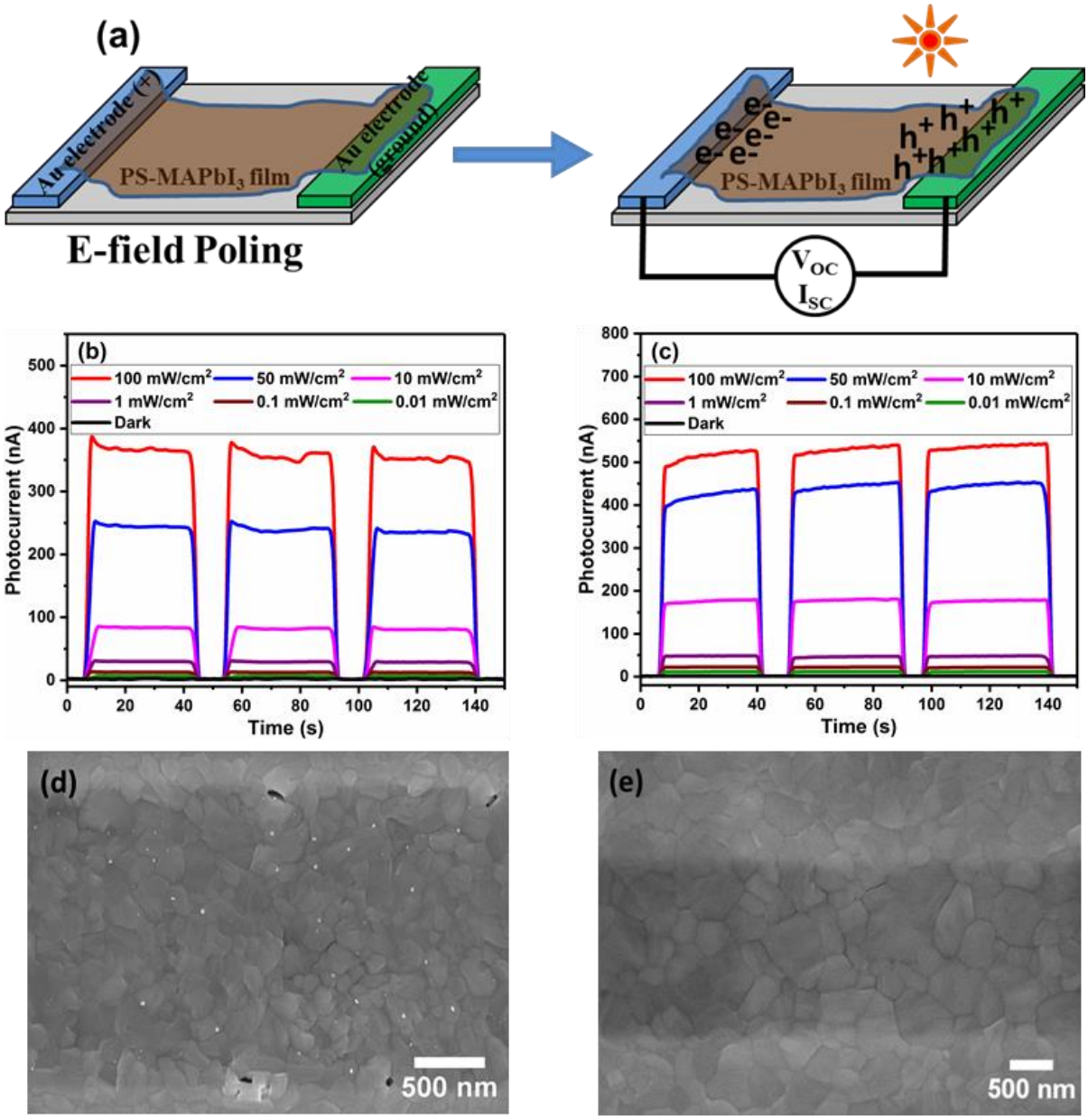

Figure 5.1A. Device architecture, morphology, and its photoresponse after poling in air and under illumination. (a) Schematic diagram of the lateral self-powered photodetector and the effect of electric field poling that generates V_{oc} and I_{sc}. Photocurrent from unpoled (b) $MAPbI_3$, (c) PS-$MAPbI_3$ devices at an applied external bias of 5 V, measured under various light illumination intensities. FESEM image of (d) $MAPbI_3$, (e) PS-$MAPbI_3$ films shows the multicrystalline nature of these films. The white dots in the $MAPbI_3$ image are just noise.

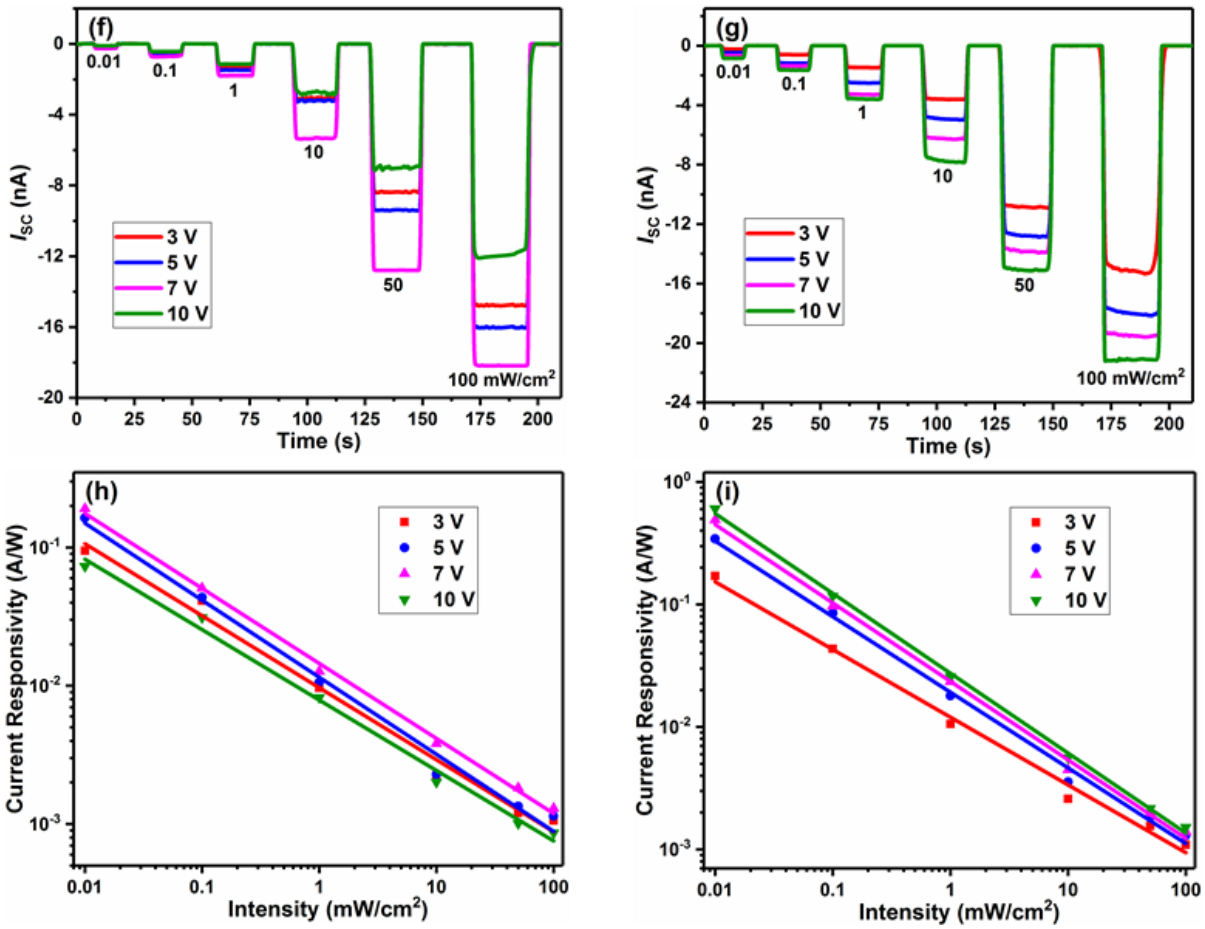

Figure 5.1B. The I_{sc} response from (f) $MAPbI_3$, (g) PS-$MAPbI_3$ devices with no applied bias to various light illumination intensities, after poling at different voltages for 10 min in air and under light illumination (1.0 sun). Current responsivity of (h) $MAPbI_3$, (i) PS-$MAPbI_3$ based photodetectors as a function of incident light intensity at different poling voltages. Typical measurements done over multiple cycles and samples (3 at least) yield an error range of 5−10% for all the samples.

The photodetection response in I_{sc} after poling the $MAPbI_3$ and PS-$MAPbI_3$ devices under N_2 and dark (the unstable conditions) is shown in **Figure 5.2**a,b, respectively. The corresponding responsivity is presented in Figure 5.2c,d. We observe that compared to Figure 5.1f,g, the I_{sc} shows a sign reversal (a similar observation is also seen in V_{oc}, see Figure A5.7a,b, Appendix). We again observe that the PS-$MAPbI_3$ devices show a much higher maximum responsivity of 0.28 A W^{-1} at illumination intensity of 0.01 mW cm^{-2} and poling voltage of 10 V. In contrast, the plain $MAPbI_3$ device reaches only 0.04 A W^{-1} in maximum responsivity at illumination intensity of 0.01 mW cm^{-2} and poling voltage of 7 V. At higher poling voltages, the plain $MAPbI_3$ device again shows unstable behavior leading to a decrease in the observed I_{sc} and

responsivity. The PS-$MAPbI_3$ device is stable even at 10 V bias, similar to the results of poling under air and illumination. We also observe (Figure 5.2a,b) that the I_{sc} shows a rapid decay for the plain $MAPbI_3$ device, in contrast, the PS-$MAPbI_3$ device has a stable response. A similar observation is also seen in the V_{oc} results (see Figure A5.7a,b, Appendix). This is due to the presence of the PS that leads to greater stability in the $MAPbI_3$ structure by limiting the ion migration effects (as confirmed in Chapter 2). The absence of decay in I_{sc} and also higher voltage stability as seen under both the conditions of poling attests to this improvement. Prior results in Chapter 3 have shown that the poling under air and illumination leads to polarization dominated response from the $MAPbI_3$ films, while poling under N_2 and dark condition leads to ion migration effects that can cause variable doping in these films.[10] In either case due to the internal electric fields generated on poling, when the $MAPbI_3$ film is illuminated by light the generated electron-hole pairs are separated. The resulting I_{sc} and V_{oc} are directly proportional to the intensity of illumination and the internal field strength (which is dependent on the strength of poling fields used), resulting in the observed self-powered photodetection capability.

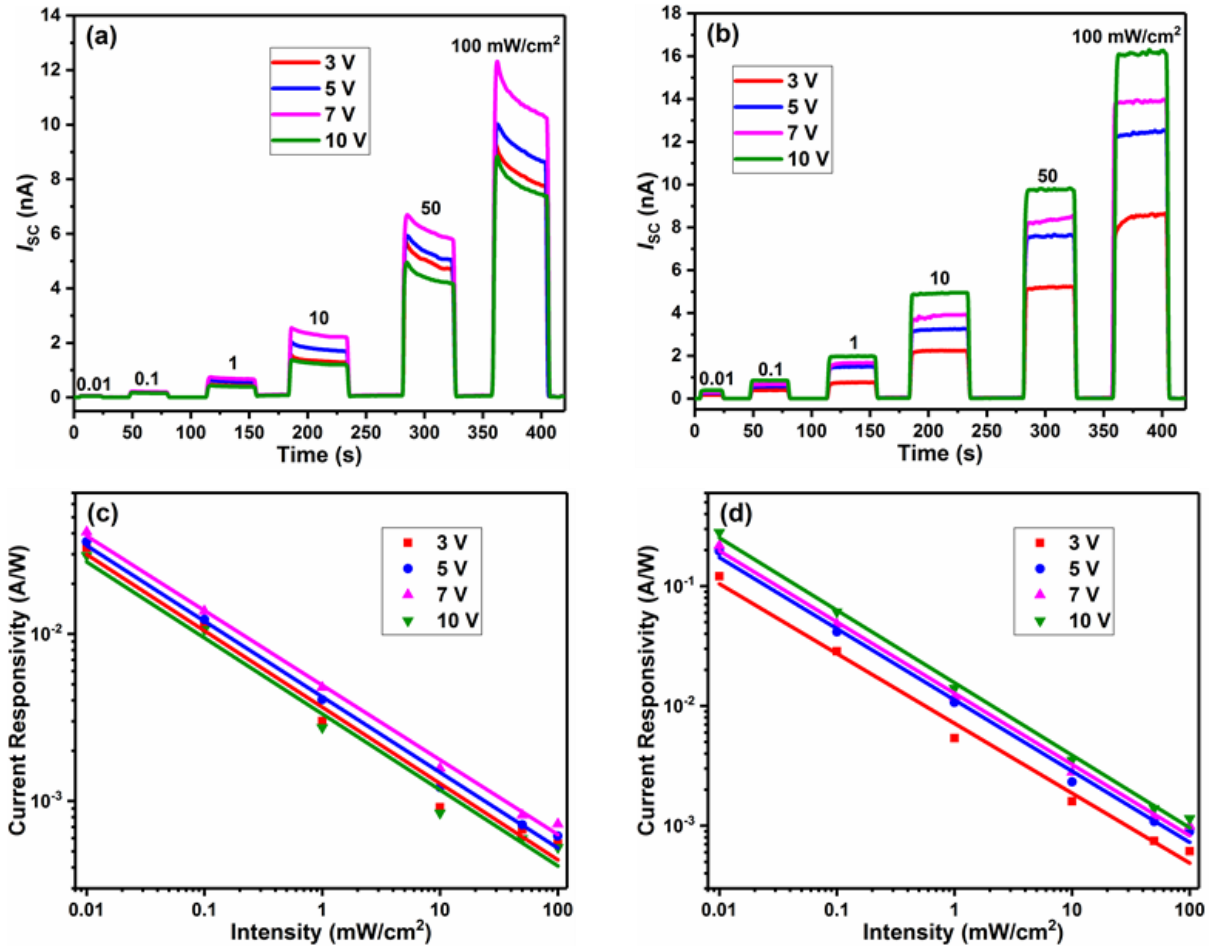

Figure 5.2. Device performance after poling under N_2 and dark. The I_{sc} response from (a) $MAPbI_3$, (b) PS-$MAPbI_3$ based photodetectors, with no applied bias to various light intensities after poling at different voltages. The current responsivity of (c) $MAPbI_3$, (d) PS-$MAPbI_3$ devices, at different light intensities and poling voltages. In all cases, the PS-$MAPbI_3$ devices show a better response. Typical measurements were done over multiple cycles and samples (3 at least) yield an error range of 5−10% for all the samples.

A direct comparison of the performance for both plain $MAPbI_3$ and PS-$MAPbI_3$ devices across the poling voltages in terms of current responsivity and detectivity (at 0.01 mW cm^{-2} illumination) is shown in **Figure 5.3**a,b. Both these parameters (responsivity for the efficiency of the detector and detectivity for the minimum optical signal that can be detected) are crucial for characterizing the performance of these devices as photodetectors. Detectivity (D^*) is commonly used as a figure of merit reflecting the sensitivity of the photodetector and can be expressed as:[251]

$$D^* = \frac{R}{\sqrt{2qJ_{\text{dark}}}} \tag{5.2}$$

where R is the responsivity, q is the elementary charge, and J_{dark} is the dark current density.

We clearly observe that the PS-$MAPbI_3$ devices have a better performance for self-powered photodetection when poled in air and under illumination. The V_{oc} characteristics of these devices also follow a similar trend with better performance observed from the PS-$MAPbI_3$ devices (Figure A5.8, Appendix). Further, the performance of the detector improves with higher poling voltages. This is expected as poling at higher voltages should lead to higher internal electric field strength which will separate the generated photocarriers more efficiently. The ratio of photocurrent to dark current (on-off ratio, at 100 mW cm^{-2} illumination) as seen in Figure 5.3c also shows that the PS-$MAPbI_3$ devices have significantly better signal-to-noise ratio. Rise and decay time on the scale of 10−20 ms (in I_{sc}) is observed in photodetection with the PS-$MAPbI_3$ devices (at 100 mW cm^{-2} intensity) under both the poling conditions (Figure 5.3d,e). Rise and decay time quantify the time needed by the photodetector to reach to a certain value (between 10% and 90%) of the maximum photocurrent during the on and off cycles of light irradiation (hence quantifying the frequency response of the detector).[251] We also calculated the transit time (τ_t) by using the formula: $\tau_t = L^2/\mu V$, L is the distance traveled by the charge carriers to reach the Au electrodes, μ is the charge carrier mobility, and V is the voltage. The estimated transit time for PS-$MAPbI_3$ device is around 3.25 μs, which is lower than the measured response time that might be due to the detection limit of our equipment. Similarly, a fast response time in V_{oc} (Figure A5.9a,b, Appendix) is also observed from the PS-$MAPbI_3$ devices poled in air and under illumination. Further, we also studied the photoresponse characteristics of PS-$MAPbI_3$ devices (after poling in air and under illumination) at different irradiance wavelengths and 1 mW cm^{-2} illumination intensity. The device shows an increase in the I_{sc} response (Figure A5.10, Appendix) as a function of wavelength in the range of 410 to 710 nm. The corresponding photoresponse parameters (responsivity and detectivity) are illustrated in Figure 5.3f, and an increase in responsivity and detectivity with the increase in irradiance wavelength is observed. The superior structural stability of the PS-$MAPbI_3$ devices compared to plain $MAPbI_3$ devices is presented in Figure 5.3g. On exposing both these devices to identical ambient conditions, with 30−40% relative humidity, we observe that the current responsivity (at an illumination of 0.01 mW cm^{-2}) in the PS-$MAPbI_3$ device is maintained by more than 84% even after 20 days. The poling effect is maintained for 2 days subsequently after which devices have to be repoled (due to loss of the poling effects) but the structural stability is maintained. While for the plain $MAPbI_3$

devices complete degradation is observed in just 8 days, with more than 70% loss within 4 days. Similar trends are also observed in current detectivity and voltage response (see Figure A5.11a,b, Appendix). We believe that the larger crystal grain size and reduced ion migration effects under the electric field in PS-$MAPbI_3$ detectors compared to plain $MAPbI_3$ lead to better performance and improved stability. The larger crystal grains in PS-$MAPbI_3$ (Figure 5.1e) effectively reduce the structural defects and hence suppress charge recombination. The suppression of ion migration effects in the PS-$MAPbI_3$ device is characterized by studying the current response at a constant bias under dark and light illumination conditions. As illustrated in Figure 5.3h under dark, the initial current at t = 0 s for PS-$MAPbI_3$ (0.36 nA at 1 V and 0.51 nA at 2 V) is more than one order of magnitude less than that of plain $MAPbI_3$ (4.47 nA at 1 V and 7.89 nA at 2 V). This is attributed to the presence of polystyrene (insulating material) in the perovskite which reduces the dark current. Further, it is also clearly observed that the PS-$MAPbI_3$ device shows a slow decay in current with time (5% and 10% of its initial value within 10 s at 1 V and 2 V, respectively). Whereas the plain $MAPbI_3$ device shows a rapid decay (23% and 57% of its initial value within 10 s at 1 V and 2 V, respectively). Moreover, in PS-$MAPbI_3$ the net drop in the current (after 600 sec.) is one order of magnitude less than that in plain $MAPbI_3$ devices. This signifies reduced ion migration effects in the PS-$MAPbI_3$ device compared to plain $MAPbI_3$ films. Under illumination (Figure A5.12, Appendix), we observe that the PS-$MAPbI_3$ device shows a higher photocurrent generation (83 nA at 1 V and 149 nA at 2 V) with no observable decay. In contrast, the $MAPbI_3$ device shows a lower photocurrent (65 nA at 1 V and 99 nA at 2 V), which also decays by 33% and 11% of its initial value within 44 s at 1 V and 2 V bias respectively, due to the ion migration effects and recombination of charge carriers.

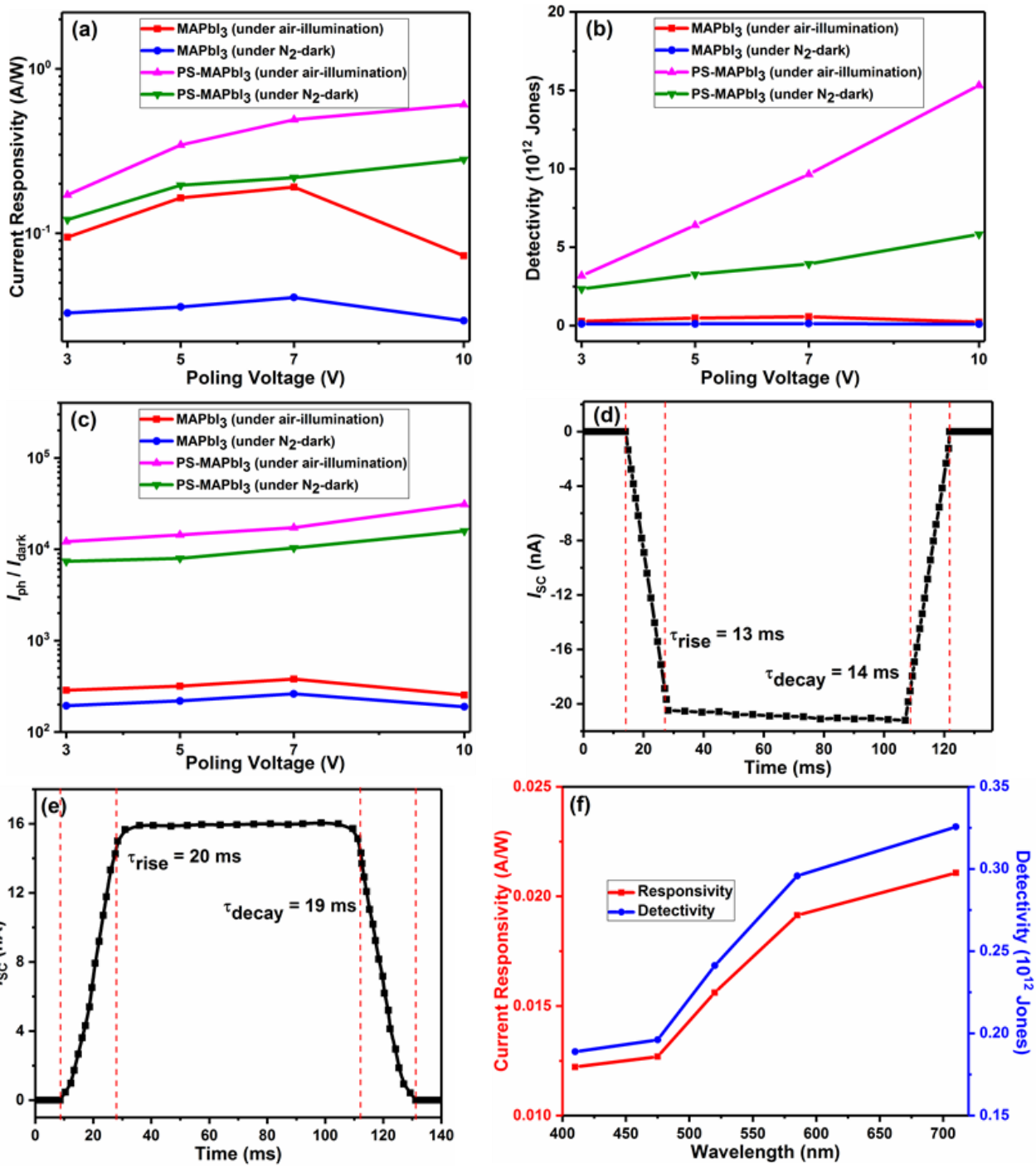

Figure 5.3A. Comparison of the performance and stability for $MAPbI_3$ and PS-$MAPbI_3$ devices under both poling conditions. (a) Current responsivity, (b) Detectivity, (c) I_{ph}/I_{dark} (on-off ratio) as a function of different poling voltages. Rise and decay times for photodetection with PS-$MAPbI_3$ devices when poled under (d) Air and illumination, (e) N_2 and dark condition. (f) Photoresponse parameters of PS-$MAPbI_3$ devices as a function of irradiance wavelength.

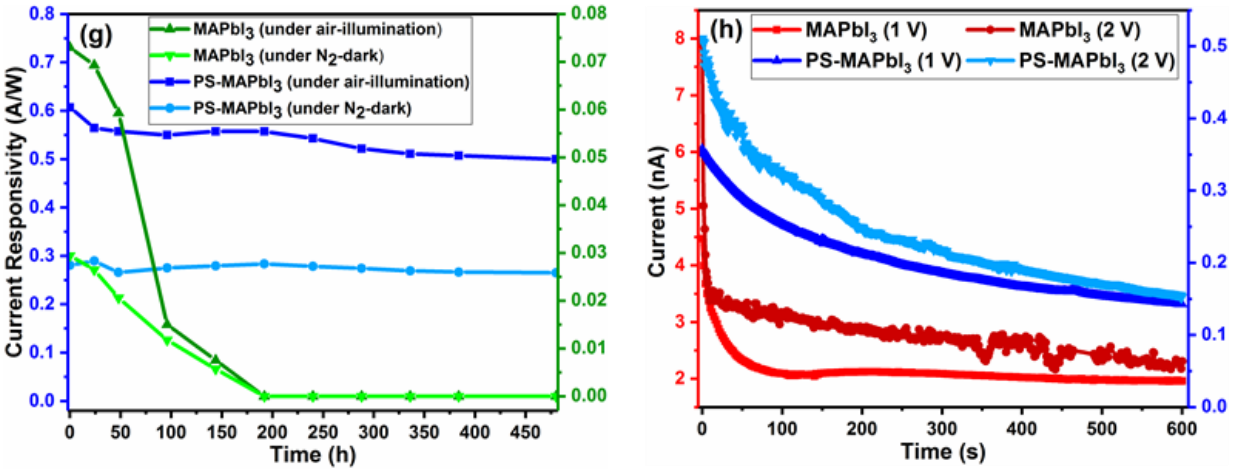

Figure 5.3B. (g) Current responsivity as a function of time showing long-term environmental stability for the PS-$MAPbI_3$ devices exposed under an ambient condition with 30−40% relative humidity. (h) Current response under dark from unpoled $MAPbI_3$ and PS-$MAPbI_3$ devices at different external biases.

5.4. Conclusions

Using the electric field-induced effects in $MAPbI_3$, we have presented a simple self-powered, monolith structured photodetector that attains a photoresponsivity of more than 0.61 A W^{-1}, and a detectivity of 1.5×10^{13} Jones. Its performance is comparable to other reported self-powered photodetectors (see **Table 5.1** for comparison), and this detector is also continuously operable for 2 days without a power source, after poling under stable conditions. Also, its fabrication is simple as it is made of a single layer of PS-$MAPbI_3$. Further, the use of PS significantly improves the structural stability of the perovskite layer to up to 20 days. The PS-$MAPbI_3$ devices also show a significantly improved performance of more than 300% in responsivity compared to plain perovskite devices. It was found that the presence of PS in the $MAPbI_3$ devices leads to larger grain size and significantly reduced ion migration and charge recombination effects and lower dark currents. Further, the PS-$MAPbI_3$ devices have a stable photocurrent under constant bias. Plain perovskite devices, in contrast, show a clear observable decay in the photocurrent. The combination of high sensitivity with the self-powered operation and extended stability presented here shows a simple method to develop such devices and sensors using the properties of perovskite, which are highly relevant for applications in remote sensing, smart systems, and optoelectronic devices.

Table 5.1. Comparison of the device performance in terms of responsivity, detectivity, light on-off ratio, rise and decay time for different self-powered photodetectors.

Device architecture and Working basis	Layer structure	Responsivity ($A\ W^{-1}$)	Detectivity (Jones)	I_{ph}/I_{dark}	t_{rise}/t_{decay} (ms)	Reference
Au/PS-$MAPbI_3$/Au and Self-powered	Monolayer	0.61	1.5×10^{13}	3×10^4	13/14	This work
ITO/PET/$MAPbI_3$/Au and Triboelectric nanogenerator	Multilayer	0.418	1.22×10^{13}	-	<80	[241]
Au/$MAPbI_3$/Au and Triboelectric nanogenerator	Multilayer	7.92	-	130	<200	[242]
FTO/C_{60}/$MAPbI_3$/ GaN/In and Solar cell	Multilayer	0.198	7.96×10^{12}	>5000	450/630	[253]
MoS_2/$MAPbI_3$ heterostructure and External bias voltage	Bilayer	0.06	-	-	2149/899	[254]
ITO/$MAPbI_3$/Au and External bias voltage	Monolayer	0.0598	-	133	91/101	[255]
FTO/TiO_2/graphene/ $MAPbI_3$/ PTAA and Solar cell	Multilayer	0.375	4.5×10^{11}	4×10^6	5	[256]
ITO/$MAPbCl_3$/PTAA/ Al and Solar cell	Bilayer	0.047	6.87×10^{10}	1371	-	[257]
FTO/c-TiO_2 /$MAPbI_3$/Spiro-OMeTAD/Ag and Solar cell	Multilayer	0.55	$\sim 10^{12}$	10^4	0.46×10^{-3}/0.94×10^{-3}	[258]
ITO/PET/ZnO/Spiro-OMeTAD/Au and Piezo-Phototronic	Multilayer	0.0008	4.2×10^9	-	160/200	[259]
FTO/Sb_2S_3/Spiro-OMeTAD/Ag and Solar cell	Multilayer	0.087	2.7×10^9	814	<25	[260]
2D black phosphorus (BP) nanosheets and Photoelectrochemical process	Electrodes	2.2×10^{-6}	-	264	500/1100	[261]

Chapter 6

Conclusions and Future Work

6.1. Summary of Contributions

The properties of organolead halide perovskites that include absorption across a wide visible range, high carrier mobility and lifetime, and low-temperature facile synthesis process, are the foundation of its application in a variety of optoelectronic fields. The challenge of stability being addressed in this thesis by understanding the basis of observed interaction between polystyrene and $MAPbI_3$ will be a significant step for the commercialization of perovskite-based devices. Further, this specific interaction also leads to the modulation of both mechanical and electro-optical properties of the perovskite films. Being a simple single-step method as presented it should also be scalable for a large-scale application.

In Chapter 2, we use the inorganic-organic interactions that routinely occur in natural systems to develop hybrid materials with an exceptional combination of properties. To address the stability challenge under illumination and exposure to ambient atmosphere, we use a similar specific interaction between polystyrene (PS) chains and PbI_2 and MAI, the common precursors that are used for making these lead halide based perovskites. The subsequently casted films consist of a polymer matrix within the perovskite layer. We report that as a result, these films have: 1. An unprecedented stability, where they show stable structure and performance for 1000 h in ambient conditions with direct and continuous illumination, and without any encapsulating or passivating layer. 2. By optimizing the polystyrene content this stability is achieved without sacrificing any device performance rather a slight improvement in efficiency is observed. This simple and effective process will significantly advance electro-optical devices based on perovskites such as solar cells and photodetectors towards commercialization while maintaining their performance and cost-effectiveness.

In Chapter 3, we develop a solar/light-powered monolith tactile sensor by combining the $MAPbI_3$ perovskite with ZnO nanostructures. The device is developed by first decoupling the polarization behavior of the $MAPbI_3$ from its ion migration effects. We show that both these effects are present simultaneously in $MAPbI_3$ films and either effect can be made to dominate based on the poling conditions. Following this understanding, we then use the combination of the

polarization-semiconducting nature of the $MAPbI_3$ films to make a tactile sensor that once poled is operable for at least 72 h using just light illumination, requiring no other power source. The sensor has a sensitivity of 0.57 kPa^{-1}, which is comparable (and in most cases better) to other transistor-based tactile sensors. It also has a linear response to load till 76 kPa, a significant advantage for sensing applications. The sensor is based on interfacing ZnO nanosheets with the poled $MAPbI_3$ film. The applied load modulates the contact area between ZnO sheets and the perovskite film, and hence ZnO sheets act as a pressure-sensitive drain for the photoelectrons generated in the $MAPbI_3$ film. This device illustrates that the hybrid polarization-semiconducting nature of the $MAPbI_3$ can be utilized to develop simple next-generation self-powering devices that can be run with just ambient light.

Chapter 4 shows that the incorporation of PS in $MAPbI_3$ makes these films softer and improves their structural stability, and hence they can be poled at higher electric fields to induce sustained polarization effects. The softer films are used by us to make tactile sensors that have a broad operating range (0.004–450 kPa) with a linear response over the entire pressure range and very high sensitivity (20 kPa^{-1}) as well as once poled is operable for more than 120 h with just light illumination, hence addressing a critical challenge in the development of tactile sensors. Further, the ability to lower the moduli of the lead halide perovskite has direct implications for their application in flexible devices where softer materials lead to greater flexibility. These films can achieve a continuous light energy harvesting density of 1.1 W m^{-2} in a plain film structure. This is among the best-reported figure for energy harvesting devices when compared to other methods such as triboelectric and piezoelectric generators (which are intermittent in nature). While the enhanced structural stability also leads to no visible degradation in performance over months. This allows us to make stable light-powered tactile sensors.

In Chapter 5, we develop a monolith PS-incorporated $MAPbI_3$ self-powered photodetector. Both the self-powered operation and photodetection are achieved in a single perovskite layer due to their semiconducting nature and polarization effects. The detector has a photoresponsivity of more than 0.61 A W^{-1}, a detectivity of 1.5×10^{13} Jones, and a switching ratio of more than 3×10^4 without the use of any external power source. Its performance is better than other reported self-powered photodetectors, and this detector is also continuously operable

for 2 days without a power source. Further, the use of PS in $MAPbI_3$ film maintains the stable structure and device performance for up to 20 days.

This simple method that uses a low cost polymer additive with no extra fabrication step presents a crucial step for bringing the research gains in the field of perovskite electro-optical devices to the commercial market. We believe that this will be of widespread interest to the research community given the intense research focus on perovskites and in general their application in the fields of solar cells, sensors, self-powered devices, detectors, and LEDs.

6.2. Future Work

To develop a comprehensive understanding of the polymer characteristics that affect the device stability and performance, the influence of polymer-based factors, such as its molecular weight, crystallinity, and tacticity on the crystal grain size in the perovskite films, charge and ion transport characteristics in bulk and at the grain boundaries of the perovskite crystals can be studied in the future. The molecular weight of the PS can be varied from 1,000 to 300,000 and tacticity from atactic to isotactic. The molecular weight critically affects the volume occupied by the chain (radius of gyration) and its available free volume (hence its mobility). Similarly, the tacticity affects the molecular order in the polymer chains and also their crystallization characteristics. Therefore, these are crucial parameters that will affect the interaction between the PS chains and the perovskite, and hence will be of great interest to be researched.

There has also been a significant interest in examining whether the origin of enhanced functionality in $MAPbI_3$ perovskite stems from ferroelectricity. Generalization of the existence of ferroelectricity in these films has been disputed, although some recent research reports confirm the ferroelectricity in $MAPbI_3$. More research needs to be done to understand the perovskite deterioration mechanism and the role of grain boundaries to bring together the ferroelectric-related knowledge in these materials.

To minimize the gap for the translation of perovskite-based devices from laboratory to industrial scale, it is crucial to tackle the scalability, durability (or reliability), and environmental sustainability challenges. Up to now in the labs, the perovskite layer, electron and hole transport layers are typically deposited by spin coating technique for small-area ($<1.0\ cm^2$) cells. Further, most of the perovskite solar cells (PSCs) with high efficiency exhibited a smaller active area of

around 0.1 cm^2. Although the research efforts have been made to enlarge the device area with current techniques, it leads to a decrease in the efficiency of perovskite solar cells. Screen printing, spray coating, slot-die coating, and soft-cover coating methods have been developed to fabricate intermediate-size (10 cm^2) perovskite solar modules. But they suffer from crystal imperfection of perovskites, non-uniform perovskite film with pinholes, and wastage of material during deposition, therefore deteriorating the device performance and increasing the manufacturing cost. Hence, new scalable processing routes must be explored to achieve large-area uniform films with efficient materials utilization.

In order to compete with the commercially available silicon solar cells, it is important to further improve the stability of PSCs so that it can last for at least 20 years with minimal degradation. However, we achieved a significant improvement in device stability without any encapsulating layer there still exists a large gap in lifetime between our PSCs (1000 h) and the silicon solar cells (20 years). Hence, more stability tests need to be done on our device to confirm its long-term reliability. To give an indication of the reliability of the solar cell, it has to pass the International Electrotechnical Commission (IEC) accelerated stress tests developed for crystalline silicon terrestrial photovoltaic modules. IEC 61215 includes three types of aging tests: temperature cycling (−40 to +85 °C for 200 cycles), humidity freeze (−40 to +85 °C and 85% RH for 10 cycles), and damp heat (+85 °C and 85% RH for 1000 h). Until now, there are no reports of PSCs that pass all these IEC testing protocols. Therefore, more research needs to be done to further improve the PSC's stability under these harsh conditions.

The lead (Pb), contained in organolead halide perovskite-based devices, is a heavy metal and toxic element that can lead to environmental toxicological implications. However, the amount of lead present in PSCs is below that produced annually by the coal industry when it generates an equivalent amount of electricity. The high aqueous solubility of PbI_2 poses a severe risk to human health. To avoid the leaching out of Pb into the water sources, the first solution is to completely encapsulate the PSCs without compromising its efficiency and much of cost. The second solution is to replace the Pb with other nontoxic elements (such as tin (Sn)) to develop Pb-free PSCs. Although Pb-free perovskites have achieved great progress, their efficiency and stability are still less than the Pb-based perovskites. Till now among all Pb replacements, the Sn-based perovskites have shown the best PCE of 10 %. The biggest challenge associated with the

Sn-based perovskites is its poor air stability (easy oxidize from Sn^{2+} to Sn^{4+}), and hence results in rapid degradation of the Sn-based perovskite materials. Therefore, either the stability of Sn-based perovskites must be improved (maybe by incorporating polystyrene into the Sn-based perovskites) or some other replacement should be used in the future.

Lastly, the polystyrene-incorporated perovskite materials can be used in conjunction with flexible substrates to develop the lightweight and potentially semi-transparent perovskite modules for portable optoelectronic devices. These features are particularly attractive for building-integrated PVs, automotive industry, indoor applications, and Internet of Things (IoT) devices or transport.

Letter of Copyright Permission

Copyright Clearance Center RightsLink®

Home | Help | Email Support | Sign In | Create Account

SPRINGER NATURE

Ionic transport in hybrid lead iodide perovskite solar cells

Author: Christopher Eames et al

Publication: Nature Communications

Publisher: Springer Nature

Date: Jun 24, 2015

Copyright © 2015, Springer Nature

Creative Commons

This is an open access article distributed under the terms of the Creative Commons CC BY license, which permits unrestricted use, distribution, and reproduction in any medium, provided the original work is properly cited.

You are not required to obtain permission to reuse this article.

To request permission for a type of use not listed, please contact Springer Nature

Ion Migration in Organometal Trihalide Perovskite and Its Impact on Photovoltaic Efficiency and Stability

Author: Yongbo Yuan, Jinsong Huang
Publication: Accounts of Chemical Research
Publisher: American Chemical Society
Date: Feb 1, 2016

PbI2 Initiated Cross-Linking and Integration of a Polymer Matrix with Perovskite Films: 1000 h Operational Devices under Ambient Humidity and Atmosphere and with Direct Solar Illumination

ACS Publications
Most Trusted. Most Cited. Most Read.

Author: Rohit Saraf, Vivek Maheshwari
Publication: ACS Applied Energy Materials
Publisher: American Chemical Society
Date: Mar 1, 2019

PERMISSION/LICENSE IS GRANTED FOR YOUR ORDER AT NO CHARGE

This type of permission/license, instead of the standard Terms & Conditions, is sent to you because no fee is being charged for your order. Please note the following:

- Permission is granted for your request in both print and electronic formats, and translations.
- If figures and/or tables were requested, they may be adapted or used in part.
- Please print this page for your records and send a copy of it to your publisher/graduate school.
- Appropriate credit for the requested material should be given as follows: "Reprinted (adapted) with permission from (COMPLETE REFERENCE CITATION). Copyright (YEAR) American Chemical Society." Insert appropriate information in place of the capitalized words.
- One-time permission is granted only for the use specified in your request. No additional uses are granted (such as derivative works or other editions). For any other uses, please submit a new request.

BACK CLOSE WINDOW

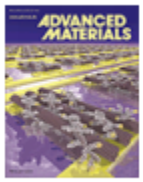

A Light Harvesting, Self-Powered Monolith Tactile Sensor Based on Electric Field Induced Effects in MAPbI3 Perovskite

Author: Rohit Saraf, Long Pu, Vivek Maheshwari
Publication: Advanced Materials
Publisher: John Wiley and Sons
Date: Jan 15, 2018

Your confirmation email will contain your order number for future reference.

License Number	4766170749500
License date	Feb 11, 2020

Printable Details

Licensed Content

Licensed Content Publisher	John Wiley and Sons
Licensed Content Publication	Advanced Materials
Licensed Content Title	A Light Harvesting, Self-Powered Monolith Tactile Sensor Based on Electric Field Induced Effects in MAPbI3 Perovskite
Licensed Content Author	Rohit Saraf, Long Pu, Vivek Maheshwari
Licensed Content Date	Jan 15, 2018
Licensed Content Volume	30
Licensed Content Issue	9
Licensed Content Pages	9

Order Details

Type of use	Dissertation/Thesis
Requestor type	Author of this Wiley article
Format	Print and electronic
Portion	Full article
Will you be translating?	No

About Your Work

Title of your thesis / dissertation	Polymer-Integrated Organolead Halide Perovskite for Solar Cells and Self-Powered Electronic Devices
Expected completion date	Apr 2020
Expected size (number of pages)	150

Additional Data

Requestor Location

Requestor Location	Rohit Saraf 200 University Ave W Waterloo, ON N2L 3G1 Canada Attn: Rohit Saraf

Tax Details

Publisher Tax ID	EU826007151

Self-Powered Photodetector Based on Electric-Field-Induced Effects in MAPbI3 Perovskite with Improved Stability

Author: Rohit Saraf, Vivek Maheshwari
Publication: Applied Materials
Publisher: American Chemical Society
Date: Jun 1, 2018

References

[1] A. S. Bhalla, R. Guo, R. Roy, *Mater. Res. Innovations* **2000**, *4*, 3.

[2] L. G. Tejuca, J. L. G. Fierro, *Perovskites and Applications of Perovskite-type Oxides*, Marcel Dekker, New York, **1992**.

[3] D. B. Mitzi, C. A. Feild, W. T. A. Harrison, A. M. Guloy, *Nature* **1994**, *369*, 467.

[4] L. Etgar, *Hole Conductor Free Perovskite-Based Solar Cells*, Springer International Publishing, Berlin, Germany, **2016**.

[5] A. Kojima, K. Teshima, Y. Shirai, T. Miyasaka, *J. Am. Chem. Soc.* **2009**, *131*, 6050.

[6] J. H. Im, C. R. Lee, J. W. Lee, S. W. Park, N. G. Park, *Nanoscale* **2011**, *3*, 4088.

[7] H. S. Kim, C. R. Lee, J. H. Im, K. B. Lee, T. Moehl, A. Marchioro, S. J. Moon, R. Humphry-Baker, J. H. Yum, J. E. Moser, M. Grätzel, N. G. Park, *Sci. Rep.* **2012**, *2*, 591.

[8] *Best Research-Cell Efficiencies* (National Renewable Energy Laboratory, 2020); https://www.nrel.gov/pv/assets/pdfs/best-research-cell-efficiencies.20200203.pdf

[9] F. P. García de Arquer, A. Armin, P. Meredith, E. H. Sargent, *Nat. Rev. Mater.* **2017**, *2*, 16100.

[10] R. Saraf, L. Pu, V. Maheshwari, *Adv. Mater.* **2018**, *30*, 1705778.

[11] J. Sun, J. Wu, X. Tong, F. Lin, Y. Wang, Z. M. Wang, *Adv. Sci.* **2018**, *5*, 1700780.

[12] Z. K. Tan, R. S. Moghaddam, M. L. Lai, P. Docampo, R. Higler, F. Deschler, M. Price, A. Sadhanala, L. M. Pazos, D. Credgington, F. Hanusch, T. Bein, H. J. Snaith, R. H. Friend, *Nat. Nanotechnol.* **2014**, *9*, 687.

[13] Y. H. Lin, P. Pattanasattayavong, T. D. Anthopoulos, *Adv. Mater.* **2017**, *29*, 1702838.

[14] N. G. Park, T. Miyasaka, M. Grätzel, *Organic-Inorganic Halide Perovskite Photovoltaics: From Fundamentals to Device Architectures*, Springer, Cham, Switzerland, **2016**.

[15] C. Eames, J. M. Frost, P. R. F. Barnes, B. C. O'Regan, A. Walsh, M. S. Islam, *Nat. Commun.* **2015**, *6*, 7497.

[16] V. M. Goldschmidt, Naturwissenschaften **1926**, *14*, 477.

[17] A. Amat, E. Mosconi, E. Ronca, C. Quarti, P. Umari, M. K. Nazeeruddin, M. Grätzel, F. De Angelis, *Nano Lett.* **2014**, *14*, 3608.

[18] T. Baikie, Y. Fang, J. M. Kadro, M. Schreyer, F. Wei, S. G. Mhaisalkar, M. Graetzel, T. J. White, *J. Mater. Chem. A* **2013**, *1*, 5628.

[19] M. T. Weller, O. J. Weber, P. F. Henry, A. M. Di Pumpo, T. C. Hansen, *Chem. Commun.* **2015**, *51*, 4180.

[20] K. P. Ong, T. W. Goh, Q. Xu, A. Huan, *J. Phys. Chem. A* **2015**, *119*, 11033.

[21] J. M. Frost, K. T. Butler, A. Walsh, *APL Mater.* **2014**, *2*, 081506.

[22] J. M. Frost, K. T. Butler, F. Brivio, C. H. Hendon, M. van Schilfgaarde, A. Walsh, *Nano Lett.* **2014**, *14*, 2584.

[23] A. Stroppa, C. Quarti, F. De Angelis, S. Picozzi, *J. Phys. Chem. Lett.* **2015**, *6*, 2223.

[24] Y. Kutes, L. Ye, Y. Zhou, S. Pang, B. D. Huey, N. P. Padture, *J. Phys. Chem. Lett.* **2014**, *5*, 3335.

[25] S. De Wolf, J. Holovsky, S. J. Moon, P. Löper, B. Niesen, M. Ledinsky, F. J. Haug, J. H. Yum, C. Ballif, *J. Phys. Chem. Lett.* **2014**, *5*, 1035.

[26] S. A. Kulkarni, T. Baikie, P. P. Boix, N. Yantara, N. Mathews, S. Mhaisalkar, *J. Mater. Chem. A* **2014**, *2*, 9221.

[27] W. Shockley, H. J. Queisser, *J. Appl. Phys.* **1961**, *32*, 510.

[28] A. Miyata, A. Mitioglu, P. Plochocka, O. Portugall, J. T. W. Wang, S. D. Stranks, H. J. Snaith, R. J. Nicholas, *Nat. Physics* **2015**, *11*, 582.

[29] J. Singh, *Smart Electronic Materials: Fundamentals and Applications*, Cambridge University Press, Cambridge, **2005**.

[30] C. Wehrenfennig, G. E. Eperon, M. B. Johnston, H. J. Snaith, L. M. Herz, *Adv. Mater.* **2014**, *26*, 1584.

[31] H. Oga, A. Saeki, Y. Ogomi, S. Hayase, S. Seki, *J. Am. Chem. Soc.* **2014**, *136*, 13818.

[32] S. D. Stranks, G. E. Eperon, G. Grancini, C. Menelaou, M. J. P. Alcocer, T. Leijtens, L. M. Herz, A. Petrozza, H. J. Snaith, *Science* **2013**, *342*, 341.

[33] G. Xing, N. Mathews, S. Sun, S. S. Lim, Y. M. Lam, M. Grätzel, S. Mhaisalkar, T. C. Sum, *Science* **2013**, *342*, 344.

[34] Z. Fan, J. Xiao, K. Sun, L. Chen, Y. Hu, J. Ouyang, K. P. Ong, K. Zeng, J. Wang, *J. Phys. Chem. Lett.* **2015**, *6*, 1155.

[35] Y. Rakita, O. Bar-Elli, E. Meirzadeh, H. Kaslasi, Y. Peleg, G. Hodes, I. Lubomirsky, D. Oron, D. Ehre, D. Cahen, *Proc. Natl. Acad. Sci. U.S.A.* **2017**, *114*, E5504.

[36] L. M. Garten, D. T. Moore, S. U. Nanayakkara, S. Dwaraknath, P. Schulz, J. Wands, A. Rockett, B. Newell, K. A. Persson, S. Trolier-McKinstry, D. S. Ginley, *Sci. Adv.* **2019**, *5*, eaas9311.

[37] H. Röhm, T. Leonhard, M. J. Hoffmann, A. Colsmann, *Energy & Environ. Sci.* **2017**, *10*, 950.

[38] M. Coll, A. Gomez, E. Mas-Marza, O. Almora, G. Garcia-Belmonte, M. Campoy-Quiles, J. Bisquert, *J. Phys. Chem. Lett.* **2015**, *6*, 1408.

[39] T. Chen, B. J. Foley, B. Ipek, M. Tyagi, J. R. D. Copley, C. M. Brown, J. J. Choi, S.-H. Lee, *Phys. Chem. Chem. Phys.* **2015**, *17*, 31278.

[40] S. Liu, F. Zheng, I. Grinberg, A. M. Rappe, *J. Phys. Chem. Lett.* **2016**, *7*, 1460.

[41] C. Quarti, F. Mosconi, F. De Angelis, *Chem. Mater.* **2014**, *26*, 6557.

[42] Y. Yuan, T. J. Reece, P. Sharma, S. Poddar, S. Ducharme, A. Gruverman, Y. Yang, J. Huang, *Nat. Mater.* **2011**, *10*, 296.

[43] S. Y. Yang, J. Seidel, S. J. Byrnes, P. Shafer, C. H. Yang, M. D. Rossell, P. Yu, Y. H. Chu, J. F. Scott, J. W. Ager, L. W. Martin, R. Ramesh, *Nat. Nanotechnol.* **2010**, *5*, 143.

[44] F. Li, H. Wang, D. Kufer, L. Liang, W. Yu, E. Alarousu, C. Ma, Y. Li, Z. Liu, C. Liu, N. Wei, F. Wang, L. Chen, O. F. Mohammed, A. Fratalocchi, X. Liu, G. Konstantatos, T. Wu, *Adv. Mater.* **2017**, *29*, 1602432.

[45] B.R. Sutherland, E.H. Sargent, *Nat. Photonics* **2016**, *10*, 295.

[46] J.-P. Correa-Baena, M. Saliba, T. Buonassisi, M. Grätzel, A. Abate, W. Tress, A. Hagfeldt, *Science* **2017**, *358*, 739.

[47] S. D. Stranks, H. J. Snaith, *Nat. Nanotechnol.* **2015**, *10*, 391.

[48] Y. Rong, Y. Hu, A. Mei, H. Tan, M. I. Saidaminov, S. I. Seok, M. D. McGehee, E. H. Sargent, H. Han, *Science* **2018**, *361*, eaat8235.

[49] Y. S. Kwon, J. Lim, H.-J. Yun, Y.-H. Kim, T. Park, *Energy Environ. Sci.* **2014**, *7*, 1454.

[50] B. Philippe, B.-W. Park, R. Lindblad, J. Oscarsson, S. Ahmadi, E. M. J. Johansson, H. Rensmo, *Chem. Mater.* **2015**, *27*, 1720.

[51] A. M. A. Leguy, Y. Hu, M. Campoy-Quiles, M. I. Alonso, O. J. Weber, P. Azarhoosh, M. van Schilfgaarde, M. T. Weller, T. Bein, J. Nelson, P. Docampo, P. R. F. Barnes, *Chem. Mater.* **2015**, *27*, 3397.

[52] E. J. Juarez-Perez, L. K. Ono, M. Maeda, Y. Jiang, Z. Hawash, Y. Qi, *J. Mater. Chem. A* **2018**, *6*, 9604.

[53] J. A. Christians, P. A. Miranda Herrera, P. V. Kamat, *J. Am. Chem. Soc.* **2015**, *137*, 1530.

[54] H. Cho, Y.-H. Kim, C. Wolf, H.-D. Lee, T.-W. Lee, *Adv. Mater.* **2018**, *30*, 1704587.

[55] E. J. Juarez-Perez, Z. Hawash, S. R. Raga, L. K. Ono, Y. Qi, *Energy Environ. Sci.* **2016**, *9*, 3406.

[56] B. Brunetti, C. Cavallo, A. Ciccioli, G. Gigli, A. Latini, *Sci. Rep.* **2016**, *6*, 31896.

[57] A. Latini, G. Gigli, A. Ciccioli, *Sustain. Energy Fuels* **2017**, *1*, 1351.

[58] N. A. Manshor, Q. Wali, K. K. Wong, S. K. Muzakir, A. Fakharuddin, L. Schmidt-Mende, R. Jose, *Phys. Chem. Chem. Phys.* **2016**, *18*, 21629.

[59] D. Bryant, N. Aristidou, S. Pont, I. Sanchez-Molina, T. Chotchunangatchaval, S. Wheeler, J. R. Durrant, S. A. Haque, *Energy Environ. Sci.* **2016**, *9*, 1655.

[60] N. Aristidou, I. Sanchez-Molina, T. Chotchuangchutchaval, M. Brown, L. Martinez, T. Rath, S. A. Haque, *Angew. Chem., Int. Ed.* **2015**, *54*, 8208.

[61] T. A. Berhe, W.-N. Su, C.-H. Chen, C.-J. Pan, J.-H. Cheng, H.-M. Chen, M.-C. Tsai, L.-Y. Chen, A. A. Dubale, B.-J. Hwang, *Energy Environ. Sci.* **2016**, *9*, 323.

[62] T. Leijtens, G. E. Eperon, N. K. Noel, S. N. Habisreutinger, A. Petrozza, H. J. Snaith, *Adv. Energy Mater.* **2015**, *5*, 1500963.

[63] L. Liu, S. Huang, Y. Lu, P. Liu, Y. Zhao, C. Shi, S. Zhang, J. Wu, H. Zhong, M. Sui, H. Zhou, H. Jin, Y. Li, Q. Chen, *Adv. Mater.* **2018**, *30*, 1800544.

[64] J. Mizusaki, K. Arai, K. Fueki, *Solid State Ion.* **1983**, *11*, 203.

[65] Y. Yuan, J. Huang, *Acc. Chem. Res.* **2016**, *49*, 286.

[66] J. Schoonman, *J. Solid State Chem.* **1972**, *4*, 466.

[67] N. Ahn, K. Kwak, M. S. Jang, H. Yoon, B. Y. Lee, J. Lee, P. V. Pikhitsa, J. Byun, M. Choi, *Nat. Commun.* **2016**, *7*, 13422.

[68] S. Chen, X. Wen, R. Sheng, S. Huang, X. Deng, M. A. Green, A. Ho-Baillie, *ACS Appl. Mater. Interfaces* **2016**, *8*, 5351.

[69] Z. Xiao, Y. Yuan, Y. Shao, Q. Wang, Q. Dong, C. Bi, P. Sharma, A. Gruverman, J. Huang, *Nat. Mater.* **2015**, *14*, 193.

[70] Z. Wang, Z. Shi, T. Li, Y. Chen, W. Huang, *Angew. Chem. Int. Ed.* **2017**, *56*, 1190.

[71] T. Hwang, B. Lee, J. Kim, S. Lee, B. Gil, A. J. Yun, B. Park, *Adv. Mater.* **2018**, *30*, 1704208.

[72] J. You, L. Meng, T. B. Song, T. F. Guo, Y. M. Yang, W. H. Chang, Z. Hong, H. Chen, H. Zhou, Q. Chen, *Nat. Nanotechnol.* **2016**, *11*, 75.

[73] J. Jiang, Q. Wang, Z. Jin, X. Zhang, J. Lei, H. Bin, Z. G. Zhang, Y. Li, S. F. Liu, *Adv. Energy Mater.* **2018**, *8*, 1701757.

[74] J. W. Lee, H. S. Kim, N. G. Park, *Acc. Chem. Res.* **2016**, *49*, 311.

[75] M. Anaya, G. Lozano, M. E. Calvo, H. Míguez, *Joule* **2017**, *1*, 769.

[76] N. S. Lewis, D. G. Nocera, *Proc. Natl. Acad. Sci. U. S. A.* **2006**, *103*, 15729.

[77] A. Rajagopal, K. Yao, A. K.-Y. Jen, *Adv. Mater.* **2018**, *30*, 1800455.

[78] J. Jean, P. R. Brown, R. L. Jaffe, T. Buonassisi, V. Bulović, *Energy Environ. Sci.* **2015**, *8*, 1200.

[79] S. Samadi, *Renewable Sustainable Energy Rev.* **2018**, *82*, 2346.

[80] M. L. Petrus, J. Schlipf, C. Li, T. P. Gujar, N. Giesbrecht, P. Müller-Buschbaum, M. Thelakkat, T. Bein, S. Hüttner, P. Docampo, *Adv. Energy Mater.* **2017**, *7*, 1700264.

[81] A. Polman, M. Knight, E. C. Garnett, B. Ehrler, W. C. Sinke, *Science* **2016**, *352*, aad4424.

[82] R. S. Dahiya, M. Valle, G. Sandini, *IEEE Trans. Robotics.* **2010**, *26*, 1.

[83] F. McGlone, D. Reilly, *Neurosci. Biobehav. Rev.* **2010**, *34*, 148.

[84] V. Maheshwari, R. Saraf, *Angew. Chemie Int. Ed.* **2008**, *47*, 7808.

[85] A. Chortos, Z. N. Bao, *Mater. Today* **2014**, *17*, 321.

[86] T. Someya, T. Sekitani, S. Iba, Y. Kato, H. Kawaguchi, T. Sakurai, *Proc. Natl. Acad. Sci. U.S.A.* **2004**, *101*, 9966.

[87] J. A. Rogers, T. Someya, Y. Huang, *Science* **2010**, *327*, 1603.

[88] D. J. Lipomi, Z. Bao, *Energy Environ. Sci.* **2011**, *4*, 3314.

[89] M. Li, H. X. Tang, M. L. Roukes, *Nat. Nanotechnol.* **2007**, *2*, 114.

[90] Y. Lee, J. Park, S. Cho, Y. E. Shin, H. Lee, J. Kim, J. Myoung, S. Cho, S. Kang, C. Baig, H. Ko, *ACS Nano* **2018**, *12*, 4045.

[91] J. Park, M. Kim, Y. Lee, H. S. Lee, H. Ko, *Sci. Adv.* **2015**, *1*, e1500661.

[92] C. Pang, G.-Y. Lee, T.-i. Kim, S. M. Kim, H. N. Kim, S.-H. Ahn, K.-Y. Suh, *Nat. Mater.* **2012**, *11*, 795.

[93] D. J. Lipomi, M. Vosgueritchian, B. C. Tee, S. L. Hellstrom, J. A. Lee, C. H. Fox, Z. Bao, *Nat. Nanotechnol.* **2011**, *6*, 788.

[94] W. Wu, X. Wen, Z. L. Wang, *Science* **2013**, *340*, 952.

[95] H. B. Yao, J. Ge, C. F. Wang, X. Wang, W. Hu, Z. J. Zheng, Y. Ni, S. H. Yu, *Adv. Mater.* **2013**, *25*, 6692.

[96] L. Pan, A. Chortos, G. Yu, Y. Wang, S. Isaacson, R. Allen, Y. Shi, R. Dauskardt, Z. Bao, *Nat. Commun.* **2014**, *5*, 3002.

[97] X. W. Wang, Y. Gu, Z. P. Xiong, Z. Cui, T. Zhang, *Adv. Mater.* **2014**, *26*, 1336.

[98] J. Park, Y. Lee, J. Hong, Y. Lee, M. Ha, Y. Jung, H. Lim, S. Y. Kim, H. Ko, *ACS Nano* **2014**, *8*, 12020.

[99] X. Pu, M. Liu, X. Chen, J. Sun, C. Du, Y. Zhang, J. Zhai, W. Hu, Z. L. Wang, *Sci. Adv.* **2017**, *3*, e1700015.

[100] Y. Zi, L. Lin, J. Wang, S. Wang, J. Chen, X. Fan, P. K. Yang, F. Yi, Z. L. Wang, *Adv. Mater.* **2015**, *27*, 2340.

[101] G. Konstantatos, E. H. Sargent, *Nat. Nanotechnol.* **2010**, *5*, 391.

[102] M. B. Sun, R. Bowman, L. E. Vittert, S. Welsh, A. Bowman, M. J. Padgett, *Science* **2013**, *340*, 844.

[103] M. Razeghi, A. Rogalski, *J. Appl. Phys.* **1996**, *79*, 7433.

[104] W. Tian, H. Zhou, L. Li, *Small* **2017**, *13*, 1702107.

[105] W. Wu, Z. L. Wang, *Nat. Rev. Mater.* **2016**, *1*, 16031.

[106] P. W. Barone, S. Baik, D. A. Heller, M. S. Strano, *Nat. Mater.* **2005**, *4*, 86.

[107] T. Y. Zhai, L. Li, Y. Ma, M. Y. Liao, X. Wang, X. S. Fang, J. N. Yao, Y. Bando, D. Golberg, *Chem. Soc. Rev.* **2011**, *40*, 2986.

[108] K. H. Hendriks, W. W. Li, M. M. Wienk, R. A. J. Janssen, *J. Am. Chem. Soc.* **2014**, *136*, 12130.

[109] N. Youngblood, C. Chen, S. J. Koester, M. Li, *Nat. Photonics* **2015**, *9*, 247.

[110] W. Zhang, G. E. Eperon, H. J. Snaith, *Nat. Energy* **2016**, *1*, 16048.

[111] H. Deng, X. Yang, D. Dong, B. Li, D. Yang, S. Yuan, K. Qiao, Y. Cheng, J. Tang, H. Song, *Nano Lett.* **2015**, *15*, 7963.

[112] X. Hu, X. Zhang, L. Liang, J. Bao, S. Li, W. Yang, Y. Xie, *Adv. Funct. Mater.* **2014**, *24*, 7373.

[113] Z. H. Lin, G. Cheng, Y. Yang, Y. S. Zhou, S. Lee, Z. L. Wang, *Adv. Funct. Mater.* **2014**, *24*, 2810.

[114] S. Xu, Y. Qin, C. Xu, Y. G. Wei, R. S. Yang, Z. L. Wang, *Nat. Nanotechnol.* **2010**, *5*, 366.

[115] L. Su, H. Y. Li, Y. Wang, S. Y. Kuang, Z. L. Wang, G. Zhu, *Nano Energy* **2017**, *31*, 264.

[116] R. Saraf, T. Tsui, V. Maheshwari, *J. Mater. Chem. A* **2019**, *7*, 14192.

[117] G. Niu, X. Guo, L. Wang, *J. Mater. Chem. A* **2015**, *3*, 8970.

[118] Y. Rong, L. Liu, A. Mei, X. Li, H. Han, *Adv. Energy Mater.* **2015**, *5*, 1501066.

[119] N. Ahn, D.-Y. Son, I.-H. Jang, S. M. Kang, M. Choi, N.-G. Park, *J. Am. Chem. Soc.* **2015**, *137*, 8696.

[120] X. Li, W. Zhang, Y. C. Wang, W. Zhang, H. Q. Wang, J. Fang, *Nature Commun.*, **2018**, *9*, 3806.

[121] D. Bi, C. Yi, J. Luo, J. D. Décoppet, F. Zhang, S. M. Zakeeruddin, X. Li, A. Hagfeldt, M. Grätzel, *Nat. Energy* **2016**, *1*, 16142.

[122] G. Niu, W. Li, F. Meng, L. Wang, H. Dong, Y. Qiu, *J. Mater. Chem. A* **2014**, *2*, 705.

[123] J. A. Christians, P. Schulz, J. S. Tinkham, T. H. Schloemer, S. P. Harvey, B. J. Tremolet de Villers, A. Sellinger, J. J. Berry, J. M. Luther, *Nat. Energy* **2018**, *3*, 68.

[124] S. Wang, Z. Ma, B. Liu, W. Wu, Y. Zhu, R. Ma, C. Wang, *Sol. RRL* **2018**, *2*, 1800034.

[125] L. Zuo, H. Guo, D. W. Dequilettes, S. Jariwala, N. D. Marco, S. Dong, R. Deblock, D. S. Ginger, B. Dunn, M. Wang, *Sci. Adv.* **2017**, *3*, e1700106.

[126] M. Chen, M. Z. Mokhtar, E. Whittaker, Q. Lian, B. Hamilton, P. O'Brien, M. Zhu, Z. Cui, S. A. Haque, B. R. Saunders, *Nanoscale* **2017**, *9*, 10126.

[127] D. P. McMeekin, G. Sadoughi, W. Rehman, G. E. Eperon, M. Saliba, M. T. Hörantner, A. Haghighirad, N. Sakai, L. Korte, B. Rech, M. B. Johnston, L. M. Herz, H. J. Snaith, *Science* **2016**, *351*, 151.

[128] N. J. Jeon, J. H. Noh, W. S. Yang, Y. C. Kim, S. Ryu, J. Seo, S. I. Seok, *Nature* **2015**, *517*, 476.

[129] X. Gong, M. Li, X. B. Shi, H. Ma, Z. K. Wang, L. S. Liao, *Adv. Funct. Mater.* **2015**, *25*, 6671.

[130] Y. Zhao, J. Wei, H. Li, Y. Yan, W. Zhou, D. Yu, Q. Zhao, *Nat. Commun.* **2016**, *7*, 10228.

[131] Y. Sun, Y. Wu, X. Fang, L. Xu, Z. Ma, Y. Lu, W.-H. Zhang, Q. Yu, N. Yuan, J. Ding, *J. Mater. Chem. A* **2017**, *5*, 1374.

[132] B. Chaudhary, A. Kulkarni, A. K. Jena, M. Ikegami, Y. Udagawa, H. Kunugita, K. Ema, T. Miyasaka, *ChemSusChem* **2017**, *10*, 2473.

[133] C. C. Zhang, M. Li, Z. K. Wang, Y. R. Jiang, H. R. Liu, Y. G. Yang, X. Y. Gao, H. Ma, *J. Mater. Chem. A* **2017**, *5*, 2572.

[134] J. Jiang, Q. Wang, Z. Jin, X. Zhang, J. Lei, H. Bin, Z. G. Zhang, Y. Li, S. F. Liu, *Adv. Energy Mater.* **2018**, *8*, 1701757.

[135] N. G. Gaylord, D. S. Hoffenberg, B. Matyska, K. Mach, *J. Polym. Sci. A* **1968**, *6*, 269.

[136] B. Pukánszky, J. P. Kennedy, T. Kelen, F. Tüdős, *Polym. Bull.* **1981**, *5*, 469.

[137] J. C. Bevington, T. N. Huckerby, *Eur. Polym. J.* **2006**, *42*, 1433.

[138] M. M. Stevens, *Mater. Today* **2008**, *11*, 18.

[139] V. I. Sikavitsas, J. S. Temenoff, A. G. Mikos, *Biomaterials* **2001**, *22*, 2581.

[140] Z. Wang, D. D. Jiang, M. A. McKinney, C. A. Wilkie, *Polym. Degrad. Stab.* **1999**, *64*, 387.

[141] L. Li, Y. Zhong, J. Li, C. Chen, A. Zhang, J. Xu, Z. Ma, *J. Mater. Chem.* **2009**, *19*, 7222.

[142] J. Yang, B. D. Siempelkamp, E. Mosconi, F. De Angelis, T. L. Kelly, *Chem. Mater.* **2015**, *27*, 4229.

[143] D. Liu, T. L. Kelly, *Nature Photon.* **2014**, *8*, 133.

[144] S. M. Jain, B. Philippe, E. M. J. Johansson, H. Rensmo, T. Edvinsson, G. Boschloo, *J. Mater. Chem. A* **2016**, *4*, 2630.

[145] Z. Liang, S. Zhang, X. Xu, N. Wang, J. Wang, X. Wang, Z. Bi, G. Xu, N. Yuan, J. Ding, *RSC Adv.* **2015**, *5*, 60562.

[146] W. M. Sears, J. L. Hunt, J. R. Stevens, *J. Chem. Phys.* **1981**, *75*, 1589.

[147] G. del C. Pizarro, O. G. Marambio, M. Jeria-Orell, C. M. González-Henríquez, M. Sarabia-Vallejos, K. E. Geckeler, *Express Polym. Lett.* **2015**, *9*, 525.

[148] A. Mei, X. Li, L. Liu, Z. Ku, T. Liu, Y. Rong, M. Xu, M. Hu, J. Chen, Y. Yang, M. Grätzel, H. Han, *Science* **2014**, *345*, 295.

[149] M. Ledinský, P. Löper, B. Niesen, J. Holovský, S.-J. Moon, J.-H. Yum, S. De Wolf, A. Fejfar, C. Ballif, *J. Phys. Chem. Lett.* **2015**, *6*, 401.

[150] J. Cao, J. Yin, S. Yuan, Y. Zhao, J. Li, N. Zheng, *Nanoscale* **2015**, *7*, 9443.

[151] G. A. Sepalage, S. Meyer, A. Pascoe, A. D. Scully, F. Huang, U. Bach, Y.-B. Cheng, L. Spiccia, *Adv. Funct. Mater.* **2015**, *25*, 5650.

[152] H. Back, G. Kim, J. Kim, J. Kong, T. K. Kim, H. Kang, H. Kim, J. Lee, S. Lee, K. Lee, *Energy Environ. Sci.* **2016**, *9*, 1258.

[153] A. Abate, S. Paek, F. Giordano, J.-P. Correa-Baena, M. Saliba, P. Gao, T. Matsui, J. Ko, S. M. Zakeeruddin, K. H. Dahmen, A. Hagfeldt, M. Grätzel, M. K. Nazeeruddin, *Energy Environ. Sci.* **2015**, *8*, 2946.

[154] F. Li, J. Yuan, X. Ling, Y. Zhang, Y. Yang, S. H. Cheung, C. H. Y. Ho, X. Gao, W. Ma, *Adv. Funct. Mater.* **2018**, *28*, 1706377.

[155] K. Wojciechowski, T. Leijtens, S. Siprova, C. Schlueter, M. T. Horantner, J. T. Wang, C. Z. Li, A. K. Jen, T. L. Lee, H. J. Snaith, *J. Phys. Chem. Lett.* **2015**, *6*, 2399.

[156] W. Li, W. Zhang, S. Van Reenen, R. J. Sutton, J. Fan, A. Haghighirad, M. Johnston, L. Wang, H. Snaith, *Energy Environ. Sci.* **2016**, *9*, 490.

[157] S. K. Pathak, A. Abate, P. Ruckdeschel, B. Roose, K. C. Gödel, Y. Vaynzof, A. Santhala, S.-I. Watanabe, D. J. Hollman, N. Noel, A. Sepe, U. Wiesner, R. Friend, H. J. Snaith, U. Steiner, *Adv. Funct. Mater.* **2014**, *24*, 6046.

[158] J. He, C.-F. Ng, K. Young Wong, W. Liu, T. Chen, *ChemPlusChem* **2016**, *81*, 1292.

[159] H. Choi, C.-K. Mai, H.-B. Kim, J. Jeong, S. Song, G. C. Bazan, J. Y. Kim, A. J. Heeger, *Nature Commun.* **2015**, *6*, 7348.

[160] Z. K. Wang, M. Li, D. X. Yuan, X. B. Shi, H. Ma, L. S. Liao, *ACS Appl. Mater. Interfaces* **2015**, *7*, 9645.

[161] R. Saraf, V. Maheshwari, *ACS Appl. Mater. Interfaces* **2018**, *10*, 21066.

[162] Y. Yuan, T. Li, Q. Wang, J. Xing, A. Gruverman, J. Huang, *Sci. Adv.* **2017**, *3*, e1602164.

[163] K. C. Kwon, K. Hong, Q. Van Le, S. Y. Lee, J. Choi, K.-B. Kim, S. Y. Kim, H. W. Jang, *Adv. Funct. Mater.* **2016**, *26*, 4213.

[164] Z. Huang, X. Hu, C. Liu, L. Tan, Y. Chen, *Adv. Funct. Mater.* **2017**, *27*, 1703061.

[165] A. Rose, *Phys. Rev.* **1955**, *97*, 1538.

[166] P. Mark, W. Helfrich, *J. Appl. Phys.* **1962**, *33*, 205.

[167] M. Bag, L. A. Renna, R. Y. Adhikari, S. Karak, F. Liu, P. M. Lahti, T. P. Russell, M. T. Tuominen, D. Venkataraman, *J. Am. Chem. Soc.* **2015**, *137*, 13130.

[168] J. B. Jorcin, M. E. Orazem, N. Pébère, B. Tribollet, *Electrochim. Acta* **2006**, *51*, 1473.

[169] E. Guillen, F. J. Ramos, J. A. Anta, S. Ahmad, *J. Phys. Chem. C* **2014**, *118*, 22913.

[170] Y. C. Mao, P. Zhao, G. McConohy, H. Yang, Y. X. Tong, X. D. Wang, *Adv. Energy Mater.* **2014**, *4*, 1301624.

[171] J. Park, Y. Lee, M. Ha, S. Cho, H. Ko, *J. Mater. Chem. B* **2016**, *4*, 2999.

[172] Y. Yang, H. Zhang, Z.-H. Lin, Y. S. Zhou, Q. Jing, Y. Su, J. Yang, J. Chen, C. Hu, Z. L. Wang, *ACS Nano* **2013**, *7*, 9213.

[173] L. Lin, Y. Xie, S. Wang, W. Wu, S. Niu, X. Wen, Z. L. Wang, *ACS Nano* **2013**, *7*, 8266.

[174] G. Zhu, W. Q. Yang, T. Zhang, Q. Jing, J. Chen, Y. S. Zhou, P. Bai, Z. L. Wang, *Nano Lett.* **2014**, *14*, 3208.

[175] G. Hodes, *Science* **2013**, *342*, 317.

[176] M. M. Lee, J. Teuscher, T. Miyasaka, T. N. Murakami, H. J. Snaith, *Science* **2012**, *338*, 643.

[177] N. G. Park, *J. Phys. Chem. Lett.* **2013**, *4*, 2423.

[178] J. Burschka, N. Pellet, S. J. Moon, R. Humphry-Baker, P. Gao, M. K. Nazeeruddin, M. Grätzel, *Nature* **2013**, *499*, 316.

[179] J. B. Han, F. R. Fan, C. Xu, S. S. Lin, M. Wei, X. Duan, Z. L. Wang, Nanotechnology **2010**, *21*, 405203.

[180] W. Peng, R. Yu, X. Wang, Z. Wang, H. Zou, Y. He, Z. L. Wang, *Nano Res.* **2016**, *9*, 3695.

[181] Y. Yuan, J. Chae, Y. Shao, Q. Wang, Z. Xiao, A. Centrone, J. Huang, *Adv. Energy Mater.* **2015**, *5*, 1500615.

[182] Q. Wang, Y. Shao, H. Xie, L. Lyu, X. Liu, Y. Gao, J. Huang, *Appl. Phys. Lett.* **2014**, *105*, 163508.

[183] H. W. Chen, N. Sakai, M. Ikegami, T. Miyasaka, *J. Phys. Chem. Lett.* **2014**, *6*, 164.

[184] Y. Yuan, Z. Xiao, B. Yang, J. Huang, *J. Mater. Chem. A* **2014**, *2*, 6027.

[185] H. S. Kim, I. Mora-Sero, V. Gonzalez-Pedro, F. Fabregat-Santiago, E. J. Juarez-Perez, N. G. Park, J. Bisquert, *Nat. Commun.* **2013**, *4*, 2242.

[186] K. Mahmood, B. S. Swain, A. Amassian, *Nanoscale* **2014**, *6*, 14674.

[187] J. Zhang, P. Barboux, T. Pauporté, *Adv. Energy Mater.* **2014**, *4*, 1400932.

[188] K. Takei, T. Takahashi, J. C. Ho, H. Ko, A. G. Gillies, P. W. Leu, R. S. Fearing, A. Javey, *Nat. Mater.* **2010**, *9*, 821.

[189] C. Wang, D. Hwang, Z. Yu, K. Takei, J. Park, T. Chen, B. Ma, A. Javey, *Nat. Mater.* **2013**, *12*, 899.

[190] M. Kaltenbrunner, T. Sekitani, J. Reeder, T. Yokota, K. Kuribara, T. Tokuhara, M. Drack, R. Schwodiauer, I. Graz, S. Bauer-Gogonea, S. Bauer, T. Someya, *Nature* **2013**, *499*, 458.

[191] R. R. Mehta, B. D. Silverman, J. T. Jacobs, *J. Appl. Phys.* **1973**, *44*, 3379.

[192] Y. C. Zhao, W. K. Zhou, X. Zhou, K. H. Liu, D. P. Yu, Q. Zhao, *Light Sci. Appl.* **2017**, *6*, e16243.

[193] C. C. Stoumpos, C. D. Malliakas, M. G. Kanatzidis, *Inorg. Chem.* **2013**, *52*, 9019.

[194] X. Wang, B. Liu, R. Liu, Q. Wang, X. Hou, D. Chen, R. Wang, G. Shen, *Angew. Chem.* **2014**, *126*, 1880.

[195] M. Bass, P. A. Franken, J. F. Ward, G. Weinreich, *Phys. Rev. Lett.* **1962**, *9*, 446.

[196] A. Rice, Y. Jin, X. F. Ma, X. C. Zhang, D. Bliss, J. Larkin, M. Alexander, *Appl. Phys. Lett.* **1994**, *64*, 1324.

[197] E. Edri, S. Kirmayer, A. Henning, S. Mukhopadhyay, K. Gartsman, Y. Rosenwaks, G. Hodes, D. Cahen, *Nano Lett.* **2014**, *14*, 1000.

[198] L. Pu, R. Saraf, V. Maheshwari, *Sci. Rep.* **2017**, *7*, 5834.

[199] M. Ha, S. Lim, J. Park, D. S. Um, Y. Lee, H. Ko, *Adv. Funct. Mater.* **2015**, *25*, 2841.

[200] Q. Sun, D. H. Kim, S. S. Park, N. Y. Lee, Y. Zhang, J. H. Lee, K. Cho, J. H. Cho, *Adv. Mater.* **2014**, *26*, 4735.

[201] I. Graz, M. Krause, S. Bauer-Gogonea, S. Bauer, S. P. Lacour, B. Ploss, M. Zirkl, B. Stadlober, S. Wagner, *J. Appl. Phys.* **2009**, *106*, 034503.

[202] G. Schwartz, B. C. K. Tee, J. Mei, A. L. Appleton, D. H. Kim, H. Wang, Z. Bao, *Nat. Commun.* **2013**, *4*, 1859.

[203] S. Y. Kim, S. Park, H. W. Park, D. H. Park, Y. Jeong, D. H. Kim, *Adv. Mater.* **2015**, *27*, 4178.

[204] S. C. B. Mannsfeld, B. C. K. Tee, R. M. Stoltenberg, C. V. H. H. Chen, S. Barman, B. V. O. Muir, A. N. Sokolov, C. Reese, Z. Bao, *Nat. Mater.* **2010**, *9*, 859.

[205] C. G. Núñez, W. T. Navaraj, E. O. Polat, R. Dahiya, *Adv. Funct. Mater.* **2017**, *27*, 1606287.

[206] H. Tian, Y. Shu, X. F. Wang, M. A. Mohammad, Z. Bie, Q. Y. Xie, C. Li, W. T. Mi, Y. Yang, T. L. Ren, *Sci. Rep.* **2015**, *5*, 8603.

[207] N. Reznikov, M. Bilton, L. Lari, M. M. Stevens, R. Kröger, *Science* **2018**, *360*, eaao2189.

[208] G. Falini, S. Albeck, S. Weiner, L. Addadi, *Science* **1996**, *271*, 67.

[209] B. Wang, T. N. Sullivan, A. Pissarenko, A. Zaheri, H. D. Espinosa, M. A. Meyers, *Adv. Mater.* **2019**, *31*, 1804574.

[210] J. S. Peng, Q. F. Cheng, *Adv. Mater.* **2017**, *29*, 1702959.

[211] V. K. Thakur, R. K. Gupta, *Chem. Rev.* **2016**, *116*, 4260.

[212] W. Liu, S. W. Lee, D. C. Lin, F. F. Shi, S. Wang, A. D. Sendek, Y. Cui, *Nat. Energy* **2017**, *2*, 17035.

[213] Y. Y. Kim, J. D. Carloni, B. Demarchi, D. Sparks, D. G. Reid, M. E. Kunitake, C. C. Tang, M. J. Duer, C. L. Freeman, B. Pokroy, K. Penkman, J. H. Harding, L. A. Estroff, S. P. Baker, F. C. Meldrum, *Nat. Mater.* **2016**, *15*, 903.

[214] F. Bouville, E. Maire, S. Meille, B. Van de Moortèle, A. J. Stevenson, S. Deville, *Nat. Mater.* **2017**, *16*, 1271.

[215] M. Chen, Y. Zhang, L. Xing, Y. Liao, Y. Qiu, S. Yang, W. Li, *Adv. Mater.* **2017**, *29*, 1607015.

[216] J. Kang, D. Son, G. J. N. Wang, Y. Liu, J. Lopez, Y. Kim, J. Y. Oh, T. Katsumata, J. Mun, Y. Lee, L. Jin, J. B.-H. Tok, Z. Bao, *Adv. Mater.* **2018**, *30*, 1706846.

[217] D. Son, J. Kang, O. Vardoulis, Y. Kim, N. Matsuhisa, J. Y. Oh, J. W. To, J. Mun, T. Katsumata, Y. Liu, A. F. McGuire, M. Krason, F. M. Lopez, J. Ham, U. Kraft, Y. Lee, Y. Yun, J. B.-H. Tok, Z. Bao *Nat. Nanotechnol.* **2018**, *13*, 1057.

[218] Y. Jie, X. T. Jia, J. D. Zou, Y. D. Chen, N. Wang, Z. L. Wang, X. Cao, *Adv. Energy Mater.* **2018**, *8*, 1703133.

[219] J. Chen, Y. Huang, N. Zhang, H. Zou, R. Liu, C. Tao, X. Fan, Z. L. Wang, *Nat. Energy* **2016**, *1*, 16138.

[220] H. Zou, Y. Zhang, L. Guo, P. Wang, X. He, G. Dai, H. Zheng, C. Chen, A. C. Wang, C. Xu, Z. L. Wang, *Nat. Commun.* **2019**, *10*, 1427.

[221] J. Chen, S. K. Oh, H. Zou, S. Shervin, W. Wang, S. Pouladi, Y. Zi, Z. L. Wang, J. H. Ryou, *ACS Appl. Mater. Interfaces* **2018**, *10*, 12839.

[222] R. Saraf, V. Maheshwari, *ACS Appl. Energy Mater.* **2019**, *2*, 2214.

[223] J. Feng, *APL Mater.* **2014**, *2*, 081801.

[224] W. C. Oliver, G. M. Pharr, *J. Mater. Res.* **1992**, *7*, 1564.

[225] D. Tranchida, S. Piccarolo, M. Soliman, *Macromolecules* **2006**, *39*, 4547.

[226] C. Yeom, K. Chen, D. Kiriya, Z. Yu, G. Cho, A. Javey, *Adv. Mat.* **2015**, *27*, 1561.

[227] Y. Joo, J. Yoon, J. Ha, T. Kim, S. Lee, B. Lee, C. Pang, Y. Hong, *Adv. Electron. Mater.* **2017**, *3*, 1600455.

[228] S. Jang, E. Jee, D. Choi, W. Kim, J. S. Kim, V. Amoli, T. Sung, D. Choi, D. H. Kim, J.-Y. Kwon, *ACS Appl. Mater. Interfaces* **2018**, *10*, 31472.

[229] S. H. Shin, S. Ji, S. Choi, K. H. Pyo, B. Wan An, J. Park, J. Kim, J. Y. Kim, K. S. Lee, S. Y. Kwon, J. Heo, B. G. Park, J. U. Park, *Nat. Commun.* **2017**, *8*, 14950.

[230] S. Gong, W. Schwalb, Y. Wang, Y. Chen, Y. Tang, J. Si, B. Shirinzadeh, W. Cheng, *Nat. Commun.* **2014**, *5*, 3132.

[231] X. W. Wang, Y. Gu, Z. P. Xiong, Z. Cui, T. Zhang, *Adv. Mater.* **2014**, *26*, 1309.

[232] Y. Pang, K. Zhang, Z. Yang, S. Jiang, Z. Ju, Y. Li, X. Wang, D. Wang, M. Jian, Y. Zhang, *ACS Nano* **2018**, *12*, 2346.

[233] J. Park, Y. Lee, J. Hong, M. Ha, Y.-D. Jung, H. Lim, S. Y. Kim, H. Ko, *ACS Nano* **2014**, *8*, 4689.

[234] Q. Hua, J. Sun, H. Liu, R. Bao, R. Yu, J. Zhai, C. Pan, Z. L. Wang, *Nat. Commun.* **2018**, *9*, 244.

[235] D. H. Ho, Q. Sun, S. Y. Kim, J. T. Han, D. H. Kim, J. H. Cho, *Adv. Mater.* **2016**, *28*, 2601.

[236] D. Kwon, T. I. Lee, J. Shim, S. Ryu, M. S. Kim, S. Kim, T. S. Kim, I. Park, *ACS Appl. Mater. Interfaces* **2016**, *8*, 16922.

[237] Z. L. Wang, *Adv. Mater.* **2012**, *24*, 280.

[238] S. Xu, Y. Qin, C. Xu, Y. G. Wei, R. S. Yang, Z. L. Wang, *Nat. Nanotechnol.* **2010**, *5*, 366.

[239] Y. S. Rim, S. H. Bae, H. J. Chen, N. De Marco, Y. Yang, *Adv. Mater.* **2016**, *28*, 4415.

[240] W. Peng, X. Wang, R. Yu, Y. Dai, H. Zou, A. C. Wang, Y. He, Z. L. Wang, *Adv. Mater.* **2017**, *29*, 1606698.

[241] S. F. Leung, K. T. Ho, P. K. Kung, V. K. Hsiao, H. N. Alshareef, Z. L. Wang, J. H. He, *Adv. Mater.* **2018**, *30*, 1704611.

[242] H. Fang, Q. Li, J. Ding, N. Li, H. Tian, L. Zhang, T. Ren, J. Dai, L. Wang, Q. Yan, *J. Mater. Chem. C* **2016**, *4*, 630.

[243] H. Si, Q. Liao, Z. Kang, Y. Ou, J. Meng, Y. Liu, Z. Zhang, Y. Zhang, *Adv. Funct. Mater.* **2017**, *27*, 1701804.

[244] W. Tress, N. Marinova, T. Moehl, S. M. Zakeeruddin, M. K. Nazeeruddin, M. Gratzel, *Energy Environ. Sci.* **2015**, *8*, 995.

[245] F. Lang, O. Shargaieva, V. V. Brus, H. C. Neitzert, J. Rappich, N. H. Nickel, *Adv. Mater.* **2018**, *30*, 1702905.

[246] H. Yuan, E. Debroye, K. Janssen, H. Naiki, C. Steuwe, G. Lu, M. Moris, E. Orgiu, H. Uji-i, F. De Schryver, P. Samorì, J. Hofkens, M. Roeffaers, *J. Phys. Chem. Lett.* **2016**, *7*, 561.

[247] S. Bae, S. Kim, S. W. Lee, K. J. Cho, S. Park, S. Lee, Y. Kang, H. S. Lee, D. Kim, *J. Phys. Chem. Lett.* **2016**, *7*, 3091.

[248] H. N. Si, Q. L. Liao, Z. Zhang, Y. Li, X. H. Yang, G. J. Zhang, Z. Kang, Y. Zhang, *Nano Energy* **2016**, *22*, 223.

[249] Y. Zhao, K. Zhu, *Chem. Soc. Rev.* **2016**, *45*, 655.

[250] G. Tong, H. Li, Z. Zhu, Y. Zhang, L. Yu, J. Xu, Y. Jiang, *J. Phys. Chem. Lett.* **2018**, *9*, 1592.

[251] L. Dou, Y. Yang, J. You, Z. Hong, W. H. Chang, G. Li, Y. Yang, *Nat. Commun.* **2014**, *5*, 5404.

[252] G. Tong, H. Li, D. Li, Z. Zhu, E. Xu, G. Li, L. Yu, J. Xu, Y. Jiang, *Small* **2018**, *14*, 1702523.

[253] H. Zhou, J. Mei, M. Xue, Z. Song, H. Wang, *J. Phys. Chem. C* **2017**, *121*, 21541.

[254] F. Bai, J. Qi, F. Li, Y. Fang, W. Han, H. Wu, Y. Zhang, *Adv. Mater. Interfaces* **2018**, 1701275.

[255] K. Pandey, M. Chauhan, V. Bhatt, B. Tripathi, P. Yadav, M. Kumar, *RSC Adv.* **2016**, *6*, 105076.

[256] J. Li, S. Yuan, G. Tang, G. Li, D. Liu, J. Li, X. Hu, Y. Liu, J. Li, Z. Yang, S. F. Liu, Z. Liu, F. Gao, F. Yan, *ACS Appl. Mater. Interfaces* **2017**, *9*, 42779.

[257] E. Zheng, B. Yuh, G. A. Tosado, Q. Yu, *J. Mater. Chem. C* **2017**, *5*, 3796.

[258] G. Tong, X. Geng, Y. Yu, L. Yu, J. Xu, Y. Jiang, Y. Sheng, Y. Shi, K. Chen, *RSC Adv.* **2017**, *7*, 18224

[259] Y. Shen, X. Yan, H. Si, P. Lin, Y. Liu, Y. Sun, Y. Zhang, *ACS Appl. Mater. Interfaces* **2016**, *8*, 6137.

[260] A. Bera, A. D. Mahapatra, S. Mondal, D. Basak, *ACS Appl. Mater. Interfaces* **2016**, *8*, 34506.

[261] X. Ren, Z. Li, Z. Huang, D. Sang, H. Qiao, X. Qi, J. Li, J. Zhong, H. Zhang, *Adv. Funct. Mater.* **2017**, *27*, 1606834.

Appendices

Appendix for Chapter 2

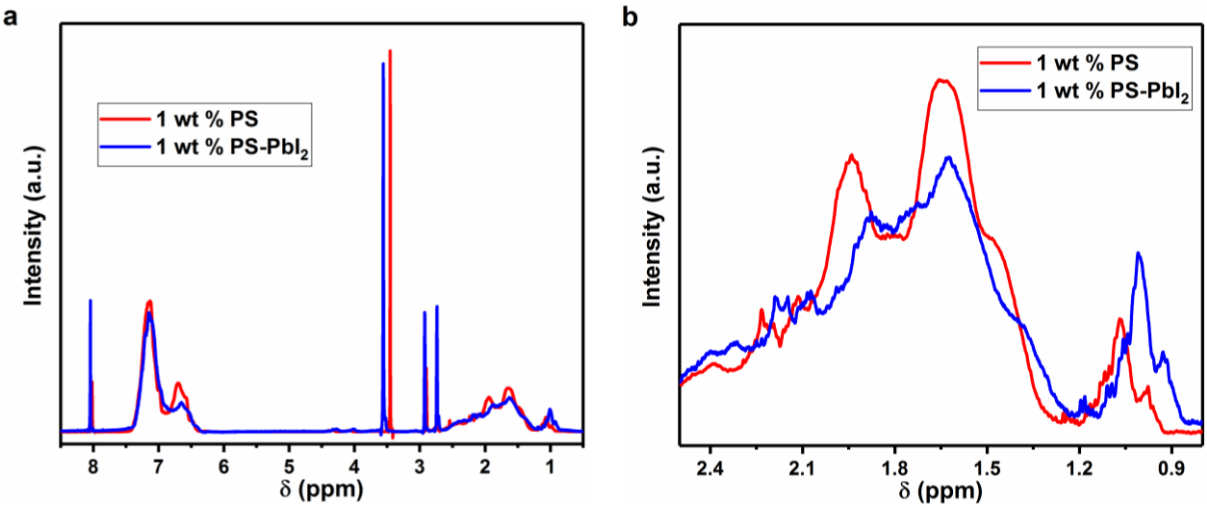

Figure A2.1. ^{1}H NMR spectra of the 1 wt % PS solution with and without PbI_2 collected in deuterated N, N-dimethylformamide-d_7 (DMF-d_7) and Dimethylsulfoxide-d_6 (DMSO-d_6). (a) Low magnification scale between 0.5 and 8.5 ppm. (b) High magnification scale between 0.8 and 2.5 ppm.

The sharp NMR peaks for 1 wt % PS solution at 2.737, 2.899, and 8.018 ppm are attributed to DMF. The intense peak at 3.557 ppm and 3.452 ppm is ascribed to the presence of water (or moisture) in DMF and DMSO. The broad peaks at δ = 6.698 and 7.125 ppm for 1 wt % PS solution is attributed to the presence of polystyrene. The peaks below 2.5 ppm are due to aliphatic regions of PS. The observed upshift for PS peaks in 1 wt % PS-PbI_2 solution is due to the interaction of PS and PbI_2 intermediates which leads to the formation of carbonium ions.

In the presence of moisture (as seen in NMR spectra), the Lewis acid (PbI_2) hydrolyzes and results in the formation of hydrogen iodide (HI). The PbI_2 interacts with PS in the presence of HI and leads to the formation of a cation complex on the main chain, i.e. polymeric cations complex with PbI_3^-. This complex upshifts the observed NMR resonances for both the aromatic and aliphatic regions of PS.

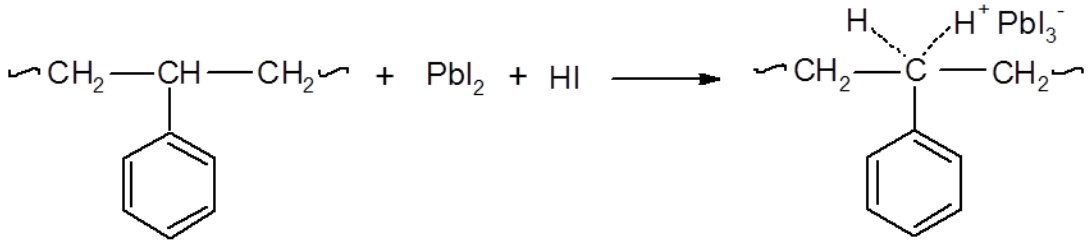

The polymeric cations complex is then converted into the carbonium ions by losing hydrogen (H_2), which subsequently causes cross-linking of the PS chains. While degradation of the PS is also a possible route but in the presence of moisture and based on the GPC results, cross-linking of the PS chains is confirmed. In the NMR spectrum also this is supported as no change in the relative intensities of the aromatic and aliphatic regions is observed, indicating that the polymeric backbone remains intact.

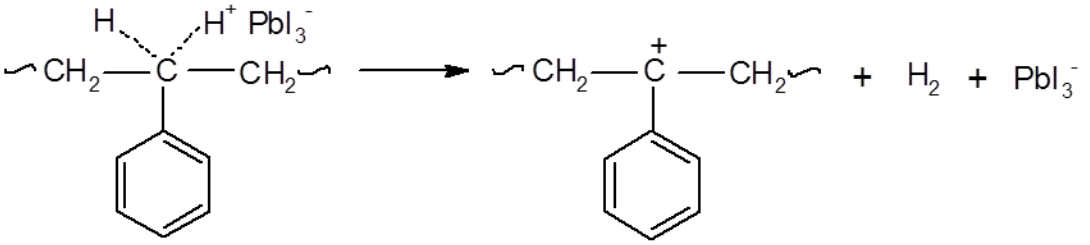

The carbonium ion on the aromatic ring then reacts with another PS chain and leads to a cross-linked PS matrix in the perovskite.

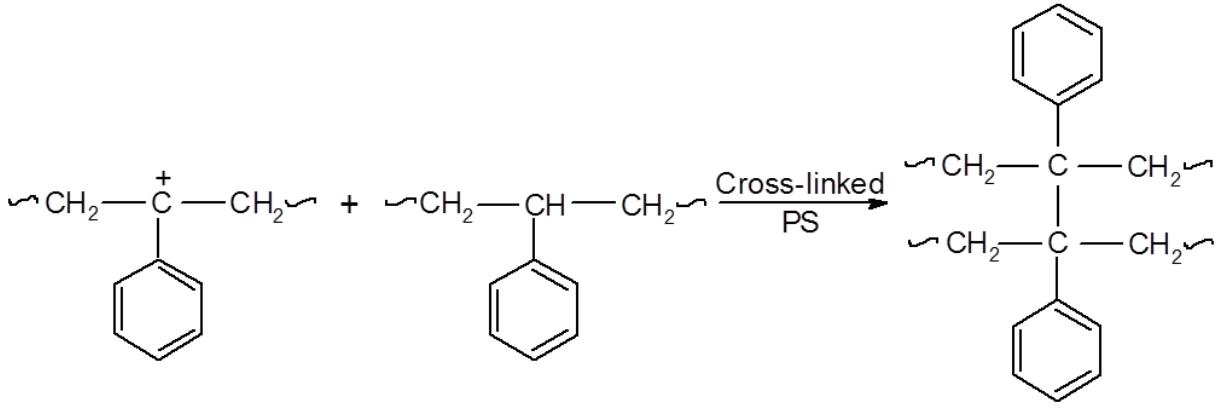

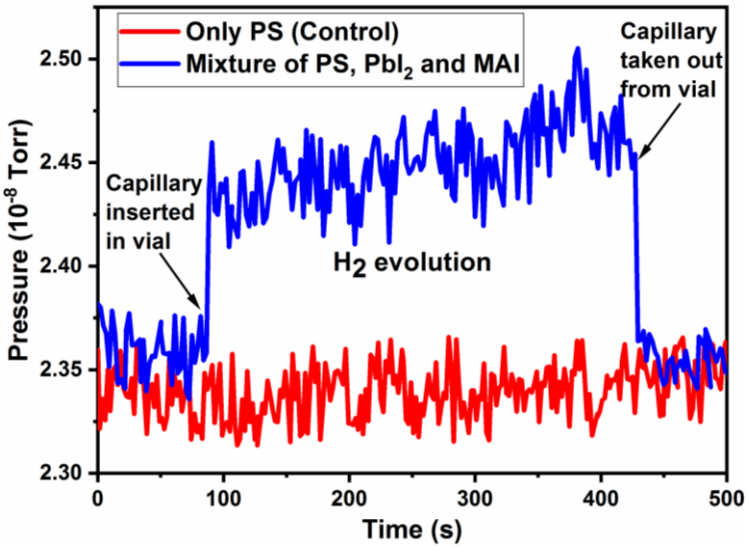

Figure A2.2. Detection of the hydrogen (H_2) evolved from the reaction mixture. The measurement is performed by mixing the required precursor materials in DMF and DMSO in the septum vials.

The H_2 gas generated from the reaction is collected by inserting the capillary tube in the vials. For the control experiment, the polystyrene (PS) was dissolved in DMF and DMSO. In contrast to confirm the in-situ cross-linking of the PS matrix with $MAPbI_3$, the PS, PbI_2, and MAI was mixed in DMF and DMSO and left for 1 day for the formation of cross-linked PS chains in $MAPbI_3$. We observed that the H_2 gas evolved from the cross-linked PS-$MAPbI_3$ solution, whereas for PS solution without perovskite precursors the H_2 is not generated. This confirms the proposed mechanism for the cross-linking of PS into the perovskite.

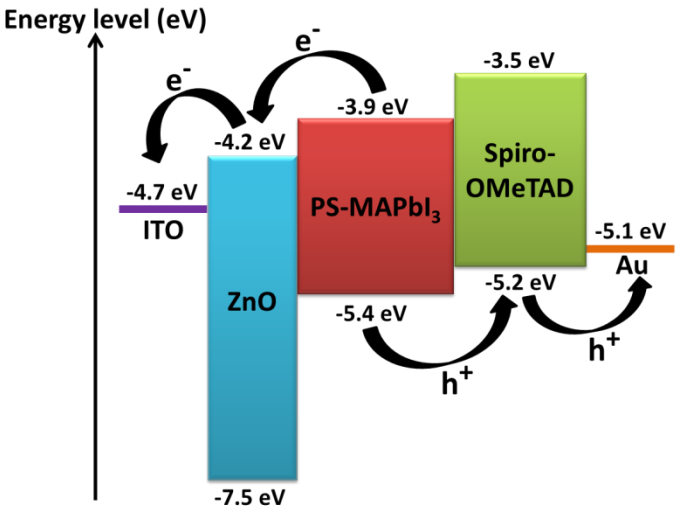

Figure A2.3. Energy level diagram of the perovskite solar cells. The schematic showing how the photogenerated charge carriers are collected. A general structure of ITO/ZnO/PS-$MAPbI_3$/Spiro-OMeTAD/Au was designed. On exposure to light, charge carriers are generated in the PS-$MAPbI_3$ perovskite layer. Electrons and holes are subsequently collected by their respective contacts ZnO and Spiro-OMeTAD, and then passed onto the electrodes.

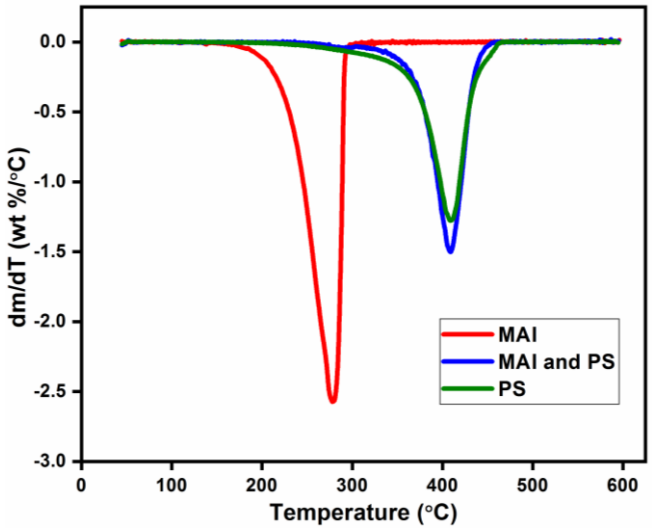

Figure A2.4. First derivative of the TGA curves showing the shifting of the initial thermal decomposition of PS to higher temperature confirms their thermal stabilization due to the MAI and PS interaction.

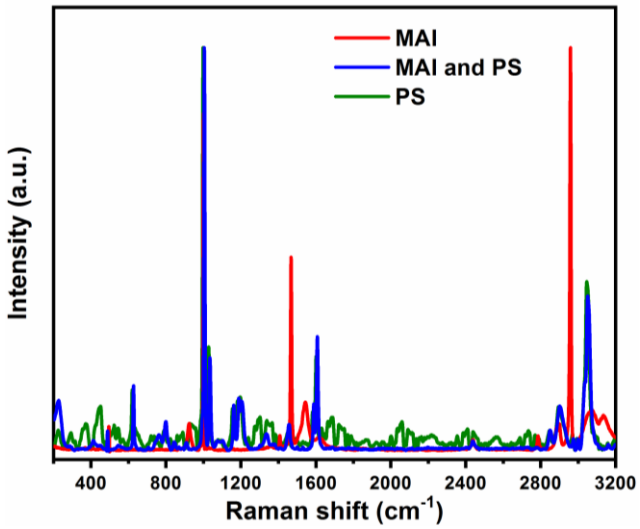

Figure A2.5. Raman spectra for plain PS, MAI, and MAI with PS powders, showing the Raman shift of MAI-PS spectrum towards higher wavenumber which confirms the interaction of the PS with MAI.

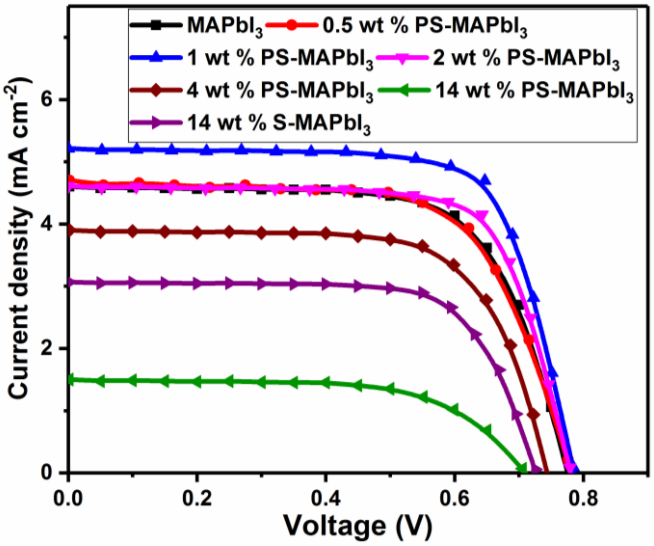

Figure A2.6. *J–V* curves of the pure $MAPbI_3$, PS-$MAPbI_3$ with different concentrations, and S-$MAPbI_3$ devices without HTL under one sun illumination.

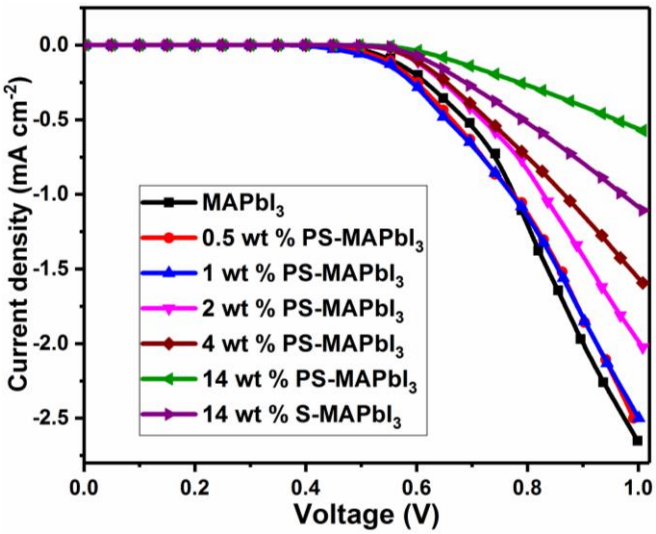

Figure A2.7. *J–V* characteristics of the pure $MAPbI_3$, PS-$MAPbI_3$ with different concentrations, and S-$MAPbI_3$ devices without HTL in dark.

It is observed that the current density decreases with the increase in the PS concentration from 0.5 to 14 wt %. This is due to the electrically insulating nature of PS which will decrease the dark current in these devices.

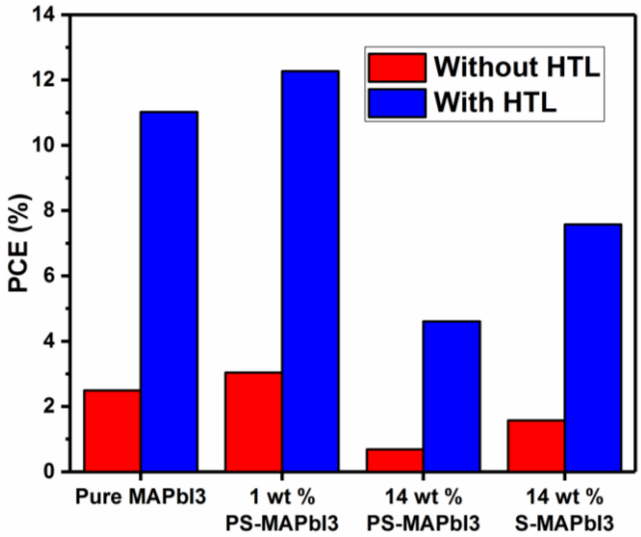

Figure A2.8. Photovoltaic performance of the pure $MAPbI_3$, 1 and 14 wt % PS-$MAPbI_3$, and 14 wt % S-$MAPbI_3$ devices with and without HTL. The devices with HTL show 4–7 times higher PCE as compared to devices without HTL, which signifies the importance of HTL (Spiro-OMeTAD) in extracting the holes.

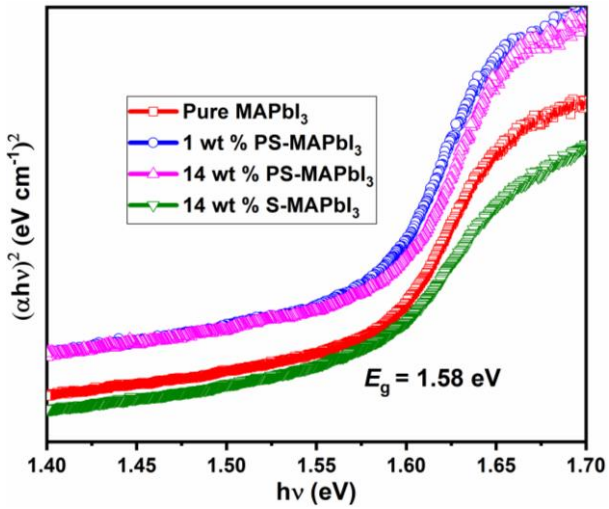

Figure A2.9. Energy band gap spectra for pure $MAPbI_3$, 1 and 14 wt % PS-$MAPbI_3$, and 14 wt % S-$MAPbI_3$ films.

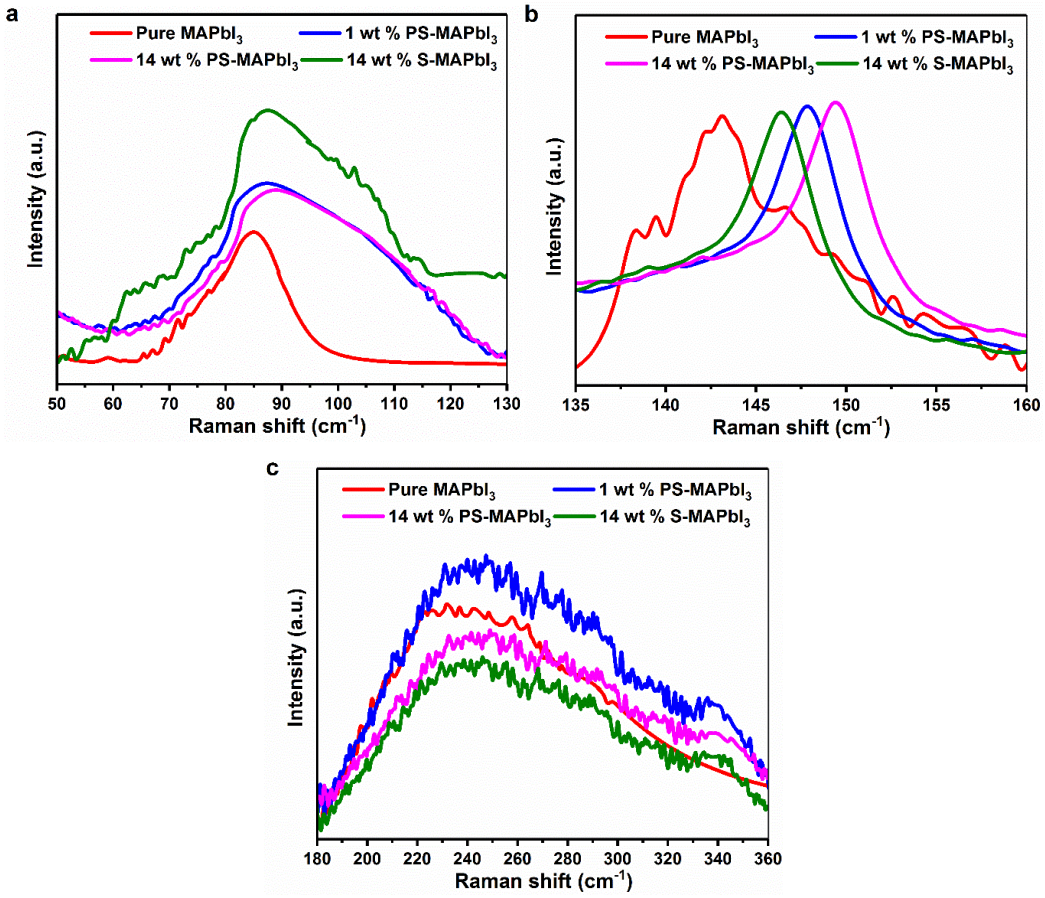

Figure A2.10. Magnified view of Raman spectra for pure $MAPbI_3$, 1 and 14 wt % PS-$MAPbI_3$, and 14 wt % S-$MAPbI_3$ films. (a) 50−130 cm^{-1}. (b) 135−160 cm^{-1}. (c) 180−360 cm^{-1} wavenumbers.

The Pb–I mode (a) shifted from 85 to 89 cm^{-1} with an increase in the PS concentration. The MA^+ libration (b) and torsional (c) modes shifted from 143 to 149 cm^{-1} and 240 to 247 cm^{-1}, respectively with increasing PS content. These Raman shifts towards higher wavenumber confirm the interaction of the PS with $MAPbI_3$.

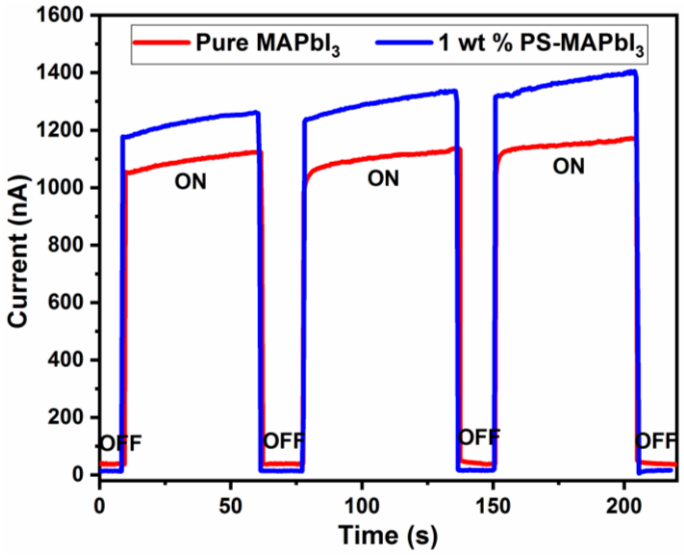

Figure A2.11. Current-response measured from a vertical device configuration of ITO/PS-$MAPbI_3$ (or $MAPbI_3$)/Au at 0.05 V. OFF refers to the current measured under dark and ON refers to current measured under light (1.0 sun) illumination.

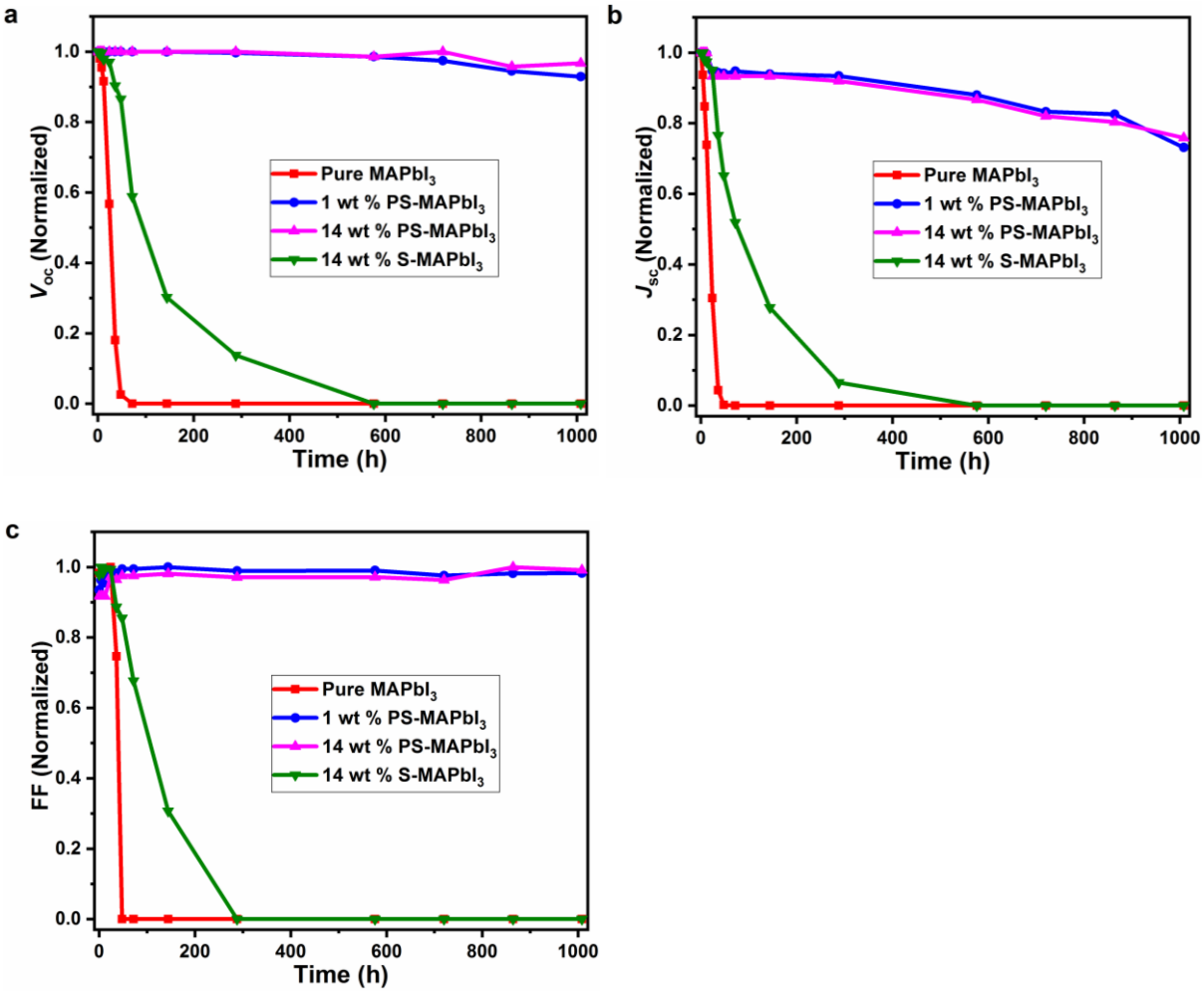

Figure A2.12. Normalized (a) V_{oc}, (b) J_{sc}, and (c) FF for the pure $MAPbI_3$, 1 and 14 wt % PS-$MAPbI_3$, and 14 wt % S-$MAPbI_3$ solar cells without HTL after aging under continuous full-sun (AM 1.5 G) illumination in ambient air with 40-50% relative humidity.

The stability of the devices was tested after exposing them in normal air atmosphere, 40-50% relative humidity at 45 °C, and continuous 1.0 sun illumination for 1008 h (42 days). 1 and 14 wt % PS-$MAPbI_3$ devices maintain more than 92% of their initial V_{oc} after 1008 h, whereas under the same conditions the measured V_{oc} decreased to zero in pure $MAPbI_3$ (after 48 h) and 14 wt % S-$MAPbI_3$ (after 300 h) solar cells. The J_{sc} of 1 and 14 wt % PS-$MAPbI_3$ PSCs maintained more than 70% of their initial values after 42 days. While the measured J_{sc} decreased to zero for pure $MAPbI_3$ (after 48 h) and 14 wt % S-$MAPbI_3$ (after 300 h) solar cells. The FF for 1 and 14 wt % PS-$MAPbI_3$ devices retain more than 98% of their initial value, while for pure $MAPbI_3$ and 14 wt % S-$MAPbI_3$ devices the FF gradually decreased to zero within 48 h and 288 h of continuous light and moisture exposure at 45 °C, respectively.

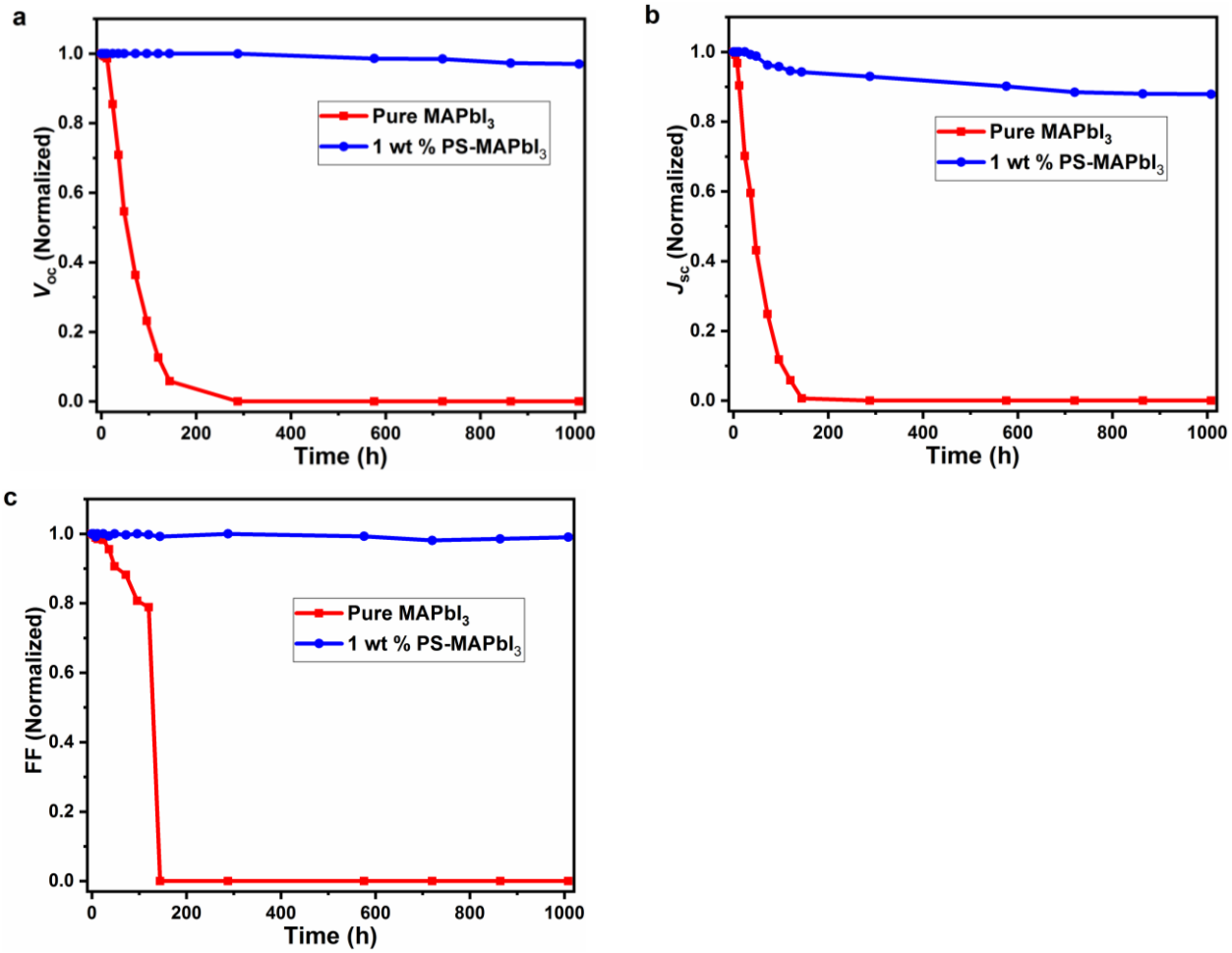

Figure A2.13. Normalized (a) V_{oc}, (b) J_{sc}, and (c) FF for the pure $MAPbI_3$, and 1 wt % PS-$MAPbI_3$ solar cells with HTL after exposing in ambient air with 40-50% relative humidity and under continuous full-sun (AM 1.5 G) illumination.

The 1 wt % PS-$MAPbI_3$ PSCs retain 97% of their highest V_{oc} after 1008 h, whereas the V_{oc} for pure $MAPbI_3$ PSCs decreased to zero after 144 h under continuous one sun illumination, and ambient air at 45 °C with a relative humidity of 40-50%. After 42 days, the J_{sc} of 1 wt % PS-$MAPbI_3$ PSCs maintained more than 87% of their initial values. In contrast, the measured J_{sc} for pure $MAPbI_3$ solar cells decreased to zero after 120 h (5 days). The 1 wt % PS-$MAPbI_3$ devices maintain 99% of their initial FF, whereas the FF gradually decreased to zero for pure $MAPbI_3$ devices after 120 h under the combined effect of continuous light, air and moisture.

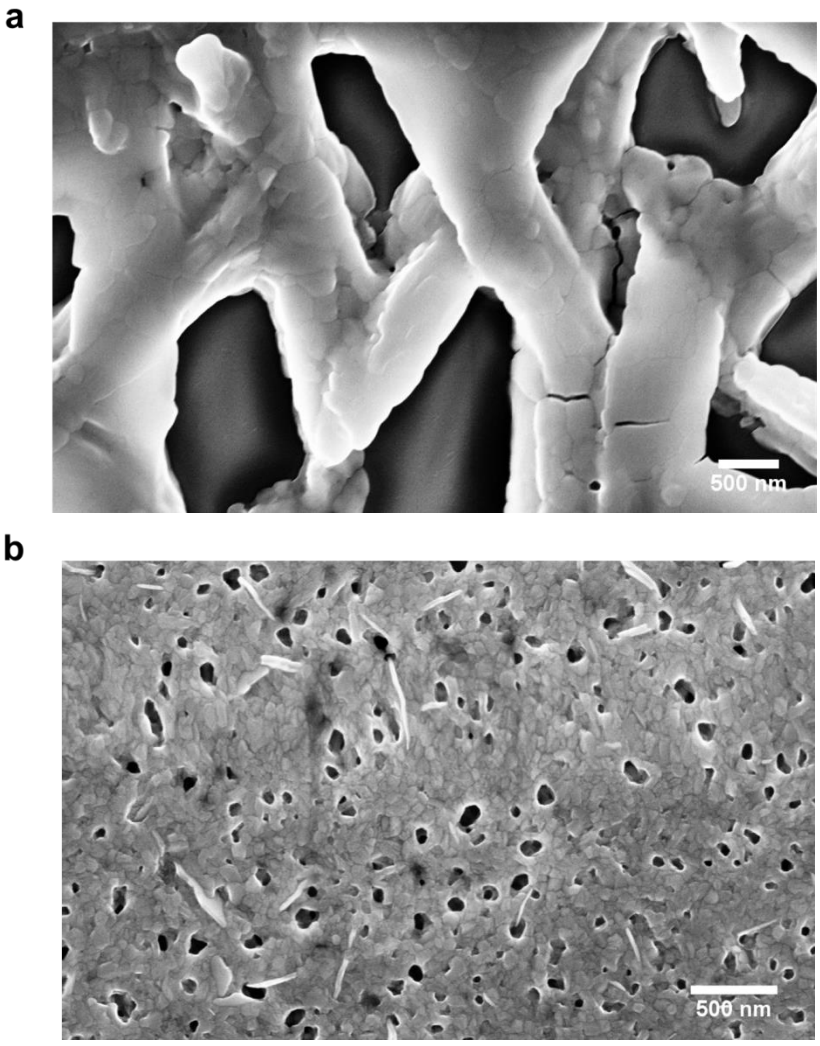

Figure A2.14. FESEM images of (a) 14 wt % PS-$MAPbI_3$, and (b) 14 wt % S-$MAPbI_3$ films on the ZnO/ITO substrate.

Table A2.1. Summary of device performance for pure $MAPbI_3$, PS-$MAPbI_3$ (different concentrations), and S-$MAPbI_3$ solar cells without HTL. A batch of 10 individual devices was fabricated and measured for each perovskite layer to gain more reliable statistical information.

Perovskite layer	J_{sc} (mA cm^{-2})	V_{oc} (V)	FF	PCE (%)
Pure $MAPbI_3$	4.61 ± 0.06	0.775 ± 0.01	0.696 ± 0.014	2.49 ± 0.13
0.5 wt % PS-$MAPbI_3$	4.70 ± 0.03	0.776 ± 0.02	0.694 ± 0.010	2.53 ± 0.14
1 wt % PS-$MAPbI_3$	5.21 ± 0.04	0.784 ± 0.01	0.745 ± 0.012	3.04 ± 0.10
2 wt % PS-$MAPbI_3$	4.61 ± 0.10	0.779 ± 0.01	0.741 ± 0.021	2.66 ± 0.15
4 wt % PS-$MAPbI_3$	3.90 ± 0.06	0.740 ± 0.02	0.695 ± 0.015	2.00 ± 0.12
14 wt % PS-$MAPbI_3$	1.50 ± 0.02	0.710 ± 0.01	0.642 ± 0.010	0.68 ± 0.10
14 wt % S-$MAPbI_3$	3.07 ± 0.07	0.725 ± 0.01	0.706 ± 0.018	1.57 ± 0.09

Table A2.2. Performance of pure $MAPbI_3$, PS-$MAPbI_3$, and S-$MAPbI_3$ devices with HTL. A batch of 10 individual devices was fabricated and measured for each perovskite layer to gain more reliable statistical information.

Perovskite layer	J_{sc} (mA cm^{-2})	V_{oc} (V)	FF	PCE (%)
Pure $MAPbI_3$	14.88 ± 1.23	1.033 ± 0.05	0.717 ± 0.015	11.02 ± 1.77
1 wt % PS-$MAPbI_3$	15.80 ± 1.18	1.044 ± 0.08	0.744 ± 0.011	12.27 ± 1.83
14 wt % PS-$MAPbI_3$	6.79 ± 0.25	0.951 ± 0.02	0.712 ± 0.019	4.60 ± 0.21
14 wt % S-$MAPbI_3$	10.66 ± 0.13	0.995 ± 0.01	0.714 ± 0.013	7.57 ± 0.15

Table A2.3. Device parameters for pure $MAPbI_3$ and 1 wt % PS-$MAPbI_3$ devices with HTL in both reverse and forward scanning directions.

Perovskite layer	Scanning direction	J_{sc} (mA cm^{-2})	V_{oc} (V)	FF	PCE (%)	Hysteresis index
Pure $MAPbI_3$	Reverse	14.88	1.033	0.717	11.02	0.032
	Forward	14.79	1.032	0.699	10.67	
1 wt % PS-$MAPbI_3$	Reverse	15.80	1.044	0.744	12.27	0.017
	Forward	15.58	1.043	0.742	12.06	

Table A2.4. Impedance spectra parameters values (with the goodness of fit, χ^2) for $MAPbI_3$ and PS-$MAPbI_3$ devices measured under dark and light illumination.

	Dark		Light	
Parameters	$MAPbI_3$	1 wt % PS-$MAPbI_3$	$MAPbI_3$	1 wt % PS-$MAPbI_3$
R_1 (MΩ)	0.11 (± 0.00358)	0.12 (± 0.003025)	0.0116 (± 0.00037)	0.0127 (± 0.000463)
C_2 (pF)	9.35 (± 1.83 × 10^{-6})	0.5 (± 0.93 × 10^{-6})	408 (± 6.50 × 10^{-4})	441 (± 1.40 × 10^{-3})
R_2 (MΩ)	4.78 (± 0.6451)	203 (± 0.5086)	0.57 (± 0.0976)	0.42 (± 0.022)
C_3 (pF)	14.07 (± 1.91 × 10^{-6})	8.82 (± 1.57 × 10^{-6})	144 (± 0.55 × 10^{-4})	127 (± 2.13 × 10^{-4})
R_3 (MΩ)	3.01 (± 0.4985)	6.20 (± 0.27)	0.33 (± 0.0542)	0.62 (± 0.058)
C_4 (nF)	0.538 (± 2.13 × 10^{-9})	0.192 (± 5.12 × 10^{-10})	1.29 (± 1.13 × 10^{-6})	0.354 (± 3.48 × 10^{-7})
R_4 (MΩ)	168.45 (± 0.6412)	533.74 (± 0.2958)	0.46 (± 0.0957)	0.98 (± 0.017)
χ^2	0.0056	0.0014	0.0058	0.0074

Appendix for Chapter 3

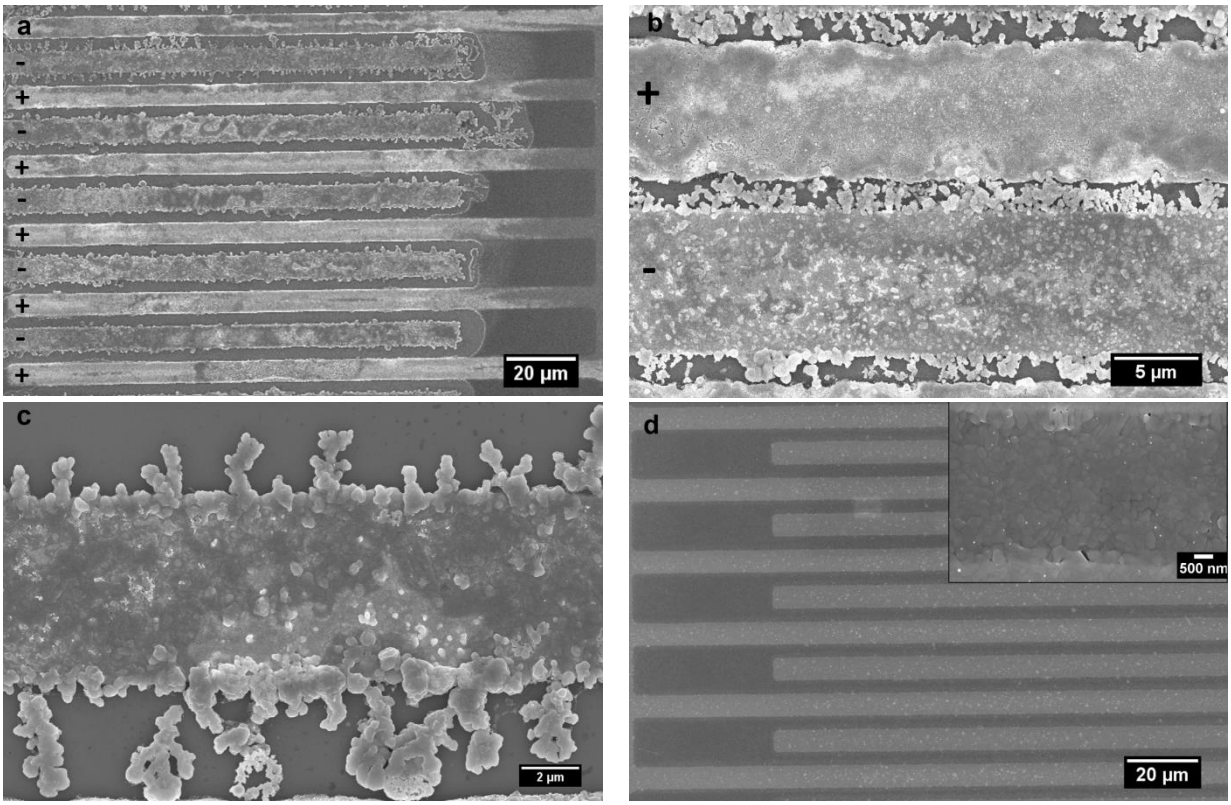

Figure A3.1. FESEM images of $MAPbI_3$ film after high poling field. (a−c) After poling at 5 V μm^{-1} for 5 min in the air under light illumination showing the segregation of the ions which leads to the formation of PbI_2 and the observed polarization behavior disappears. (d) After poling at 5 V μm^{-1} for 5 min under N_2 in dark condition showing no change in the material.

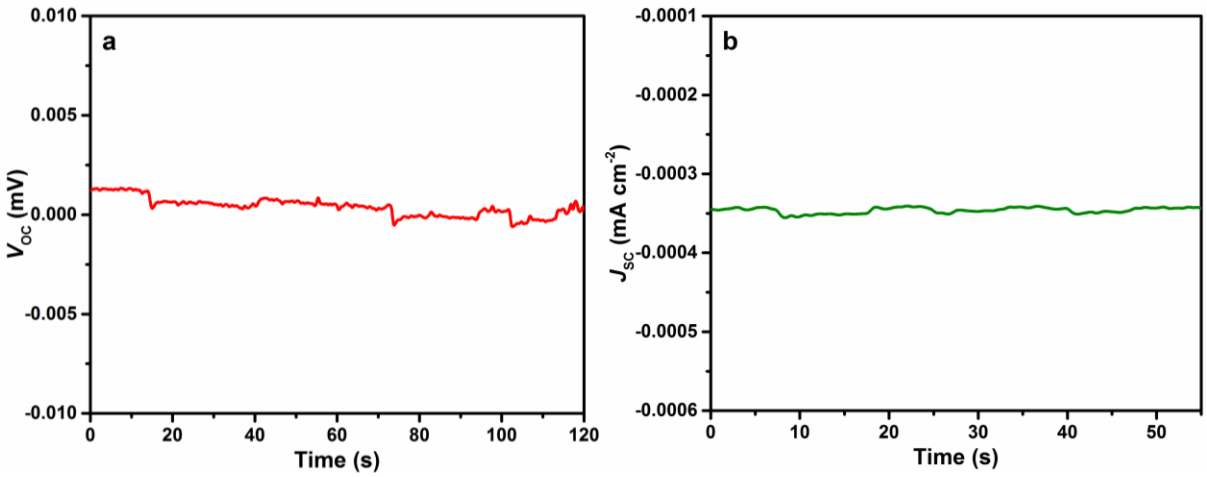

Figure A3.2. Effect of high poling field on the polarization behavior. (a) V_{oc} and (b) J_{sc} disappeared after poling at 5 V μm^{-1} for 5 min in the air under light illumination due to the complete separation of the ions which will lead to the formation of PbI_2.

Stability of the electrodes in the device and ion back diffusion currents

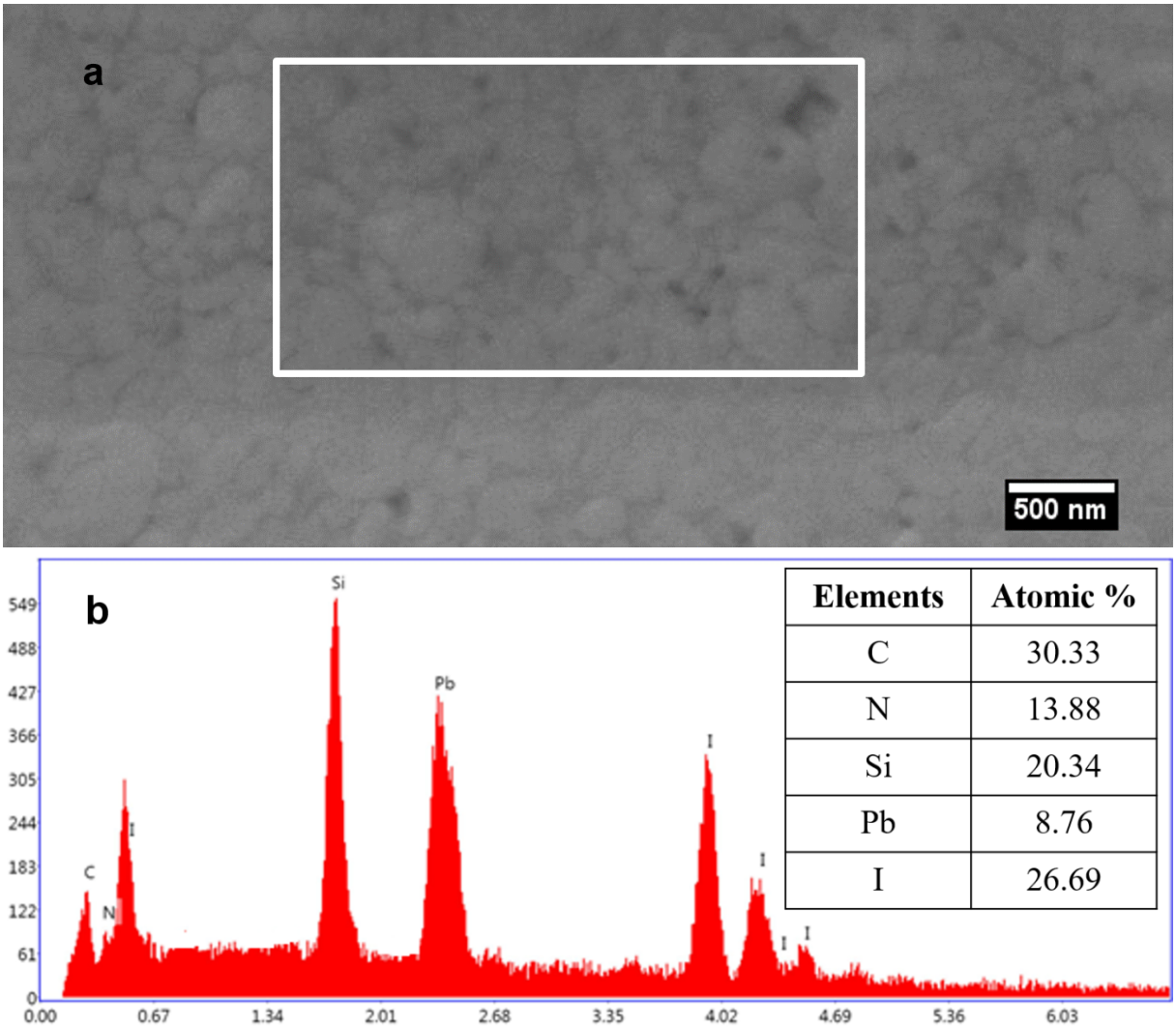

Elements	Atomic %
C	30.33
N	13.88
Si	20.34
Pb	8.76
I	26.69

Figure A3.3. (a) FESEM image of $MAPbI_3$ film after the poling process. (b) EDX spectrum and elemental composition of the selected area showing no electrode migration.

The characterization of the device is conducted in FESEM after multiple cycles of measurements at room temperature. From the elemental analysis, we can see that no Au migration is observed in the perovskite layer. This is consistent with the reports that the presence of a Cr adhesion layer with Au electrodes and restricting the device operation to room temperature limits Au migration.

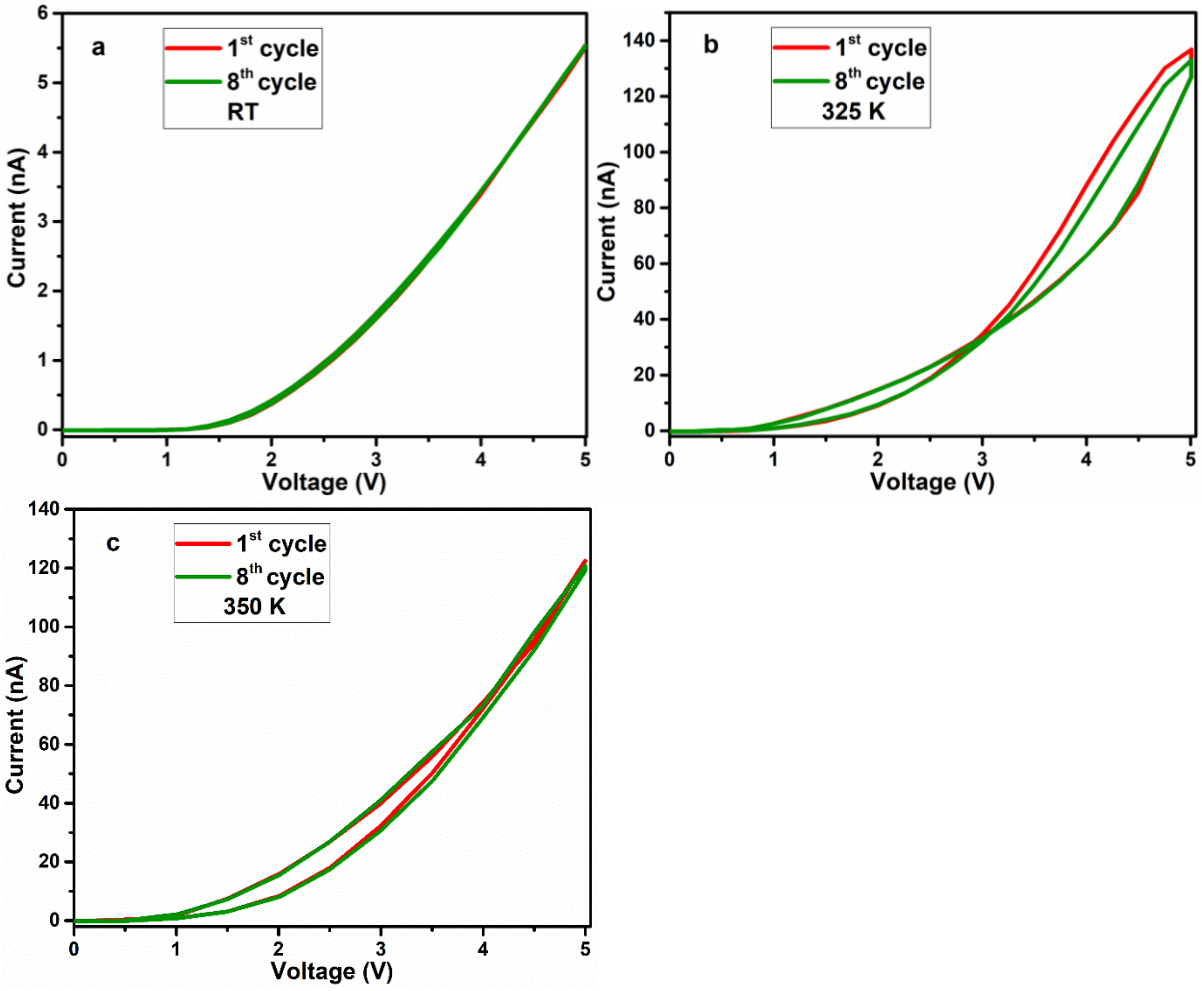

Figure A3.4. Current-voltage (*I*−*V*) scans from 0-5 Vat (a) room temperature (RT), (b) 325 K and (c) 350 K.

The stability of the perovskite layer against any redox reactions within the voltage ranges used in the device operation is characterized in multiple ways. First multiple cycles of *I*−*V* are conducted by going up and down in voltage. Degradation of the perovskite due to a redox reaction leads to the possible formation of PbI_2, an insulator, with the oxidation of iodide ions to I_2 (g), reaction detailed below. As seen in Figure A3.4a, the current-voltage characteristics remain consistent which shows that no degradation of the perovskite layer is occurring. Further, we do not observe any hysteresis between going up and down in voltage which indicative of the capacitive behavior due to the ion diffusion current and corresponding electric field, illustrates that these effects are minimal at the applied conditions in this device. The hysteresis in current-voltage characteristics is observed only at higher temperatures (325 and 350 K), as seen in Figure

A3.4b,c. This ion separation leads to the development of an opposing internal field and a charge compensating layer in the material similar to a capacitive response. The CV analysis present in the next section further shows that the capacitive response from the device is minimal at room temperature and redox reaction is not observed at these conditions.

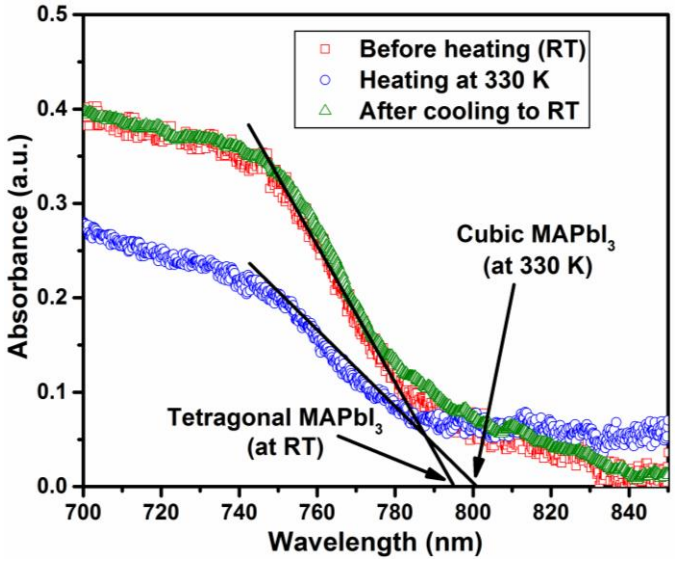

Figure A3.5. UV-Visible absorption spectrum of $MAPbI_3$ film at room temperature (RT), 330 K, and after cooling to RT.

It is known that the tetragonal phase of $MAPbI_3$ is stable at room temperature (~296 K) and it undergoes a transformation from tetragonal to the cubic phase at 327 K. The UV-Vis absorption spectrum of a tetragonal $MAPbI_3$ presents a steep absorption edge at 794 nm. The optical band gap energy (E_g) was calculated by Planck relation, $E = hc/\lambda$ where h is Planck constant (6.626×10^{-34} J.s), c is the speed of light (3×10^8 m/s), and λ is the cut off wavelength. The extrapolation gives the bandgap value of 1.562 eV for a tetragonal $MAPbI_3$. After heating the $MAPbI_3$ film at 330 K, the cubic $MAPbI_3$ shows an absorption edge at 800 nm with a bandgap of 1.55 eV. Further, the bandgap is restored on cooling the film back to room temperature. This confirms that there is a phase transition from tetragonal to cubic when the $MAPbI_3$ film is heated at 330 K.

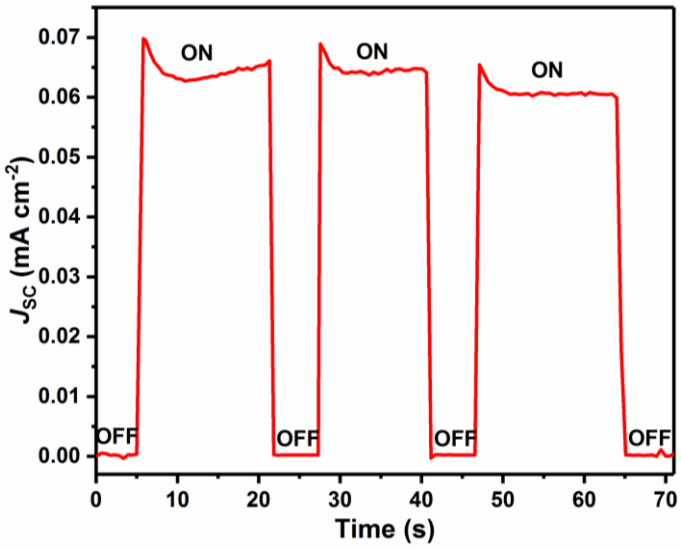

Figure A3.6. J_{sc} response showing no observable ion back diffusion current in dark. OFF refers to J_{sc} measured under dark and ON refers to J_{sc} measured under 1.0 sun illumination.

The short circuit current density (J_{sc}) response is shown for a typical device poled under the p-n conditions. As seen in Figure A3.6, we note that under dark no observable J_{sc} is recorded, which illustrates the absence of any ion back diffusion current, hence correspondingly there cannot be any internal electric field due to ion separation. On illuminating the sample, a significant J_{sc} is observed which indicates that the photogenerated electron-hole pairs are being separated in the poled sample hence there is an internal electric field present in the sample and should be the result of the formation of an internal p-n junction from electric field induced poling. It should be noted that an unpoled perovskite film does not show any J_{sc} on illumination.

Redox reaction in the perovskite layer

Anode process:

$$2\ (PbI_2)^*I^- \rightarrow 2\ PbI_2 + I_2 + 2\ e^- \quad \text{(A3.1)}$$

Cathode process:

$$2\ (CH_3NH_2)^*H^+ + 2\ e^- \rightarrow H_2 + 2\ CH_3NH_2 \quad \text{(A3.2)}$$

Overall reaction:

$$2\ CH_3NH_3PbI_3 \xrightarrow{\text{electrolysis}} I_2 + H_2 + 2\ PbI_2 + 2\ CH_3NH_2 \quad \text{(A3.3)}$$

The degradation of the perovskite layer as illustrated by the equations above has been reported. As with any redox-active species, such oxidation and/or reduction reactions occur only above an energy threshold that will enable an electron transfer between the redox-active species and the electrode. The occurrence of the redox reaction is hence dependent on the applied bias to the electrode where the reaction occurs (working electrode in electrochemical terms) and also the temperature.

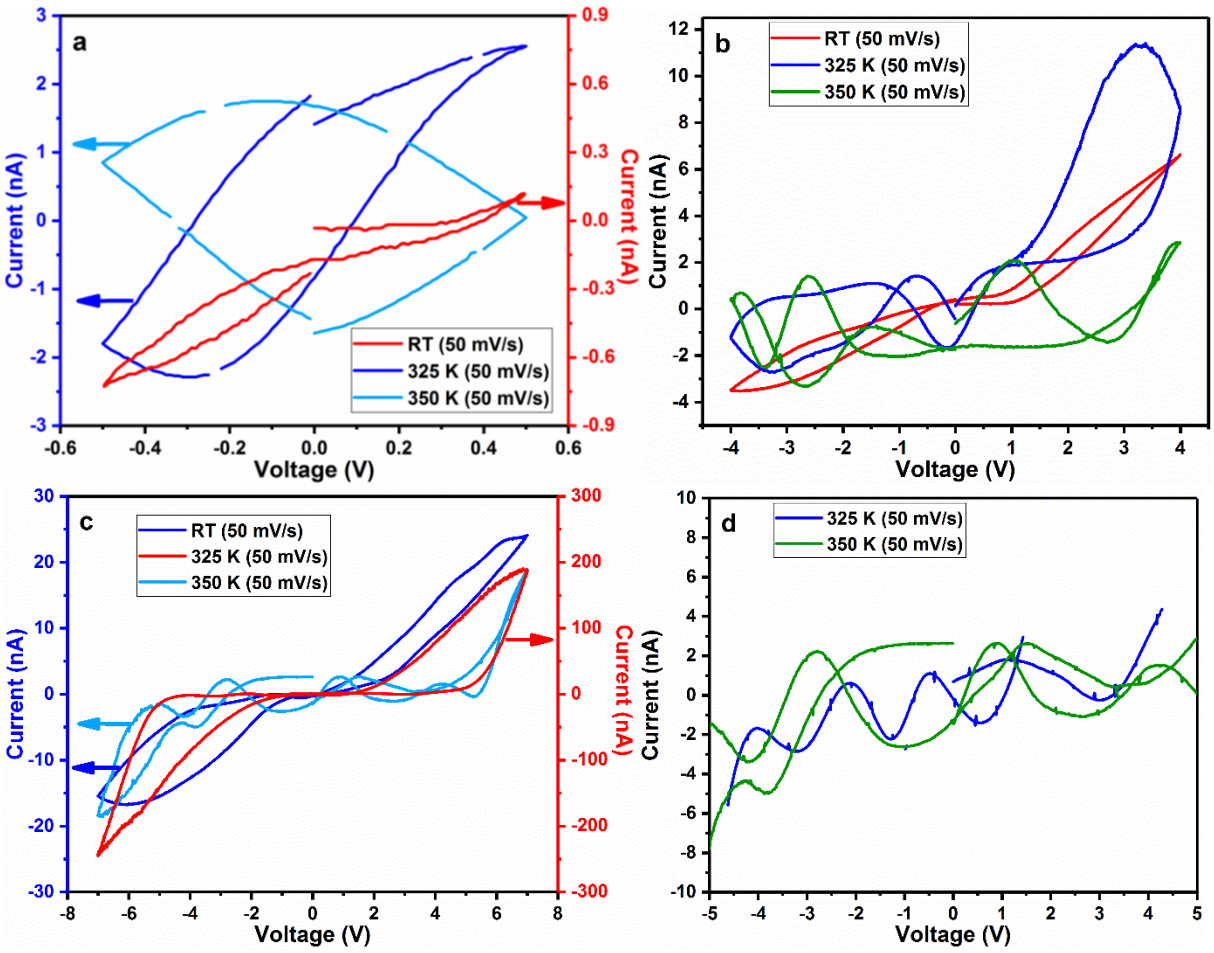

Figure A3.7. Cyclic voltammetry (CV) scans of (a) ±0.5, (b) ±4, (c) ±7 V at room temperature, 325, and 350 K. (d) Magnified CV scans at 325 and 350 K.

Under the conditions used in these devices for poling and operation, we do not observe any redox-based degradation of the perovskite occurring. The repeated current-voltage measurements discussed in the previous section show that the perovskite layer is not changing in performance. To further corroborate this result, CV was done on the device in the two-electrode set-up. The CV's were done for different voltage ranges and at different temperatures. At room temperature, the CV's for voltage ranges of ±0.5V, ±4V and ±7 V at scan speeds of 50 mV s^{-1} do not show any observable redox associated peak or a sudden increase in current indicating the start of a redox process. Further, we do not observe any significant capacitive currents that would indicate the presence of ion diffusion and back diffusion currents. On increasing the temperature to 325 K, we observe that the currents in the CV's increase and the capacitive nature of the device, as illustrated by increased hysteresis, is also amplified due to increased mobility of the

ions. We start to observe the redox signature in the scans. At 350 K at lower voltages (±0.5V) a much higher capacitive behavior is observed from the greater hysteresis in the current response. At higher voltages (±4, ±7) we start to see the appearance of maxima's and minima's in the current indicating the start of redox processes at the higher temperatures.

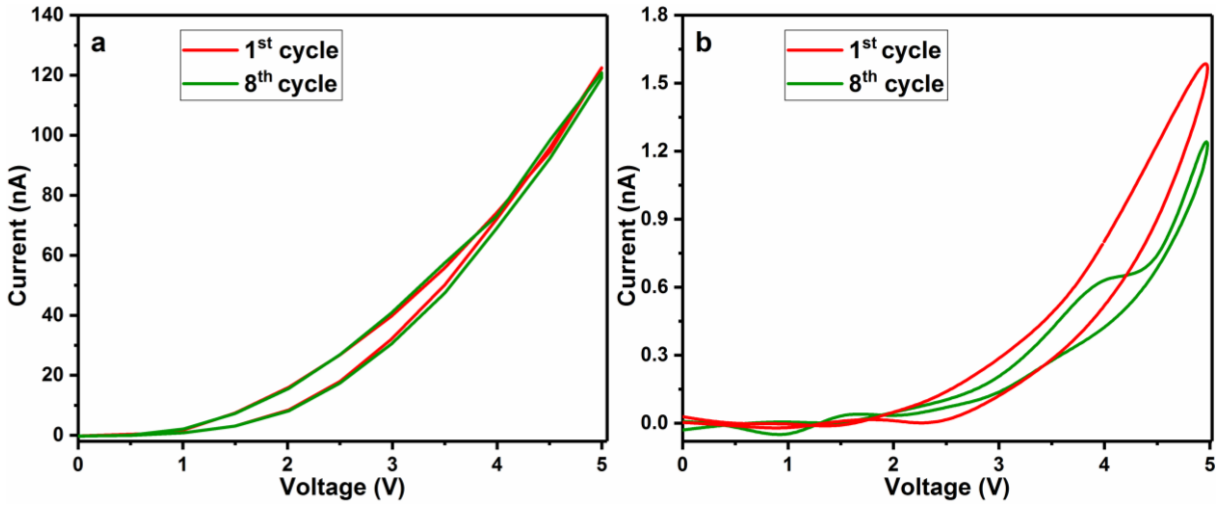

Figure A3.8. *I*−*V* scans (a) before and (b) after redox CV cycles at 350 K.

The current in the device decreases substantially following these redox processes at the higher temperatures indicating the formation of PbI_2. We confirm this by conducting an *I*−*V* scan on the device following the observation of the redox peak, compared to a device exposed to only room temperature processing we observe that the current has decreased by more than 80 times. On poling this device under the p-n conditions, we do not observe any J_{sc} or V_{oc}.

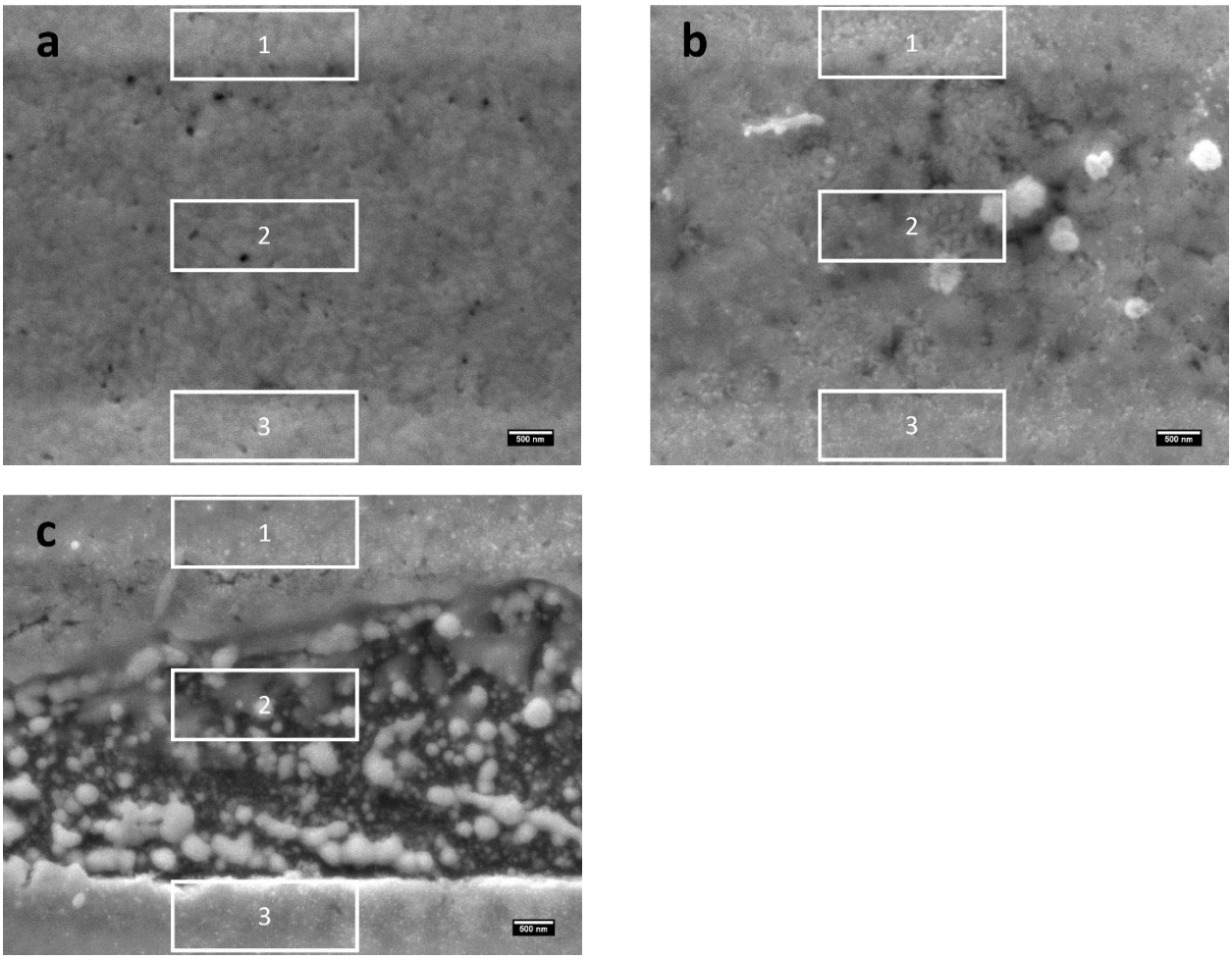

Figure A3.9. FESEM images of the device at (a) room temperature (RT), (b) 350 K after 8 CV cycles at ±7V and (c) 350 K after processing at 70 V.

Table A3.1. Summary of the atomic percentage ratio of the device under three different conditions.

I/Pb (Atomic percentage ratio)	Region 1	Region 2	Region 3
After processing at 7 V (RT)	3.12	3.04	3.07
After 8 CV cycles at 7 V (350 K)	2.23	3.10	2.83
After processing at 70 V (350 K)	2.04	1.46	2.55

FESEM images of the devices after CV scans at room temperature do not show any change but at 350 K (after 8 CV cycles and after processing at 70 V) we observe that the morphology of the perovskite layer has changed. The elemental analysis (EDX) (Table A3.1) also shows that the ratio of I:Pb is close to 3:1 in the device processed at room temperature

(corresponding to $MAPbI_3$), while in the 350 K devices it progressively changes to closer to 2:1, indicating the formation of PbI_2. These results confirm that redox processes do lead to degradation of the perovskite layer to PbI_2 at a higher temperature and applied bias. The conditions used for our device operation do not lead to any observable degradation of the perovskite layer and any appreciable ion diffusion current.

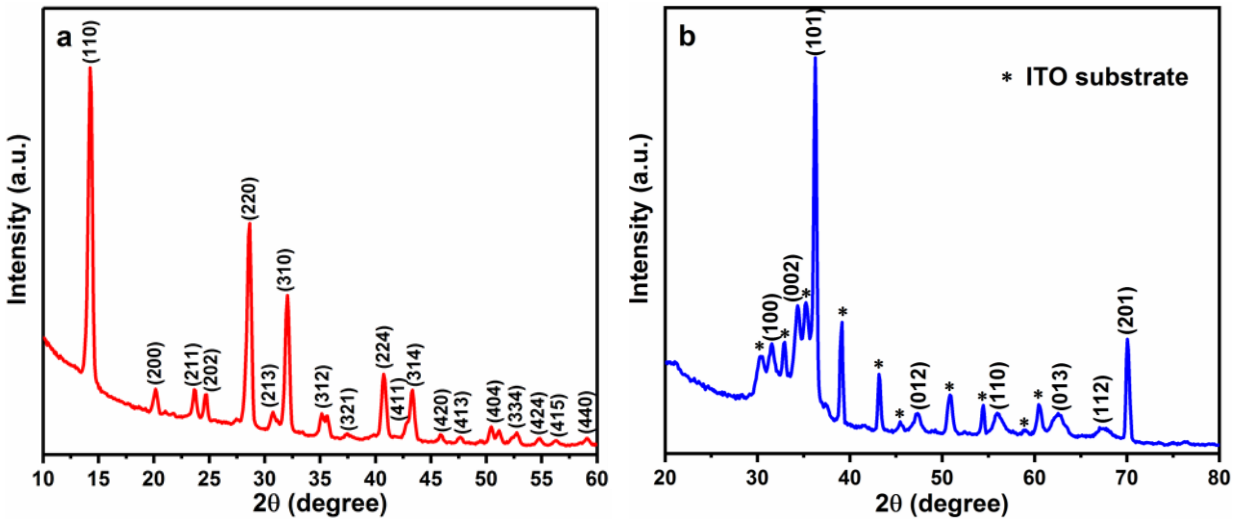

Figure A3.10. Indexed X-ray diffraction patterns of (a) $MAPbI_3$ film with tetragonal structure and (b) ZnO nanosheets on the ITO substrate. Both XRD patterns are measured at room temperature.

The sharp intense peak in Figure A3.10a reveals the crystalline nature of $MAPbI_3$. The $MAPbI_3$ film gives diffraction peaks at 14.22, 28.66, 32.13, 40.59 and 43.21°, which can be assigned to the (110), (220), (310), (224) and (314) planes of the tetragonal perovskite structure with a = 8.874 Å and c = 12.671 Å. It exhibits tetragonal symmetry with the *I*4/*mcm* space group. The XRD pattern of the ZnO sheets (Figure A3.10b) shows that they are oriented along the (101) [or $(10\bar{1}0)$] plane and highly crystalline.

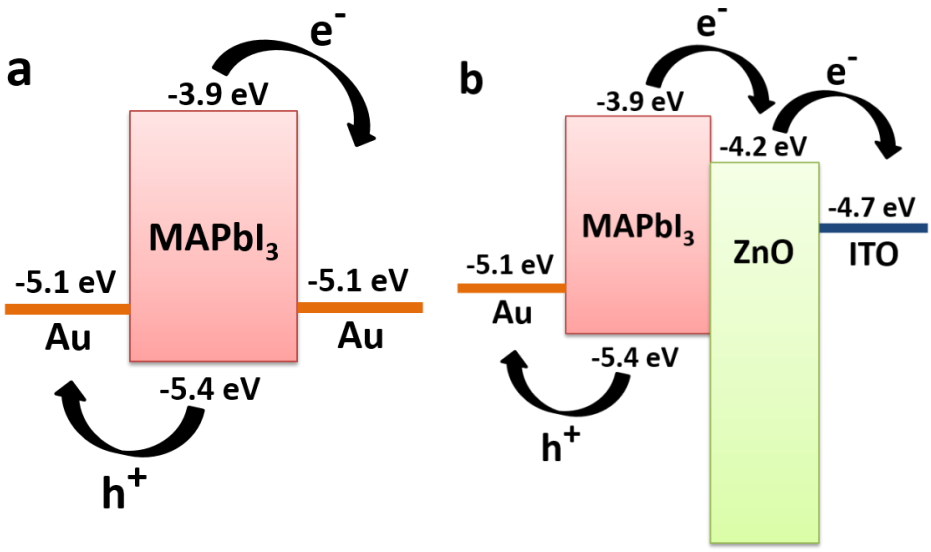

Figure A3.11. Energy level diagram of the (a) Au/$MAPbI_3$/Au and (b) Au/$MAPbI_3$/ZnO devices.

The energy band schematic illustrates that the symmetric planar device of Au/$MAPbI_3$/Au (shown on the left) is suited for conduction of the photo-generated holes in the $MAPbI_3$ layer. While the interfacing ZnO layer (shown on right) is more suited for the extraction of the photo-generated electrons.

Tactile sensor stability and performance

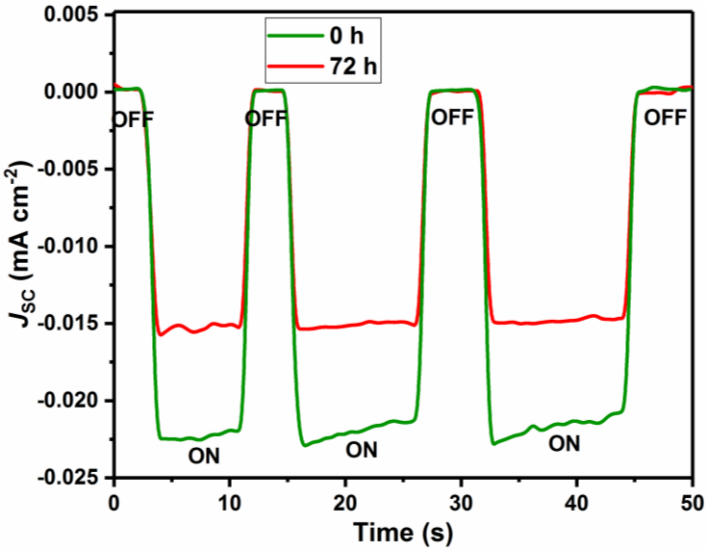

Figure A3.12. Loss in base J_{sc} of the device after 72 hours. The time-based mode of failure is due to the loss of poling effect. The base J_{sc} decreases by 30% which we consider as the limit for stable operation. On repoling the device though the performance is recovered.

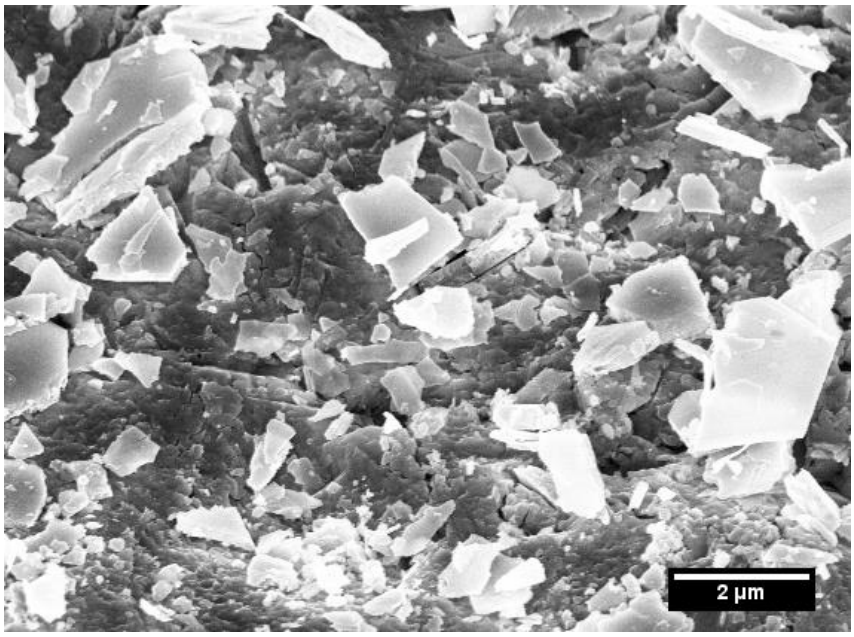

Figure A3.13. FESEM image showing the broken ZnO sheet fragments on the perovskite layer after applying high pressure (500 kPa).

The device failure occurs at pressures exceeding 500 kPa due to the breakage of the ZnO sheets. FESEM images of such as device clearly show multiple ZnO sheet fragments on the perovskite layer indicating the failure of the ZnO sheets.

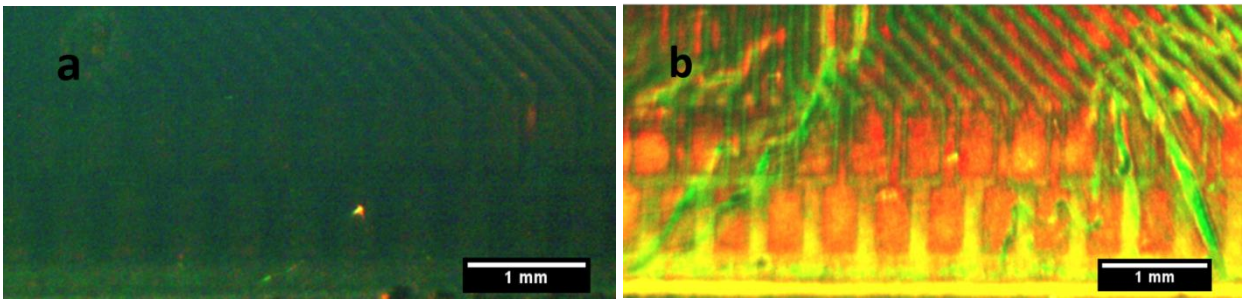

Figure A3.14. Optical images of (a) ZnO covered $MAPbI_3$ on Au chip after 5 days and (b) exposed region showing degradation after 1 day.

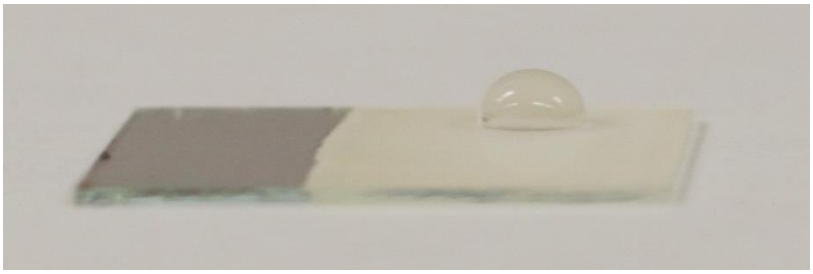

Figure A3.15. Optical image showing the hydrophobicity of the ZnO nanostructure.

The degradation of the perovskite layer due to interaction with ambient oxygen and moisture is well known. In these devices since the perovskite layer is interfaced with ZnO sheets, we observe no degradation even after 5 days (Figure A3.14). This is attributed to the fact that the ZnO layer limits the direct interaction between the perovskite and ambient species. Also, ZnO sheets are hydrophobic in nature and hence repel moisture (Figure A3.15), further limiting the degradation of the perovskite layer. The optical images above (Figure A3.14) show that the perovskite region covered with ZnO (Figure A3.14a) shows no color change even after 5 days while exposed perovskite (Figure A3.14b) has changed to yellow color within 1 day signifying its degradation to PbI_2. The device after 5 days is still operable though there is some loss in J_{sc}, which is recovered by repoling.

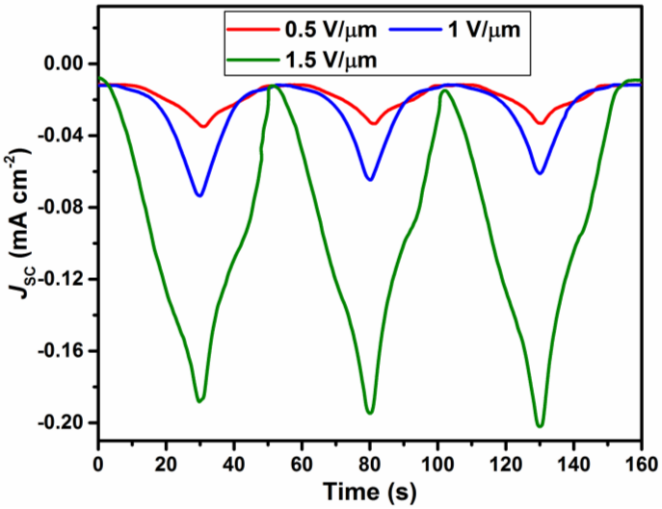

Figure A3.16. J_{sc} cycles of the tactile sensor (ZnO sheets and polarization-semiconducting nature of $MAPbI_3$) for different poling electric fields in the air under 1.0 sun illumination with a maximum of 37 kPa pressure. It is observed that the J_{sc} response is dependent on the poling field strength and is increasing with the increase in the poling field strength. With the increase in the pressure from 0 to 37 kPa, the interfacing area between the ZnO sheets and $MAPbI_3$ film will effectively increase which will lead to a higher charge collection resulting in increased J_{sc}.

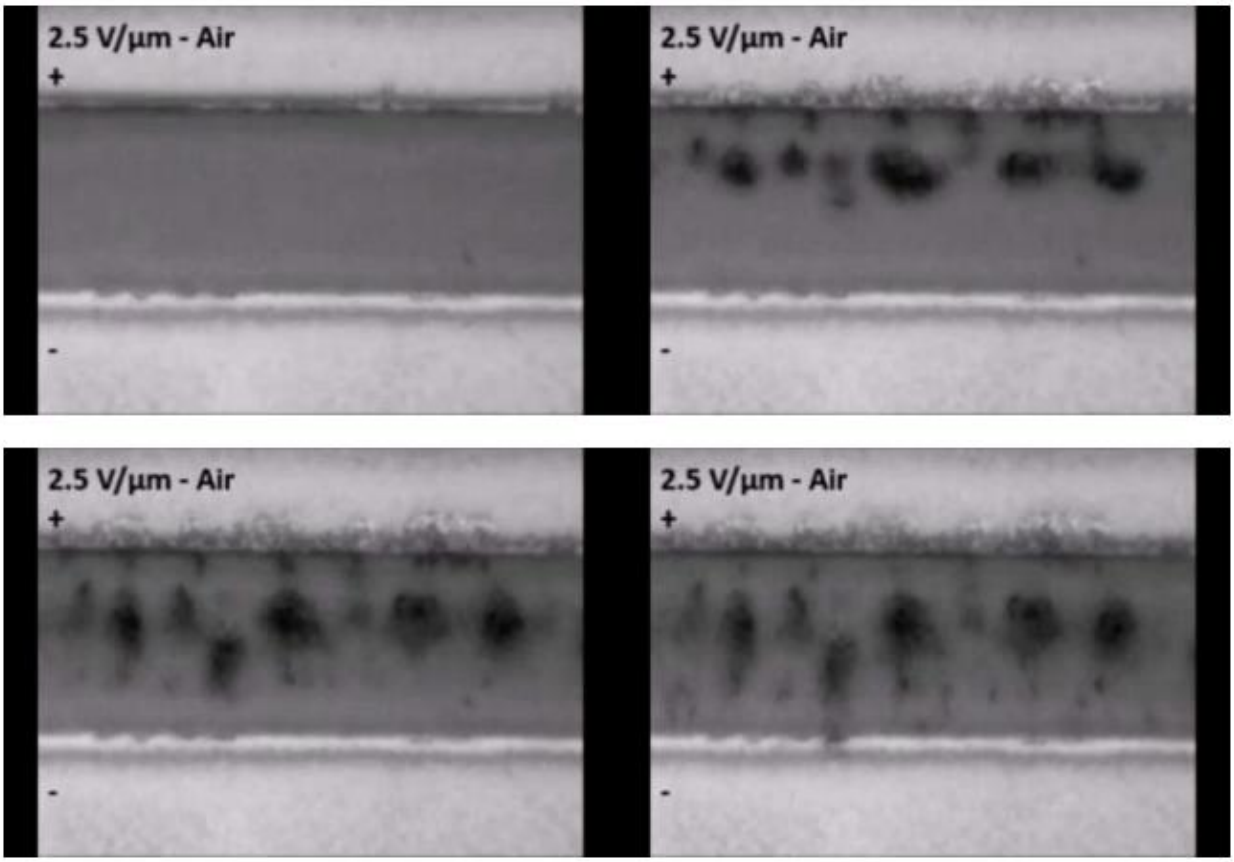

Photo A3.1. Poling at a constant 2.5 V μm^{-1} electric field in the air (images were taken every 3 s).

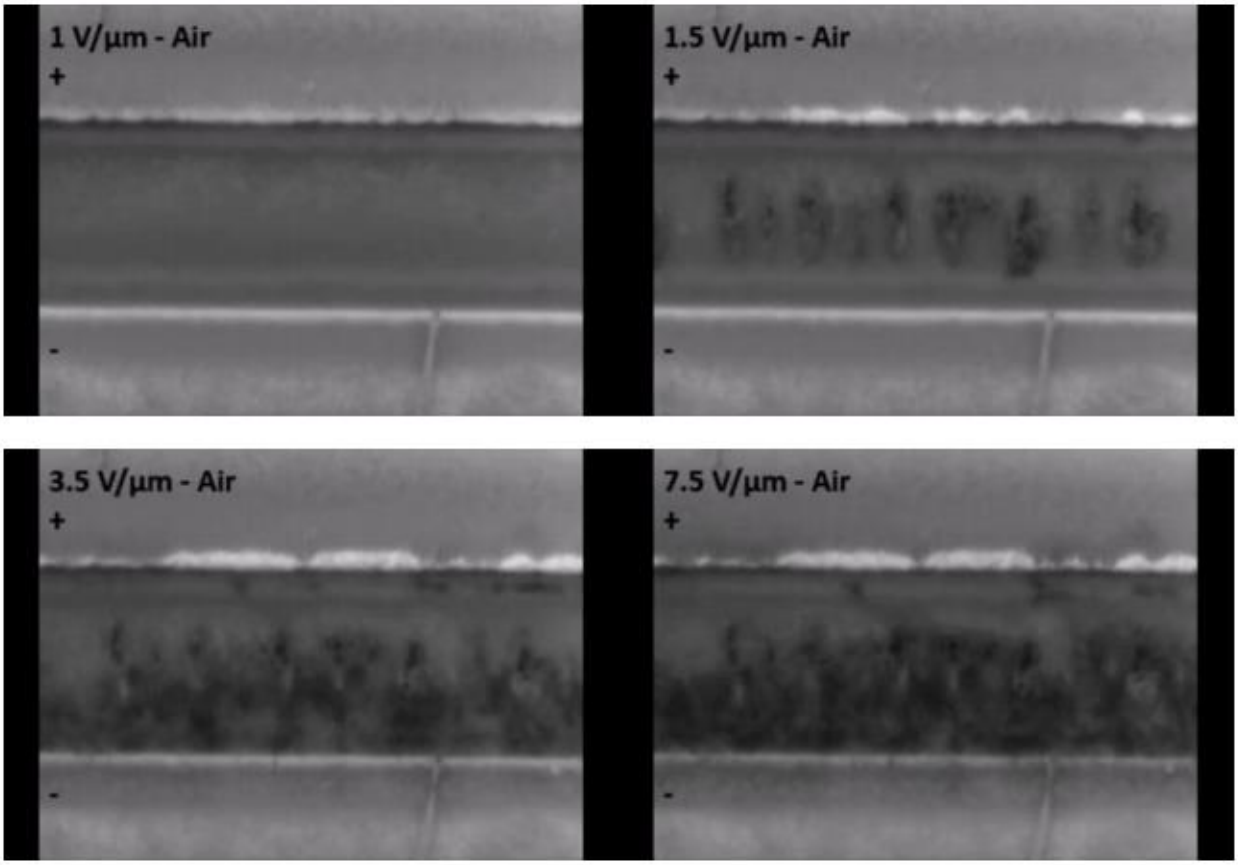

Photo A3.2. Poling at different electric fields in the air (images were taken every 10 s).

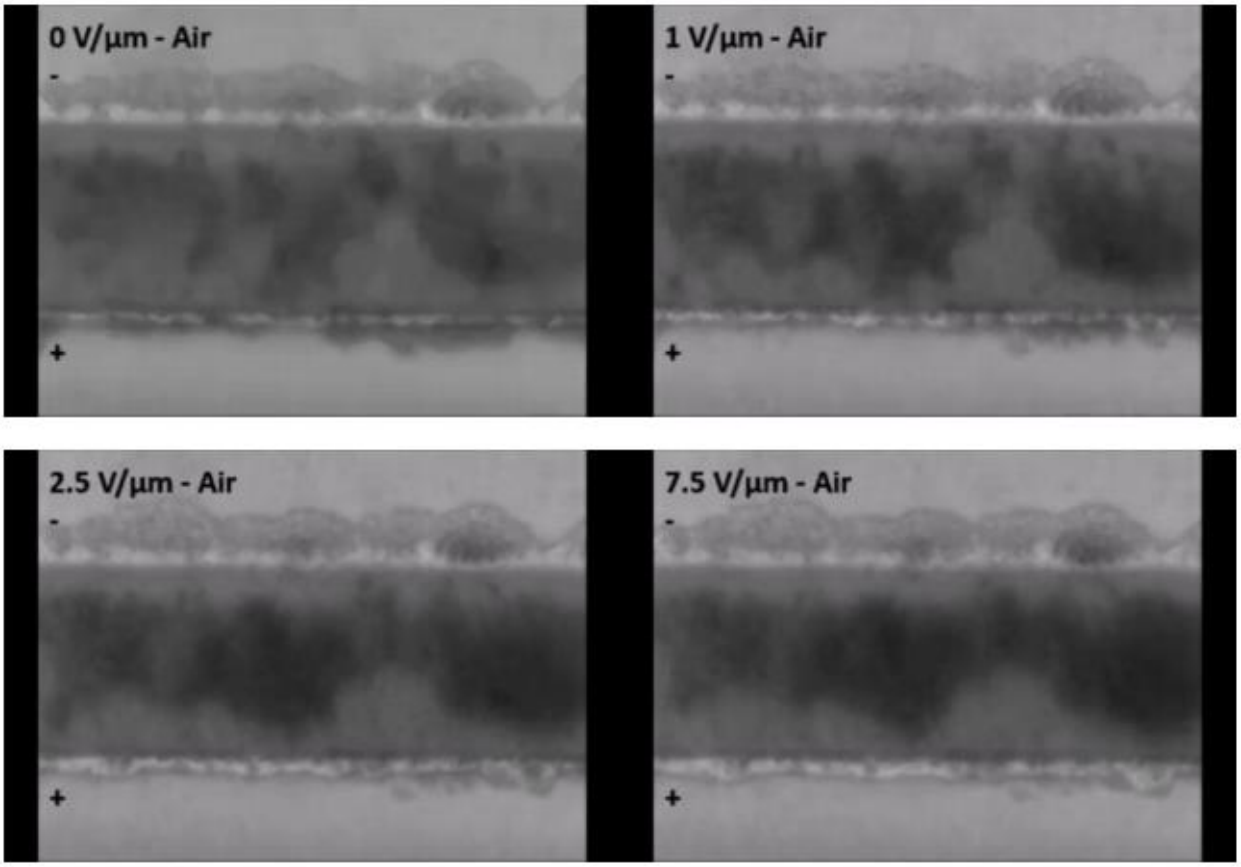

Photo A3.3. Reversing the poling field direction (images were taken every 1 s).

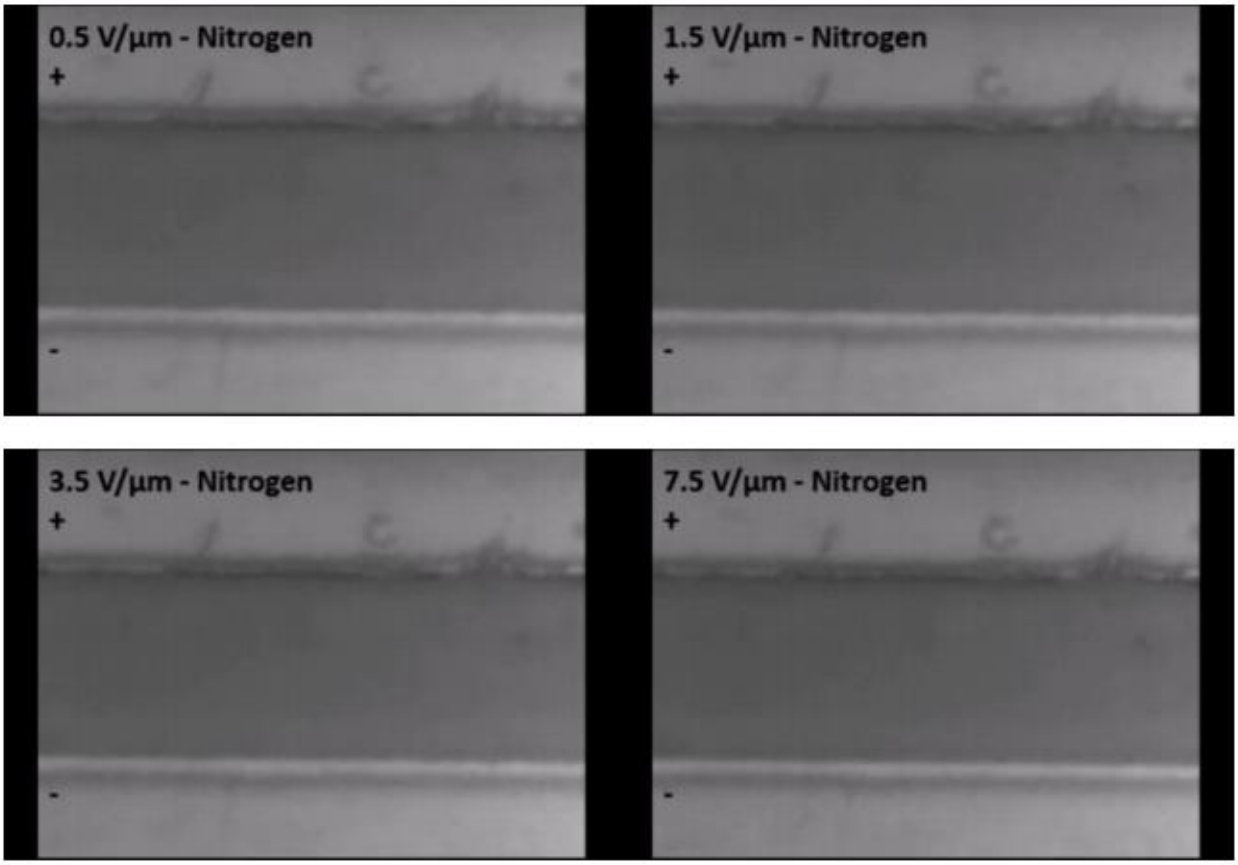

Photo A3.4. Poling at different electric fields in N_2 (images were taken every 10 s).

Appendix for Chapter 4

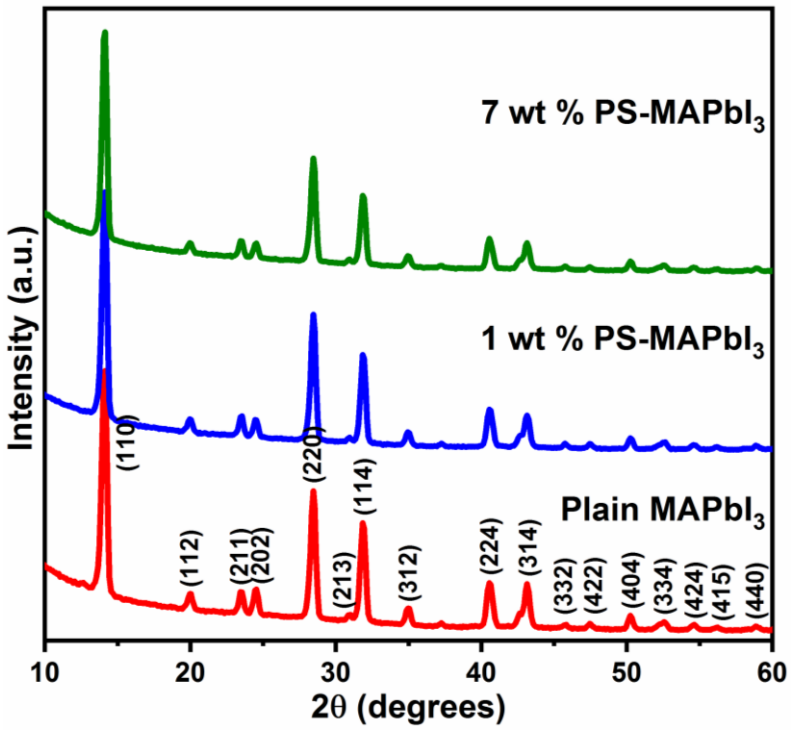

Figure A4.1. X-ray diffraction patterns of plain $MAPbI_3$, 1 wt %, and 7 wt % PS-$MAPbI_3$ films.

The crystal structure of the perovskite films was examined by conducting the glancing incidence XRD measurements. All the samples show the same tetragonal perovskite phase with the dominant (110) lattice plane.

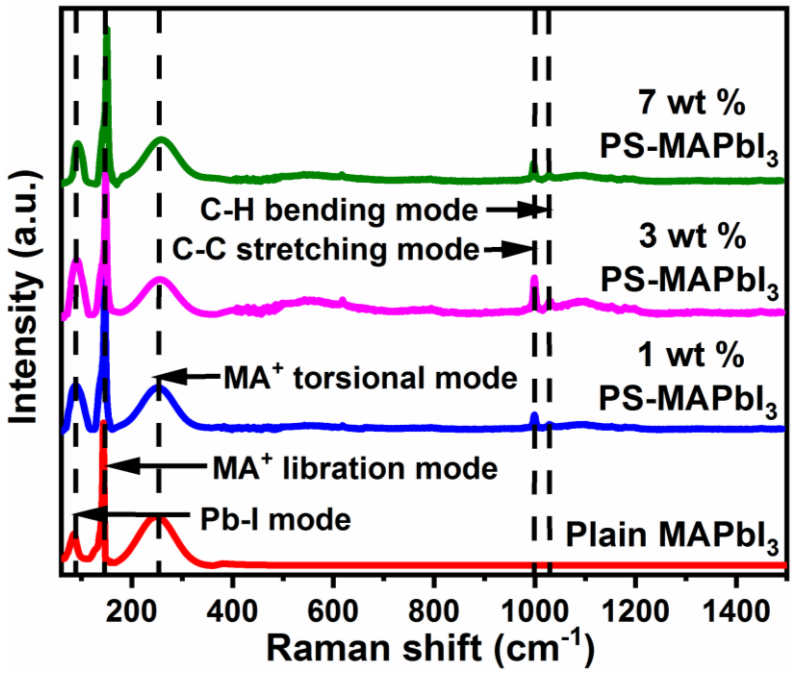

Figure A4.2. Raman spectra of plain $MAPbI_3$, 1 wt %, 3 wt %, and 7 wt % PS-$MAPbI_3$ films.

The sharp characteristic Raman peaks observed at 84 cm^{-1} and 143 cm^{-1} in plain $MAPbI_3$ can be assigned to the Pb–I and MA^+ libration modes, respectively. The broad band with maxima around 247 cm^{-1} attributed to the MA^+ torsional mode in the plain $MAPbI_3$. The shift of the Pb–I, MA^+ libration, and MA^+ torsional modes from 84 to 92 cm^{-1}, 143 to 150 cm^{-1}, and 247 to 258 cm^{-1}, respectively with the increase in the PS content to 7 wt % is indicative of the interaction of PS with Lewis acid PbI_2 and MA^+ cations. This interaction leads to the formation of an intermediate PS-PbI_2 and PS-MA^+ adducts, which will improve the crystallinity of the perovskite films. Further, we also observed the stretching vibration of C–C aromatic in 1 wt %, 3 wt %, and 7 wt % PS-$MAPbI_3$ at 998 cm^{-1}. The bending vibration of C–H aromatic in all PS-$MAPbI_3$ films appears at 1030 cm^{-1}. Both the stretching and bending vibrations observed in PS-$MAPbI_3$ films reflect the incorporation of PS into $MAPbI_3$.

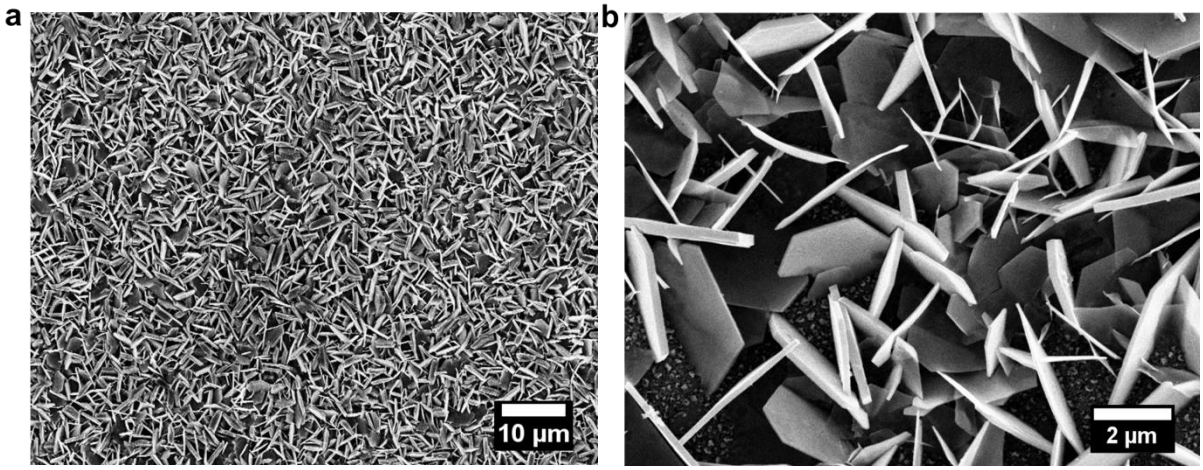

Figure A4.3. FESEM images of electrochemically-deposited ZnO nanosheets.

The lower resolution image (Figure A4.3a) shows the high density of the ZnO nanosheets on the ITO substrate. The higher resolution image (Figure A4.3b) reveals that the average sheet size is 3 µm with a thickness on the scale of 50–150 nm.

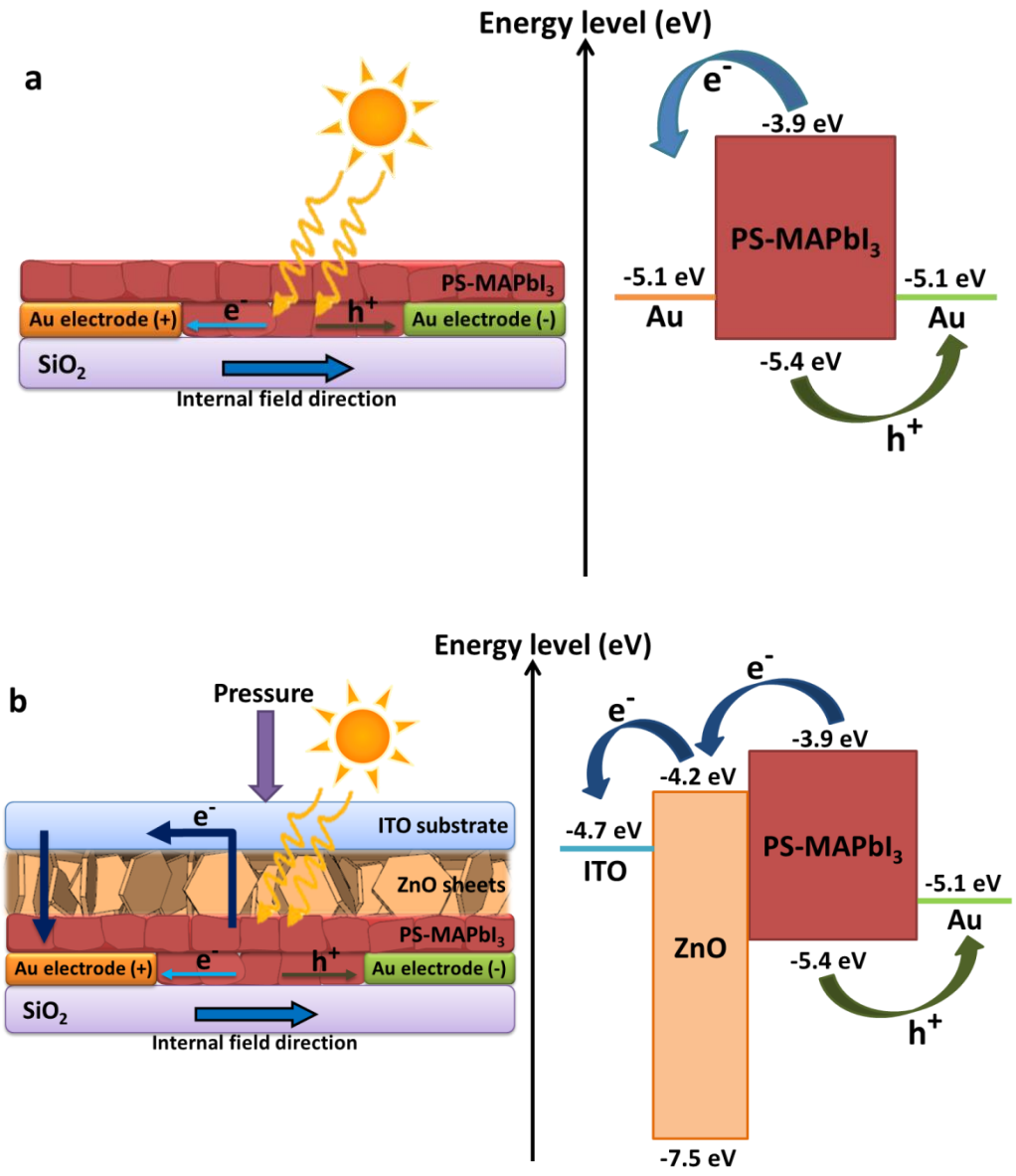

Figure A4.4. Energy level diagram of the PS-MAPbI$_3$ device (a) Without ZnO (Au/PS-MAPbI$_3$/Au), and (b) With ZnO (ITO/ZnO/PS-MAPbI$_3$/Au).

When the light is illuminated on the device, the photo-generated charge carriers (electrons and holes) in the PS-MAPbI$_3$ layer will separate under the polarization field. In the symmetric device configuration (Au/PS-MAPbI$_3$/Au) as shown in Figure A4.4a, the work function of Au closely matches the PS-MAPbI$_3$ perovskite Highest Occupied Molecular Orbital (HOMO) which leads to favorable hole collection by the negative gold electrode. Whereas, the electrons are not easily collected by the positive Au electrode due to the large difference in the energy level of PS-MAPbI$_3$ LUMO (Lowest Unoccupied Molecular Orbital) and Au. By

interfacing the ZnO sheets with the PS-$MAPbI_3$ film (Figure A4.4b), the electron extraction efficiency will improve due to the matching of the energy level of PS-$MAPbI_3$ LUMO with the ZnO LUMO and hence leads to increased J_{sc}. In the absence of external pressure, the vertically oriented microstructured ZnO sheets have a limited area of interaction with the PS-$MAPbI_3$ layer. When the pressure is applied, the contact area of ZnO sheets with the PS-$MAPbI_3$ film will increase either due to bending or penetration of the ZnO sheets. The increase in an interfacing area will improve the charge collection, which facilitates the pressure-sensitive modulation in J_{sc}.

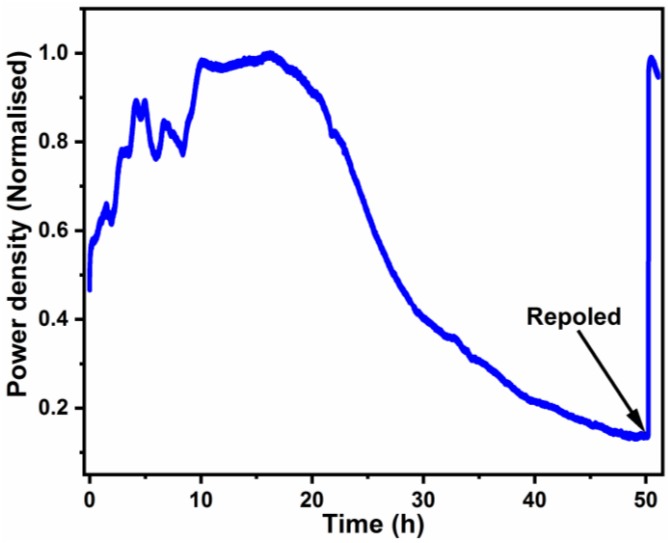

Figure A4.5. Operational stability and continuous power generation test for the 1 wt % PS-$MAPbI_3$ device (after 5 V μm^{-1} poling) without the ZnO interface, examined at maximum power point with a constant resistance of 20 MΩ under continuous 0.1 sun illumination in air.

The 1 wt % PS-$MAPbI_3$ device (without ZnO layer) after poling for just 5 min generates stable and continuous power density for more than 24 h. We observed a decrease in the power density with time due to the depolarization of the films and not to any structural degradation. This is confirmed by repoling the device at 5 V μm^{-1} for 5 min and subsequently the efficiency is recovered.

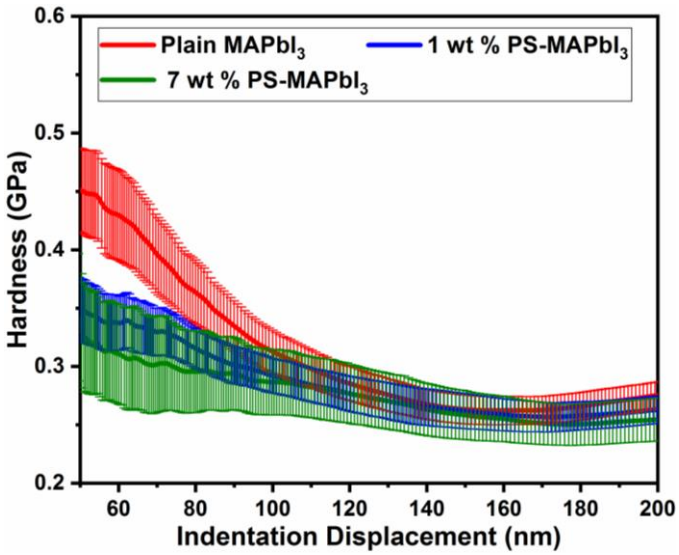

Figure A4.6. Hardness of plain $MAPbI_3$, 1 wt %, and 7 wt % PS-$MAPbI_3$ films.

The average hardness value for plain $MAPbI_3$ films at the indentation depth of 75 nm is found to be 0.38 GPa. It can be clearly observed that this value reduces to 0.33 GPa, and 0.30 GPa as the PS content in the precursor solution is increased to 1 wt %, and 7 wt %, respectively. This reveals that the increment in the wt % of PS in the precursor solution leads to the formation of softer films, which allows us to tune the dynamic pressure range of the sensors.

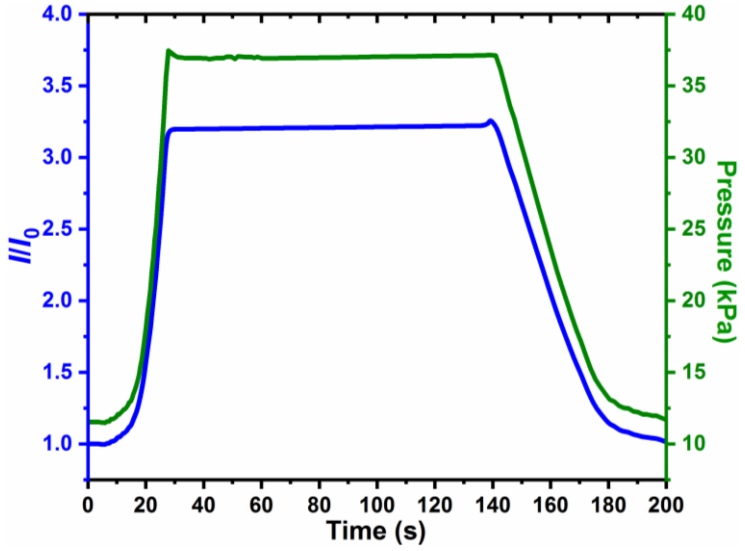

Figure A4.7. Relative current (I/I_0) for plain $MAPbI_3$ device increases with the increase in pressure from 0 kPa to 37 kPa and is maintained constant under a constant load.

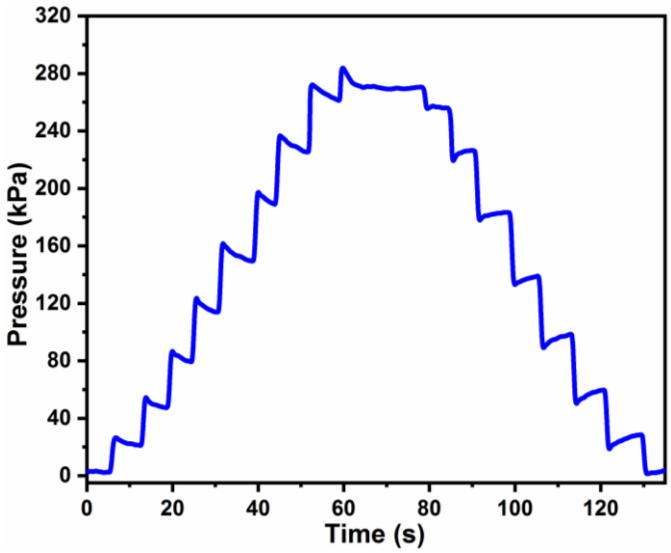

Figure A4.8. Pressure curves as a step function recorded using two glass slides.

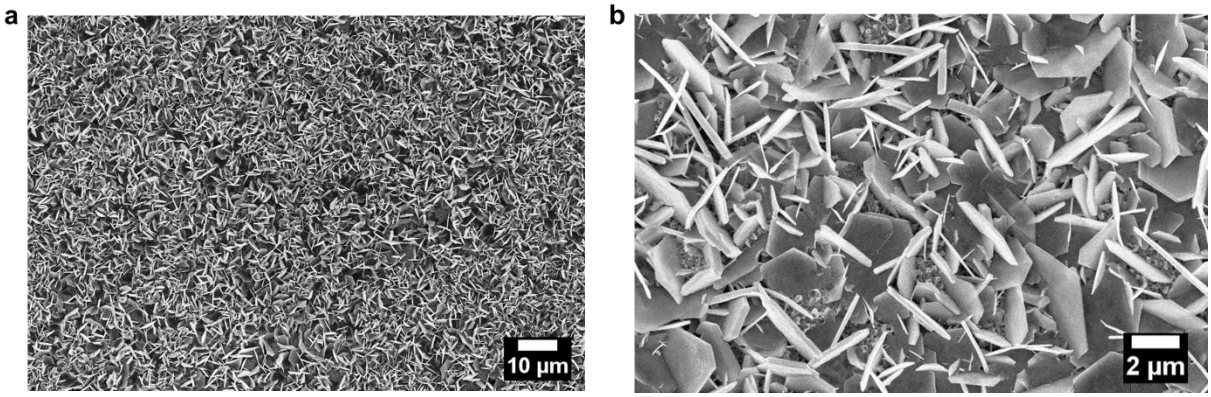

Figure A4.9. FESEM images of the ZnO sheets after 100 load cycles of 200 kPa pressure shows no change in the morphology, thus confirming the stability of the device.

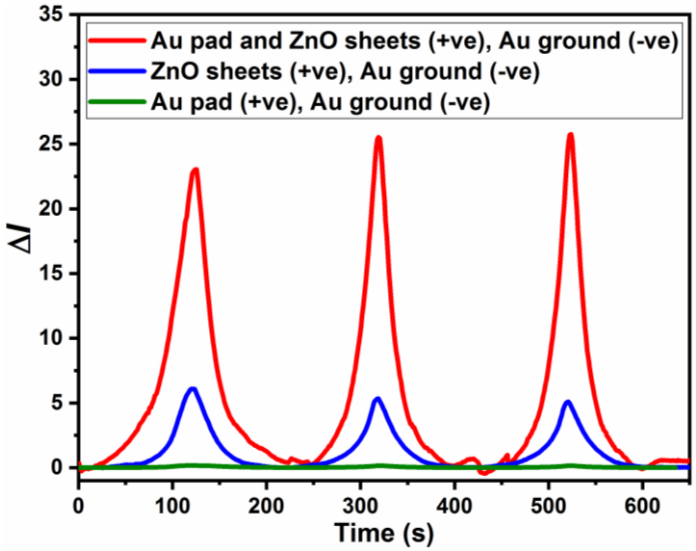

Figure A4.10. Change in the current (ΔI) for plain $MAPbI_3$ with different circuits after initial poling at 1.5 V μm^{-1} for 5 min with a maximum of 37 kPa pressure under 0.1 sun illumination in air. The red curve shows the total current modulations in the device, the blue curve represents the current modulations only through the ZnO layer and the green curve displays the current modulations through only the perovskite layer.

We observed a higher change in current when both the Au pad and ZnO sheets on ITO are positive and Au ground is negative. This is attributed to overall more electron extraction by Au and ZnO sheets. In contrast, when the ZnO sheets on ITO are positive and Au ground is negative; ΔI is less because in this case, only the ZnO sheets can extract the electron. While in the case where the Au pad is positive and Au ground is negative, the pressing of ZnO sheets on $MAPbI_3$ will not make any difference in current.

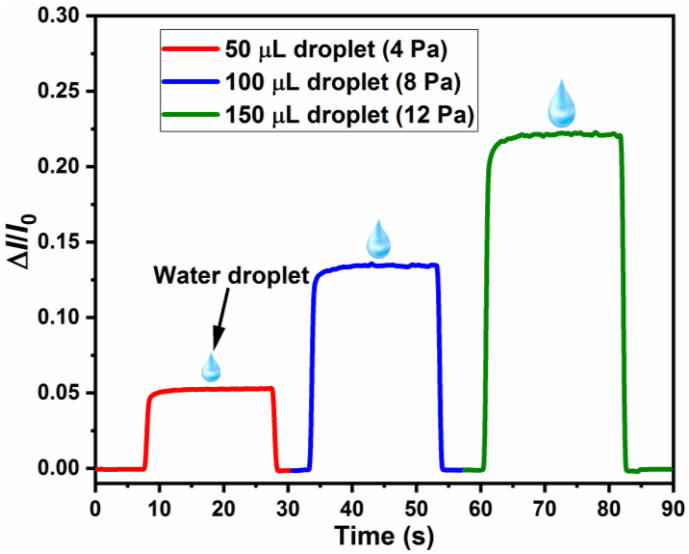

Figure A4.11. Minimum pressure limit of detection for the 1 wt % PS-$MAPbI_3$ sensor.

The 1 wt % PS-$MAPbI_3$ device once poled at 5 V μm^{-1} for 5 min can sense the pressure changes due to the placing of small water droplets. On placing the 50 µL water droplet on the device which corresponds to an extremely low static pressure of 4 Pa, the relative current increased from 0 to 0.05 and it reverts to the original level on removing the 50 µL droplet. Further on increasing the volume of the water droplets from 50 µL (4 Pa) to 150 µL (12 Pa), the relative current also increases from 0.05 to 0.22. The device also tracks the removal of the droplets. There is no significant noise in the signals even at the ultralow pressure regime which signifies the stable operation of the device.

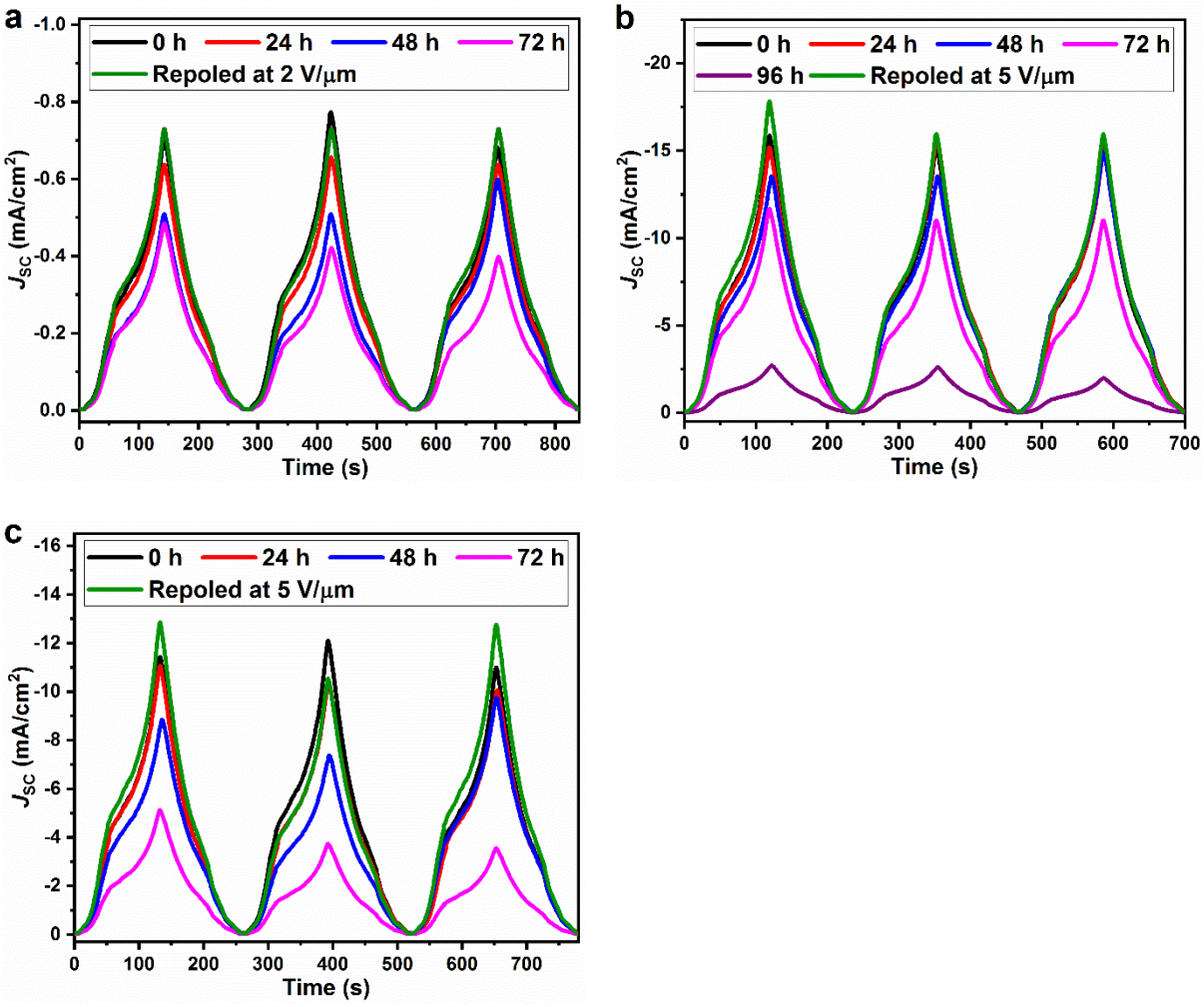

Figure A4.12. Self-powered operation of (a) Plain $MAPbI_3$, (b) 3 wt % PS-$MAPbI_3$, and (c) 7 wt % PS-$MAPbI_3$ pressure sensors.

At maximum poling fields of 2 V μm^{-1}, the J_{sc} response from plain $MAPbI_3$ devices to load cycles of 111 kPa is maintained for almost 48 h. Afterward, the J_{sc} decreased to half of its initial value for 72 h. We observed the decrease in the base J_{sc} (at base pressure) with time, which relates to the loss of poling. But the device can be repoled to recover its performance and can be reused again. Similarly, the 3 wt % and 7 wt % PS-$MAPbI_3$ devices once poled at 5 V μm^{-1} field can easily function for 72 h and 48 h, respectively without an active power source.

Table A4.1. Comparison of the operating voltage, dynamic pressure range, linear sensing response, and sensitivity of different reported pressure sensors.

Sensing principle	Key material	Operating voltage (V)	Pressure range (kPa)	Linearity	Sensitivity (kPa^{-1})	Ref.
Transistor	ZnO nanosheets and PS-$MAPbI_3$	Self-powered	0.004 – 450	Linear	20	This work
Transistor	Printed SWCNT active-matrix backplane	10	1 – 20	Linear	8	[226]
Transistor	Silver nanowires embedded PDMS electrode	1	0.0009 – 6.6	Linear upto 0.6 kPa	9.9 (<0.6 kPa)–0.6 (0.6–6.6 kPa)	[227]
Transistor	Indium-gallium-zinc oxide and polyurethane	4	5 – 50	Linear	43.6 (50 kPa)	[228]
Transistor	Graphene with air-dielectric layers	25	0.25 – 3000	Linear upto 500 kPa	2.05×10^{-4} (<500 kPa)–9.43×10^{-6} (500–3000 kPa)	[229]
Transistor	Microstructured PDMS and PII2T-Si	200	0.03 – 55	Linear upto 8 kPa	8.2 (<8 kPa)–0.38 (30–55 kPa)	[202]
Transistor	Graphene and ion gel	2	5 – 40	Linear	0.12	[200]
Piezoresistive	Ultrathin gold nanowires	1.5	0.013 – 5	Linear	1.14	[230]
Piezoresistive	Graphene–polyurethane sponge	1	0.009 – 10	Linear upto 2 kPa	0.26 (<2 kPa), 0.03 (2–10 kPa)	[95]
Piezoresistive	SWNT and PDMS	2	0.0006 – 1.2	Linear upto 0.3 kPa	1.8 (<0.3 kPa)	[231]
Piezoresistive	Pt-coated polymer nanofibres	0.5	0.003 – 1.5	Linear	11.45	[92]
Piezoresistive	Hollow-sphere polypyrrole structure	–	0.0008 – 100	Linear	7.7 (0.1 kPa), 0.4 (1 kPa), 0.004 (100 kPa)	[96]
Piezoresistive	rGO and PDMS microstructure	–	0.016 – 40	Linear upto 2.6	25.1 (<2.6 kPa), 0.45	[232]

				kPa	(2.6–40 kPa)	
Piezoresistive	Laser-scribed graphene	–	5 – 113	Nonlinear	0.96 (<50 kPa), 0.005 (50–113 kPa)	[206]
Piezoresistive	CNT–composite elastomers	10	0.0002 – 59	Linear upto 0.5 kPa	15.1 (<0.5 kPa)	[233]
Piezoresistive	Multilayer Microdome-patterned rGO/PVDF composite	–	0.0013 − 353	Linear	47.7	[90]
Piezoelectric	Micropattern PDMS structures and Ag nanowires	Self-powered	0.0021 – 13	Linear upto 3.2 kPa	0.31 (<3.2 kPa), 0.01 (3.2–13 kPa)	[173]
Piezoelectric	PDMS and PAAm-LiCl hydrogel	Self-powered	1.3 – 101.2	Linear upto 70 kPa	0.013 (<70 kPa)	[99]
Capacitive	Microstructured PDMS	80	0.003 – 7	Linear upto 2 kPa	0.55 (<2 kPa)–0.15 (2–7 kPa)	[204]
Capacitive	Ecoflex dielectric layer and Ag electrode	–	0.0073 – 360	Linear upto 16 kPa	0.0224 (<16 kPa), 0.00125 (16–360 kPa)	[234]
Capacitive	Single-layer graphene	–	0.11 – 80	Linear upto 20 kPa	0.0093 (<20 kPa)–0.0077 (60–80 kPa)	[205]
Capacitive	Graphene	–	0.5 – 450	Nonlinear	0.002	[235]
Capacitive	Carbon Nanotube and Ecoflex	–	0.00016 – 130	Linear upto 5 kPa	0.601 (<5 kPa), 0.077 (30–130 kPa)	[236]
Capacitive	Carbon nanotubes	–	50 – 900	Linear	0.23×10^{-3}	[93]

Appendix for Chapter 5

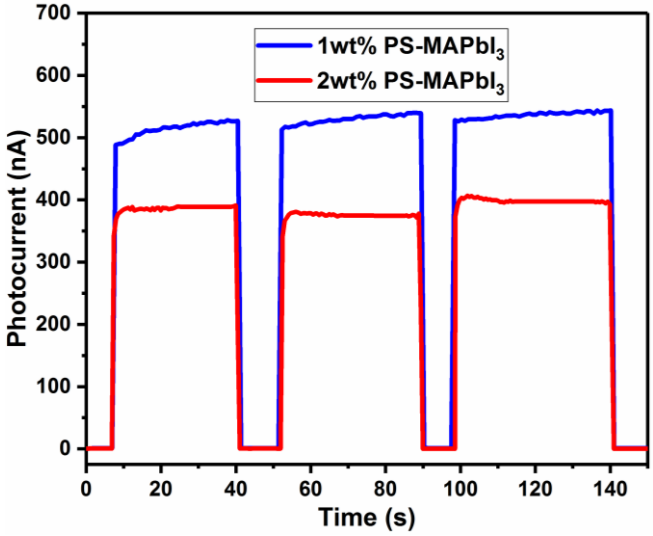

Figure A5.1. Photocurrent from unpoled 1 wt % and 2 wt % PS-$MAPbI_3$ devices at an applied external bias of 5 V. We observed that the photocurrent for 2 wt % PS-$MAPbI_3$ devices is less than the 1wt % PS-$MAPbI_3$ devices.

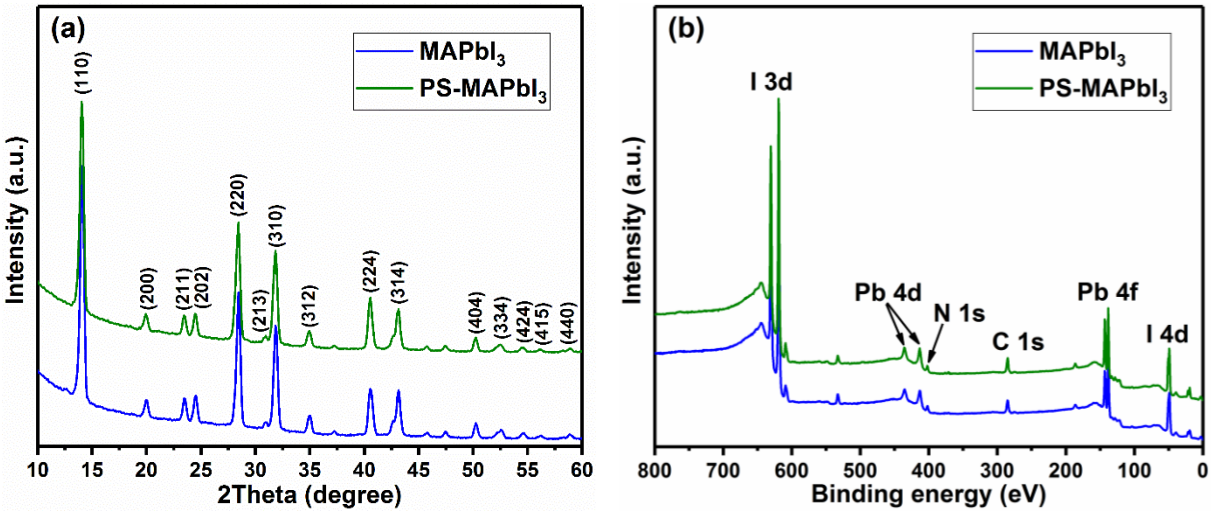

Figure A5.2. (a) X-ray diffraction patterns of plain $MAPbI_3$ and PS-$MAPbI_3$ films. (b) XPS spectra of $MAPbI_3$ and PS-$MAPbI_3$ films. The diffraction peaks from both $MAPbI_3$ and PS-$MAPbI_3$ exhibit tetragonal symmetry with the *I*4/*mcm* space group. From the XPS survey scan, we observed that the presence of C, N, I, and Pb elements and their atomic ratios in both films show a reasonably good $MAPbI_3$ stoichiometry. XRD and XPS results show a negligible change in the crystalline phase of $MAPbI_3$ with and without PS.

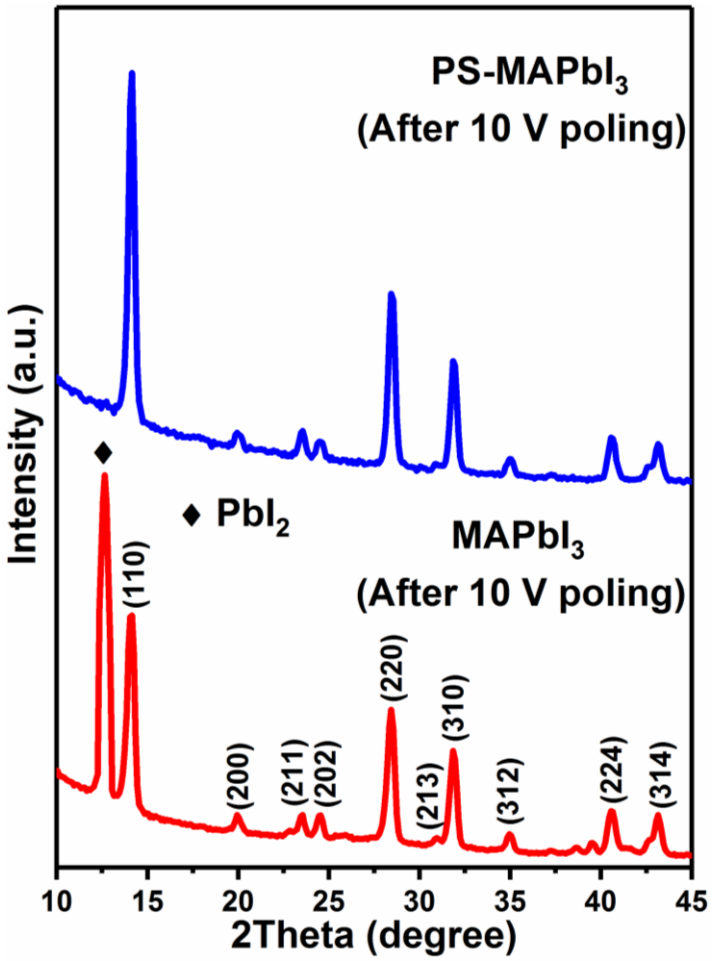

Figure A5.3. XRD patterns of plain $MAPbI_3$ and PS-$MAPbI_3$ films after 10 V poling for 10 min in air and under light illumination. In the case of the PS-$MAPbI_3$ film after 10 V, there is no significant change in the crystal structure and the diffraction peaks are in good agreement with the tetragonal perovskite structure. While for $MAPbI_3$ film after 10 V poling, the new phase PbI_2 starts appearing, indicating the degradation of the perovskite material. This implies that the PS-$MAPbI_3$ film is stable after high poling field strength.

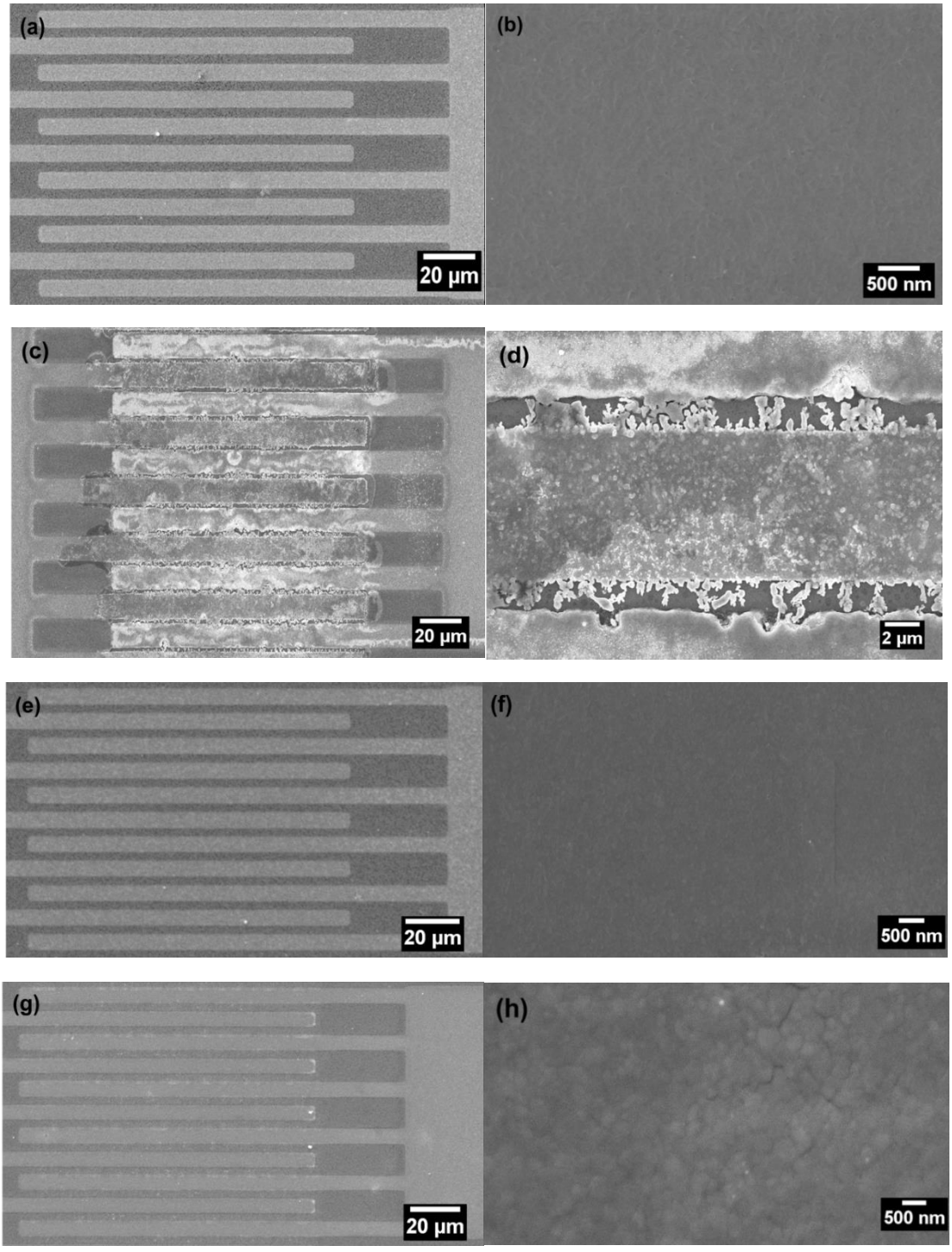

Figure A5.4. FESEM (low and high magnification) images of (a−d) Plain $MAPbI_3$, and (e−h) PS-$MAPbI_3$ films after (a,b,e,f) 5 V poling, and (c,d,g,h) 10 V poling for 10 min in air and under light illumination. Both $MAPbI_3$ and PS-$MAPbI_3$ films are stable after 5 V poling, as we did not observe any change in morphology (Figure A5.4a,b and e,f). But after 10 V poling, many plane-dendritic structures (Figure A5.4c,d) formed in $MAPbI_3$ film which is due to more severe ion migration. While the morphology of PS-$MAPbI_3$ film remains intact even after 10 V (Figure A5.4g,h), confirming the effect of PS in increasing the stability of the PS-$MAPbI_3$ devices.

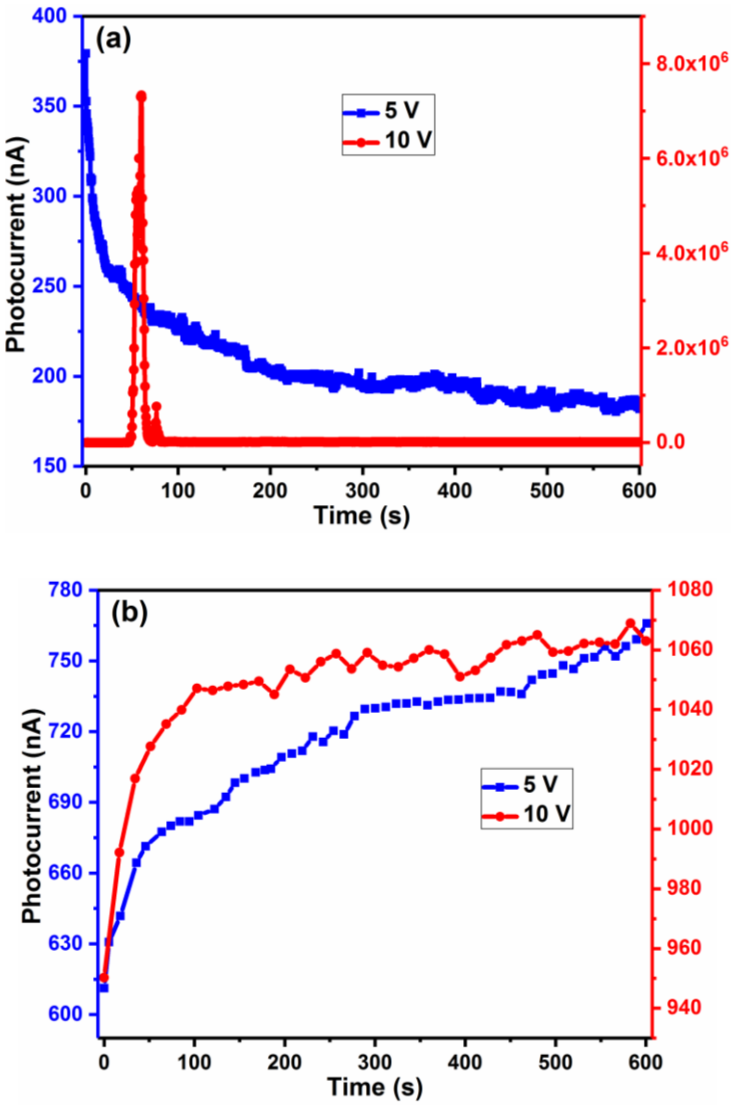

Figure A5.5. Photocurrent of (a) $MAPbI_3$, and (b) PS-$MAPbI_3$ devices during 5 and 10 V poling in air and under light illumination.

It is observed that the photocurrent for plain $MAPbI_3$ device (Figure A5.5a) measured during 10 V poling suddenly spikes to several mA which is 4 orders of magnitude more than the current at 5 V, such high current results in the segregation of the ions which leads to the formation of PbI_2. In contrast, for the PS-$MAPbI_3$ device, the photocurrent is in the range of 610 nA to 1060 nA during 5 and 10 V poling (Figure A5.5b), which reveals that the presence of PS leads to greater stability in the $MAPbI_3$ structure by suppressing the ion migration effects.

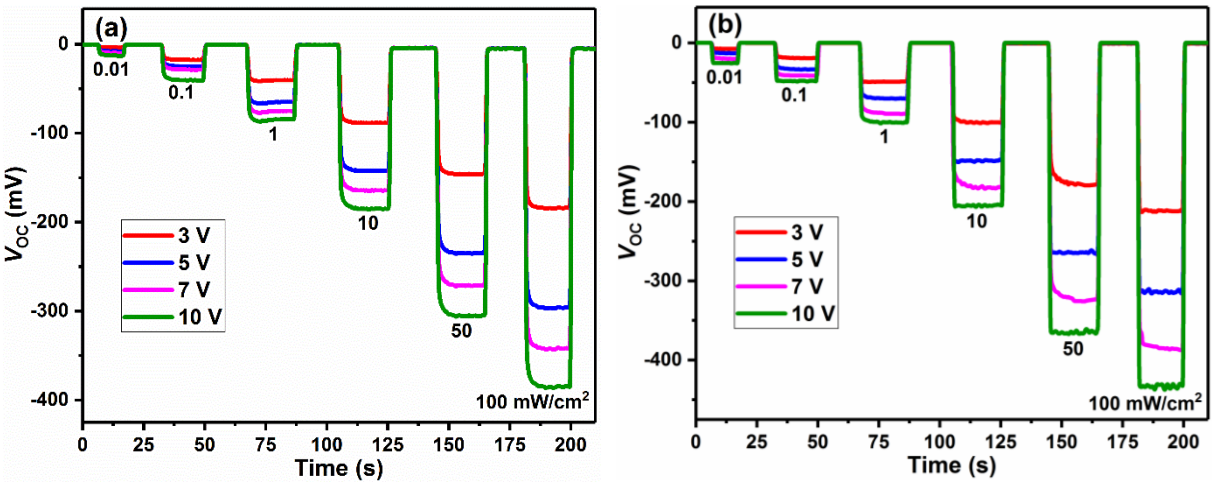

Figure A5.6. V_{oc} response from (a) $MAPbI_3$, and (b) PS-$MAPbI_3$ devices with no applied bias to various light illumination intensities, after poling at different voltages for 10 min in air and under light illumination (1.0 sun). The V_{oc} increases monotonically with the poling field strength in both devices. But in the case of the PS-$MAPbI_3$ device, the V_{oc} generated is larger than the plain $MAPbI_3$ device.

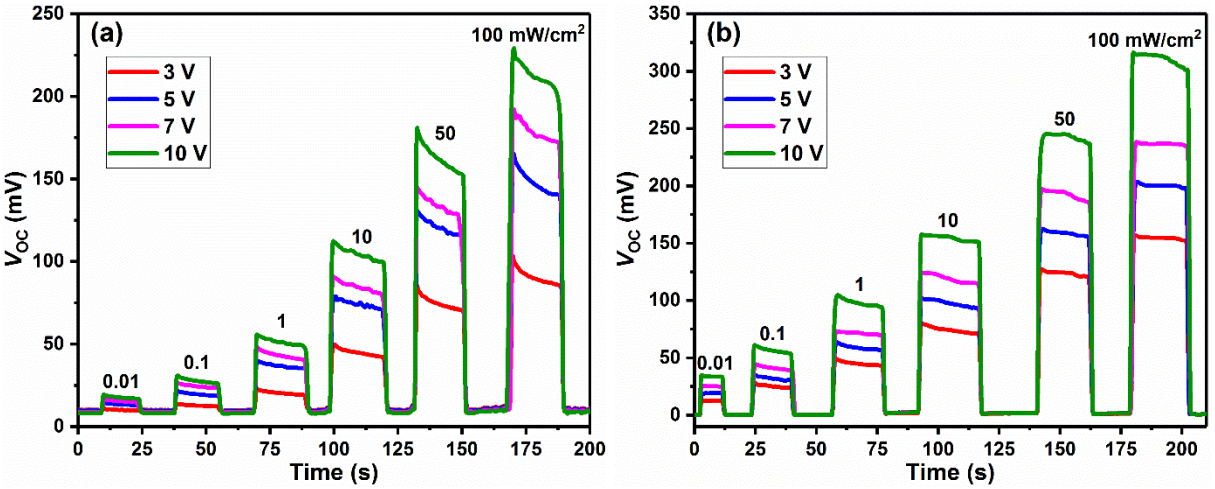

Figure A5.7. V_{oc} response from (a) $MAPbI_3$, and (b) PS-$MAPbI_3$ based photodetectors with no applied bias to various light intensities, after poling at different voltages under N_2 and in dark conditions. The distinction between the two poling conditions is based on the reversal of the sign in V_{oc}. We also observed that the V_{oc} decays rapidly for the plain $MAPbI_3$ device, in contrast, the PS-$MAPbI_3$ device has a more stable response.

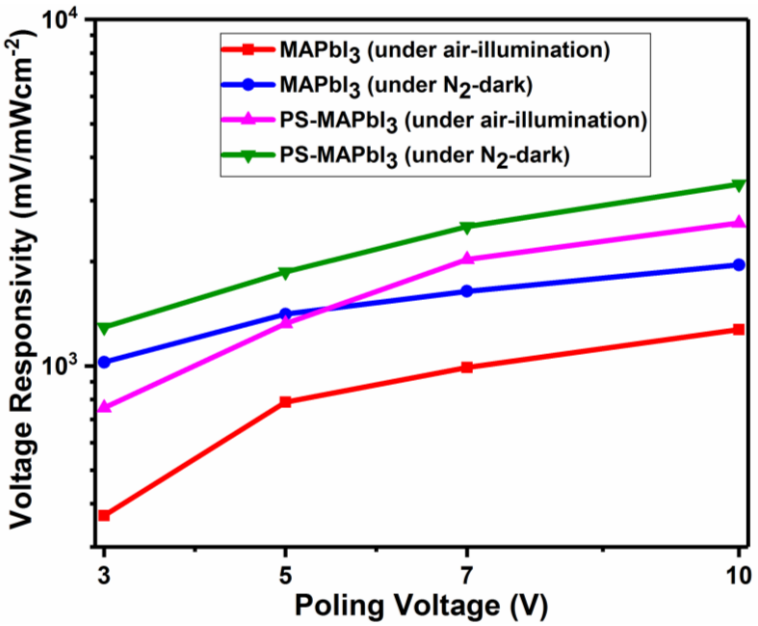

Figure A5.8. Comparison of the Voltage responsivity for $MAPbI_3$ and PS-$MAPbI_3$ devices under both poling conditions. We observed that the PS-$MAPbI_3$ device, when poled in dark and under N_2, achieves a large responsivity of 3346 $mV/mWcm^{-2}$.

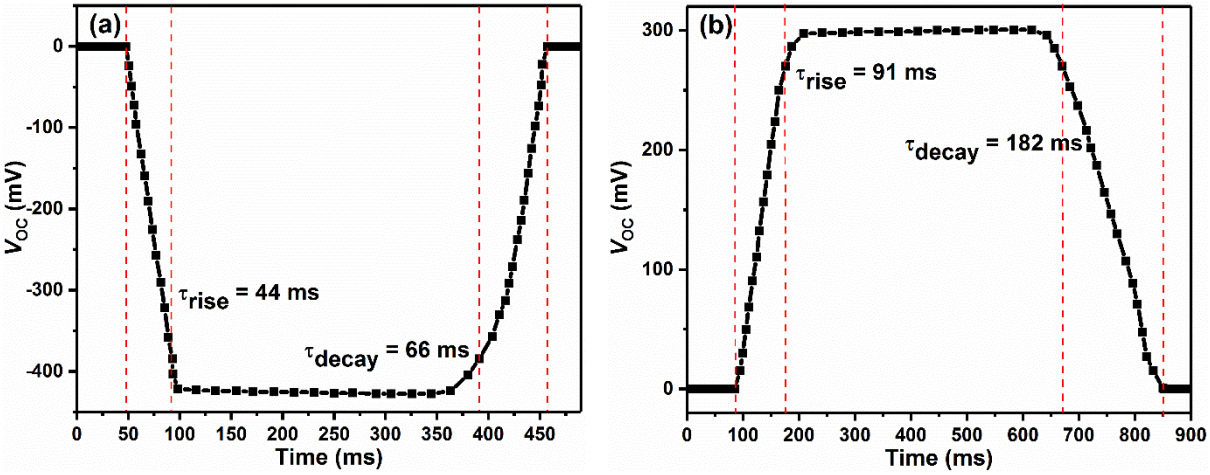

Figure A5.9. Rise and decay time observed in V_{oc} for PS-$MAPbI_3$ device when poled under (a) Air and light illumination, and (b) N_2 and dark condition. We observed a faster response time from the PS-$MAPbI_3$ devices poled in air and under illumination.

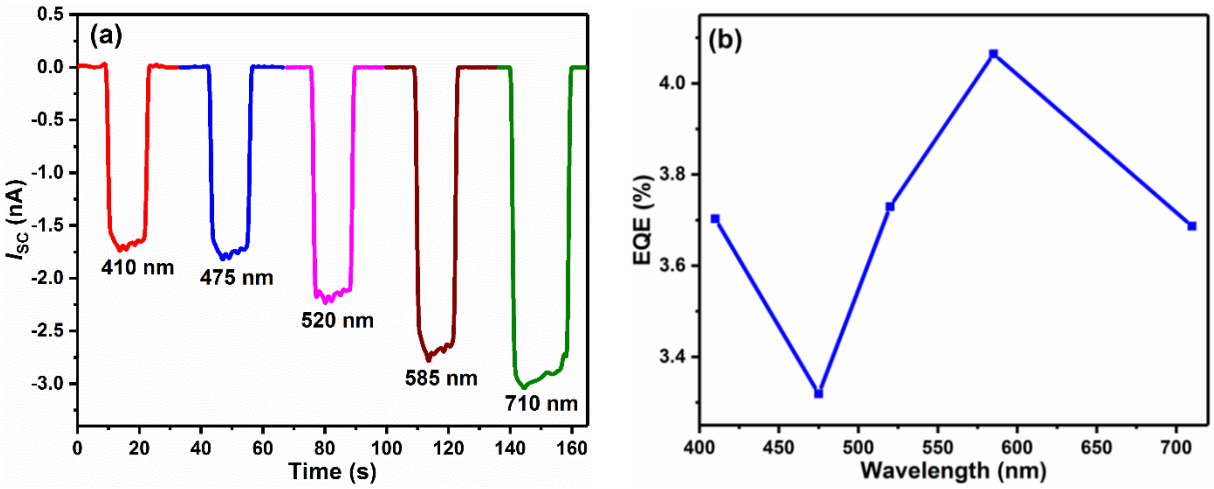

Figure A5.10. (a) I_{sc} response, and (b) External quantum efficiency (EQE) from PS-$MAPbI_3$ device at different wavelengths under 1 mW cm^{-2} illumination intensity, after poling at 10 V for 10 min in air and under light illumination. The device shows a monotonic increase in the photoresponse as a function of irradiance wavelength in the range of 410 to 710 nm. The EQE observed in the range of 3.3−4.1% (at 1 mW cm^{-2} illumination) in the visible spectrum is comparable to other planar $MAPbI_3$ photodetectors.

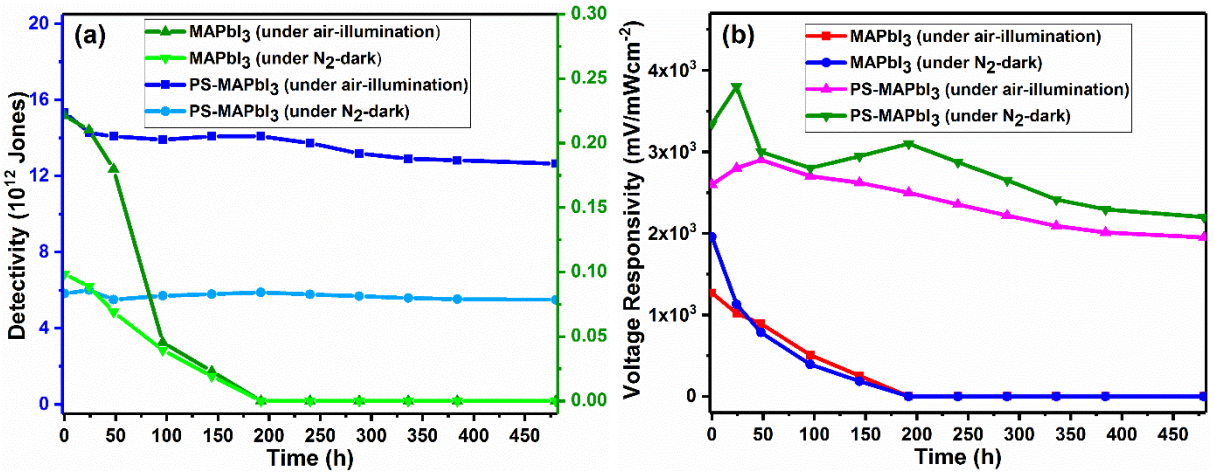

Figure A5.11. Comparison of the stability in terms of (a) Current detectivity, and (b) Voltage responsivity for $MAPbI_3$ and PS-$MAPbI_3$ based photodetectors under both poling conditions after exposing the devices to an ambient condition with 30−40% relative humidity for 480 h (20 days). It was observed that the plain $MAPbI_3$ devices degrade completely within 192 h (8 days). While the PS-$MAPbI_3$ devices retain 85-90% of the performance even after 20 days.

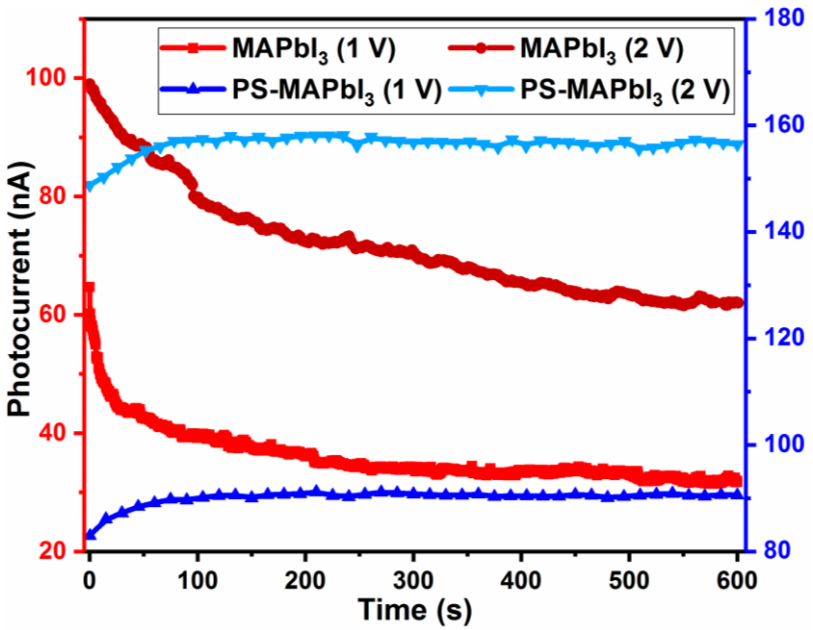

Figure A5.12. Photocurrent from unpoled $MAPbI_3$ and PS-$MAPbI_3$ devices at different external biases and at illumination intensity of 100 mW cm^{-2}. We observed that the PS-$MAPbI_3$ device shows a higher photocurrent with no observable decay. In contrast, the $MAPbI_3$ device shows a lower photocurrent which decays as a function of time due to ion migration effects or charge carrier recombination. This implies that the presence of PS in the $MAPbI_3$ devices greatly reduced the ion migration effects and recombination of charge carriers which consequently improved the stability and performance of the photodetector.